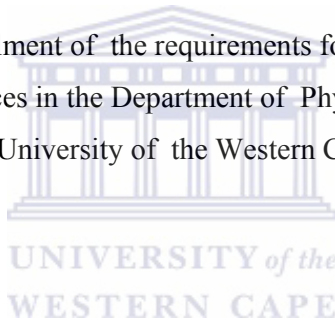


**SIGNATURE SPLITTING AND INVERSION IN THE $^{186-194}\text{Au}$ NUCLEI
PREDICTED BY THE TOTAL ROUTHIAN SURFACE (TRS) AND
CRANKED SHELL MODEL (CSM) CALCULATIONS**

Obed Shirinda

Thesis presented in fulfillment of the requirements for the degree of Master of
Sciences in the Department of Physics at
the University of the Western Cape.



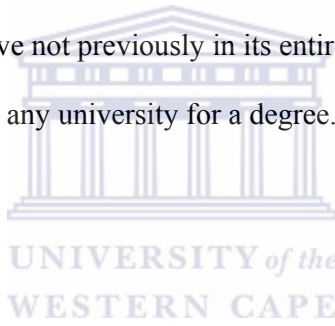
Supervisor: Dr. E. A. Gueorguieva
Nuclear Physics Group
iThemba LABS

Co-supervisor: Prof. R. Lindsay
Department of Physics
University of the Western Cape

February 2007

DECLARATION

I, the undersigned, hereby declare that the work contained in this thesis is my own original work and that I have not previously in its entirety or in part submitted it at any university for a degree.



Signature:

Date:

ABSTRACT

SIGNATURE SPLITTING AND INVERSION IN THE $^{186-194}\text{Au}$ NUCLEI PREDICTED BY THE TRS AND CSM CALCULATIONS

Obed Shirinda

February 2007

iThemba LABS, P. O. Box 722, Somerset West, 7129, South Africa

The nearly oblate deformed Au nuclei show rotational bands built on multi quasiparticle excitations [Bou89, Bou92, Gue03, Gue02, Gue01, Ven92]. Several of these bands are built on rotationally aligned high-j proton and neutron excitations. In many cases bands consisting of two or three signature-partner E2 sequences are observed. For some of these bands signature inversion is found and this feature gives a great challenge to the theoretical models. In this study we performed TRS and CSM calculations for all the high-j rotational bands in the $^{186-194}\text{Au}$ nuclei aiming to predict the signature splitting and inversion phenomena, alignments, gains in alignment and band crossing frequencies observed. Thus TRS calculations were performed for the $\pi h_{11/2}^{-1} \otimes \nu i_{13/2}^{-1}$, $\pi h_{11/2}^{-1} \otimes \nu i_{13/2}^{-3}$ and $\pi h_{11/2}^{-1} \otimes \nu i_{13/2}^{-2} h_{9/2}^{-1}$ bands in the odd-odd $^{186-194}\text{Au}$ nuclei, and for the $\pi h_{11/2}^{-1}$, $\pi h_{11/2}^{-1} \otimes \nu i_{13/2}^{-2}$, and $\pi h_{11/2}^{-1} \otimes \nu i_{13/2}^{-1} h_{9/2}^{-1}$ bands in the odd-even $^{187-193}\text{Au}$ nuclei. A very good agreement was obtained between the theoretical predictions and experiment data, although discrepancies have been found for the band crossing frequencies and signature splitting in some of the bands.

ACKNOWLEDGEMENTS

I wish to express my sincere gratitude to the following for making the realization of this thesis possible:

- Dr E. Gueorguieva¹ for supervision, support, guidance and encouragement throughout the duration of this project,
- Prof R. Lindsay² for the guidance and support throughout the duration of this project,
- Prof R. A. Wyss³, Dr R. A. Bark¹ and Dr D. G. Roux² for reading this entire thesis,
- Dr J. J. Lawrie¹ for allowing me to pursue this research in the Physics group,
- All staff members within the Physics group at iThemba LABS,
- My parents and family members, for their guidance, support and so many things, just being there for me in time I needed them most and for inspiring me in my studies,
- The postgraduate students past and present, male and female at iThemba LABS for supporting me,
- The University of the Western Cape (UWC) and iThemba LABS for the funding I received,
- The Almighty and all my ancestors.

This work is dedicated to my parents (Mr. P. W. Shirinda and Mrs. K. A. Shirinda).

Obed Shirinda

February 2007

-
1. *iThemba LABS, P. O. Box 722, Somerset West, 7129, South Africa*
 2. *Dept. of Physics, University of the Western Cape, Private Bag X17, Bellville 7535, South Africa*
 3. *Royal Institute of Technology, Frescativagen 24, S-10405 Stockholm, Sweden*

CONTENTS

CHAPTER 1 Introduction.....	1
CHAPTER 2 Nuclear theoretical models	3
2.1 Nuclear excitations and deformation parameters.....	3
2.1.1 Nuclear excitations	3
2.1.1.1 Non-collective (single particle) motion.....	3
2.1.1.2 Collective motion.....	3
2.2 Nuclear deformation parameters	4
2.3 The shell model	8
2.3.1 The shell model Hamiltonian	8
2.3.2 Nuclear potential well	9
2.3.3 Modification of the harmonic oscillator potential	13
2.3.3.1 Addition of l^2 term	13
2.3.3.2 Addition of spin-orbit interaction term ($\vec{l} \cdot \vec{s}$)	14
2.3.4 Example of the application of the shell model	15
2.4 The deformed shell model	16
2.4.1 Splitting of the levels according to the projection K	19
2.5 Rotational motion	22
2.5.1 Moment of inertia.....	25
2.6 The asymmetric rotor model	28
2.7 The particle-plus-rotor model (PRM).....	29
2.7.1 The axial symmetry case	31
2.7.1.1 The strong coupling limit (deformation alignment).....	33
2.7.1.2 The decoupling limit (rotational alignment).....	34

2.8	The triaxial particle-plus-rotor model	34
2.9	The cranked shell model (CSM)	36
2.9.1	The cranking Hamiltonian.....	36
2.9.2	Symmetries in the cranking Hamiltonian	38
2.9.3	Comparison of experimental observables with CSM theoretical quantities.....	39
2.10	Total potential energy at $\omega = 0$	41
2.10.1	Liquid drop model (LDM)	41
2.10.2	The Strutinsky shell correction method.....	42
2.11	Total potential energy at $\omega \neq 0$ and $I \neq 0$	44
2.11.1	The rotating liquid drop model.....	44
2.11.2	Shell correction method for $I \neq 0$	44
2.12	The total Routhian surface (TRS) calculations	45
2.13	Signature inversion phenomenon	47
 CHAPTER 3 Results from the TRS and CSM		
	<i>calculations for the bands in the $^{186-194}\text{Au}$</i>	
	<i>nuclei</i>	48
3.1	Previous calculations performed for the rotational	
	bands in the $^{186-194}\text{Au}$ nuclei and suggested	
	interpretation	48
3.1.1	The particle-plus-rotor model.....	48
3.1.2	Cranked shell model.....	49
3.1.3	Total Routhian surface (TRS) together with cranked shell model (CSM)	49

3.2	Experimental quantities in rotating frame	52
3.2.1	Calculations for the odd-odd $^{186-194}\text{Au}$ nuclei	52
3.2.2	Calculations for the odd-even $^{187-193}\text{Au}$ nuclei.....	54
3.3	Theoretical Calculations.....	55
3.3.1	TRS Calculations.....	55
3.3.2	TRS calculations for the odd-odd $^{186-194}\text{Au}$ nuclei.....	59
3.3.2.1	The 11^- and 12^- bands of the odd-odd $^{186-194}\text{Au}$ isotopes	59
3.3.2.2	The 22^- band of the odd-odd $^{186-194}\text{Au}$ isotopes.....	63
3.3.2.3	The 20^+ , 21^+ and 22^+ bands of the odd-odd $^{186-194}\text{Au}$ isotopes	64
3.3.3	TRS calculations for the odd-even $^{187-193}\text{Au}$ nuclei	69
3.3.3.1	The $11/2^-$ bands of the odd-even $^{187-193}\text{Au}$ nuclei.....	69
3.3.3.2	The $31/2^-$, $33/2^-$ and $35/2^-$ bands of the odd-even $^{187-193}\text{Au}$ nuclei	70
3.3.3.3	The $31/2^+$ and $33/2^+$ bands of the odd-even $^{187-193}\text{Au}$ nuclei	74
3.3.4	CSM calculations	77
3.3.5	CSM calculations for the odd-odd $^{186-194}\text{Au}$ nuclei.....	78
3.3.5.1	The 11^- and 12^- bands of the odd-odd $^{186-194}\text{Au}$ nuclei	79
3.3.5.2	The 22^- band of the odd-odd $^{186-194}\text{Au}$ nuclei.....	81
3.3.5.3	The 20^+ , 21^+ and 22^+ bands of the odd-odd $^{186-194}\text{Au}$ nuclei.....	82
3.3.6	CSM calculations for the odd-even $^{187-193}\text{Au}$ nuclei	83
3.3.6.1	The $11/2^-$ band of the odd-even $^{187-193}\text{Au}$ nuclei	83
3.3.6.2	The $31/2^-$, $33/2^-$ and $35/2^-$ bands of the odd-even $^{187-193}\text{Au}$ nuclei	84
3.3.6.3	The $31/2^+$ and $33/2^+$ bands of the odd-even $^{187-193}\text{Au}$ nuclei	85
CHAPTER 4	Discussion.....	86
4.1.1	Experimental and theoretical band crossing frequencies, alignments and alignment gains	86
4.1.1.1	The 11^- and 12^- bands of the odd-odd $^{186-194}\text{Au}$ nuclei.....	86
4.1.1.2	The 22^- bands of the odd-odd $^{186-194}\text{Au}$ nuclei	87
4.1.1.3	The 20^+ , 21^+ and 22^+ bands of the odd-odd $^{186-194}\text{Au}$ nuclei.....	88
4.1.1.4	The $11/2^-$ band of the odd-even $^{187-193}\text{Au}$ nuclei	89
4.1.1.5	The $31/2^-$, $33/2^-$ and $35/2^-$ bands of the odd-even $^{187-193}\text{Au}$ nuclei	90
4.1.1.6	The $31/2^+$ and $33/2^+$ bands of the odd-even $^{187-193}\text{Au}$ nuclei.....	91
4.2	Routhians and signature splitting	92

<i>CHAPTER 5 Summary</i>	<i>126</i>
<i>REFERENCES</i>	<i>128</i>
<i>Appendix A Level schemes of the ¹⁸⁶⁻¹⁹⁴Au nuclei</i>	<i>132</i>
<i>Appendix B Tables of experimental quantities</i>	<i>142</i>
<i>Appendix C Tables of results from CSM calculations</i>	<i>153</i>



LIST OF FIGURES

2.1:	Schematic representation of dipole, quadrupole, octupole and hexadecupole deformations [Mab03].	4
2.2:	Diagrammatic representation of the nuclear shape ($\lambda = 2$) in the β_2, γ plane [And76].	6
2.3:	A comparison of two-dimensional harmonic oscillator potential, square well potential and Woods-Saxon potential [Kee99].	10
2.4:	Energy levels in a modified oscillator potential. The levels on the left are those for the harmonic oscillator potential. These are split by the l^2 term to produce the second set of levels, and then again by the spin-orbit term to produce the experimentally observed shells on the right [Kee99].	12
2.5:	The filling of shells in ${}^{15}_8O_7$ and ${}^{17}_8O_9$. The filled protons shells do not contribute to the structure. The properties of the ground state are determined primarily by the odd neutron [Kra98a].	15
2.6:	Single particle orbits with $j = 7/2$ and the possible projections of j along the symmetry axis, for prolate (top) and oblate (bottom) deformations. The possible projections are $\Omega = 1/2, 3/2, 5/2, 7/2$ (for clarity only the positive projections are shown). Note that in the prolate case, orbit 1 lies closest (on the average) to the core and will interact most strongly with the core while in the oblate case, it is orbit 4 that has the strongest interaction with the core [Kra98b].	20
2.7:	Energy levels for neutrons in a prolate deformed potential. The numbers in the brackets label the states, solid lines show states with positive parity and dashed lines show negative parity states [Gus67].	21
2.8:	Schematic representation of the spherical (a), oblate (b) and prolate (c) nuclear shapes. The x-axis represents the symmetric axis for this nucleus [Mab03].	22
2.9:	Schematic of the coupling of the collective angular momentum \vec{R} , and the intrinsic angular momentum of valence nucleons \vec{J} . The projection of the total angular momentum \vec{I} , onto the symmetry axis is K [Gre99].	23
2.10:	The energy eigenvalues of a deformed asymmetric rotor with the hydrodynamic moment of inertia (From [Mey75]).	29
2.11:	Coupling schemes in the particle-plus-rotor model: a) strong coupling, b) rotational alignment [Rin90].	33
2.12:	Spectrum of $j = 11/2$ particle coupled to an asymmetric rotor as function of γ , for Fermi surface at the bottom of the $j = 11/2$ shell. The states with	

	$(\pi, \alpha) = (+, +1/2)$ are represented with bold-dashed and faint-dashed lines, $(+, -1/2)$ with solid and dotted lines (From [Mey74]).	35
3.1:	Cranked shell model calculations for ^{191}Au performed for protons and neutrons. A Woods-Saxon potential with universal parameters is used. The deformation of $\beta_2 = 0.14$ and $\beta_4 = -0.02$, appropriate for ^{191}Au , is chosen. The panels from top to bottom correspond to $\gamma = -60^\circ, -70^\circ, -80^\circ$, and -90° . The Routhians with $(\pi, \alpha) = (+, +1/2)$ are represented with solid line, $(+, -1/2)$ with a dotted line, $(-, +1/2)$ with dash-dotted line, and $(-, -1/2)$ with dashed line [Gue02].	51
3.3:	TRS plots showing the nuclear shapes for the eB configuration of ^{186}Au as the rotational frequency increases. The left plot corresponds to the 11^- band, the middle plot shows the potential energy surface above the first $\nu i_{13/2}$ band crossing and the right plot is related to the nuclear shape above the second band crossing. The rotational frequency is measured in MeV/h, and the proton (Ip), neutron (In) and total (I) aligned angular momenta are given in \hbar .	61
3.4:	TRS plots showing the nuclear shapes for the eA configuration of ^{186}Au as the rotational frequency increases. The left plot corresponds to the 12^- band, the middle plot shows the potential energy surface above the first $\nu i_{13/2}$ (22^- band) band crossing and the right plot is related to the nuclear shape above the second band crossing. The rotational frequency is measured in MeV/h and the proton (Ip), neutron (In) and total (I) aligned angular momenta are given in \hbar .	62
3.5:	TRS plots showing the nuclear shapes for the eB configuration of ^{190}Au as the rotational frequency increases. The left plot corresponds to the 11^- band, the middle plot shows the potential energy surface above the first $\nu i_{13/2}$ band crossing and the right plot is related to the nuclear shape above the second band crossing. The rotational frequency is measured in MeV/h, and the proton (Ip), neutron (In) and total (I) aligned angular momenta are given in \hbar .	62
3.6:	TRS plots showing the nuclear shapes for the eA configuration of ^{190}Au as the rotational frequency increases. The left plot corresponds to the 12^- band, the middle plot shows the potential energy surface above the first $\nu i_{13/2}$ band crossing (22^- band) and the right plot is related to the nuclear shape above the second $\nu i_{13/2}$ band crossing. The rotational frequency is measured in MeV/h and the proton (Ip), neutron (In) and total (I) aligned angular momenta are given in \hbar .	63
3.7:	TRS plots showing the nuclear shapes for the eF configuration of ^{186}Au as the rotational frequency increases. The left plot corresponds to the 20^+ band, and the right plot corresponds to the same configuration but after the $\nu i_{13/2}$ band crossing. The rotational frequency is measured in MeV/h and the proton (Ip), neutron (In) and total (I) aligned angular momenta are given in \hbar .	66

3.8:	TRS plots showing the nuclear shapes for the eFAC configuration of ^{186}Au as the rotational frequency increases. The left plot corresponds to the 21^+ band, and the right plot corresponds to the same configuration but after the $U_{i_{13/2}}$ band crossing. The rotational frequency is measured in MeV/ \hbar and the proton (Ip), neutron (In) and total (I) aligned angular momenta are given in \hbar	66
3.9:	TRS plots showing the nuclear shapes for the eFAB configuration of ^{186}Au as the rotational frequency increases. The left plot corresponds to the 22^+ band, and the right plot corresponds to the same configuration but after the $U_{i_{13/2}}$ band crossing. The rotational frequency is measured in MeV/ \hbar and the proton (Ip), neutron (In) and total (I) aligned angular momenta are given in \hbar	67
3.10:	TRS plots showing the nuclear shapes for the eF configuration of ^{186}Au as the rotational frequency increases. The left plot corresponds to the 20^+ band, and the right plot corresponds to the same configuration but after the $U_{i_{13/2}}$ band crossing. The rotational frequency is measured in MeV/ \hbar and the proton (Ip), neutron (In) and total (I) aligned angular momenta are given in \hbar	67
3.11:	TRS plots showing the nuclear shapes for the eFAC configuration of ^{190}Au as the rotational frequency increases. The left plot corresponds to the 21^+ band, and the right plot corresponds to the same configuration but after the $U_{i_{13/2}}$ band crossing. The rotational frequency is measured in MeV/ \hbar and the proton (Ip), neutron (In) and total (I) aligned angular momenta are given in \hbar	68
3.12:	TRS plots showing the nuclear shapes for the eFAB configuration of ^{190}Au as the rotational frequency increases. The left plot corresponds to the 22^+ band, and the right plot corresponds to the same configuration but after the $U_{i_{13/2}}$ band crossing. The rotational frequency is measured in MeV/ \hbar and the proton (Ip), neutron (In) and total (I) aligned angular momenta are given in \hbar	68
3.13:	TRS plots showing the nuclear shapes for the e proton and vacuum neutron configuration of ^{187}Au as the rotational frequency increases. The left plot corresponds to the $11/2^-$ band, the middle plot correspond to the $31/2^-$ band, and the right plot corresponds to the same band, but above the $U_{i_{13/2}}$ band crossing. The rotational frequency is measured in MeV/ \hbar and the proton (Ip), neutron (In) and total (I) aligned angular momenta are given in \hbar	71
3.14:	TRS plots showing the nuclear shapes for the eAC configuration of ^{187}Au as the rotational frequency increases. The left plot corresponds to the $33/2^-$ band, and the right plot corresponds to the same band above the $U_{i_{13/2}}$ band crossing. The rotational frequency is measured in MeV/ \hbar and the proton (Ip), neutron (In) and total (I) aligned angular momenta are given in \hbar	72
3.15:	TRS plots showing the nuclear shapes for the eAB configuration of ^{187}Au as the rotational frequency increases. The left plot corresponds to the $35/2^-$ band, and the right	

	plot corresponds to the same band above the $\nu i_{13/2}$ band crossing. The rotational frequency is measured in MeV/h and the proton (Ip), neutron (In) and total (I) aligned angular momenta are given in \hbar	72
3.16:	TRS plots showing the nuclear shapes for the e proton and vacuum neutron configuration of ^{193}Au as the rotational frequency increases. The left plot corresponds to the $11/2^-$ band, the middle plot correspond to the $31/2^-$ band, and the right plot corresponds to the same band, but above the $\nu i_{13/2}$ band crossing. The rotational frequency is measured in MeV/h and the proton (Ip), neutron (In) and total (I) aligned angular momenta are given in \hbar	73
3.17:	TRS plots showing the nuclear shapes for the eAC configuration of ^{193}Au as the rotational frequency increases. The left plot corresponds to the $33/2^-$ band, and the right plot corresponds to the same band above the $\nu i_{13/2}$ band crossing. The rotational frequency is measured in MeV/h and the proton (Ip), neutron (In) and total (I) aligned angular momenta are given in \hbar	73
3.18:	TRS plots showing the nuclear shapes for the eAB configuration of ^{193}Au as the rotational frequency increases. The left plot corresponds to the $35/2^-$ band, and the right plot corresponds to the same band above the $\nu i_{13/2}$ band crossing. The rotational frequency is measured in MeV/h and the proton (Ip), neutron (In) and total (I) aligned angular momenta are given in \hbar	74
3.19:	TRS plots showing the nuclear shapes for the eFB configuration of ^{187}Au as the rotational frequency increases. The left plot corresponds to the $31/2^+$ band, and the right plot corresponds to the same band above the band crossing. The rotational frequency is measured in MeV/h and the proton (Ip), neutron (In) and total (I) aligned angular momenta are given in \hbar	75
3.20:	TRS plots showing the nuclear shapes for the eFA configuration of ^{187}Au as rotational frequency increases. The left plot corresponds to the $33/2^+$ band, and the right plot corresponds to the same band, but above the band crossing. The rotational frequency is measured in MeV/h and the proton (Ip), neutron (In) and total (I) aligned angular momenta are given in \hbar	76
3.21:	TRS plots showing the nuclear shapes for the eFB configuration of ^{193}Au as the rotational frequency increases. The left plot corresponds to the $31/2^+$ band, and the right plot corresponds to the same band above the band crossing. The rotational frequency is measured in MeV/h and the proton (Ip), neutron (In) and total (I) aligned angular momenta are given in \hbar	76
3.22:	TRS plots showing the nuclear shapes for the eFA configuration of ^{193}Au as rotational frequency increases. The left plot corresponds to the $33/2^+$ band, and the right plot corresponds to the same band, but above the band crossing. The rotational frequency is measured in MeV/h and the proton (Ip), neutron (In) and total (I) aligned angular momenta are given in \hbar	77

3.23:	Quasiproton Routhian diagram for ^{190}Au , performed using $\beta_2 = 0.137$, $\beta_4 = -0.026$ and $\gamma = -70.8^\circ$ predicted by the TRS for the eB configuration. Solid lines represent $(\pi, \alpha) = (+, +1/2)$, dotted $(+, -1/2)$, dash-dotted $(-, +1/2)$ and dashed $(-, -1/2)$	80
3.24:	Quasineutron Routhian diagram for ^{190}Au , performed using $\beta_2 = 0.137$, $\beta_4 = -0.026$ and $\gamma = -70.8^\circ$ predicted by the TRS for the eB configuration. Solid lines represent $(\pi, \alpha) = (+, +1/2)$, dotted $(+, -1/2)$, dash-dotted $(-, +1/2)$ and dashed $(-, -1/2)$	81
3.25:	Quasineutron Routhian diagram for ^{190}Au , performed using $\beta_2 = 0.141$, $\beta_4 = -0.018$ and $\gamma = -68.7^\circ$ predicted by the TRS for the eA configuration after an alignment of a pair of $i_{13/2}$ neutron. Solid lines represent $(\pi, \alpha) = (+, +1/2)$, dotted $(+, -1/2)$, dash-dotted $(-, +1/2)$ and dashed $(-, -1/2)$	82
3.26:	Quasineutron Routhian diagram for ^{190}Au , performed using $\beta_2 = 0.135$, $\beta_4 = -0.024$ and $\gamma = -80.6^\circ$ predicted by the TRS calculations for the eFAC configuration. Solid lines represent $(\pi, \alpha) = (+, +1/2)$, dotted $(+, -1/2)$, dash-dotted $(-, +1/2)$ and dashed $(-, -1/2)$	83
3.27:	Quasineutron Routhian diagram for ^{191}Au performed using $\beta_2 = 0.136$, $\beta_4 = -0.024$ and $\gamma = -71.1^\circ$ predicted by the TRS for the eAC configuration. Solid lines represent $(\pi, \alpha) = (+, +1/2)$, dotted $(+, -1/2)$, dash-dotted $(-, +1/2)$ and dashed $(-, -1/2)$	84
3.28:	Quasineutron Routhian diagram for ^{191}Au performed using $\beta_2 = 0.140$, $\beta_4 = -0.030$ and $\gamma = -82.7^\circ$ predicted by the TRS for the eBF configuration. Solid lines represent $(\pi, \alpha) = (+, +1/2)$, dotted $(+, -1/2)$, dash-dotted $(-, +1/2)$ and dashed $(-, -1/2)$	85
4.1:	Comparison of the band crossing frequencies for the $11/2^-$ band with $31/2^-$ (a) and $35/2^-$ (b) bands of the odd-even $^{187-193}\text{Au}$ nuclei.....	90
4.2:	Comparison of theoretical and experimental signature splitting for the 11^- and 12^- bands of the odd-odd $^{186-194}\text{Au}$ nuclei.....	94
4.3:	Comparison of theoretical and experimental signature inversion frequencies for the 11^- and 12^- bands of the odd-odd $^{186-194}\text{Au}$ nuclei.....	95
4.4:	Experimental quasiparticle Routhians for the 11^- , 12^- and 20^+ bands of ^{186}Au calculated with Harris parameters of $J_0 = 6 \hbar^2 (\text{MeV})^{-1}$ and $J_1 = 30 \hbar^4 (\text{MeV})^{-3}$ and $K = 0$	99
4.5:	Theoretical quasiparticle Routhians for the 11^- , 12^- , 22^- , 20^+ , 21^+ , 22^+ bands of ^{186}Au	99
4.6:	Experimental quasiparticle alignments for the 11^- , 12^- and 20^+ bands of ^{186}Au calculated with Harris parameters of $J_0 = 6 \hbar^2 (\text{MeV})^{-1}$ and $J_1 = 30 \hbar^4 (\text{MeV})^{-3}$ and $K = 0$	100
4.7:	Experimental quasiparticle Routhians for the 11^- , 12^- , 20^+ and 21^+ bands of ^{188}Au calculated with Harris parameters of $J_0 = 6 \hbar^2 (\text{MeV})^{-1}$ and $J_1 = 30 \hbar^4 (\text{MeV})^{-3}$ and $K = 0$	101
4.8:	Theoretical quasiparticle Routhians for the 11^- , 12^- , 22^- , 20^+ , 21^+ , 22^+ bands of ^{188}Au	101

4.9:	Experimental quasiparticle alignments for the 11^- , 12^- , 20^+ and 21^+ bands of ^{188}Au calculated with Harris parameters of $J_0 = 6 \hbar^2 (\text{MeV})^{-1}$ and $J_1 = 30 \hbar^4 (\text{MeV})^{-3}$ and $K = 0$.	102
4.10:	Experimental quasiparticle Routhians for the 11^- , 12^- , 22^- , 20^+ , 21^+ , 22^+ bands of ^{190}Au calculated with Harris parameters of $J_0 = 6 \hbar^2 (\text{MeV})^{-1}$ and $J_1 = 30 \hbar^4 (\text{MeV})^{-3}$ and $K = 0$.	103
4.11:	Theoretical quasiparticle Routhians for the 11^- , 12^- , 22^- , 20^+ , 21^+ , 22^+ bands of ^{190}Au .	103
4.12:	Experimental quasiparticle alignments for the 11^- , 12^- , 22^- , 20^+ , 21^+ , 22^+ bands of ^{190}Au calculated with Harris parameters of $J_0 = 6 \hbar^2 (\text{MeV})^{-1}$ and $J_1 = 30 \hbar^4 (\text{MeV})^{-3}$ and $K = 0$.	104
4.13:	Experimental quasiparticle Routhians for the 11^- , 12^- , 20^+ bands of ^{192}Au calculated with Harris parameters of $J_0 = 6 \hbar^2 (\text{MeV})^{-1}$ and $J_1 = 30 \hbar^4 (\text{MeV})^{-3}$ and $K = 0$.	105
4.14:	Theoretical quasiparticle Routhians for the 11^- , 12^- , 22^- , 20^+ , 21^+ , 22^+ bands of ^{192}Au .	105
4.15:	Experimental quasiparticle alignments for the 11^- , 12^- , 20^+ bands of ^{192}Au calculated with Harris parameters of $J_0 = 6 \hbar^2 (\text{MeV})^{-1}$ and $J_1 = 30 \hbar^4 (\text{MeV})^{-3}$ and $K = 0$.	106
4.16:	Experimental quasiparticle Routhians for the 11^- , 12^- bands of ^{194}Au calculated with Harris parameters of $J_0 = 6 \hbar^2 (\text{MeV})^{-1}$ and $J_1 = 30 \hbar^4 (\text{MeV})^{-3}$ and $K = 0$.	107
4.17:	Theoretical quasiparticle Routhians for the 11^- , 12^- , 22^- , 20^+ , 21^+ , 22^+ bands of ^{194}Au .	107
4.18:	Experimental quasiparticle alignments for the 11^- , 12^- bands of ^{194}Au calculated with Harris parameters of $J_0 = 6 \hbar^2 (\text{MeV})^{-1}$ and $J_1 = 30 \hbar^4 (\text{MeV})^{-3}$ and $K = 0$.	108
4.19:	Experimental quasiparticle Routhians for the $11/2^-$, $31/2^-$, $33/2^-$, $35/2^-$, $31/2^+$ bands of ^{187}Au calculated with Harris parameters of $J_0 = 6 \hbar^2 (\text{MeV})^{-1}$ and $J_1 = 30 \hbar^4 (\text{MeV})^{-3}$ and $K = 0$.	109
4.20:	Theoretical quasiparticle Routhians for the $11/2^-$, $31/2^-$, $33/2^-$, $35/2^-$, $31/2^+$, $33/2^+$ bands of ^{187}Au .	109
4.21:	Experimental quasiparticle alignments for the $11/2^-$, $31/2^-$, $33/2^-$, $35/2^-$, $31/2^+$ bands of ^{187}Au calculated with Harris parameters of $J_0 = 6 \hbar^2 (\text{MeV})^{-1}$ and $J_1 = 30 \hbar^4 (\text{MeV})^{-3}$ and $K = 0$.	110
4.22:	Experimental quasiparticle Routhians for the $11/2^-$, $31/2^-$, $33/2^-$, $35/2^-$, $31/2^+$, $33/2^+$ bands of ^{189}Au calculated with Harris parameters of $J_0 = 6 \hbar^2 (\text{MeV})^{-1}$ and $J_1 = 30 \hbar^4 (\text{MeV})^{-3}$ and $K = 0$.	111

4.23:	Theoretical quasiparticle Routhians for the $11/2^-$, $31/2^-$, $33/2^-$, $35/2^-$, $31/2^+$, $33/2^+$ bands of ^{189}Au	111
4.24:	Experimental quasiparticle alignments for the $11/2^-$, $31/2^-$, $33/2^-$, $35/2^-$, $31/2^+$, $33/2^+$ bands of ^{189}Au calculated with Harris parameters of $J_0 = 6 \hbar^2(\text{MeV})^{-1}$ and $J_1 = 30 \hbar^4(\text{MeV})^{-3}$ and $K = 0$	112
4.25:	Experimental quasiparticle Routhians for the $11/2^-$, $31/2^-$, $33/2^-$, $35/2^-$, $31/2^+$, $33/2^+$ bands of ^{191}Au calculated with Harris parameters of $J_0 = 6 \hbar^2(\text{MeV})^{-1}$ and $J_1 = 30 \hbar^4(\text{MeV})^{-3}$ and $K = 0$	113
4.26:	Theoretical quasiparticle Routhians for the $11/2^-$, $31/2^-$, $33/2^-$, $35/2^-$, $31/2^+$, $33/2^+$ bands of ^{191}Au	113
4.27:	Experimental quasiparticle alignments for the $11/2^-$, $31/2^-$, $33/2^-$, $35/2^-$, $31/2^+$, $33/2^+$ bands of ^{189}Au calculated with Harris parameters of $J_0 = 6 \hbar^2(\text{MeV})^{-1}$ and $J_1 = 30 \hbar^4(\text{MeV})^{-3}$ and $K = 0$	114
4.28:	Experimental quasiparticle Routhians for the $11/2^-$, $31/2^-$, $31/2^+$ bands of ^{193}Au calculated with Harris parameters of $J_0 = 6 \hbar^2(\text{MeV})^{-1}$ and $J_1 = 30 \hbar^4(\text{MeV})^{-3}$ and $K = 0$	115
4.29:	Theoretical quasiparticle Routhians for the $11/2^-$, $31/2^-$, $33/2^-$, $35/2^-$, $31/2^+$, $33/2^+$ bands of ^{193}Au	115
4.30:	Experimental quasiparticle alignments for the $11/2^-$, $31/2^-$, $31/2^+$ bands of ^{193}Au calculated with Harris parameters of $J_0 = 6 \hbar^2(\text{MeV})^{-1}$ and $J_1 = 30 \hbar^4(\text{MeV})^{-3}$ and $K = 0$	116
4.31:	Experimental quasiparticle Routhians for the 11^- bands of the odd-odd $^{186-194}\text{Au}$ nuclei calculated with Harris parameters of $J_0 = 6 \hbar^2(\text{MeV})^{-1}$ and $J_1 = 30 \hbar^4(\text{MeV})^{-3}$ and $K = 0$	117
4.32:	Theoretical quasiparticle Routhians for the 11^- bands of the odd-odd $^{186-194}\text{Au}$ nuclei.....	117
4.33:	Experimental quasiparticle Routhians for the 12^- bands of the odd-odd $^{186-194}\text{Au}$ nuclei calculated with Harris parameters of $J_0 = 6 \hbar^2(\text{MeV})^{-1}$ and $J_1 = 30 \hbar^4(\text{MeV})^{-3}$ and $K = 0$	118
4.34:	Theoretical quasiparticle Routhians for the 12^- bands of the odd-odd $^{186-194}\text{Au}$ nuclei.....	118
4.35:	Experimental quasiparticle Routhians for the 20^+ bands of the odd-odd $^{186-192}\text{Au}$ nuclei calculated with Harris parameters of $J_0 = 6 \hbar^2(\text{MeV})^{-1}$ and $J_1 = 30 \hbar^4(\text{MeV})^{-3}$ and $K = 0$	119
4.36:	Theoretical quasiparticle Routhians for the 20^+ bands of the odd-odd $^{186-194}\text{Au}$ nuclei.....	119

4.37:	Experimental quasiparticle Routhians for the 21^+ bands of the odd-odd $^{188-190}\text{Au}$ nuclei calculated with Harris parameters of $J_0 = 6 \hbar^2 (\text{MeV})^{-1}$ and $J_1 = 30 \hbar^4 (\text{MeV})^{-3}$ and $K = 0$	120
4.38:	Theoretical quasiparticle Routhians for the 21^+ bands of the odd-odd $^{186-194}\text{Au}$ nuclei.....	120
4.39:	Experimental quasiparticle Routhians for the $11/2^-$ bands of the odd-even $^{187-193}\text{Au}$ nuclei calculated with Harris parameters of $J_0 = 6 \hbar^2 (\text{MeV})^{-1}$ and $J_1 = 30 \hbar^4 (\text{MeV})^{-3}$ and $K = 0$	121
4.40:	Theoretical quasiparticle Routhians for the $11/2^-$ bands of the odd-even $^{187-193}\text{Au}$ nuclei.....	121
4.41:	Experimental quasiparticle Routhians for the $31/2^-$ bands of the odd-even $^{187-193}\text{Au}$ nuclei calculated with Harris parameters of $J_0 = 6 \hbar^2 (\text{MeV})^{-1}$ and $J_1 = 30 \hbar^4 (\text{MeV})^{-3}$ and $K = 0$	122
4.42:	Theoretical quasiparticle Routhians for the $31/2^-$ bands of the odd-even $^{187-193}\text{Au}$ nuclei.....	122
4.43:	Experimental quasiparticle Routhians for the $33/2^-$ bands of the odd-even $^{187-191}\text{Au}$ nuclei calculated with Harris parameters of $J_0 = 6 \hbar^2 (\text{MeV})^{-1}$ and $J_1 = 30 \hbar^4 (\text{MeV})^{-3}$ and $K = 0$	123
4.44:	Theoretical quasiparticle Routhians for the $33/2^-$ bands of the odd-even $^{187-193}\text{Au}$ nuclei.....	123
4.45:	Experimental quasiparticle Routhians for the $35/2^-$ bands of the odd-even $^{187-191}\text{Au}$ nuclei calculated with Harris parameters of $J_0 = 6 \hbar^2 (\text{MeV})^{-1}$ and $J_1 = 30 \hbar^4 (\text{MeV})^{-3}$ and $K = 0$	124
4.46:	Theoretical quasiparticle Routhians for the $35/2^-$ bands of the odd-even $^{187-193}\text{Au}$ nuclei.....	124
4.47:	Experimental quasiparticle Routhians for the $31/2^+$ bands of the odd-even $^{187-193}\text{Au}$ nuclei calculated with Harris parameters of $J_0 = 6 \hbar^2 (\text{MeV})^{-1}$ and $J_1 = 30 \hbar^4 (\text{MeV})^{-3}$ and $K = 0$	125
A.1:	Level scheme of ^{186}Au [Jan92].....	133
A.2:	Level scheme of ^{188}Au [Jan92].....	134
A.3:	Level scheme of ^{190}Au [Gue03].....	134
A.4:	Level scheme of ^{192}Au [Gue01].....	135
A.5:	Level scheme of ^{194}Au [Nes82].....	136
A.6:	Level scheme of ^{187}Au [Joh89].....	137
A.7:	Level scheme of ^{187}Au [Bou89].....	138
A.8:	Level scheme of ^{189}Au [Ven92].....	139
A.9:	Level scheme of ^{189}Au [Per93]. Spins are multiplied by two.....	140
A.10:	Level scheme of ^{191}Au [Gue02].....	141
A.11:	Level scheme of ^{193}Au [Köl84].....	141

LIST OF TABLES

2.1:	Spectroscopic notations for l values.	11
2.2:	Allowed values of l , level label, oscillator energy E_N , maximum number of identical nucleons in each oscillator shell, and the total number of nucleons.....	13
2.3:	The database of the TRS calculations	45
3.1:	Convention for labeling the orbitals described by different parity and signature quantum numbers. Upper and lower case describe the neutron and proton configuration respectively. Labels E, G, etc refer to the lowest, second-lowest, etc Routhians with negative parity and negative signature. Labels F, H, etc refer to the lowest, second-lowest, etc Routhians with negative parity and positive signature. Labels B, D, etc refer to the lowest, second-lowest, etc Routhians with positive parity and negative signature. Labels A, C, etc refer to the lowest, second-lowest, etc Routhians with positive parity and positive signature.	56
3.2:	Convention for labeling the neutron orbitals by the parity and signature quantum numbers, shell model and Nilsson labels.	59
3.3:	Convention for labeling the proton orbitals by the parity and signature quantum numbers, shell model and Nilsson labels.	59
3.4:	The values of the nuclear deformation parameters β_2, γ, β_4 corresponding to the 11^- and 12^- band of the odd-odd $^{186-194}\text{Au}$ nuclei.	61
3.5:	The values of the nuclear deformation parameters β_2, γ, β_4 corresponding to the 22^- bands of the odd-odd $^{186-194}\text{Au}$ nuclei.....	64
3.6:	The values of the nuclear deformation parameters β_2, γ, β_4 corresponding to the $20^+, 21^+$ and 22^+ bands of the odd-odd $^{186-194}\text{Au}$ nuclei.....	65
3.7:	The values of the nuclear deformation parameters β_2, γ, β_4 corresponding to the $11/2^-$ band of the odd-even $^{187-193}\text{Au}$ nuclei.....	70
3.8:	The values of the nuclear deformation parameters β_2, γ, β_4 corresponding to the $31/2^-, 33/2^-$ and $35/2^-$ bands of the odd-even $^{187-193}\text{Au}$ nuclei.	71
3.9:	The values of the nuclear deformation parameters β_2, γ, β_4 corresponding to the $31/2^-$ and $33/2^-$ bands of the odd-even $^{187-193}\text{Au}$ nuclei.	75
4.1:	The alignment, band crossing frequency and alignment gain for the 11^- and 12^- bands of the odd-odd $^{186-194}\text{Au}$ nuclei predicted by CSM calculations. The experimental results are calculated with Harris parameters of $J_0 = 6 \hbar^2 (\text{MeV})^{-1}$ and $J_1 = 30 \hbar^4 (\text{MeV})^{-3}$ and $K = 0$	87
4.2:	Comparison between theoretical and experimental alignments for the 22^- bands of the odd-odd $^{186-194}\text{Au}$ nuclei predicted by CSM calculations. The experimental results are	

	calculated with Harris parameters of $J_0 = 6 \hbar^2 (MeV)^{-1}$ and $J_1 = 30 \hbar^4 (MeV)^{-3}$ and $K = 0$.	88
4.3:	Comparison of the theoretical and experimental alignments for the 20^+ , 21^+ and 22^+ bands of the odd-odd $^{186-194}\text{Au}$ nuclei. The experimental results are calculated with Harris parameters of $J_0 = 6 \hbar^2 (MeV)^{-1}$ and $J_1 = 30 \hbar^4 (MeV)^{-3}$ and $K = 0$.	88
4.4:	Comparison between the theoretical and experimental alignment and band crossing frequency for the $11/2^-$ band of the odd-even $^{187-193}\text{Au}$ nuclei. The experimental results are calculated with Harris parameters of $J_0 = 6 \hbar^2 (MeV)^{-1}$ and $J_1 = 30 \hbar^4 (MeV)^{-3}$ and $K = 0$.	89
4.5:	Comparison between the theoretical and experimental gains in alignment for the $11/2^-$ band of the odd-even $^{187-193}\text{Au}$ nuclei.	90
4.6:	Comparison between theoretical and experimental alignments for the $31/2^-$, $33/2^-$ and $35/2^-$ bands of the odd-even $^{187-193}\text{Au}$ nuclei. The experimental results are calculated with Harris parameters of $J_0 = 6 \hbar^2 (MeV)^{-1}$ and $J_1 = 30 \hbar^4 (MeV)^{-3}$ and $K = 0$.	91
4.7:	The alignment, band crossing frequency and alignment gain for the $31/2^+$ and $33/2^+$ bands of the odd-even $^{187-193}\text{Au}$ nuclei predicted by CSM calculations. The experimental results are calculated with Harris parameters of $J_0 = 6 \hbar^2 (MeV)^{-1}$ and $J_1 = 30 \hbar^4 (MeV)^{-3}$ and $K = 0$.	92
4.8:	Comparison of the theoretical and experimental signature inversion frequency for the 11^- and 12^- of the odd-odd $^{186-194}\text{Au}$ nuclei. The experimental results are calculated with Harris parameters of $J_0 = 6 \hbar^2 (MeV)^{-1}$ and $J_1 = 30 \hbar^4 (MeV)^{-3}$ and $K = 0$.	93
4.9:	Comparison of the theoretical and experimental signature splitting for the 11^- and 12^- of the odd-odd $^{186-194}\text{Au}$ nuclei. The experimental results are calculated with Harris parameters of $J_0 = 6 \hbar^2 (MeV)^{-1}$ and $J_1 = 30 \hbar^4 (MeV)^{-3}$ and $K = 0$.	93
4.10:	Comparison between theoretical and experimental signature splitting for the 20^+ , 21^+ and 22^+ bands of the odd-odd $^{188-190}\text{Au}$ nuclei. The experimental results are calculated with Harris parameters of $J_0 = 6 \hbar^2 (MeV)^{-1}$ and $J_1 = 30 \hbar^4 (MeV)^{-3}$ and $K = 0$.	94
4.11:	Comparison between the theoretical and experimental signature splitting for the $31/2^-$, $33/2^-$ and $35/2^-$ bands of the odd-even $^{187-191}\text{Au}$ nuclei. The experimental results are calculated with Harris parameters of $J_0 = 6 \hbar^2 (MeV)^{-1}$ and $J_1 = 30 \hbar^4 (MeV)^{-3}$ and $K = 0$.	96

4.12:	Comparison between the theoretical and experimental signature splitting for the $31/2^+$ and $33/2^+$ bands of the odd-even $^{189-191}\text{Au}$ nuclei. The experimental results are calculated with Harris parameters of $J_0 = 6 \hbar^2 (\text{MeV})^{-1}$ and $J_1 = 30 \hbar^4 (\text{MeV})^{-3}$ and $K = 0$	96
B.1-5:	Spins $I (\hbar)$, aligned angular momentum $I_x (\hbar)$, rotational frequency $\hbar\omega (\text{MeV})$, Routhians $E' (\text{MeV})$ and $e' (\text{MeV})$, reference Routhians $E'_{\text{ref}} (\text{MeV})$ and reference aligned angular momentum $I_{x\text{ref}} (\hbar)$ and alignment $i_x (\hbar)$ for the 11^- and 12^- band of the odd-odd $^{186-194}\text{Au}$ nuclei calculated with Harris parameters of $J_0 = 6 \hbar^2 (\text{MeV})^{-1}$ and $J_1 = 30 \hbar^4 (\text{MeV})^{-3}$ and $K = 0$	143
B.6-10:	Rotational frequency $\hbar\omega$, Routhians $e' (\text{MeV})$, and signature splitting $[e'(12^-)-e'(11^-)] (\text{MeV})$ for the 11^- and 12^- bands of the odd-odd $^{186-192}\text{Au}$ nuclei	144
B.11:	Spins $I (\hbar)$, aligned angular momentum $I_x (\hbar)$, rotational frequency $\hbar\omega (\text{MeV})$, Routhians $E' (\text{MeV})$ and $e' (\text{MeV})$, reference Routhians $E'_{\text{ref}} (\text{MeV})$ and reference aligned angular momentum $I_{x\text{ref}} (\hbar)$ and alignment $i_x (\hbar)$ for the 22^- band of the odd-odd ^{190}Au nuclei calculated with Harris parameters of $J_0 = 6 \hbar^2 (\text{MeV})^{-1}$ and $J_1 = 30 \hbar^4 (\text{MeV})^{-3}$ and $K = 0$	145
B.12-15:	Spins $I (\hbar)$, aligned angular momentum $I_x (\hbar)$, rotational frequency $\hbar\omega (\text{MeV})$, Routhians $E' (\text{MeV})$ and $e' (\text{MeV})$, reference Routhians $E'_{\text{ref}} (\text{MeV})$ and reference aligned angular momentum $I_{x\text{ref}} (\hbar)$ and alignment $i_x (\hbar)$ for the 20^+ , 21^+ and 22^+ bands of the odd-odd ^{190}Au nuclei calculated with Harris parameters of $J_0 = 6 \hbar^2 (\text{MeV})^{-1}$ and $J_1 = 30 \hbar^4 (\text{MeV})^{-3}$ and $K = 0$	146
B.16-17:	Rotational frequency $\hbar\omega (\text{MeV})$, Routhians $e' (\text{MeV})$, and signature splitting $[e'(20^+)-e'(21^+)] (\text{MeV})$, $[e'(22^+)-e'(20^+)] (\text{MeV})$ and $[e'(22^+)-e'(21^+)] (\text{MeV})$ for the 20^+ , 21^+ and 22^+ bands of the odd-odd $^{188,190}\text{Au}$ nuclei calculated with Harris parameters of $J_0 = 6 \hbar^2 (\text{MeV})^{-1}$ and $J_1 = 30 \hbar^4 (\text{MeV})^{-3}$ and $K = 0$	147
B.18-21:	Spins $I (\hbar)$, aligned angular momentum $I_x (\hbar)$, rotational frequency $\hbar\omega (\text{MeV})$, Routhians $E' (\text{MeV})$ and $e' (\text{MeV})$, reference Routhians $E'_{\text{ref}} (\text{MeV})$ and reference aligned angular momentum $I_{x\text{ref}} (\hbar)$ and alignment $i_x (\hbar)$ for the $11/2^-$ band of the odd-even $^{187-193}\text{Au}$ nuclei calculated with Harris parameters of $J_0 = 6 \hbar^2 (\text{MeV})^{-1}$ and $J_1 = 30 \hbar^4 (\text{MeV})^{-3}$ and $K = 0$	148

B.22-25: Spins I (\hbar), aligned angular momentum I_x (\hbar), rotational frequency $\hbar\omega$ (MeV), Routhians E' (MeV) and e' (MeV), reference Routhians E'_{ref} (MeV) and reference aligned angular momentum I_{xref} (\hbar) and alignment i_x (\hbar) for the $31/2^-$, $33/2^-$ and $35/2^-$ bands of the odd-even $^{187-191}Au$ nuclei calculated with Harris parameters of $J_0 = 6\hbar^2(MeV)^{-1}$ and $J_1 = 30\hbar^4(MeV)^{-3}$ and $K = 0$	149
B.26-28: Rotational frequency $\hbar\omega$ (MeV), Routhians e' (MeV), and signature splitting $[e'(31/2^-)-e'(35/2^-)]$ (MeV), $[e'(31/2^-)-e'(33/2^-)]$ (MeV) and $[e'(33/2^-)-e'(35/2^-)]$ (MeV) for the $31/2^-$, $33/2^-$ and $35/2^-$ bands of the odd-even $^{187-191}Au$ nuclei calculated with Harris parameters of $J_0 = 6\hbar^2(MeV)^{-1}$ and $J_1 = 30\hbar^4(MeV)^{-3}$ and $K = 0$	150
B.29-32: Spins I (\hbar), aligned angular momentum I_x (\hbar), rotational frequency $\hbar\omega$ (MeV), Routhians E' (MeV) and e' (MeV), reference Routhians E'_{ref} (MeV) and reference aligned angular momentum I_{xref} (\hbar) and alignment i_x (\hbar) for the $31/2^+$ and $33/2^+$ bands of the odd-even $^{187-191}Au$ nuclei calculated with Harris parameters of $J_0 = 6\hbar^2(MeV)^{-1}$ and $J_1 = 30\hbar^4(MeV)^{-3}$ and $K = 0$	151
C.1-5: Rotational frequency $\hbar\omega$ (MeV), quasiproton Routhian $e'(e)$ (MeV), quasineutron Routhians $e'(B)$ (MeV) and $e'(A)$ (MeV), and the total quasiparticle Routhians $e'(eA)$ (MeV) and $e'(eA)$ (MeV) for the 11^- and 12^- bands of the odd-odd $^{186-194}Au$ nuclei	154
C.6-8: Rotational frequency $\hbar\omega$ (MeV), the total quasiparticles Routhians $e'(eA)$ (MeV) and $e'(eB)$ (MeV), and quasiparticle signature splitting $[e'(eA)- e'(eB)]$ (MeV) for the 11^- and 12^- bands of the odd-odd $^{186-194}Au$ nuclei	155
C.9-11: Rotational frequency $\hbar\omega$ (MeV), quasiproton Routhians $e'(e)$ (MeV), quasineutron Routhians $e'(A)$ (MeV), $e'(B)$ (MeV), $e'(C)$ (MeV), and the total quasiparticle Routhians $e'(eABC)$ (MeV) for the 22^- bands of the odd-odd $^{186-194}Au$ nuclei	157
C.12-16: Rotational frequency $\hbar\omega$ (MeV), quasiproton Routhians $e'(e)$, quasineutron Routhians $e'(A)$ (MeV), $e'(B)$ (MeV), $e'(C)$ (MeV), $e'(F)$ (MeV) and the total quasiparticle Routhians $e'(eFBC)$ (MeV) and $e'(eFAB)$ (MeV) for the 20^+ and 22^+ bands of the odd-odd $^{186-194}Au$ nuclei	158

C.17-19: Rotational frequency $\hbar\omega$ (MeV), quasiproton Routhians $e'(e)$ (MeV), quasineutron Routhians $e'(A)$ (MeV), $e'(C)$ (MeV), $e'(F)$ (MeV) and the total quasiparticle Routhians $e'(eFAC)$ (MeV) for the 21^+ band of the odd-odd $^{186-194}Au$ nuclei.	160
C.20-24: Rotational frequency $\hbar\omega$ (MeV), total quasiparticle Routhians $e'(eFAB)$ (MeV), $e'(eFBC)$ (MeV), $e'(eFAC)$ (MeV) and signature splitting $[e'(eFAB) - e'(eFBC)]$ (MeV), $[e'(eFAB) - e'(eFAC)]$ (MeV), $[e'(eFBC) - e'(eFAC)]$ (MeV) for the 20^+ , 21^+ and 22^+ bands of the odd-odd $^{186-194}Au$ nuclei.....	161
C.25-30: Rotational frequency $\hbar\omega$ (MeV), quasiproton Routhians $e'(e)$ (MeV), quasineutron Routhians $e'(A)$ (MeV), $e'(B)$ (MeV), $e'(C)$ (MeV) and the total quasiparticle Routhians $e'(eAB)$ (MeV), $e'(eBC)$ (MeV) and $e'(eAC)$ (MeV) for the $31/2^-$, $33/2^-$ and $35/2^-$ bands of the odd-even $^{187-193}Au$ nuclei.	163
C.31-34: Rotational frequency $\hbar\omega$ (MeV), total quasiparticle Routhians $e'(eAB)$ (MeV), $e'(eAC)$ (MeV), $e'(eBC)$ (MeV) and signature splitting $[e'(eAB) - e'(eAC)]$ (MeV), $[e'(eAB) - e'(eBC)]$ (MeV), $[e'(eAC) - e'(eBC)]$ (MeV) for the $31/2^-$, $33/2^-$ and $35/2^-$ bands of the odd-even $^{187-193}Au$ nuclei.	165
C.35-38: Rotational frequency $\hbar\omega$ (MeV), quasiproton Routhians $e'(e)$ (MeV), quasineutron Routhians $e'(A)$ (MeV), $e'(B)$ (MeV), $e'(F)$ (MeV) and the total quasiparticle Routhians $e'(eAF)$ (MeV), and $e'(eBF)$ (MeV) for the $31/2^+$ and $33/2^+$ bands of the odd-even $^{187-193}Au$ nuclei.	166
C.39-40: Rotational frequency $\hbar\omega$ (MeV), total quasiparticle Routhians $e'(eAF)$ (MeV), $e'(eBF)$ (MeV) and signature splitting $e'(eAF) - e'(eBF)$ (MeV) for the $31/2^+$ and $33/2^+$ bands of the odd-even $^{187-193}Au$ nuclei.	168

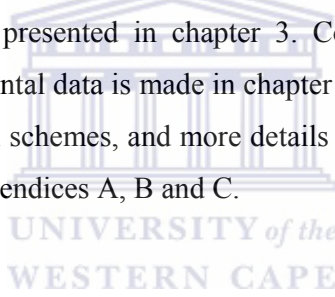
CHAPTER 1 Introduction

Heavy Au isotopes ($A \geq 187$) show rotation aligned bands corresponding to oblate nuclear deformation, while in the lighter Au isotopes rotational bands corresponding to prolate deformation dominate [Hey83]. In the odd-even nuclei where j of the odd particle is rotation aligned, one observes a decoupled band with spin sequence of $j, j+2, j+4, j+6, \dots$, (for instance the $\pi h_{11/2}^{-1}$ band in ^{191}Au [Gue02]). In the odd-odd nuclei where two odd particles are rotation aligned, we expect to observe a decoupled band with spin sequence of $j_1+j_2, j_1+j_2+2, j_1+j_2+4, j_1+j_2+6, \dots$ (for instance the $\nu i_{13/2}^2$ band based on the 12^+ level in ^{190}Hg nuclei [Hüb86]). However, for several two and multi-quasiparticle configurations in the odd-even and odd-odd Au nuclei two or three sets of rotation aligned bands are observed [Gue01, Gue02, Gue03, Jan92, Nes82]. Several attempts to describe some of the bands in these nuclei have been made, using the axially symmetric or triaxial particle-plus-rotor model (PRM) as well as the cranked shell model (CSM). The PRM and CSM models account very well for the energy spectra of the 11^- and 12^- bands in the $^{190-194}\text{Au}$ and $^{186,188}\text{Au}$ respectively [Tok77, Jan92]. These models predict that there is signature inversion in the Routhians of the 11^- and 12^- bands, but fail to reproduce the magnitude of signature inversion frequency accurately. The PRM could not be applied to other bands in the $^{190-194}\text{Au}$ nuclei because it is applicable for maximum of two-quasiparticle configuration.

Recently the TRS and CSM calculations were performed for several high- j multi-quasiparticle bands in the $^{190,191}\text{Au}$ nuclei suggesting that the non-axial shape of the nucleus plays a major role in their properties [Gue02, Gue03]. A very good agreement between the theory and the experimental results was obtained. In this study we want to see if these calculations can describe the features of all the high- j bands in all Au isotopes (i.e. in $^{186,187,188,189,192,193,194}\text{Au}$). So, in this study, TRS and CSM calculations were performed for the $\pi h_{11/2}^{-1} \otimes \nu i_{13/2}^{-1}$ (11^- and 12^- bands), $\pi h_{11/2}^{-1} \otimes \nu i_{13/2}^{-3}$ (22^- band) and $\pi h_{11/2}^{-1} \otimes \nu i_{13/2}^{-2} h_{9/2}^{-1}$ (20^+ , 21^+ and 22^+ bands) bands in the odd-odd $^{186-194}\text{Au}$ nuclei, the $\pi h_{11/2}^{-1}$ ($11/2^-$ band), $\pi h_{11/2}^{-1} \otimes \nu i_{13/2}^{-2}$ ($31/2^-$, $33/2^-$ and $35/2^-$ bands) and

$\pi h_{11/2}^{-1} \otimes \nu i_{13/2}^{-1} h_{9/2}^{-1}$ ($31/2^+$ and $33/2^+$ bands) bands in the odd-even $^{187-193}\text{Au}$ nuclei. TRS calculations predict triaxial shapes for all these bands in the $^{186-194}\text{Au}$ nuclei except for the $\pi h_{11/2}^{-1} \otimes \nu i_{13/2}^{-3}$ bands where a only small non-axiality is predicted for the lighter $^{186,188}\text{Au}$ nuclei. CSM calculations performed using these deformation parameters show that the positive parity A, B and C Routhians lie close to each other for $\gamma \leq -70^\circ$ and for $\gamma \leq -75^\circ$ the negative parity F Routhian is pushed down in energy and competes with these positive parity Routhians in the rotational frequency region of $0 \text{ MeV} < \hbar\omega < 0.20 \text{ MeV}$. Good agreement between the theory and experiment was obtained for the alignments, alignment gains and relative positions of the Routhians in all these bands of $^{186-194}\text{Au}$, whereas discrepancies have been found for the band crossing frequencies and signature splitting in some of these bands.

The nuclear theoretical models are discussed in chapter 2. The results from the theoretical calculations are presented in chapter 3. Comparison of the theoretical predictions and the experimental data is made in chapter 4. A summary of this work is given in chapter 5. The level schemes, and more details on some results about the $^{186-194}\text{Au}$ nuclei are given in appendices A, B and C.



CHAPTER 2 Nuclear theoretical models

2.1 Nuclear excitations and deformation parameters

2.1.1 Nuclear excitations

Heavy ion reactions allow the transfer of very large amounts of angular momentum (up to $80-100\hbar$) to a nucleus. At such high excitations the nucleus can show two types of behavior when it de-excites to its ground state. The two possible modes of de-excitation can either be non-collective (single particle motion) or collective.

2.1.1.1 Non-collective (single particle) motion

Non-collective motion is mainly observed in spherical or weakly deformed nuclei. The total angular momentum is generated by the alignment of the individual nucleons spins. The resulting level scheme shows an irregular sequences of states connected by γ -transitions with different energies and multipolarities.

2.1.1.2 Collective motion

Well-deformed nuclei characterized by non-spherical mass distribution are known to show collective motion. The well-deformed nuclei give rise to regular sequences of states with consecutively increasing angular momentum known as rotational bands. The total angular momentum comes from the coherent motion of the whole nucleus. For an ellipsoidal nucleus (prolate or oblate) rotation takes place about the axis perpendicular to the symmetry axis of the nucleus, while for a triaxial nucleus rotation takes place about any one of the three axes. The relation between the excitation energy E_{exc} and spin I for the states in the rotational bands can be approximated by $E_{exc} \propto I(I+1)$. The lowest level of the rotational band is called the bandhead.

2.2 Nuclear deformation parameters

The nuclear shape can be parameterized in terms of spherical harmonics or multipole expansions:

$$R(\theta, \phi) = R_0 \left[1 + \alpha_{00} + \sum_{\lambda=1}^{\infty} \sum_{\mu=-\lambda}^{\lambda} \alpha_{\lambda\mu} Y_{\lambda\mu}(\theta, \phi) \right] \quad (2.1)$$

where R_0 is the radius of the sphere with the same volume as the nucleus and $Y_{\lambda\mu}$ are the spherical harmonics. The constant α_{00} describes changes of the nuclear volume. The parameter λ gives the deformation type of the nucleus and μ is an integer taking its values from $-\lambda$ to $+\lambda$. For $\lambda=1, 2, 3$ and 4 we have dipole, quadrupole, octupole and hexadecupole deformations respectively. Shapes of nuclei associated with these kind of deformations are shown in Figure 2.1.

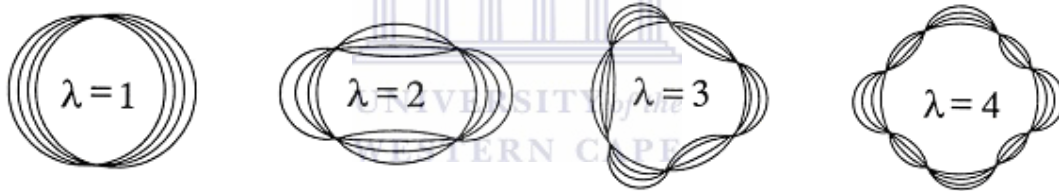


Figure 2.1: Schematic representation of dipole, quadrupole, octupole and hexadecupole deformations [Mab03].

Constraints on R and therefore on the parameters $\alpha_{\lambda\mu}$ is that R should be invariant under a reflection and a rotation of the coordinate system. In order for this to be the case, the $\alpha_{\lambda\mu}$ must be multiplied by a factor $(-)^{\lambda}$ under a parity transformation, and must behave like $Y_{\lambda\mu}(\theta, \phi)$ under a rotation of the coordinate system characterized by the Euler angles $\Omega = (\alpha, \beta, \gamma)$ [Edm57].

In the case of quadrupole deformations ($\lambda = 2$), we have five parameters $\alpha_{2\mu}$. Not all of them describe the shape of the nucleus. Three determine only the orientation of the

nucleus in space, and correspond to the three Euler angles $\Omega = (\alpha, \beta, \gamma)$. By a suitable rotation we can transform to the body fixed system characterized by three axes 1, 2, 3, which coincide with the mass distribution of the nucleus. Then the five coefficients $\alpha_{2\mu}$ reduce to two really independent variables α_{20} and $\alpha_{22} = \alpha_{2-2}$ ($\alpha_{21} = \alpha_{2-1} = 0$), which, together with the three Euler angles $\Omega = (\alpha, \beta, \gamma)$ give a complete description of the system. The coefficients, α_{20} and α_{22} are related to the Hill-Wheeler [Hil53] coordinates β_2, γ ($\beta_2 > 0$) through the following equations:

$$\alpha_{20} = \beta_2 \cos \gamma \quad (2.2)$$

$$\alpha_{22} = \frac{1}{\sqrt{2}} \beta_2 \sin \gamma \quad (2.3)$$

from which we have

$$\sum_{\mu} |\alpha_{2\mu}|^2 = \alpha_{20}^2 + 2\alpha_{22}^2 = \beta_2^2 \quad (2.4)$$

and

$$R(\theta, \phi) = R_0 \left\{ 1 + \beta_2 \sqrt{\frac{5}{16\pi}} \left[\cos \gamma (3 \cos^2 \theta - 1) + \sqrt{3} \sin \gamma \sin^2 \theta \cos 2\phi \right] \right\} \quad (2.5)$$

The nuclear shape is then determined only in terms of β_2 and γ , where β_2 represents the extent of quadrupole deformation and γ gives the degree of axial asymmetry.

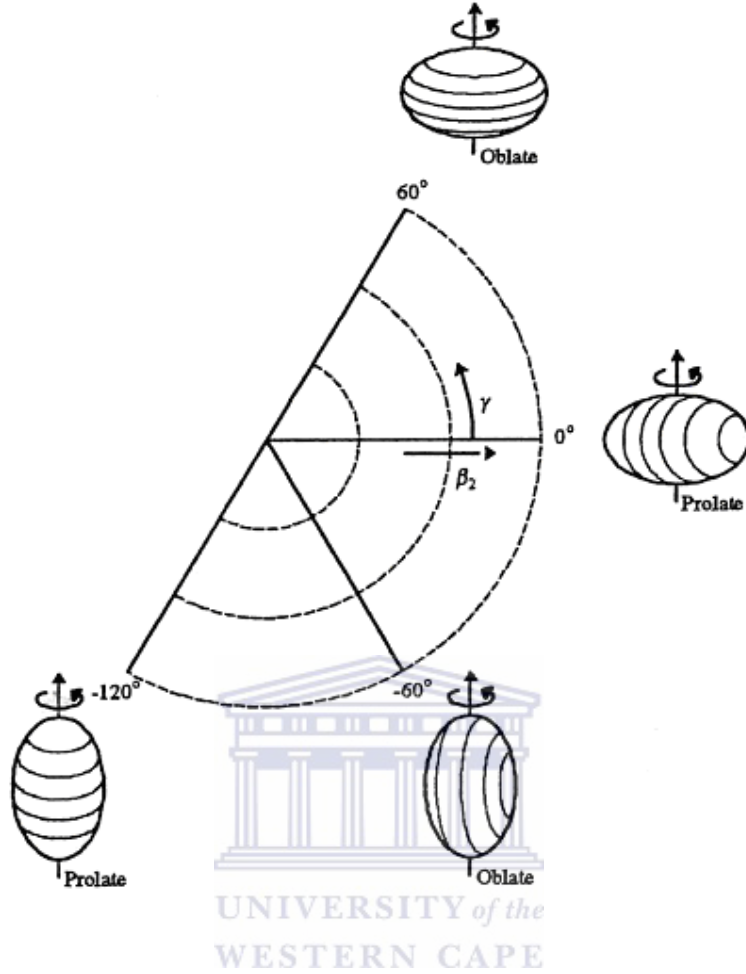


Figure 2.2: Diagrammatic representation of the nuclear shape ($\lambda = 2$) in the β_2, γ plane [And76].

In Figure 2.2 the quadrupole shapes ($\lambda = 2$) are represented in the polar coordinates β_2, γ . We see that γ values of 0° and -120° correspond to prolate spheroids which rotate collectively and non-collectively (about their axis of symmetry) respectively, while $\gamma = -60^\circ$ and 60° correspond to oblate nuclei which rotate collectively and non-collectively (about their axis of symmetry) respectively. Within the sector $-60^\circ < \gamma < 0^\circ$, we have maximum collective rotation of the nucleus. When γ is not a multiple of 60° (i.e. $0^\circ < \gamma < 60^\circ$, $-60^\circ < \gamma < 0^\circ$, and $-120^\circ < \gamma < -60^\circ$) it corresponds to a triaxial shape. Within these three sectors i.e. $-120^\circ < \gamma < -60^\circ$, $-60^\circ < \gamma < 0^\circ$ and $0^\circ < \gamma < 60^\circ$ the nucleus rotates around the longest, the medium and the shortest axis respectively [And76]. The Cranked Shell Model (CSM) and Total Routhian Surface (TRS) calculations discussed in section 2.9 and 2.12 use this parameterization.

The increments of the three semi-axes in the body-fixed frame as a function of β_2 and γ are

$$\delta R_k = R_0 \sqrt{\frac{5}{4\pi}} \beta_2 \cos\left(\gamma - \frac{2\pi}{3} \kappa\right), \quad (2.6)$$

where $\kappa = 1, 2, 3$ refers to the three principal axes of the nucleus.

The parameterization using the quadrupole parameters β_2 and γ is suitable when the nuclear potential is of the Woods-Saxon type.

There is another parameterization of the nuclear shape in terms of the quadrupole deformation parameters ε_2 and γ , which is often referred to as the Nilsson parameterization. It is used when the deformed harmonic oscillator potential is involved in the description of nuclear potential. More details about description of the nuclear potential are given in the following sections. The parameters of deformation are included in the expression of the three harmonic oscillator frequencies, which correspond to the motion of the nucleon along the three principal axes (labelled 1, 2 and 3):

$$\begin{aligned} \omega_1(\varepsilon_2, \gamma) &= \omega_0 \left\{ 1 + \frac{1}{3} \varepsilon_2 \cos \gamma + \frac{1}{\sqrt{3}} \varepsilon_2 \sin \gamma \right\} \\ \omega_2(\varepsilon_2, \gamma) &= \omega_0 \left\{ 1 + \frac{1}{3} \varepsilon_2 \cos \gamma - \frac{1}{\sqrt{3}} \varepsilon_2 \sin \gamma \right\} \\ \omega_3(\varepsilon_2, \gamma) &= \omega_0 \left\{ 1 - \frac{2}{3} \varepsilon_2 \cos \gamma \right\} \end{aligned} \quad (2.7)$$

where ω_0 is the oscillator frequency of a harmonic motion of the particle in a spherical potential.

The parameter ε_2 indicates the elongation of the nuclear potential, and the parameter γ describes its non-axiality. If $\gamma = 0^\circ$ or 60° , two of the axes will have the same

length and therefore the nucleus is axially symmetric. For $\gamma = 0^\circ$ the nucleus has a prolate ellipsoidal shape with the major axis being the axis of symmetry. For $\gamma = 60^\circ$ the nucleus has an oblate shape with the axis of symmetry being the minor axis. The range $0^\circ < \gamma < 60^\circ$ is sufficient to describe all the nuclear shapes, the three axes having different length. The shape parameters (ε_2, γ) are used in the Rigid Triaxial Rotor (RTR) calculations with Nilsson nuclear potential.

Both (ε_2, γ) and (β_2, γ) parameterizations of nuclear shape are equivalent. The γ parameter has the same value in both parameterizations, while the elongation parameters are not the same. $\beta_2 \approx 0.96\varepsilon_2$, for not very large deformations.

2.3 The shell model

The shell model was first developed in the 1940s and many unsuccessful attempts were made in constructing a nuclear potential that will fit the observed properties of the nuclei.

Mayer [May49], Haxel, Jensen and Suess [Hax49] further developed this model in 1949. It now accounts very well for the observed nuclear properties such as nuclear transitions, spins and parities of the states. It is also called a single particle model because it treats the nucleons individually. The so-called magic numbers gave the strongest formulation of the shell model.

2.3.1 The shell model Hamiltonian

The Shell Model Hamiltonian can be represented by:

$$H = \sum_{i=1}^A \left[-\frac{\hbar^2}{2m} \Delta_i + V(r_i) \right], \quad (2.8)$$

where the first term represents the kinetic energy of the individual nucleons and the second term represents the nuclear potential. In order to determine the potential correctly, the difference between the nucleons at the centre and those at the surface

must be taken into account. Nucleons at the centre of the nucleus experience the nuclear forces uniformly, i.e.

$$\left(\frac{\partial V(r)}{\partial r}\right)_{r=0} = 0 \quad (2.9)$$

Nucleons at the surface experience a large force towards the centre, i.e.

$$\left(\frac{\partial V}{\partial r}\right)_{r < R_0} > 0 \quad (2.10)$$

2.3.2 Nuclear potential well

The shell model proposes that a valence nucleon moves in an attractive potential well created by the other nucleons in the nucleus. In this model, a lot of work was done in constructing the form of a potential well which when included in the three-dimensional time independent Schrödinger equation will approximate the observed excitation energy levels of the nucleus. The most often discussed potential wells are an isotropic harmonic oscillator, square well and Woods-Saxon potential, which are shown in Figure 2.3. The square well potential is an oversimplification of the nuclear potential because it does not approximate the shape of the nuclear matter, and only requires uniform charge distribution within the nuclear radius and to be zero outside the nucleus. The Woods-Saxon potential is an intermediate between the harmonic oscillator and square well potentials and it represents a more realistic shape of the nucleus.

The harmonic oscillator potential gives an unrealistic shape of the nucleus. It is a first approximation of the nuclear potential and it can be represented by

$$V_{HO}(r) = -V_0 + \frac{1}{2} m \omega_0^2 r^2, \quad (2.11)$$

where V_0 is the well depth, m is the mass of the nucleon, and ω_0 is the oscillator frequency of a harmonic motion of the particle in a spherical potential. When r increases, the potential tends unrealistically to infinity.

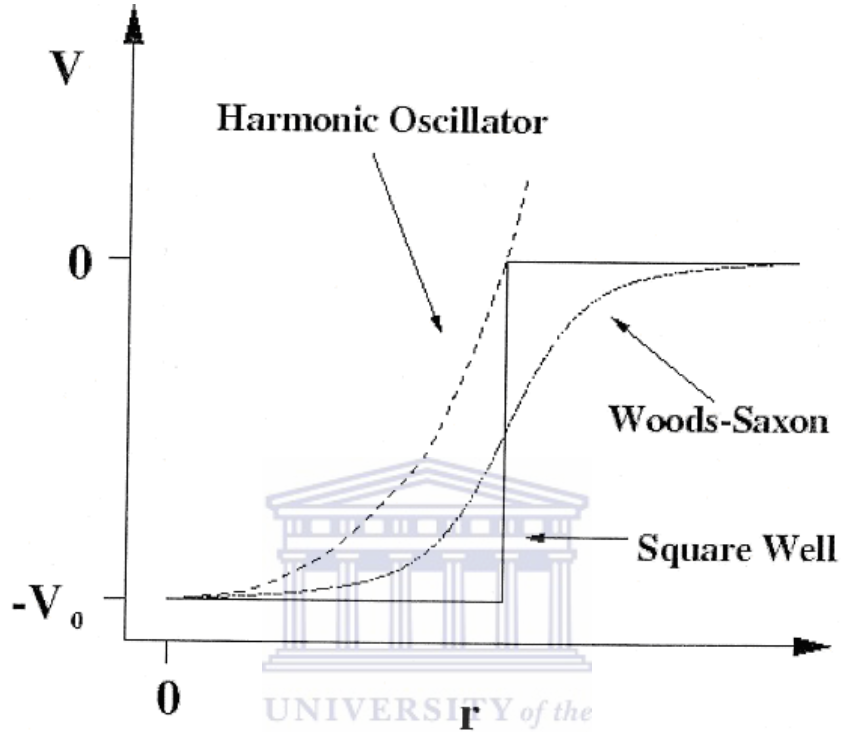


Figure 2.3: A comparison of two-dimensional harmonic oscillator potential, square well potential and Woods-Saxon potential [Kee99].

When the potential in (2.11) is included in the three-dimensional time independent Schrödinger equation, eigenvalues of the Hamiltonian with equally spaced energy levels are obtained,

$$E_{nl} = \left(N + \frac{3}{2} \right) \hbar \omega_0, \quad (2.12)$$

where n is the radial quantum number and l is the orbital angular momentum as shown in Figure 2.4. Note that n takes values 1, 2, 3, ... and l takes even values 0, 2, ...N if N is even and odd values 1, 3, ..., N if N is odd. The l values are labelled using spectroscopic notation shown in Table 2.1.

Table 2.1: Spectroscopic notations for l values.

l value	0	1	2	3	4	5	6
Symbol	s	p	d	f	g	h	i

In Figure 2.4, each energy level is degenerate and is called a shell and it is labelled by integer values of N , where $N = 0, 1, 2, \dots$ represents the number of the energy shell and does not represent the principal quantum number as in atomic physics. Each shell can be occupied by $(N+1)(N+2)$ identical nucleons and this is shown in Table 2.2.

In terms of n and l , the integer N is given by

$$N = 2(n-1) + l. \quad (2.13)$$

The degeneracy of each oscillator shell is calculated by


$$D(N) = \frac{1}{2}(N+1)(N+2). \quad (2.14)$$

The parity of each level is determined from

$$\pi = (-1)^l = (-1)^N. \quad (2.15)$$

The shells corresponding to $N \geq 2$ consist of more than one degenerate level called subshells. For example, for the shell corresponding to $N = 2$, $2s$ and $1d$ levels are subshells. Note that the shells are separated from each other by large gaps. The following magic numbers 2, 8, 20, 40, 70, 112, 168 are obtained by the shell model calculations when a harmonic oscillator potential is used and this is shown in Figure 2.4. The first three magic numbers meet experimental observation but the model fails in predicting the higher ones.

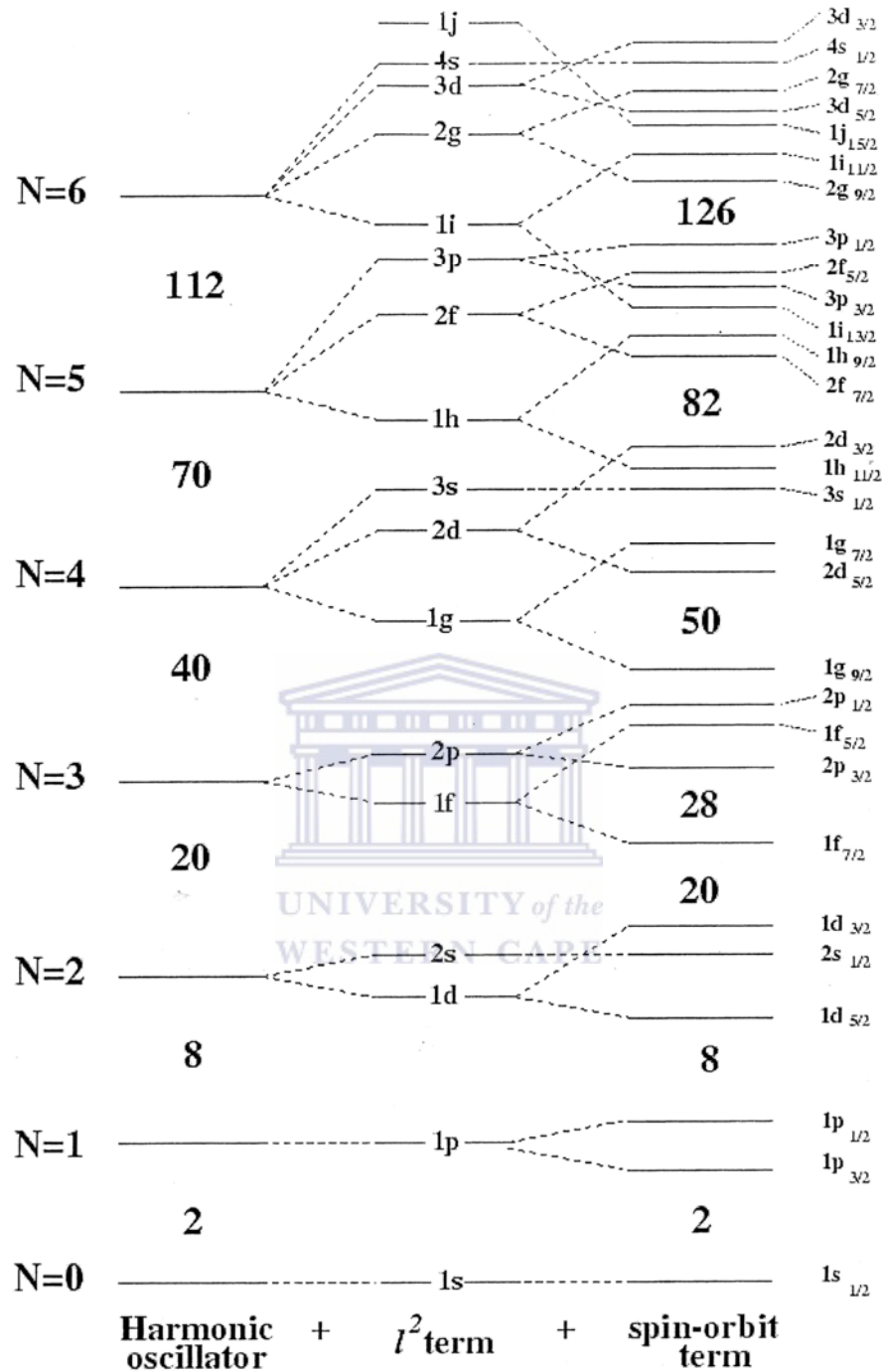


Figure 2.4: Energy levels in a modified oscillator potential. The levels on the left are those for the harmonic oscillator potential. These are split by the l^2 term to produce the second set of levels, and then again by the spin-orbit term to produce the experimentally observed shells on the right [Kee99].

Table 2.2: Allowed values of l , level label, oscillator energy E_N , maximum number of identical nucleons in each oscillator shell, and the total number of nucleons.

N	Allowed l	Level label	$E_N(\hbar\omega)$	Occupation	Total
0	0	1s	3/2	2	2
1	1	1p	5/2	6	8
2	2, 0	1d, 2s	7/2	12	20
3	3, 1	1f, 2p	9/2	20	40
4	4, 2, 0	1g, 2d, 3s	11/2	30	70
5	5, 3, 1	1h, 2f, 3p	13/2	42	112

2.3.3 Modification of the harmonic oscillator potential

2.3.3.1 Addition of l^2 term

Inclusion of a term proportional to l^2 leads to the following harmonic oscillator potential

$$V_{HO}(r) = -V_0 + \frac{1}{2}m\omega_0^2 r^2 - A\bar{l}^2, \quad (2.16)$$

where A is an empirically determined constant. The actual correction is $A(\bar{l}^2 - \langle \bar{l}^2 \rangle_N)$, where $\langle \bar{l}^2 \rangle_N = \frac{1}{2}N(N+3)$ is the expectation value of \bar{l}^2 averaged over one major shell with quantum number N . With this correction, only states within the shell are shifted and the centre of gravity between different major shells remains unaffected. This provides a more realistic shape of the nuclear potential. The last term in equation (2.16) has an effect in splitting the degenerate oscillator levels into levels with different energies, particularly oscillator levels with $N \geq 2$ (see Figure 2.4). This shifts levels with higher l -values downward. But even when this term is added to the harmonic oscillator potential, the calculated magic numbers are not correct except the first three, which are 2, 8 and 20.

2.3.3.2 Addition of spin-orbit interaction term ($\vec{l} \cdot \vec{s}$)

The second correction that was done to the harmonic oscillator potential so that it produces the observed higher magic numbers is the addition of a term due to spin-orbit coupling. Mayer [May49], Haxel, Jensen and Suess [Hax49] proposed this correction. The mathematical form of the spin-orbit potential is

$$V_{SO} = f(r)\vec{l} \cdot \vec{s}, \quad (2.17)$$

where $f(r)$ is the strength of the spin-orbit coupling which is peaked at the nuclear surface. One chooses $f(r)$ related to the spin independent part of the average potential in:

$$f(r) = \lambda \frac{1}{r} \frac{\partial V(r)}{\partial r} \quad (2.18)$$

Hence the modified harmonic oscillator potential takes the form

$$V(r) = V_{HO}(r) + V_{SO}. \quad (2.19)$$

The spin-orbit interaction is proportional to the inner product of the orbital angular momentum l and spin s of the nucleon. The spin-orbit coupling causes further splitting of the p, d, f, g, h, \dots levels into two levels. The energy splitting of the levels increases with orbital angular momentum l . Choosing V_{SO} to be negative, the state with total angular momentum $j = l + s$ will be pushed down and the state with total angular momentum $j = l - s$ will be raised up. Figure 2.4 shows the effect of this splitting. The $1f_{7/2}$ level now appears in the gap between the second and the third oscillator shells, and by adding a capacity of 8 more nucleons the magic number 28 is obtained. The p and d level splittings do not result in any major regrouping of the levels. The $1g_{9/2}$ level is pushed down to lower major shell and taking into account its capacity of 10 nucleons a magic number of 50 is calculated. A similar effect is observed at other higher major shells. Note that the capacity of each level (with spin-

orbit interaction included) is given by $2j + 1$. The magic numbers produced with the modified harmonic oscillator potential are 2, 8, 20, 28, 50, 82, 126 in agreement with experiment. The neutron or proton number 40 is sometimes called a semi-magic number.

2.3.4 Example of the application of the shell model

Consider the filling of levels needed to produce $^{15}_8\text{O}_7$ and $^{17}_8\text{O}_9$ as shown in Figure 2.5. The 8 protons fill the first two shells and do not contribute further to the structure. According to the shell model, the unpaired nucleon determines the properties of the nucleus. In $^{15}_8\text{O}_7$ the unpaired neutron is in the $p_{1/2}$ level, thus the ground state of $^{15}_8\text{O}_7$ has spin $\frac{1}{2}$ and negative parity, (the parity of the state is determined from $(-1)^l$). Due to the unpaired neutron in the $d_{5/2}$ shell the ground state of $^{17}_8\text{O}_9$ has spin $5/2$ and positive parity. These two predictions of the shell model are in agreement with the observed properties of these two nuclei. Similar agreement is observed for many other nuclei for which the shell model is applicable.

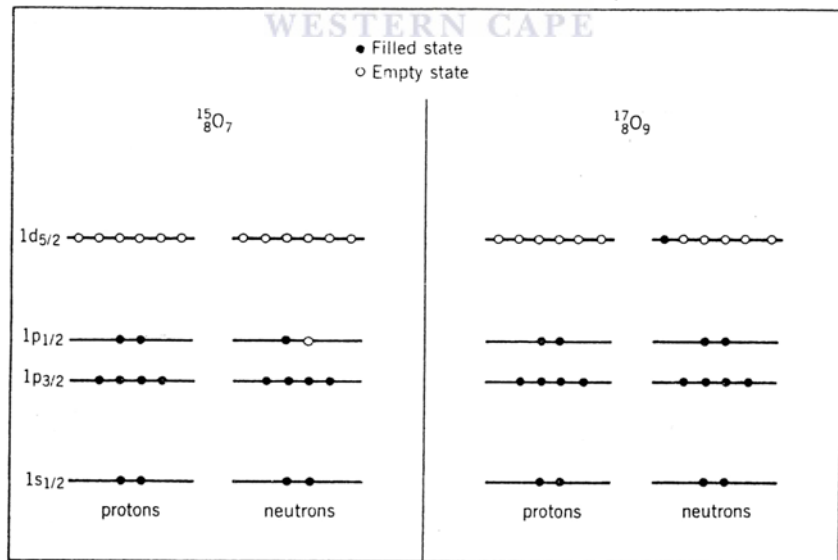


Figure 2.5: The filling of shells in $^{15}_8\text{O}_7$ and $^{17}_8\text{O}_9$. The filled protons shells do not contribute to the structure. The properties of the ground state are determined primarily by the odd neutron [Kra98a].

2.4 The deformed shell model

If the nuclear shape is not spherical, the average nuclear potential created by the nucleons within the nucleus will no longer be spherically symmetric. Therefore the average nuclear potential proposed for the shell model needs to be modified in order to predict experimental observations for deformed nuclei. In this section two cases of a deformed potential well that approximate axially symmetric ellipsoidal shape of the nucleus are used. The two ellipsoidal shapes are prolate and oblate. The prolate nucleus has positive values of the deformation parameter ε_2 or β_2 , whereas an oblate nucleus has negative values of ε_2 or β_2 .

Assuming that the nuclear shape is ellipsoidal, the average harmonic oscillator potential takes the form

$$V_{HO}(x, y, z) = \frac{M}{2} (\omega_x^2 x^2 + \omega_y^2 y^2 + \omega_z^2 z^2) \quad (2.20)$$

Frequencies $\omega_x, \omega_y, \omega_z$ must be proportional to the inverse of the half-axes a_x, a_y, a_z of the ellipsoid, i.e.

$$\omega_\nu = \omega_0 \frac{R_0}{a_\nu}, \quad \text{where } (\nu = x, y, z) \quad (2.21)$$

with a necessary condition of volume conservation

$$\omega_x \omega_y \omega_z = \omega_0^3. \quad (2.22)$$

The Hamiltonian for the single particle moving within the nucleus in the presence of the above-mentioned potential (2.20) is

$$h_o = -\frac{\hbar^2}{2M} \Delta + V_{HO}(x, y, z). \quad (2.23)$$

The Hamiltonian h_o is separable in x, y, z and the eigenstates of h_o are characterized by quantum numbers n_x, n_y, n_z . The eigenvalues are:

$$\varepsilon_0(n_x, n_y, n_z) = \hbar\omega_x(n_x + \frac{1}{2}) + \hbar\omega_y(n_y + \frac{1}{2}) + \hbar\omega_z(n_z + \frac{1}{2}). \quad (2.24)$$

For spherical nuclei, the three frequencies $\omega_x, \omega_y, \omega_z$ are the same. For axially symmetric deformed nuclei taking the z-axis as the symmetry axis, the deformation parameter δ is defined by:

$$\begin{aligned} \omega_x^2 = \omega_y^2 = \omega_z^2 &= \omega_0^2(\delta)\left(1 + \frac{2}{3}\delta\right) \\ \omega_z^2 &= \omega_0^2(\delta)\left(1 - \frac{4}{3}\delta\right), \end{aligned} \quad (2.25)$$

where the volume conservation is guaranteed up to second order in δ giving the deformation dependence $\omega_0(\delta)$ as

$$\omega_0(\delta) = \omega_0 \left(1 + \frac{2}{3}\delta^2\right). \quad (2.26)$$

Nilsson introduced a deformation that depends on the length of the oscillator

$b(\delta) = \left(\frac{\hbar}{m\omega_0(\delta)}\right)^{1/2}$ and dimensionless coordinate $r' = r/b$. Then the Hamiltonian h_o

takes the form

$$h_o(\delta) = \hbar\omega_0(\delta) \left(-\frac{1}{2}\Delta' + \frac{1}{2}r'^2 - \frac{1}{3}\sqrt{\frac{16\pi}{5}}\delta r'^2 Y_{20}(\theta', \Phi') \right). \quad (2.27)$$

For ellipsoids, the deformation parameter δ is approximately equal to β_2 since

$$\beta_2 = \frac{1}{3}\sqrt{\frac{16\pi}{5}}\delta + \dots = 1.057\delta + \dots \text{ and } r' \sim 1 + \beta_2 Y_{20}(\theta', \Phi'). \quad (2.28)$$

In the case of axial symmetry, cylindrical coordinates are used for the Hamiltonian [Flü71]. The eigenstates of h_0 are characterized by quantum numbers n_z, n_ρ, m_l , where m_l is the projection of the orbital angular momentum on to the symmetry axis. Substituting $N = n_x + 2n_\rho + m_l = n_x + n_y + n_z$ in (2.24) we get:

$$\begin{aligned}\varepsilon_0(n_z, n_\rho, m_l) &= \hbar\omega_z(n_z + \frac{1}{2}) + \hbar\omega_\perp(2n_\rho + m_l + 1) \\ &\cong \hbar\omega_0 \left\{ \left(N + \frac{1}{2} \right) + \delta \left(\frac{N}{3} - n_z \right) \right\}.\end{aligned}\quad (2.29)$$

In this case m_l , the spin component s_z and the j -component j_z are good quantum numbers. The eigenvalue of j_z is given by:

$$\Omega = m_l + m_s = m_l \pm \frac{1}{2}.\quad (2.30)$$

Nilsson quantum numbers $\Omega^\pi [N n_z m_l]$ are used to label eigenstates of h_0 in cylindrical coordinates. From (2.29), the levels with different values of n_z are split for small deformation proportional to δ .

This deformed harmonic oscillator potential was modified in order to give correct single particle energies by Nilsson [Nil55], who added two terms similar to the ones included in the case of spherical potential. His Hamiltonian is

$$\begin{aligned}h &= -\frac{\hbar^2}{2m}\Delta + \frac{m}{2}\omega_\perp^2(x^2 + y^2) + \frac{m}{2}\omega_z^2 z^2 + C\vec{l}\cdot\vec{s} + D(\vec{l}^2 - \langle \vec{l}^2 \rangle_N) \\ &= \hbar\omega_0(\delta) \left(-\frac{1}{2}\Delta + \frac{1}{2}r'^2 - \beta_2 r'^2 Y_{20} \right) - \kappa\hbar\omega_0 \left(2\vec{l}\cdot\vec{s} + \mu(\vec{l}^2 - \langle \vec{l}^2 \rangle_N) \right)\end{aligned}\quad (2.31)$$

where C and D are constants given in the form:

$$C = -2\hbar\omega_0\kappa, \quad D = -\hbar\omega_0\kappa\mu\quad (2.32)$$

Nilsson's Hamiltonian in (2.31) does not contain a Coulomb term, the effect of that term is contained in the appropriate choice of the constants κ and μ . To get a good fit of the experimental data, different values of κ and μ for different shells are used.

In cylindrical coordinate, $\vec{l} \cdot \vec{s}$ and the l^2 terms are no longer diagonal. The only quantum numbers that remain conserved are the parity π and the eigenvalue Ω of j_z . The $\vec{l} \cdot \vec{s}$ and the l^2 terms can be neglected in comparison with $\beta_2 Y_{20}$ for large nuclear deformation. In this limit, the quantum numbers $\Omega^\pi [N n_z m_l]$ are used to label single particle orbitals. The numbers in the square bracket are called asymptotic quantum numbers.

2.4.1 Splitting of the levels according to the projection K

For the deformed modified harmonic oscillator potential the single particle levels are split according to the projection Ω of total angular momentum j along the symmetry axis of the nucleus. The splitting of the levels depends on the total angular momentum j of the level. For example, a $1p_{3/2}$ orbital will have four possible orientations of j ranging from $-3/2$ to $3/2$. Due to the reflection symmetry of the nucleus, Ω has two-fold degeneracy, i.e. $+\Omega$ and $-\Omega$ and the corresponding single particle levels have the same energy. Therefore $1p_{3/2}$ level will split into two states labelled $\Omega = 1/2, 3/2$ and with negative parity, since the parity is determined from $(-1)^l$. Figure 2.7 shows how the levels would split as the deformation increases.

Figure 2.6 indicates the different projections of the total angular momentum j of the odd particle for the prolate and oblate deformation along the symmetry axis of the nucleus. For prolate deformation, the state with smallest possible value of Ω (equal to $1/2$) interacts more strongly with the core and is thus strongly bound and lowest in energy. The orbital with $\Omega=1/2$ covers a long path around the nucleus surface compared to other orbits of higher projections. The situation is different for oblate deformation, in which the state with maximum Ω (equal to j) has the strongest

interaction with the core and thus is lowest in energy. Nilsson asymptotic quantum numbers $\Omega^\pi [N n_z m_l]$ are used as labels of the single particle states.

Note that Figure 2.7 is not strictly correct because the spherical-particle quantum numbers l and j are not good quantum numbers when the nuclear potential is no longer spherically symmetric. When the deformation increases the spherical states mix with each other resulting into new shells, hence new magic numbers are produced. Figure 2.7 shows this kind of situation.

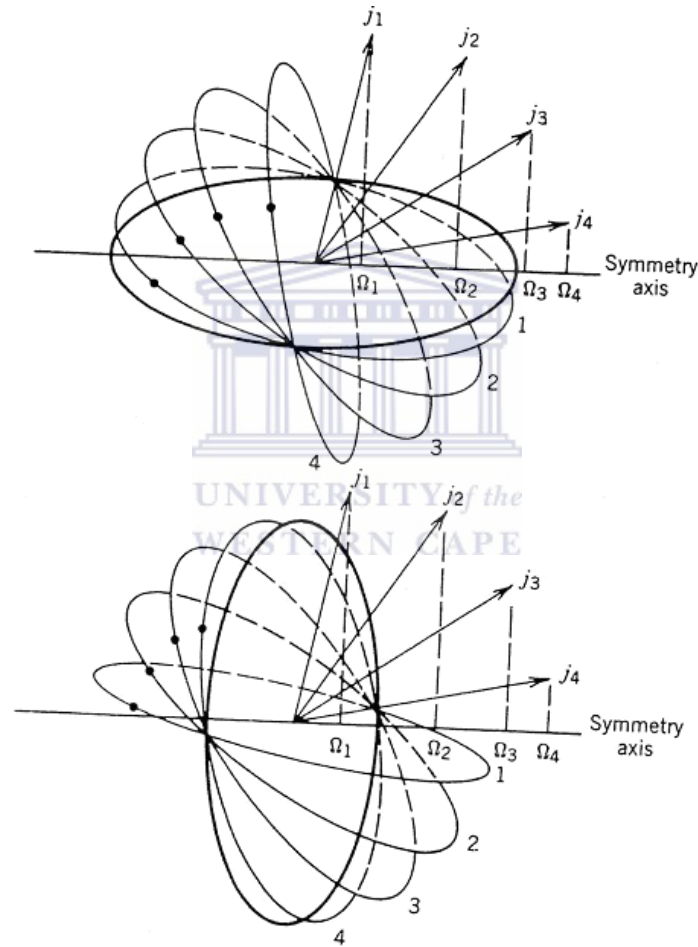


Figure 2.6: Single particle orbits with $j = 7/2$ and the possible projections of j along the symmetry axis, for prolate (top) and oblate (bottom) deformations. The possible projections are $\Omega = 1/2, 3/2, 5/2, 7/2$ (for clarity only the positive projections are shown). Note that in the prolate case, orbit 1 lies closest (on the average) to the core and will interact most strongly with the core while in the oblate case, it is orbit 4 that has the strongest interaction with the core [Kra98b].

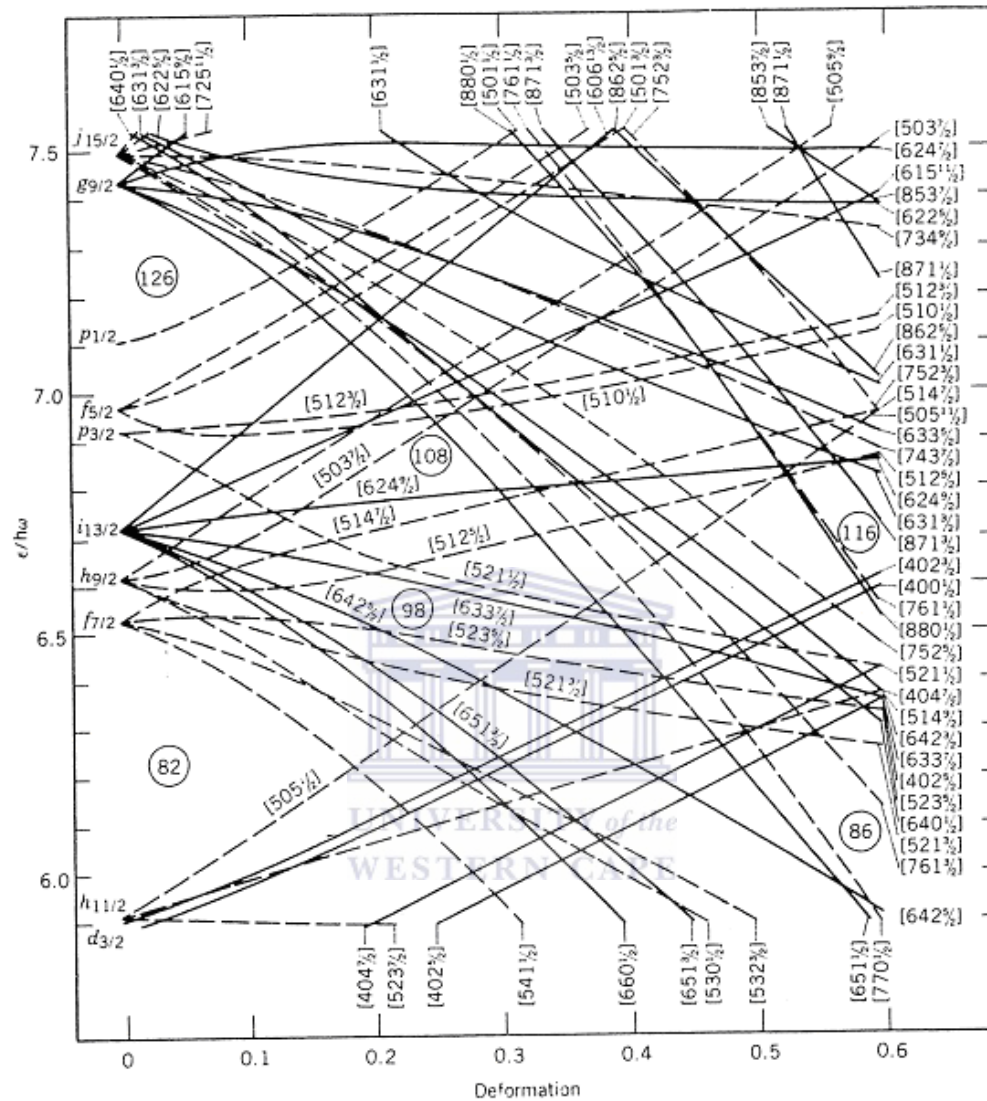


Figure 2.7: Energy levels for neutrons in a prolate deformed potential. The numbers in the brackets label the states, solid lines show states with positive parity and dashed lines show negative parity states [Gus67].

2.5 Rotational motion

An important consequence of deformation is the fact that rotational motion is a possible mode of excitation. In the spherical case shown in Figure 2.8 (a), it is not possible to observe collective rotation about an axis of symmetry, since the different orientations of the nucleus are quantum-mechanically indistinguishable. In the case of an axially symmetric nucleus shown in Figure 2.8 (b) and (c), there is a set of axes of rotation, perpendicular to the symmetry axis. The collective motion of many nucleons about this rotation axis generates the rotational angular momentum \vec{R} . Additional angular momentum can be generated by the intrinsic angular momentum of any valence nucleons, \vec{J} . The total angular momentum, \vec{I} , of the nucleus is given by

$$\vec{I} = \vec{R} + \vec{J}. \quad (2.33)$$

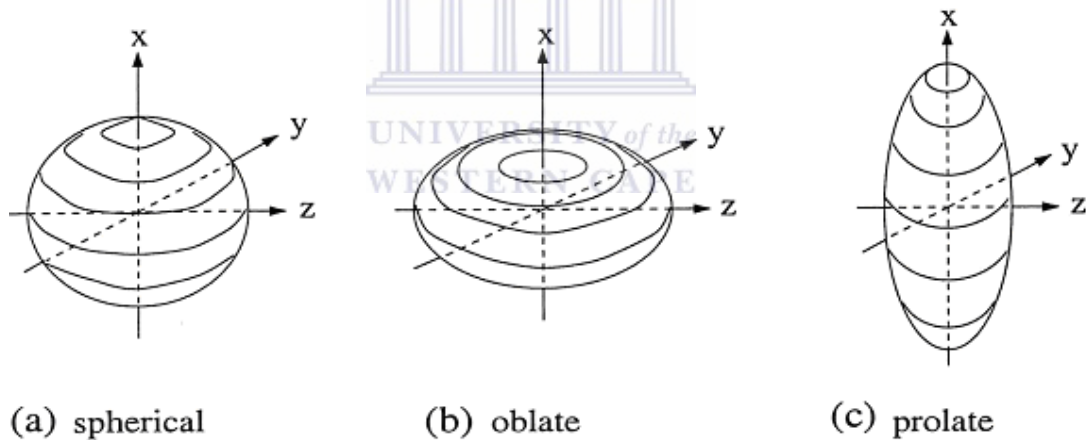


Figure 2.8: Schematic representation of the spherical (a), oblate (b) and prolate (c) nuclear shapes. The x-axis represents the symmetric axis for this nucleus [Mab03].

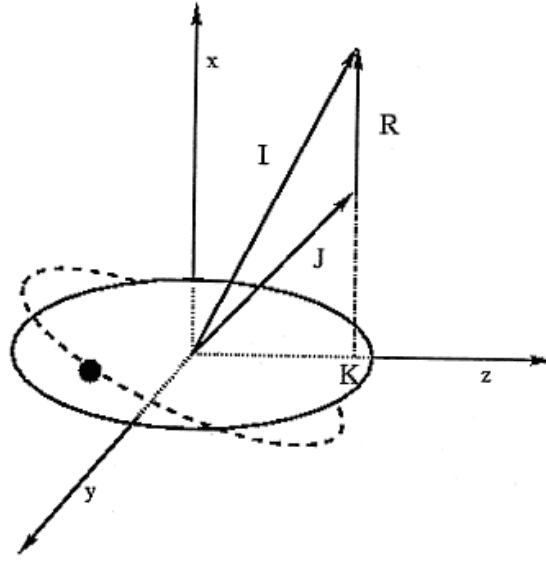


Figure 2.9: Schematic of the coupling of the collective angular momentum \vec{R} , and the intrinsic angular momentum of valence nucleons \vec{J} . The projection of the total angular momentum \vec{I} , onto the symmetry axis is K [Gre99].

This angular momentum coupling is shown schematically in Figure 2.9. The intrinsic angular momentum of the valence nucleons \vec{J} is the sum of the angular momentum of the individual valence nucleons, i.e. $\vec{J} = \sum_{i=1}^A \vec{j}_i$. The projection of the total angular

momentum onto the symmetry axis is K , and is the same as the projection of \vec{J} .

The projection of the angular momentum \vec{j} , of a valence nucleon is Ω , thus

$$K = \sum_{i=1}^A \Omega_i.$$

In the ground state rotational band of an even-even nucleus, the valence particles are paired such that $J = 0$, and the total angular momentum is $\vec{I} = \vec{R}$. Therefore the collective rotational energy can be determined through analogy with a classical rotating rigid body. The classical kinetic energy of the rotating body is given by

$$E = \frac{1}{2\mathfrak{I}} \vec{R}^2 = \frac{1}{2\mathfrak{I}} \vec{I}^2 \quad (2.34)$$

where \mathfrak{I} is the classical moment of inertia. Quantum mechanically, the length of \vec{I}^2 is $I(I+1)\hbar^2$. Using this relation, equation (2.34) becomes

$$E = \frac{\hbar^2}{2\mathfrak{I}} I(I+1) \quad (2.35)$$

Thus the rotational motion of the nucleus leads to a sequence of states with energies given by equation (2.35). However, real nuclei deviate from the $I(I+1)$ law. This deviation may be expressed by an expansion in powers of the quantity $I(I+1)$ as follows:

$$E(I) = AI(I+1) + B[I(I+1)]^2 + C[I(I+1)]^3 + \dots \quad (2.36)$$

It turns out that this expansion is poorly convergent for higher values of the angular momentum I , and an expansion in the angular frequency ω is more appropriate. In principle, ω is not a measurable quantity. We can define it classically as

$$\hbar\omega \equiv \frac{dE}{dI} \quad (2.37)$$

The quantum-mechanical analogue of this is given by

$$\hbar\omega = \frac{dE(I)}{d\sqrt{I(I+1) - K^2}} \quad (2.38)$$

where $\sqrt{I(I+1) - K^2}$ is the projection of the total angular momentum onto the rotational axis, known as the aligned angular momentum, I_x . For $K = 0$, a rotational band of stretched $E2$ transitions is formed. Thus a transition from an initial state with spin I to a final state with spin $I-2$ has γ -ray energy $E_\gamma = E(I) - E(I-2)$. If the rotational frequency ω is expanded along the average value of the angular momentum between I and $I-2$, we obtain:

$$\hbar\omega(I-1) = \frac{E(I) - E(I-2)}{\sqrt{I(I+1)} - \sqrt{(I-2)(I-1)}} \approx \frac{E_\gamma}{2} \quad \text{when } I \gg 0. \quad (2.39)$$

Thus rotational frequency is directly related to the γ -ray energy.

Another energy expansion in powers of angular velocity of rotation introduced by Harris [Har65] is as follows:

$$E(I) = \alpha\omega^2 + \beta\omega^4 + \gamma\omega^6 + \dots \quad (2.40)$$

Odd powers of ω do not occur, since E cannot change by reversing the angular velocity. The series in equation (2.40) are often taken up to second term only.

2.5.1 Moment of inertia

It should be noted that the nucleus, however, is not a rigid body, and measured moments of inertia are less than rigid body values at low spins [Bar57]. This is due to the effects of the pairing interactions, which make the nucleus behave like a superfluid. Experimental moments of inertia are larger than corresponding irrotational flow of a superfluid, showing that the nucleus is somewhere between these two extremes. Superfluidity plus rigid body accounts in fact for the moment of inertia. As the nucleus rotates, it is found that the moment of inertia changes as a function of spin.

Rotational energy spectra can be discussed in terms of three spin-dependent moments of inertia, which are related to the zero, first- and second-order derivatives of the excitation energy with respect to the aligned angular momentum I_x .

The static moment of inertia $\mathfrak{I}^{(0)}$, which is related to the excitation energy E , and spin I , in the $K = 0$ rotational band by

$$E = \frac{\hbar^2}{2\mathfrak{I}^{(0)}} I(I+1). \quad (2.41)$$

Substituting an expression of the total aligned angular momentum $I_x = \sqrt{I(I+1)}$ into equation (2.41) one obtains an expression which can be used to calculate the static moment of inertia.

$$\mathfrak{I}^{(0)} = \frac{\hbar^2}{2} \left(\frac{E}{I_x^2} \right)^{-1} = \frac{\hbar^2 I_x^2}{2 E} \quad (2.42)$$

The first derivative is the kinematical moment of inertia, $\mathfrak{I}^{(1)}$, which is related to the total angular momentum of the nucleus [Boh81]. The kinematical moment of inertia is given by:

$$\mathfrak{I}^{(1)} = I_x \left(\frac{dE}{dI_x} \right)^{-1} \hbar^2 = \hbar \frac{I_x}{\omega} \quad (2.43)$$

The kinematical moment of inertia can be related to the transition energy, E_γ , through equation (2.39). For $K = 0$ rotational band

$$E_\gamma = \frac{\hbar^2}{\mathfrak{I}^{(1)}} (2I - 1). \quad (2.44)$$

The second derivative is the dynamical moment of inertia $\mathfrak{I}^{(2)}$, which carries information about the response of the nucleus if it is subjected to an applied torque [Boh81]. This dynamical moment of inertia is given by:

$$\mathfrak{I}^{(2)} = \left(\frac{d^2 E}{dI_x^2} \right)^{-1} \hbar^2 = \hbar \frac{dI_x}{d\omega}. \quad (2.45)$$

For a rotational band consisting of E2 γ -ray transitions, the dynamical moment of inertia can be related to the difference in transition energy of consecutive γ -rays,

$$\Delta E_\gamma = \frac{4\hbar^2}{\mathfrak{I}^{(2)}}. \quad (2.46)$$

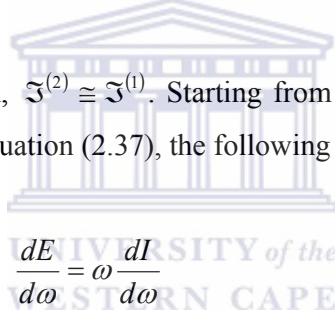
For a dipole band consisting of M1 γ -ray transitions, the dynamical moment of inertia is related to the difference of the energy of the consecutive γ -rays as

$$\Delta E_\gamma = \frac{\hbar^2}{\mathfrak{I}^{(2)}}. \quad (2.47)$$

If the dynamical moment of inertia was constant, the transition energy difference would be the same for all values of spin. Often $\mathfrak{I}^{(2)}$ is found to vary with increasing spin. The two moments of inertia $\mathfrak{I}^{(1)}$ and $\mathfrak{I}^{(2)}$ can be related as follows:

$$\mathfrak{I}^{(2)} = \frac{dI_x}{d\omega} = \frac{d}{d\omega}(\omega\mathfrak{I}^{(1)}) = \mathfrak{I}^{(1)} + \omega \frac{d\mathfrak{I}^{(1)}}{d\omega}. \quad (2.48)$$

In the limit of rigid rotation, $\mathfrak{I}^{(2)} \cong \mathfrak{I}^{(1)}$. Starting from the explicit definition of the rotational frequency ω in equation (2.37), the following relation can be derived:



$$\frac{dE}{d\omega} = \omega \frac{dI}{d\omega} \quad (2.49)$$

which leads to the expansion for $\mathfrak{I}^{(2)}$, which is similar to the Harris expansion in equation (2.40):

$$\mathfrak{I}^{(2)} = 2\alpha + 4\beta\omega^2 + 6\gamma\omega^4 + \dots \quad (2.50)$$

The integration of equation (2.48) yields the expansion for $\mathfrak{I}^{(1)}$:

$$\mathfrak{I}^{(1)} = 2\alpha + \frac{4}{3}\beta\omega^2 + \frac{6}{5}\gamma\omega^4 + \dots \quad (2.51)$$

In practice, instead of α, β, γ , etc., the parameters J_0, J_1, J_2 , (called the Harris parameters), are commonly used, where $J_0 = 2\alpha, J_1 = \frac{4}{3}\beta, J_2 = \frac{6}{5}\gamma$. Then:

$$\mathfrak{I}^{(1)} = J_0 + J_1\omega^2 + J_2\omega^4 + \dots \quad (2.52)$$

$$\mathfrak{I}^{(2)} = J_0 + 3J_1\omega^2 + 5J_2\omega^4 + \dots \quad (2.53)$$

The Harris expansion equation (2.52 and 2.53), even if they are taken up to the first two terms, give very good agreement with the experimental data in the low spin region of even-even deformed nuclei. The shortened expansions are used to fit the moment of inertia of a band structure, which can serve later as a reference for other rotational bands in the nucleus, e.g. the reference rotor.

2.6 The asymmetric rotor model

Further attempts to explain the deviation from the $I(I+1)$ law and the low lying second 2^+ states in many nuclei have been undertaken by Davydov *et al.* using the picture of a pure triaxial rotor [Dav58, Dav59a, Dav59b and Dav65]. They did not consider vibrational excitations and diagonalise only the rotational energy operator

$$\hat{T}_{rot} = \frac{\hat{I}_1^2}{2\mathfrak{I}_1} + \frac{\hat{I}_2^2}{2\mathfrak{I}_2} + \frac{\hat{I}_3^2}{2\mathfrak{I}_3} \quad (2.54)$$

with the moments of inertia

$$\mathfrak{I}_k = 4B_2\beta_2^2 \sin^2\left(\gamma - \frac{2\pi}{3}k\right), \quad k = 1, 2, 3 \quad (2.55)$$

With these moments of inertia (2.55), the rotational energy operator is proportional to β_2^{-2} and one can diagonalise it for all values of γ . The constant factor B_2 can afterwards be adjusted so as to reproduce the first state.

Figure 2.10 shows the energy eigenvalues of (2.54). For $\gamma = 0^\circ$ and $\gamma = 60^\circ$ one gets an $I(I+1)$ dependence for the excitation energy E_I . Even for strong triaxial deformations, one gets only slight deviations of this form. However additional

2_2^+ , 3_1^+ , 4_2^+ , etc levels come down in energy. It is a characteristic feature of a non-axial shape to have a low-lying second 2_2^+ state. The 0_1^+ , 2_1^+ , 4_1^+ , ... and 2_2^+ , 3_1^+ , 4_2^+ , ... states belong to the ground band and the γ – band respectively.

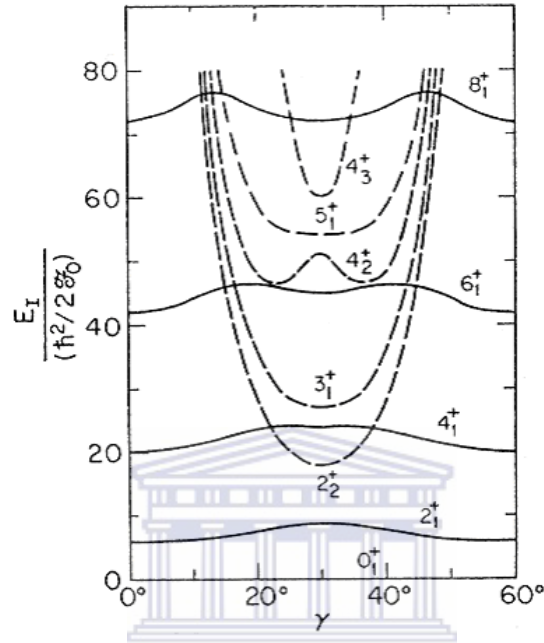


Figure 2.10: The energy eigenvalues of a deformed asymmetric rotor with the hydrodynamic moment of inertia (From [Mey75]).

In the case of maximal triaxiality ($\gamma = 30^\circ$), $\mathfrak{I}_2 = \mathfrak{I}_3 = \frac{1}{4}\mathfrak{I}_1 = \frac{1}{3}\mathfrak{I}_0$ (\mathfrak{I}_0 is the moment of inertia at $\gamma = 0^\circ$).

2.7 The particle-plus-rotor model (PRM)

This model developed by Bohr and Mottelson [Boh53] describes the interplay between the motion of the particles and the collective rotation. Bohr and Mottelson proposed to take into account only a few so-called valence particles, which move more or less independently in the deformed well of the core. These valence particles are coupled to a collective rotor, which stands for the rest of the particles. In an odd mass nucleus the unpaired nucleon is treated as a valence nucleon coupled to an even-

even core. One can also attribute the particle-hole excitations in this nucleus to the excitations of the valence particles.

The nuclear Hamiltonian is divided into two parts: an intrinsic part H_{int} , which describes microscopically one or more valence particles near the Fermi surface, and a phenomenological part H_{coll} which describes the collective nuclear rotation, $\frac{\hbar^2}{2\mathfrak{I}}R^2$.

The expression for the total Hamiltonian is

$$H = H_{\text{int}} + H_{\text{coll}}. \quad (2.56)$$

The intrinsic part has the form:

$$H_{\text{int}} = \sum_k \varepsilon_k a_k^+ a_k + \frac{1}{4} \sum_{klmn} \bar{v}_{klmn} a_k^+ a_l^+ a_n a_m \quad (2.57)$$

where ε_k are single particle energies in the deformed potential (e.g. Nilsson energies) and \bar{v} is the interaction between the valence particles which is neglected in many cases.



The collective part has the form:

$$H_{\text{coll}} = \frac{R_1^2}{2\mathfrak{I}_1} + \frac{R_2^2}{2\mathfrak{I}_2} + \frac{R_3^2}{2\mathfrak{I}_3} \quad (2.58)$$

where R_i are the body fixed components of the collective angular momentum of the core. The sum of the collective angular momentum \vec{R} of the core and the intrinsic angular momentum of the valence particles \vec{j} give the total angular momentum of the system (see section 2.5).

$$\vec{I} = \vec{R} + \vec{j} \quad (2.59)$$

Substituting \vec{R} , H_{coll} can be decomposed into three parts:

$$H_{coll} = H_{rot} + H_{rec} + H_{cor} \quad (2.60)$$

where

$$H_{rot} = \frac{I_1^2}{2\mathfrak{I}_1} + \frac{I_2^2}{2\mathfrak{I}_2} + \frac{I_3^2}{2\mathfrak{I}_3} \quad (2.61)$$

is the pure rotational operator of the core which acts only on the degrees of freedom of the rotor, i.e. the Euler angles.

$$H_{rec} = \sum_{i=1}^3 \frac{j_i^2}{2\mathfrak{I}_i} \quad (2.62)$$

The term in (2.62) is called the recoil term which represents the recoil energy of the rotor.



$$H_{cor} = -\sum_{i=1}^3 \frac{I_i j_i}{\mathfrak{I}_i} \quad (2.63)$$

The Coriolis interaction term in (2.63) couples the degree of freedom of the valence particles to the degree of freedom of the rotor.

This model is effective in describing slow nuclear rotation. Using it, a large number of the experimental spectra of odd nuclei have been reproduced very accurately.

2.7.1 The axial symmetry case

Assuming that the 3-axis is the axis of symmetry of the rotor, that is, $\mathfrak{I}_1 = \mathfrak{I}_2 = \mathfrak{I}$, there can be no collective rotation around this axis and the 3-component of \vec{R} has to vanish. From (2.59) it follows immediately that K , the 3-component of the total angular momentum \vec{I} , has to be equal to Ω , the 3-component of \vec{j} :

$$K = \Omega \quad (2.64)$$

For the different terms of the Hamiltonian (2.56, 2.60), we obtain in this case

$$H_{\text{int}} = \sum_{i,\Omega} \varepsilon_{\Omega}^i a_{i\Omega}^+ a_{i\Omega} \quad (2.65)$$

$$H_{\text{rot}} = \frac{\vec{I}^2 - I_3^2}{2\mathfrak{I}} \quad (2.66)$$

$$H_{\text{rec}} = \frac{1}{2\mathfrak{I}} (j_1^2 + j_2^2) \quad (2.67)$$

$$H_{\text{cor}} = -\frac{1}{\mathfrak{I}} (I_1 j_1 + I_2 j_2) = -\frac{1}{2\mathfrak{I}} (I_+ j_- + I_- j_+), \quad (2.68)$$

where I_+, I_- and j_+, j_- are the raising and lowering operators of total angular momentum and particle angular momentum respectively.

In (2.65) we have neglected the residual interaction. The single particle levels in the axially symmetric well are labelled by $k = (i, \Omega)$, and the corresponding eigenfunctions are denoted by Φ_{Ω}^i , where i stands for all other quantum numbers associated with that eigenfunctions. The recoil term only acts in the intrinsic coordinate system. It is often neglected because the intrinsic single particle energies ε_{Ω}^i are adjusted to experimental data. In the following discussion we will omit H_{rec} . However, the different terms in (2.65-2.68) are of different importance, depending on the physical situation. Therefore, it is useful to consider two limits in which one of the terms becomes predominant and which as a consequence can be solved analytically (see [Ste75]):

- a) the strong coupling limit (deformation alignment),
- b) the decoupling limit (rotational alignment).

2.7.1.1 The strong coupling limit (deformation alignment)

The strong coupling limit is realized when the Coriolis term is small compared with the level splitting of the single particle energies in the deformed shell model for different values of Ω . The deformation alignment takes place in a nucleus with large deformations β_2 , and at low spins I or when nucleons occupy orbitals with small angular momentum j . It is called strong coupling or deformation alignment limit because in this case K is a good quantum number. The angular momentum j of the valence particles is strongly coupled to the motion of the core as shown in Figure 2.11a.

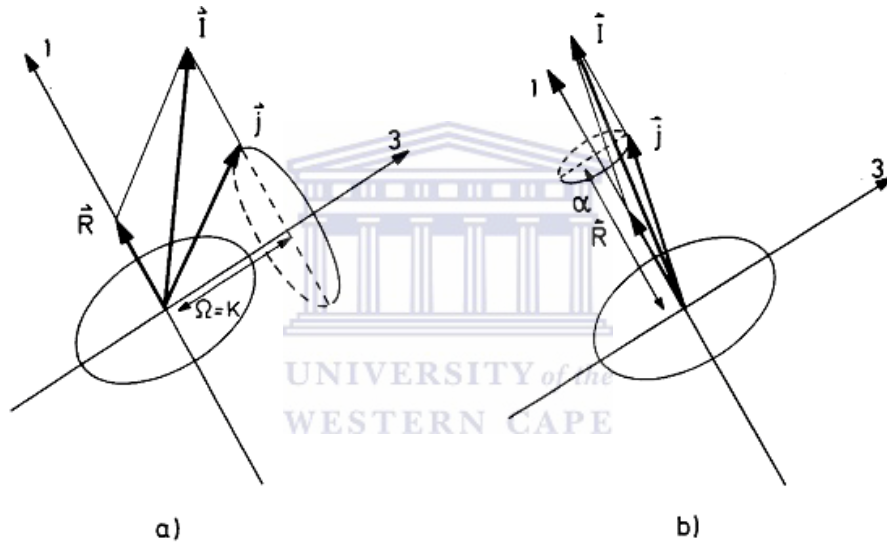


Figure 2.11: Coupling schemes in the particle-plus-rotor model: a) strong coupling, b) rotational alignment [Rin90].

In this case, the rotational band has spins increasing with $\Delta I = 1$ and its moment of inertia is that of a rotor. For $I \geq K$, the spins $I = K, K + 1, K + 2, \dots$ are observed. The expression for the energy of the levels of the band is

$$E_k^i(I) = \varepsilon_k^i + \frac{1}{2\mathfrak{I}} [I(I+1) - K^2] \quad \text{for } K \neq \frac{1}{2}. \quad (2.69)$$

In the strong coupling limit the Coriolis interaction is neglected completely.

2.7.1.2 The decoupling limit (rotational alignment).

In the case of intermediate deformation, the energy splitting in the intrinsic part of the Hamiltonian can no longer be neglected. In this case, the orientation of the external large- j particle with low Ω is no longer independent of the motion of the core. The Coriolis force is so strong that the coupling to the deformation core may be neglected. The total angular momentum and the single particle angular momentum are then parallel to one another. We find for the spectrum of the Hamiltonian:

$$\begin{aligned} E(I, j = \alpha) &= \frac{1}{2\mathfrak{I}} [I(I+1) + j(j+1) - 2I\alpha] \\ &= \frac{1}{2\mathfrak{I}} (I - \alpha)(I - \alpha + 1) + 2\alpha \\ &= \frac{1}{2\mathfrak{I}} R(R+1) + 2\alpha \end{aligned} \quad (2.70a)$$

where $R = I - \alpha$ describes the collective rotation and α is the projection of single particle angular momentum along the rotational axis.

Generally for $\alpha = j - n$, where $n = 0, 1, 2, 3, \dots$ the spectrum of the Hamiltonian is

$$\begin{aligned} E(I, j = \alpha + n) &= \frac{1}{2\mathfrak{I}} [(I - \alpha)(I - \alpha + 1) + (2\alpha + n)(n + 1)] \\ &= \frac{1}{2\mathfrak{I}} R(R + 1) + (2\alpha + n)(n + 1) \end{aligned} \quad (2.70b)$$

In this case the values of n correspond to different bands. For $n = 0$ we have maximally aligned band with a band head spin of $\alpha = j$ and this is a favored band. For the values of n different from zero we have lesser-aligned unfavored bands with band head spins of $\alpha = j - 1, j - 2, \dots$

2.8 The triaxial particle-plus-rotor model

We have already seen that Davydov *et al.* [Dav59a] used a triaxial rotor to explain the low-lying states in some transitional nuclei (see section 2.6). This model can be extended to odd mass nuclei by coupling of an external particle to a triaxial rotor. It

has been applied to cases where the external particle is placed in a high j – shell, and has turned out to be very powerful as a description of energy levels and decay scheme of many transitional nuclei. Restricting to one external particle in a high j – shell, the Hamiltonian has the form [Mey74]:

$$H = \sum_{i=1}^3 \frac{R_i^2}{2\mathfrak{I}_i} + h_0 + kr^2 \beta_2 \left\{ \cos \gamma Y_{20} + \sin \gamma \frac{1}{\sqrt{2}} (Y_{22} - Y_{2-2}) \right\} \quad (2.71)$$

The constant k is given by the splitting of the j – shell in the Nilsson scheme. h_0 is the spherical harmonic oscillator Hamiltonian.

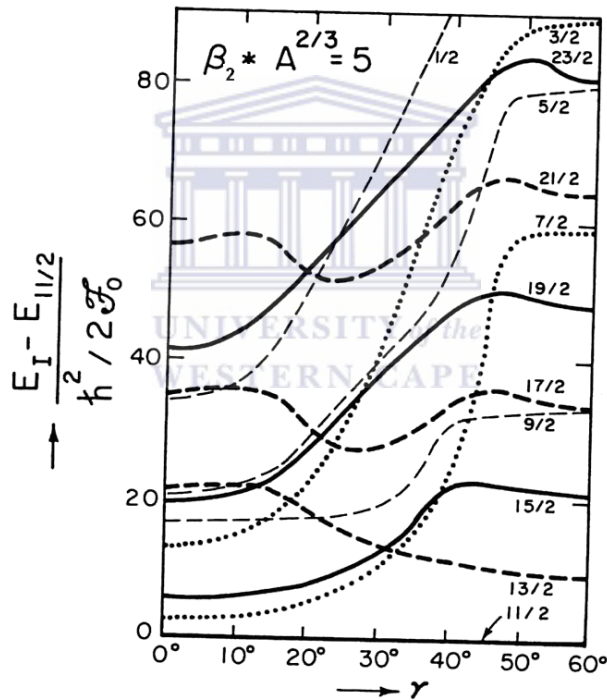


Figure 2.12: Spectrum of $j=11/2$ particle coupled to an asymmetric rotor as function of γ , for Fermi surface at the bottom of the $j=11/2$ shell. The states with $(\pi, \alpha) = (+, +1/2)$ are represented with bold-dashed and faint-dashed lines, $(+, -1/2)$ with solid and dotted lines (From [Mey74]).

Figure 2.12 shows the spectrum of the Hamiltonian (2.71) as a function of γ at a deformation of $\beta_2 = 5A^{-2/3}$. At $\gamma = 0^\circ$ we have decoupled structure with the favored

11/2, 15/2, 19/2, 23/2 and unfavored 13/2, 17/2, 21/2 states respectively. The unfavored 13/2, 17/2, 21/2 states lie relatively high at $\gamma = 0^\circ$, but come down sharply around $\gamma = 25^\circ$. In the region $30^\circ \leq \gamma \leq 60^\circ$ we have strongly coupled structure. At $\gamma = 60^\circ$ the high spin levels correspond to a situation in which the particle angular momentum points along the oblate symmetry axis, whereas the core angular momentum is perpendicular to it. At $\gamma = 60^\circ$ the low spin levels correspond to opposite direction of the core and particle angular momentum and may also be grouped into favored 7/2, 3/2 and unfavored 9/2, 5/2, 1/2 states. At $\gamma = 30^\circ$ transition from the strongly coupled to the decoupled scheme takes place.

2.9 The cranked shell model (CSM)

For the description of near yrast high spin states in nuclei, the cranked shell model has been used with great success. This model was introduced by Inglis [Ing54, Ing56] and further developed by Bengtsson and Frauendorf [Ben79]. The model provides a fully microscopic description of a nuclear rotation, it also handles both collective and single particle excitations on the same footing and it is correct for up to a very large angular momentum. Its disadvantages are as follows: (i) the model is non-linear at high rotation, (ii) the total angular momentum of the rotating nucleus is not conserved.

2.9.1 The cranking Hamiltonian

The single particle cranking Hamiltonian can be derived both semi-classically or quantum mechanically. In this section, the cranking Hamiltonian will be briefly explained, but only major steps will be considered. The basic assumption of this model is that one considers a coordinate system, which rotates with constant angular frequency ω with reference to the fixed frame (laboratory frame). The independent particles are assumed to be moving in a rotating potential with reference to the fixed frame. It is shown by Inglis [Ing54, Ing56] and in many review articles and text books, for instance [Szy83, Boh76b] that the Schrödinger equation in the rotating system can be solved in the standard way as an eigenvalue problem. If the rotation

vector coincides with the rotational axis of the nucleus, then the single particle cranking Hamiltonian is given by

$$h^\omega = h_0 - \hbar\omega j_x \quad (2.72)$$

where h^ω is the Hamiltonian of the particle in the rotating frame, h_0 is its Hamiltonian in a fixed frame, and j_x is the projection of the angular momentum of the particle on to the rotation axis. The term $\hbar\omega j_x$ contains Coriolis and Centrifugal forces, which modify the nucleon orbital. The energy eigenvalues (e^ω) of (2.72) are called Routhians. The total cranking Hamiltonian of the rotating system H^ω , can be obtained by summation of the single particle Hamiltonians h^ω . Thus,

$$H^\omega = H_0 - \hbar\omega I_x \quad (2.73)$$

where I_x is the total aligned angular momentum over all occupied orbitals. If one denotes the occupied orbitals by ν , then I_x can be determined from

$$I_x = \sum_{\nu} j_x \cdot \quad (2.74)$$

The total energy of the rotating system in a fixed frame can be determined by finding the expectation value of (2.72). Thus,

$$E_0 = E^\omega + \hbar\omega I_x \cdot \quad (2.75)$$

A diagram of the single particle Routhians against rotational frequency is called a Routhian plot. The derivative of a Routhian is related to the aligned angular momentum i_x ,

$$i_x = -\frac{de^\omega}{d\omega} \quad (2.76)$$

where e^{ω} and i_x are the experimental single-quasiparticle Routhian and the alignment respectively.

2.9.2 Symmetries in the cranking Hamiltonian

At high rotation of the nucleus, the time reversal symmetry of the nucleus is broken by the Coriolis term $-\hbar\omega j_x$ and a splitting into two single particle levels is observed. The only two remaining symmetries are parity π , which describes the symmetry under reflection and signature, which describes the invariant under a rotation of 180° around the rotational x-axis. The two single particle levels belong to the eigenstates of the rotational operator \mathfrak{R}_x , which is given by

$$\mathfrak{R}_x = e^{-i\pi j_x} \quad (2.77)$$

The eigenvalue of (2.77) is the quantum number r [Boh76a, Boh76b], called in the past signature. More recently another quantum number, α , defined as

$$r = e^{-i\pi\alpha} \quad (2.78)$$

is called signature. For even mass system, $r = \pm 1$, corresponding to $\alpha = 0$ and $\alpha = 1$ respectively. For odd-mass system, $r = \pm i$, corresponding to $\alpha = \mp 1/2$. The parity assignments are $\pi = \pm$, depending on the behavior of the single particle wave function under space reflection.

The signature quantum number α is commonly used nowadays, since it is an additive quantum number. A simple relation can be found between the total spin I and α (see [Boh75, Szy83]).

$$I = \alpha + \text{even number} \quad (2.79)$$

2.9.3 Comparison of experimental observables with CSM theoretical quantities

In order to compare the CSM theoretical quantities (e.g. the Routhians, frequency, band crossing frequency, and the aligned angular momentum) with the experimental observables one should first transform the experimental quantities into the rotating frame. It was shown by Bengtsson [Ben79], that it is easier to transform the experimental quantities into the intrinsic rotating basis instead of vice versa.

Considering the nucleus decaying from a state with spin $I + 1$ to a state with spin $I - 1$, the aligned angular momentum I_x is defined as:

$$I_x = \sqrt{I(I+1) - K^2} \sim \sqrt{\left(I + \frac{1}{2}\right)^2 - K^2} . \quad (2.80)$$

For the same transition the total experimental Routhian is given by:

$$E_{\text{exp}}^{\omega}(I) = \frac{1}{2} [E(I+1) + E(I-1)] - \hbar\omega(I)I_x(I) \quad (2.81)$$

where $E(I+1), E(I-1)$ are the excitation energy of the levels with spin $I+1$ and $I-1$, and $I_x(I)$ is the aligned angular momentum between levels with spin $I+1$ and $I-1$.

The experimental rotational frequency, $\hbar\omega$, between the two intermediate spin levels is given by:

$$\hbar\omega(I) = \frac{dE}{dI_x} = \frac{E(I+1) - E(I-1)}{I_x(I+1) - I_x(I-1)} . \quad (2.82)$$

A comparison between the experimental Routhians and aligned angular momenta I_x with the CSM theoretical quantities requires a subtraction of the Routhian and aligned angular momentum of a reference core from the experimental data. A subtraction of

this kind removes the contribution from the core, and shows the behavior of the quasi-particles only. The experimental quasi-particle Routhian and alignment are defined by:

$$e_{\text{exp}}^{\omega}(I) = E_{\text{exp}}^{\omega}(I) - E_{\text{ref}}^{\omega}(I) \quad (2.83)$$

and

$$i_x^{\text{exp}}(\omega) = I_x(\omega) - I_x^{\text{ref}}(\omega). \quad (2.84)$$

The energy reference of the core can be calculated using a variable moment of inertia fit to the low-lying transitions of an even-even core as a function of ω^2 :

$$\mathfrak{I}_{\text{ref}}^{(1)}(\omega) = J_0 + \omega^2 J_1 \quad (2.85)$$

where J_0 and J_1 are known as the Harris parameters [Har65]. Following the discussion of the moment of inertia in section 2.5.1, the aligned angular momentum of the reference core is given by:

$$I_x^{\text{ref}}(\omega) = \frac{1}{\hbar} (J_0 + \omega^2 J_1) \omega + i, \quad (2.86)$$

where $i = 0$ if the ground band of an even-even nucleus is used as the reference. If the non-yrast band is used then i will be its alignment.

The energy of the reference core is given by:

$$E_x^{\text{ref}}(\omega) = -\frac{1}{2} \omega^2 J_0 - \frac{1}{4} \omega^4 J_1 + \frac{1}{8} \frac{\hbar^2}{J_0}. \quad (2.87)$$

The integration constant $\hbar^2/8J_0$ is introduced to ensure that the ground state reference energy is set to zero. The experimental alignment $i_x(\omega)$ and the Routhian $e_{\text{exp}}^\omega(\omega)$ can be compared directly with the theoretical alignment and Routhian.

2.10 Total potential energy at $\omega = 0$

2.10.1 Liquid drop model (LDM)

The model considers the nucleus as a liquid drop, which has very low compressibility and well-defined surface of radius, $R = r_0 A^{1/3}$, where the parameter r_0 has empirically the value $r_0 = 1.3 \text{ fm}$ and A denotes the mass number of the nucleus.

For a LDM, the nuclear binding energy $B(N, Z)$ is defined in the following way:

$$m(N, Z) = \frac{1}{c^2} E(N, Z) = NM_n + ZM_H - \frac{1}{c^2} B(N, Z). \quad (2.88)$$

where $m(N, Z)$ is the atomic mass of an atom with N neutron and Z proton, M_n and M_H correspond to the free neutron and hydrogen atom masses, and $B(N, Z)$ is the nuclear binding energy.

For a homogeneously charged liquid drop, the binding energy is given by [Wei53, Bet36]:

$$B = a_{\text{vol}} A - a_{\text{surf}} A^{2/3} - \frac{1}{2} a_{\text{asym}} \frac{(N - Z)^2}{A} - \frac{3}{5} \frac{Z^2 e^2}{4\pi\epsilon_0 R_c}. \quad (2.89)$$

where the first two terms are volume and surface energies and $a_{\text{vol}} \sim 16 \text{ MeV}$ and $a_{\text{surf}} \sim 17 - 20 \text{ MeV}$. The last term is the Coulomb repulsion energy of a

homogeneously charged sphere of radius R_c and the third term gives the symmetry energy.

This model is very useful in describing overall properties of the nucleus (like binding energy, fission in heavy mass nuclei) and in introducing many concepts of collective phenomena in nuclear physics in a simple way.

2.10.2 The Strutinsky shell correction method

Since the shell model fails to give the total binding energy of the nucleus and the liquid drop model fails to predict the existence of stable deformation in the nuclear ground state and other properties such as the fission barrier of actinide nuclei, a method that eliminates their defects and keeps their qualities is required. Strutinsky [Str67, Str68] came up with such a method. The method accurately reproduces observed experimental nuclear ground-state energies and also their dependence on deformation parameters. The basis of the method is that the total energy is split into two terms, the first is a smoothly varying energy derived from the liquid drop model, and the second is a rapidly varying part E_{osc} (this is fluctuating energy due to shell closures), which is calculated from the shell model energy, i.e.

$$E_{tot} = E_{osc} + E_{LDM} \quad (2.90)$$

In the shell model, the total nuclear energy could be obtained as the sum of the single particle energies,

$$E_{sh} = \sum_{\nu} e_{\nu} = E_{osc} + \tilde{E}_{sh} \quad (2.91)$$

where E_{osc} is the oscillating part arising from shell effects and \tilde{E}_{sh} is the smoothly varying part reflecting the nuclear bulk properties.

The shell energy, E_{osc} , is calculated independently for protons and neutrons, and can be defined as the difference between the actual discrete level density $g(e)$, and a smoothed level density $\tilde{g}(e)$. The discrete and smoothed level densities are given by:

$$g(e) = \sum_{\nu} \delta(e - e_{\nu}) \quad (2.92)$$

and:

$$\tilde{g}(e) = \frac{1}{\gamma\sqrt{\pi}} \sum_{\nu} f_{corr} \left(\frac{e - e_{\nu}}{\gamma} \right) \exp \left(- \frac{(e - e_{\nu})^2}{\gamma^2} \right) \quad (2.93)$$

Here γ is energy of the order of the shell spacing $\hbar\omega_0$, and f_{corr} is a correction function. The shell energy can thus be calculated using:

$$E_{osc} = 2 \sum e_i - 2 \int e \tilde{g}(e) de \quad (2.94)$$

where the factor 2 arises because of the double degeneracy of the deformed levels. This method has been used to good effect to predict the existence of stably deformed reflection-asymmetric nuclear ground states [Möl81, Naz65].

From equation (2.90) and (2.91) the total energy becomes

$$E_{tot} = E_{LDM} + E_{osc} \quad (2.95)$$

Including the pairing interaction, the total energy becomes

$$E_{tot} = E_{LDM} + E_{osc} + P_{BCS} - \tilde{P}_{BCS} \quad (2.96)$$

where the difference between the pairing energy P_{BCS} and its smooth part \tilde{P}_{BCS} is obtained using the same philosophy as in the Bardeen-Cooper-Schrieffer (BCS) model.

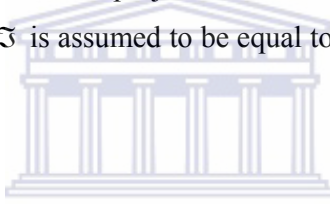
2.11 Total potential energy at $\omega \neq 0$ and $I \neq 0$

2.11.1 The rotating liquid drop model

Ignoring the quantal effects and considering the rotation of a nucleus according to the laws of classical mechanics, the LDM energy is given by:

$$E_{macr}(E, N, def, I) = E(Z, N, def) + \frac{\hbar^2 I^2}{2\mathfrak{I}(Z, N, def)} \quad (2.97)$$

The energy $E(Z, N, def)$ is taken as the static liquid-drop energy. The variable “def” denotes a number of deformation parameters. The second term gives the rotation energy of the nucleus, where I is the projection of the nuclear spin along the rotation axis. The moment of inertia \mathfrak{I} is assumed to be equal to the corresponding rigid body value.



2.11.2 Shell correction method for $I \neq 0$

When the ground state potential energy has been calculated at some fixed deformations, it should be possible to get the I – dependence simply by adding the rotational energy as extracted from CSM. Thus for a prescribed spin I_0 , the frequency ω_0 is determined so that:

$$I_0 = \sum_{i \text{ occ}} \langle j_x \rangle_i \quad (2.98)$$

Then the excitation energy is obtained as:

$$E_{exc} = \sum_{i \text{ occ}} e_i |_{\omega=\omega_0} - \sum_{i \text{ occ}} e_i |_{\omega=0} \quad (2.99)$$

The spin-dependent shell correction energy is [And76]:

$$E_{sh}(I_0) = \sum e_i \Big|_{I=I_0} - \widetilde{\sum} e_i \Big|_{\widetilde{I}=I_0} \quad (2.100)$$

where the smoothed single particle Routhians sum (indicated by “ $\widetilde{\sum}$ ”) is calculated from the Strutinsky procedure. Therefore, the total energy is calculated as the sum of the rotating liquid drop energy and the shell model energy:

$$E_{tot}(def, I) = E_{L.D}(def, I = 0) + \frac{\hbar^2}{2\mathfrak{I}_{rig}(def)} I^2 + E_{sh}(def, I) \quad (2.101)$$

where ‘def’ stand for deformation parameters and \mathfrak{I}_{rig} is the moment of inertia of a rigid body.

2.12 The total Routhian surface (TRS) calculations

In this research, we have used the TRS calculations performed by R. Wyss [Wys90]. They were performed for the nuclei with $30 \leq Z \leq 84$, and for all possible combinations of the 16 lowest nucleon Routhians. The data are stored as five different databases for nuclei in the different mass regions, see Table 2.3.

Table 2.3: *The database of the TRS calculations*

IMESH=0	$30 \leq Z \leq 44$	$32 \leq N \leq 48$
IMESH=1	$50 \leq Z \leq 62$	$60 \leq N \leq 78$
IMESH=2	$58 \leq Z \leq 70$	$72 \leq N \leq 90$
IMESH=11	$64 \leq Z \leq 74$	$84 \leq N \leq 104$
IMESH=8	$72 \leq Z \leq 84$	$92 \leq N \leq 118$

The total Routhian $E_{LD}^\omega(Z, N, \hat{\beta})$ of nucleus (Z, N) at frequency ω and deformation $\hat{\beta}$ is obtained within the cranked Woods-Saxon Bogolyubov-Strutinsky approach, as the sum of the macroscopic liquid-drop energy, the shell correction energy and the pairing energy:

$$E^\omega(Z, N, \hat{\beta}) = E_{LD}^\omega(Z, N, \hat{\beta}) + E_{shell}^\omega(Z, N, \hat{\beta}) + E_{pair}^\omega(Z, N, \hat{\beta}) \quad (2.102)$$

For the liquid-drop macroscopic term the standard liquid-drop mass formula is used [Mye67]. The nuclear mean field is parameterized by a Woods-Saxon single particle potential and a BCS pair field. The Woods-Saxon deformed shell-model potential [Naz85] is employed with the parameters of ref. [Dud81]. It contains a central potential, a spin-orbit term, and the Coulomb potential. The shape is parameterized in terms of the quadrupole β_2 and hexadecupole β_4 degree of freedom including the non-axial deformation γ , $\hat{\beta} = (\beta_2, \gamma, \beta_4)$. The surface deformation parameters $\hat{\beta}$ are treated as variational parameters. Cranking implies that the system is constrained to rotate around a fixed axis (the x -axis) with a given rotational frequency ω . Therefore the Routhian \hat{H}^ω is minimized at a fixed deformation and fixed ω by solving the cranked Hartree-Fock-Bogolyubov equations. The solution provides thus the angular momentum and the energy relative to the non-rotating state with $\omega = 0$. The primary deformation lattice is transformed into Cartesian coordinates, $X = \beta_2 \cos(\gamma + 30^\circ)$ and $Y = \beta_2 \sin(\gamma + 30^\circ)$, and has 9×11 points in the (X, Y) plane starting from $X = 0.05$ and $Y = -0.20$ with step length of about 0.05. The minimization is performed in such a way that for a fixed configuration the total Routhian is first minimized at each (β_2, γ) grid point with respect to β_4 and in a second step the equilibrium deformation is obtained by minimizing over the whole grid. The calculations for the Au nuclei have been performed for 18 different rotational frequencies, starting from $\hbar\omega = 0.00$ MeV with a step length of 0.04 MeV.

At each grid point, the pairing gap Δ_0 was determined self-consistently for $\omega = 0$ according to the BCS method [Bar57]. In the cranking calculations the self-consistently determined pairing gap was allowed to decrease with ω in accordance with the following function:

$$\Delta(\omega) = \begin{cases} \Delta_0 (1 - (\omega/\omega_c)^2) & \text{if } \omega \leq \omega_c \\ \Delta_0 \frac{1}{2} (\omega/\omega_c) & \text{if } \omega > \omega_c \end{cases} \quad (2.103)$$

where ω_c is defined as the critical frequency at which the pairing gap is reduced to half its original value Δ_0 . The chemical potentials λ_n and λ_p were adjusted separately at each frequency in order to give the correct expectation value of the number of nucleons.

Examples of TRS plot for the $^{186-196}\text{Au}$ nuclei will be discussed in Chapter 3.

2.13 Signature inversion phenomenon

Signature inversion is the phenomenon in which the unfavoured signature α_u of a certain band un-actually lies lower in energy than the corresponding favoured α_f component. This phenomenon is mostly exhibited by the doubly odd nuclei of mass $A \sim 150$ light rare earth region. Signature inversion has also been studied at length in the mass $A \sim 120$ region. The rotational frequency at which the two bands restore their position is called signature inversion frequency. Recent theories relate this phenomenon to triaxiality, strong neutron-proton interaction and quadrupole pairing of the nucleus. The energy difference $\Delta e(\omega)$ between the two signature partners of a rotational band is called signature splitting and can be calculated by:

$$\Delta e(\omega) = e_{\alpha_u}(\omega) - e_{\alpha_f}(\omega). \quad (2.104)$$

The energy splitting between the two signature partners can be a sensitive indicator of the properties of the nuclei.

For a high- j one-quasiparticle configuration, the favoured signature is given by [Ste75]:

$$\alpha_f = \frac{1}{2}(-1)^{j-\frac{1}{2}}. \quad (2.105)$$

CHAPTER 3 Results from the TRS and CSM calculations for the bands in the $^{186-194}\text{Au}$ nuclei

3.1 Previous calculations performed for the rotational bands in the $^{186-194}\text{Au}$ nuclei and suggested interpretation

In a moderately deformed axially symmetric nucleus, bands built on high-j low-K configurations should be decoupled (i.e. should consist of one sequence of E2 transitions). In the Au nuclei, bands consisting of more than one sequence of E2 transitions are observed (see the level schemes of the $^{186-194}\text{Au}$ nuclei isotopes in Appendix A.1-10). Several theoretical models had been applied attempting to explain this unusual behavior of these bands in the Au nuclei. These models were able to explain some of the features of these bands.

The theoretical models that were applied in order to explain this unusual behavior of the bands in $^{186-194}\text{Au}$ nuclei were the particle-rotor model [Tok79], cranked shell model (CSM) [Jan92] and the TRS together with CSM [Gue02, Gue03]. But none of these calculations were systematically applied for all high-j bands in all $^{186-194}\text{Au}$ nuclei.

3.1.1 The particle-plus-rotor model

The particle-plus-rotor model is only limited to one- or two- quasiparticle configurations, hence can only be applied for the low lying states of the odd-even or odd-odd Au nuclei (i.e. one and two quasiparticle bands). In odd-odd nuclei, the two particles (proton and neutron) are assumed to be moving in a triaxially deformed field. In the $^{190,192,194}\text{Au}$ nuclei, this model was able to explain the energy spectra of the 11^- and 12^- bands ($\pi h_{11/2}^{-1} \otimes \nu i_{13/2}^{-1}$) and it was in good agreement with the measured value of the magnetic moment of the 12^- level in the $^{198,200}\text{Au}$ nuclei [Tok79]. The $\pi h_{11/2}^{-1} \otimes \nu i_{13/2}^{-1}$ spectrum in odd-odd $^{190-194}\text{Au}$ nuclei corresponds to a physical situation called “peaceful case” [Tok79], where a decoupled $h_{11/2}$ proton hole and a decoupled

$i_{13/2}$ neutron hole are present. The intrinsic total angular momentum J of these two holes is practically a good quantum number, and states 12, 14, 16, ... and 11, 13, 15, ... constitute rotation like bands with $J = 12$ and $J = 11$ states [Tok77]. The model predicts that there is signature inversion in the quasiparticle Routhian of the 11^- and 12^- bands of Au, as a result of the assumed $\gamma = 40^\circ$ non-axiality parameter of the Hg core. Such values of γ were calculated for even-even Hg nuclei using the energies of the 2_2^+ states from the observed γ bands. Other bands in the Au nuclei could not be interpreted with this model, because they are built on three- or more- quasiparticle configurations.

3.1.2 Cranked shell model

Calculations were performed for the $\pi h_{11/2}^{-1} \otimes \nu i_{13/2}^{-1}$ bands in the $^{186,188}\text{Au}$ nuclei [Jan92] only. Non-axially symmetric shape with $\gamma = -70^\circ$ was assumed in order to explain the two E2 sequences of these bands. It was found that for $\gamma < -60^\circ$ the Routhians A and B move towards each other, and thus the unfavored E2 sequence of the $\pi h_{11/2}^{-1} \otimes \nu i_{13/2}^{-1}$ band, eB, could compete with the favored one, eA. Thus possible signature inversion could be qualitatively explained through the frame of this model, but the magnitude of the signature inversion frequency and signature splitting could not be predicted accurately.

It is worth noting that CSM was also performed for a number of Hg isotopes [Hüb86] assuming an axially symmetric nuclear shape. The calculated Routhians, band crossing frequencies, alignments and alignment gains were in good agreement with the experimentally measured ones for bands of $^{190-194}\text{Hg}$.

3.1.3 Total Routhian surface (TRS) together with cranked shell model (CSM)

In this case the deformation of the nucleus was predicted by the TRS calculations and the CSM calculations were performed using the values of the nuclear deformation parameters predicted by the TRS. These calculations were performed for all bands in $^{190,191}\text{Au}$ nuclei only. The $^{190,191}\text{Au}$ nuclei are expected to have near oblate shape

with moderate deformation of $\beta_2 \sim 0.13$ [Tok79]. The orbitals closest to the Fermi surface for this deformation are the low- K orbitals from the $\nu i_{13/2}$ and $\nu h_{9/2}$ (and/or $\nu f_{7/2}$) shells and low- j orbitals from the $\nu p_{3/2}$ and $\nu f_{5/2}$ shells, as well as low- K $\pi h_{11/2}$ orbitals [Gue02]. TRS calculations for several configurations in these nuclei showed that the e ($\pi h_{11/2}$) proton and the F ($\nu h_{9/2}$) neutron configuration in ^{191}Au nuclei drive the nucleus to large negative values of γ -deformations of $\gamma = -80^\circ$. CSM calculations performed with Woods-Saxon potential for such γ -deformation shows that the positive parity A, B, C Routhians (originating from low- K $\nu i_{13/2}$ orbitals) are strongly affected and become close in energy (see Figure 3.1). Thus if one $\nu i_{13/2}$ quasiparticle is excited, it can occupy any of these three Routhians, which would result in a set of three rotation-aligned bands (i.e. eA, eB, eC bands) all of them assigned to the $\pi h_{11/2}^{-1} \otimes \nu i_{13/2}^{-1}$ configuration. If two $\nu i_{13/2}$ quasiparticles are excited, they can occupy all possible combinations of the AB, AC and BC Routhians, resulting into three sets of rotation-aligned bands (i.e. eAB, eAC, eBC bands) assigned to the $\pi h_{11/2}^{-1} \otimes \nu i_{13/2}^{-2}$ configuration. If three $\nu i_{13/2}$ quasiparticles are excited they will occupy all three Routhians resulting into one rotation-aligned band (i.e. eABC band) assigned to $\pi h_{11/2}^{-1} \otimes \nu i_{13/2}^{-3}$ configuration.

It was noted that for $\gamma \leq -80^\circ$ the negative parity F Routhian is pushed down in energy and competes with the positive parity A, B and C Routhians (see Figure 3.1). Therefore, if one $\nu h_{9/2}$ and one $\nu i_{13/2}$ quasiparticle are excited, the $\nu i_{13/2}$ may occupy either one of the A, B, and C Routhians resulting into three sets of rotation-aligned bands, eFA, eFC, eFB bands, all of them assigned to $\pi h_{11/2}^{-1} \otimes \nu i_{13/2}^{-1} h_{9/2}^{-1}$ configuration. If one $\nu h_{9/2}$ and two $\nu i_{13/2}$ quasiparticles are excited, they can occupy all possible three combinations of FAB, FAC and FBC Routhians, resulting into three sets of rotation-aligned bands, eFAB, eFAC and eFBC bands, all of them assigned to $\pi h_{11/2}^{-1} \otimes \nu i_{13/2}^{-2} h_{9/2}^{-1}$ configuration.

It is interesting to find that, when these models were applied together for $^{190,191}\text{Au}$, a very good agreement was obtained between the theoretical predictions and the experimentally measured features of all bands in $^{190,191}\text{Au}$ [Gue02, Gue03].

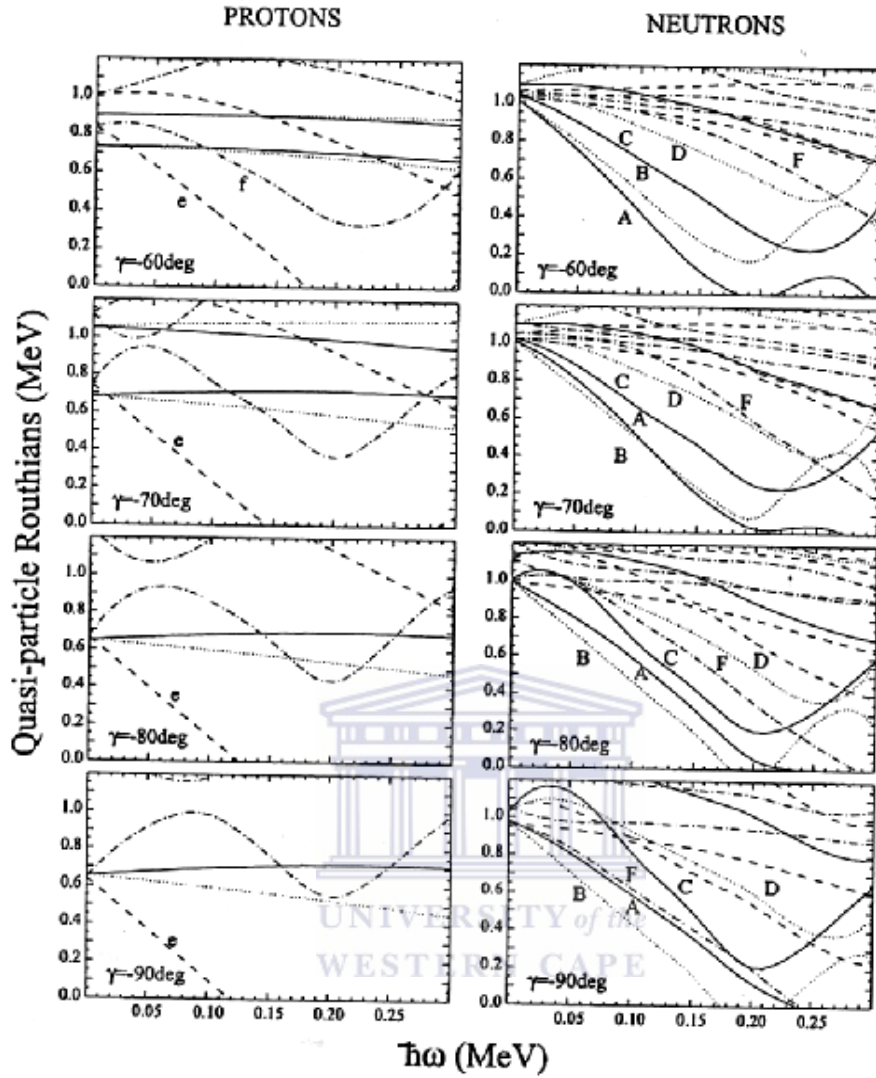


Figure 3.1: Cranked shell model calculations for ^{191}Au performed for protons and neutrons. A Woods-Saxon potential with universal parameters is used. The deformation of $\beta_2 = 0.14$ and $\beta_4 = -0.02$, appropriate for ^{191}Au , is chosen. The panels from top to bottom correspond to $\gamma = -60^\circ$, -70° , -80° , and -90° . The Routhians with $(\pi, \alpha) = (+, +1/2)$ are represented with solid line, $(+, -1/2)$ with a dotted line, $(-, +1/2)$ with dash-dotted line, and $(-, -1/2)$ with dashed line [Gue02].

A question remained open as to whether the TRS and CSM models will show good predictions of the features of the rotational bands in the other odd-odd $^{186,188,192,194}\text{Au}$ and odd-even $^{187,189,193}\text{Au}$ nuclei. In this work we address this question by performing the TRS and CSM calculation for all high- j bands in all $^{186-194}\text{Au}$ nuclei.

In particular the signature inversion phenomenon is very difficult to reproduce accurately, thus it is very interesting how well the TRS and CSM models would be able to predict it.

3.2 Experimental quantities in rotating frame

In order to compare theoretical predictions with experimental observations, experimental quantities need to be transformed into rotating frame [Ben79]. As a core reference, the Harris expansions

$$I_{xref} = J_0 \omega + J_1 \omega^3 \quad (3.1)$$

$$E'_{ref} = -\frac{1}{2} J_0 \omega^2 - \frac{1}{4} J_1 \omega^4 + \frac{1}{8 J_0} \quad (3.2)$$

with $J_0 = 6 \hbar^2 (\text{MeV})^{-1}$ and $J_1 = 30 \hbar^4 (\text{MeV})^{-3}$ were used in the calculations for the $^{186-194}\text{Au}$ nuclei. More detailed information of the other equations used to perform this transformation can be found in reference [Ben86] and also in section 2.9.3 in this thesis. Complete results of these calculations are given in Appendix B.

3.2.1 Calculations for the odd-odd $^{186-194}\text{Au}$ nuclei

The rotational bands that develop above the 11^- and 12^- states are called the 11^- and 12^- bands respectively. The 11^- and 12^- bands in the odd-odd $^{186-194}\text{Au}$ nuclei were assigned to a rotation-aligned $\pi h_{1/2}^{-1} \otimes \nu i_{13/2}^{-1}$ [Nes82, Tok79] configuration. The plots of the experimental Routhians and aligned angular momenta for these bands are shown in Figures 4.4, 4.6, 4.7, 4.9, 4.10, 4.12, 4.13, 4.15, 4.16, and 4.18 in Chapter 4. For the ^{194}Au nuclei signature inversion frequency was determined by linear

extrapolation of the quasiparticle Routhians of the 11^- and 12^- bands to lower rotational frequencies. The values of the signature inversion frequencies, alignments and signature splittings for the 11^- and 12^- bands of the odd-odd $^{186-194}\text{Au}$ nuclei are summarized in Table 4.1 and 4.9 in Chapter 4.

Bands that develop above the 22^- state are called the 22^- bands. The 22^- band has only been identified in ^{190}Au . In the rest of the $^{186,188,192,194}\text{Au}$ nuclei it was not observed probably because no studies were performed at high spin. The $\pi h_{11/2}^{-1} \otimes \nu i_{13/2}^{-3}$ configuration was assigned to the 22^- band [Gue02, Gue03]. The plots of the experimental quasiparticle Routhians and alignment are shown in Figures 4.10 and 4.12 in Chapter 4.

In $^{190,192}\text{Au}$ the 20^+ isomers were assigned to the $\pi h_{11/2}^{-1} \otimes \nu i_{13/2}^{-2} h_{9/2}^{-1}$ configuration by considering the orbitals closest to the Fermi surface and the systematics of configuration assignments in this mass region [Gue01]. The 20^+ , 21^+ and 22^+ bands in ^{190}Au were associated with three sets of rotation-aligned bands [Gue03]. In the $^{186,192}\text{Au}$ isotopes only one, the 20^+ band was observed probably because of limited data of high-spin states [Gue01, Jan92], while in ^{188}Au two bands, the 20^+ and 21^+ bands were observed [Jan92]. In the study of $^{190,192}\text{Au}$ [Gue01], data with considerable statistics at high spins were obtained. The analysis showed that low-energy transitions were missed out in the previous studies of these two nuclei, and assigned spin of 20^+ to the levels at excitation energies of 2172 keV and 2153 keV in ^{190}Au and ^{192}Au respectively. These levels were found to be isomeric and assigned as bandheads of the $\pi h_{11/2}^{-1} \otimes \nu i_{13/2}^{-2} h_{9/2}^{-1}$ bands. We compared the γ -ray energies around the 20^+ levels of all odd-odd $^{186-192}\text{Au}$ nuclei in order to separate the bands related to the $\pi h_{11/2}^{-1} \otimes \nu i_{13/2}^{-2} h_{9/2}^{-1}$ configuration from the states based on the $\pi h_{11/2}^{-1} \otimes \nu i_{13/2}^{-1} \nu j$ ($j = p_{3/2}, p_{5/2}, f_{5/2}$) configuration and found that most likely low energy transitions were also missed in $^{186,188}\text{Au}$. We thus associated the levels at 2604 keV and 2257 keV in $^{186,188}\text{Au}$ respectively as the bandhead of the 20^+ band and assigned likely spin and parity of 20^+ to them. The spins of the levels above these states were increased with $2\hbar$ accordingly.

3.2.2 Calculations for the odd-even ¹⁸⁷⁻¹⁹³Au nuclei

The rotational bands that develop above the $11/2^-$ state are called the $11/2^-$ band. This band has been observed in each odd-even ¹⁸⁷⁻¹⁹³Au nucleus (see the level schemes of Au in Appendix A). This band is thought to result from the decoupled proton-hole state $\pi h_{11/2}^{-1}$ coupled to a slightly deformed even-even Hg core [Köl85]. Thus this band is assigned to the $\pi h_{11/2}^{-1}$ configuration. Alignments and band crossing frequencies observed in this band are discussed in Chapter 4 and summarized in Table 4.5. Note that the band crossing frequencies between the Routhians of the $11/2^-$ and $35/2^-$ bands have been determined through linear extrapolation of the Routhians of the $35/2^-$ bands towards lower rotational frequencies.

The $31/2^-$ isomeric levels in the odd-even ¹⁸⁷⁻¹⁹³Au nuclei are assigned to the $\pi h_{11/2}^{-1} \otimes \nu i_{13/2}^{-2}$ configuration [Bou89, Bou92, Joh89, Köl85, Ven92]. The $\pi h_{11/2}^{-1} \otimes \nu i_{13/2}^{-2}$ assignment agrees with the systematically suggested $\nu i_{13/2}$ nature of the first band crossing in the neighboring ¹⁹⁰⁻¹⁹⁴Hg [Hüb86], and ^{190,192}Pt [Cun76, Hjo76] isotopes. Alignments observed for the $31/2^-$, $33/2^-$ and $35/2^-$ bands of the odd-even ¹⁸⁷⁻¹⁹³Au isotopes are summarized in Table 4.7 of Chapter 4.

The rotational bands that develop above the $31/2^+$ and $33/2^+$ states are called the $31/2^+$ and $33/2^+$ bands respectively. In the odd-even Au isotopes, the $31/2^+$ and $33/2^+$ bands are assigned to the $\pi h_{11/2}^{-1} \otimes \nu i_{13/2}^{-1} h_{9/2}^{-1}$ configuration [Bou89, Bou92, Joh89, Köl85, Per79, Ven92]. The level schemes of ¹⁸⁷Au obtained from the works of [Bou89] and [Joh89] are not consistent for the $31/2^+$ and $33/2^+$ bands. We compared the γ -ray energies of these bands to those in the ^{189,191}Au nuclei where better statistics were obtained and calculated the experimental quantities, under the following assumptions.

- 1) The spin and parity of the 2563 keV isomer was assumed to be $31/2^+$ as in the heavier isotopes probably due to unobserved transitions. Note that similar assumption was made for ¹⁸⁹Au [Ven92].
- 2) The order of the transitions in the $31/2^+$ band was accepted to be 492-754-766-211-587 keV, because this matches the order of the transitions in the heavier ^{189,191}Au isotopes.

Small differences occur also in the $31/2^+$ and $33/2^+$ bands in ^{189}Au as suggested in the works of [Ven92] and [Bou92]. We accepted the level scheme published in [Ven92] because it is more complete. Furthermore the suggested unobserved transition [Ven92] below the isomeric level was later detected [Per97] and the spin and parity of the bandhead was confirmed as $31/2^+$.

The alignments of the $31/2^+$ and $33/2^+$ bands of $^{187,189,191,193}\text{Au}$ observed experimentally are listed in Table 4.8 of Chapter 4.

3.3 Theoretical Calculations

3.3.1 TRS Calculations

To extract data from the TRS data basis, the software program called GAMLATZN [Wys99] was used. This program reads the files corresponding to Z and N of the nucleus, given in the input file. Since the data are stored in different data bases according to nuclear mass, one has to specify the value of the parameter IMESH, which corresponds to the data base needed. The program also needs information about the configuration of the band. This is done by supplying this information in a few lines in the input file. The first line specifies the number of excited neutron quasiparticles. If the nucleus of interest contains odd number of neutrons, the number of excited neutron quasiparticles can be 1, 3, 5, etc. The next few lines specify the neutron configuration, one line for each quasiparticle excitation. Each excitation is specified by a number I , shown in Table 3.1. If the nucleus of interest contains even number of neutrons, therefore the number of excited particles could be 0, 2, 4, etc. The proton configuration is specified in the same manner. If one wants to extract information about the proton or neutron vacuum configuration (i.e. zero excited quasiparticles), no configuration needs to be specified. The particle states above the Fermi surface are labelled with latin letters as shown in Table 3.1.

The TRS plots provide us with the nuclear deformation parameters β_2 , γ , β_4 and proton and neutron pairing gap parameters Δ_p , Δ_n at a particular rotational frequency.

The most confusing thing about the TRS calculations is that if one specifies a particular quasiparticle configuration the program (GAMLATZN) does not extract information corresponding to this quasiparticle configuration only, but also shows information corresponding to excited quasiparticle configurations with the same parity

and signature. Therefore, one needs to be very careful when dealing with the TRS calculations, so that the correct information corresponding to the band configuration of interest is selected. For example, if one specifies a neutron vacuum configuration, with positive parity $\pi = +$ and zero signatures $\alpha = 0$, the TRS calculations will also extract information corresponding to the lowest energy two-, four-, etc quasiparticle configurations. To know that the information corresponds to either vacuum or a two-quasiparticles configuration, one needs to check if the quasiparticle alignment predicted by TRS corresponds approximately to the expected alignment for this quasiparticle configuration. For example consider Figure 3.2 showing the TRS plots

Table 3.1: *Convention for labeling the orbitals described by different parity and signature quantum numbers. Upper and lower case describe the neutron and proton configuration respectively. Labels E, G, etc refer to the lowest, second-lowest, etc Routhians with negative parity and negative signature. Labels F, H, etc refer to the lowest, second-lowest, etc Routhians with negative parity and positive signature. Labels B, D, etc refer to the lowest, second-lowest, etc Routhians with positive parity and negative signature. Labels A, C, etc refer to the lowest, second-lowest, etc Routhians with positive parity and positive signature.*

Parity (π)	Signature (α)	Number of Configuration	I	Label
-	-1/2	4	1-4	E, G, M, O
-	+1/2	4	5-8	F, H, N, P
+	-1/2	4	9-12	B, D, J, L
+	+1/2	4	13-16	A, C, I, K

calculated for the e configuration of ^{191}Au . In the left plot of Figure 3.2, the alignment of the proton and neutron predicted by TRS calculations at 0.167 MeV/h are $\sim 5.5 \hbar$ and ~ 0 respectively, which is consistent with the expected alignment of the yrast $11/2^-$ band assigned to the rotationally aligned $\pi h_{11/2}^{-1}$ configuration. In the right plot of Figure 3.2, calculated for the same configuration but at 0.207 MeV/h the alignment of the proton and neutrons predicted by TRS are $5.9 \hbar$ and $12.9 \hbar$ respectively. The increase in the aligned neutron angular momentum reflects a $\nu i_{13/2}$ alignment which is typical for the nuclei in this mass region. Indeed the pair of $\nu i_{13/2}$ neutrons can supply this large gain in the alignment (i.e. $\sim 12 \hbar$). Thus the right

plot on Figure 3.2 corresponds to the $\pi h_{11/2}^{-1} \otimes \nu i_{13/2}^{-2}$ band although it is calculated for the e configuration.

We shall briefly explain why the TRS calculations give also information corresponding to other excited quasiparticle configurations with the same parity and signature although a lower energy configuration has been specified.

The TRS calculates the total Routhians and the values of the nuclear deformation parameters only at the prescribed points of rotational frequencies, and values between these points must be interpolated. There are some rotational frequencies at which band crossings take place. At these rotational frequencies two Routhians cross each other. Assume TRS is calculating the total Routhians for the lowest configuration. But after the lowest Routhian is crossed by another one, the TRS model will continue calculating the total Routhians for the lowest configuration, not being aware that the configuration has actually changed when the Routhians crossed each other.

Generally for an odd neutron nucleus the lowest Routhian could either be A(+, +1/2), B(+, -1/2), E(-, -1/2) or F(-, +1/2) depending on the orbital that the odd neutron has occupied. Hence when the TRS model calculates the total Routhians for the lowest one quasiparticle configuration, the results may correspond to one-, three-, five-, etc neutron quasiparticle bands, depending on the band crossings that have occurred.

For an even-even nucleus the lowest configuration is the vacuum configuration with positive parity and zero signature. Hence when the TRS model calculates the total Routhians for the vacuum configuration, the results may correspond to the vacuum or two-, four-, etc quasiparticle configurations, depending on the band crossings that have occurred.

In the TRS plots, the black dot surrounded by regular contour lines represents the minimum potential energy of the nucleus at an equilibrium nuclear shape (i.e. the shape that the nucleus possesses in order to have lowest energy). The TRS plots contain a sequence of circular lines and straight lines. The radii of the circular lines give the values of nuclear deformation parameter β_2 . By using one of the expressions $X = \beta_2 \cos(\gamma + 30^\circ)$ and $Y = \beta_2 \sin(\gamma + 30^\circ)$, which define the values of X and Y along the x- and y-axis respectively, one can give an appropriate value of γ .

The same value of γ corresponds to each straight line passing through the origin. For example, for each point lying on the x-axis, the value of y must be zero, and this is

possible only if $\gamma = -30^\circ$, while for each point lying on the y-axis, the value of x must be zero, and this is possible only if $\gamma = 60^\circ$ or -120° .

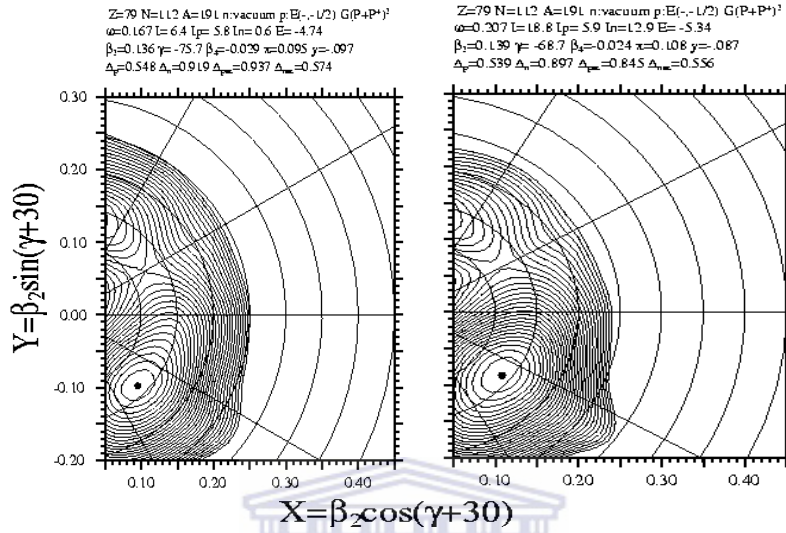


Figure 3.2: TRS plots showing the nuclear shapes for the e proton and vacuum neutron configuration of ^{191}Au as the rotational frequency increases. The left plot corresponds to the $11/2^-$ band, and the right plot corresponds to the same band, but above the $\nu_{i_{13/2}}$ band crossing. The rotational frequency is measured in MeV/\hbar and the proton (I_p), neutron (I_n) and total (I) aligned angular momenta are given in \hbar .

3.3.2 TRS calculations for the odd-odd $^{186-194}\text{Au}$ nuclei

These calculations were performed for the $\pi h_{11/2}^{-1} \otimes \nu i_{13/2}^{-1}$ (11^- and 12^- bands), $\pi h_{11/2}^{-1} \otimes \nu i_{13/2}^{-2} h_{9/2}^{-1}$ (20^+ , 21^+ and 22^+ bands) and $\pi h_{11/2}^{-1} \otimes \nu i_{13/2}^{-3}$ (22^- band) bands in the odd-odd $^{186-194}\text{Au}$ nuclei. In terms of CSM labels these bands were assigned to eB and eA; eFAB, eFAC and eFBC; and eABC configurations respectively. Tables 3.2 and 3.3 show the relationship between the CSM labels, shell model and Nilsson model quantum numbers.

Table 3.2: Convention for labeling the neutron orbitals by the parity and signature quantum numbers, shell model and Nilsson labels.

odd neutron orbital		
CSM labels (π, α)	shell model label	Nilsson label
A (+, +1/2)	$\nu i_{13/2}$	$1/2^+[660]$
B (+, -1/2)	$\nu i_{13/2}$	$1/2^+[660]$
C (+, +1/2)	$\nu i_{13/2}$	$3/2^+[651]$
D (+, -1/2)	$\nu i_{13/2}$	$3/2^+[651]$
E (-, -1/2)	$\nu h_{9/2}$	$1/2^-[530]$
F (-, +1/2)	$\nu h_{9/2}$	$1/2^-[530]$

Table 3.3: Convention for labeling the proton orbitals by the parity and signature quantum numbers, shell model and Nilsson labels.

odd proton orbital		
CSM labels (π, α)	shell model label	Nilsson label
e (-, -1/2)	$\pi h_{11/2}$	$1/2^-[550]$
F (-, +1/2)	$\pi h_{11/2}$	$1/2^-[550]$

3.3.2.1 The 11^- and 12^- bands of the odd-odd $^{186-194}\text{Au}$ isotopes

The TRS calculations were performed for the e proton and B neutron configuration for the 11^- band, and for the same proton but A neutron configuration for the 12^- band and the TRS minima of interest were selected. These are the ones for which the

alignment of the proton is $I_p \approx 5.5 \hbar$ and that of the neutron is $I_n \approx 5.5 \hbar$ for the eB configuration and $I_n \approx 6.5 \hbar$ for the eA configuration. The nuclear deformation parameters were then extracted from these selected minima. Only TRS plots corresponding to $^{186,190}\text{Au}$ nuclei are shown, since the TRS plots for the other odd-odd Au nuclei are similar. TRS plots for the eB and eA configurations in $^{186,190}\text{Au}$ are shown in Figures 3.3-3.6.

For instance the minimum in the left panel of Figure 3.5 calculated at rotational frequency of 0.089 MeV corresponds to a triaxial shape of the nucleus associated with deformation parameters $(\beta_2, \gamma) = (0.137, -78.6^\circ)$. For some configurations and for some rotational frequencies more than one minimum can be observed. Each minimum will correspond to different nuclear deformation parameters, and often to occupation of different Nilsson orbitals. For example, the TRS plot in the left panel of Figure 3.3 calculated for the eB configuration of ^{186}Au at a rotational frequency of 0.129 MeV shows two minima. One minimum corresponds to a triaxial shape of the nucleus with $(\beta_2, \gamma) = (0.141, -75.8^\circ)$ and the other minimum corresponds to prolate axially symmetric shape with $(\beta_2, \gamma) = (0.220, 0^\circ)$. Although these two minima appear at the same rotational frequency and for the same eB configuration they correspond to different Nilsson orbitals, i.e. $\pi h_{11/2}^{-1} \otimes \nu i_{13/2}^{-1}$ for oblate and $\pi h_{9/2}^{-1} \otimes \nu i_{13/2}^{-1}$ for prolate shape as was shown in [Jan92]. For the lighter mass $^{186,188}\text{Au}$ isotopes, the TRS plots for the eB and eA configurations show a great competition between prolate and near oblate nuclear shapes, whereas in heavier mass $^{190,192,194}\text{Au}$ nuclei only one shape is predicted (for instance see the TRS plots for the eB and eA configurations of the odd-odd $^{186,190}\text{Au}$ isotopes in Figure 3.3-3.6).

TRS plots show triaxial nuclear shapes for the eB and eA configurations of each odd-odd $^{186-194}\text{Au}$ nuclei with $-79^\circ \leq \gamma \leq -76^\circ$ and $\gamma \sim -71^\circ$ respectively. This model predicts that after the first band crossing, which occurs at rotational frequency of $0.206 \text{ MeV}/\hbar < \omega < 0.248 \text{ MeV}/\hbar$, and has gain in the alignment which lies in the region of $7.8-11 \hbar$, the triaxiality decreases (e.g. see Figures 3.3 and 3.5). This first band crossing is due to an alignment of a pair of $i_{13/2}$ neutrons. Similar $\nu i_{13/2}$ band crossing occurs for the eA configuration of each odd-odd $^{186-194}\text{Au}$ nuclei, but in this case the gain in the alignment is about $12 \hbar$, and this crossing is predicted at a rotational frequency of $0.168 \text{ MeV}/\hbar < \omega < 0.248 \text{ MeV}/\hbar$ (e.g. see TRS plots for the

eA configurations of the odd-odd $^{186,190}\text{Au}$ isotopes in Figure 3.4 and 3.6). The values of the nuclear deformation parameters are recorded in Table 3.4.

Table 3.4: The values of the nuclear deformation parameters β_2 , γ , β_4 corresponding to the 11^- and 12^- band of the odd-odd $^{186-194}\text{Au}$ nuclei.

Odd-odd Au nuclei	I^π	Band configuration		$\hbar\omega$ (MeV)	Nuclear deformation parameters		
		Assignment	TRS configuration		β_2	γ (degree)	β_4
^{186}Au	12^-	eA	eA	0.208	0.146	-71.4	-0.019
	11^-	eB	eB	0.129	0.141	-75.8	-0.021
^{188}Au	12^-	eA	eA	0.168	0.141	-71.2	-0.023
	11^-	eB	eB	0.089	0.139	-77.5	-0.024
^{190}Au	12^-	eA	eA	0.128	0.137	-70.8	-0.026
	11^-	eB	eB	0.128	0.137	-78.5	-0.027
^{192}Au	12^-	eA	eA	0.088	0.134	-70.7	-0.028
	11^-	eB	eB	0.088	0.135	-79.2	-0.029
^{194}Au	12^-	eA	eA	0.088	0.130	-72.4	-0.029
	11^-	eB	eB	0.088	0.132	-77.6	-0.031

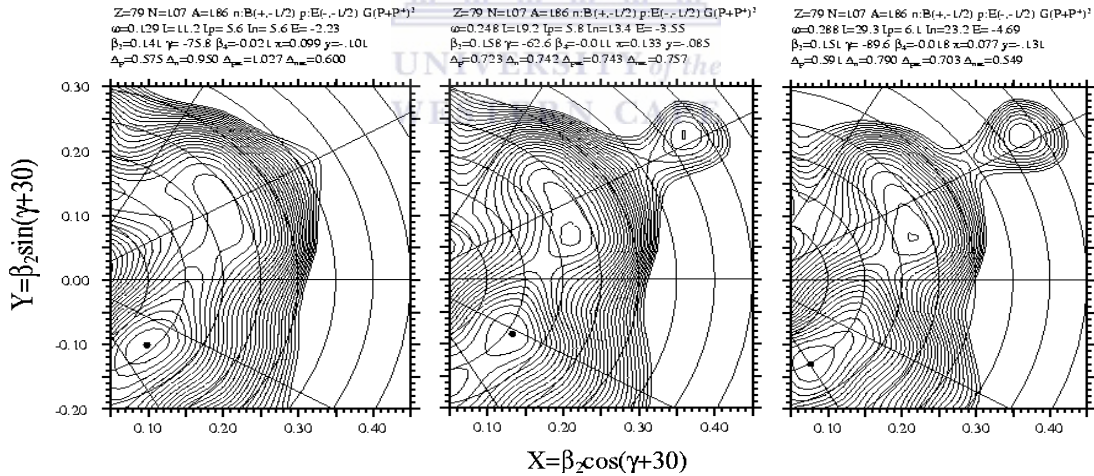


Figure 3.3: TRS plots showing the nuclear shapes for the eB configuration of ^{186}Au as the rotational frequency increases. The left plot corresponds to the 11^- band, the middle plot shows the potential energy surface above the first $\nu_{13/2}$ band crossing and the right plot is related to the nuclear shape above the second band crossing. The rotational frequency is measured in MeV/\hbar , and the proton (I_p), neutron (I_n) and total (I) aligned angular momenta are given in \hbar .

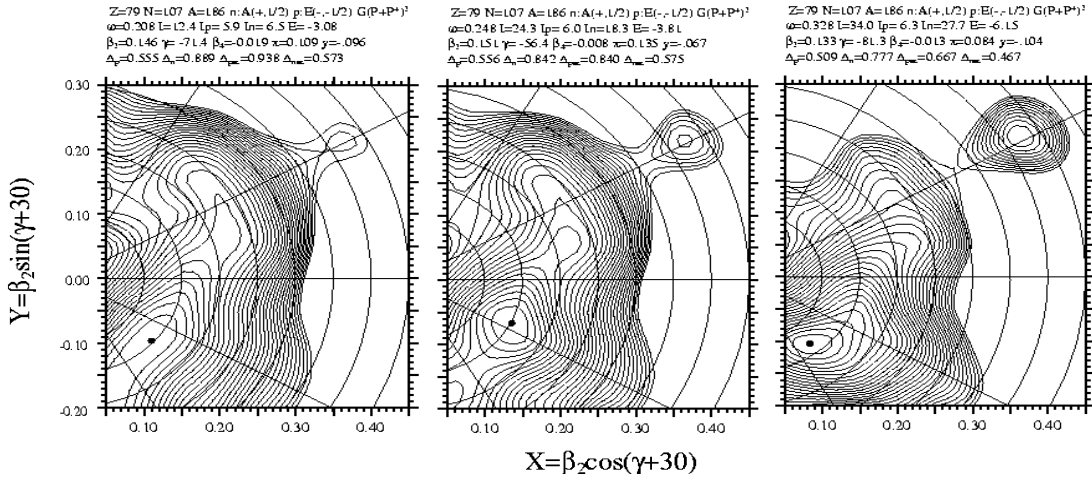


Figure 3.4: TRS plots showing the nuclear shapes for the eA configuration of ^{186}Au as the rotational frequency increases. The left plot corresponds to the 12^- band, the middle plot shows the potential energy surface above the first $\nu_{i_{13/2}}$ (22^- band) band crossing and the right plot is related to the nuclear shape above the second band crossing. The rotational frequency is measured in MeV/\hbar and the proton (I_p), neutron (I_n) and total (I) aligned angular momenta are given in \hbar .

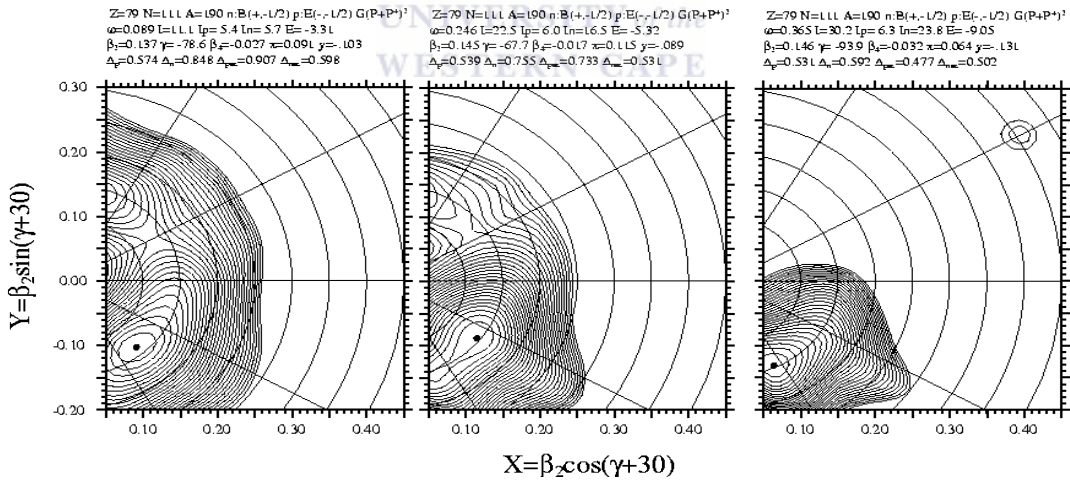


Figure 3.5: TRS plots showing the nuclear shapes for the eB configuration of ^{190}Au as the rotational frequency increases. The left plot corresponds to the 11^- band, the middle plot shows the potential energy surface above the first $\nu_{i_{13/2}}$ band crossing and the right plot is related to the nuclear shape above the second band crossing. The rotational frequency is measured in MeV/\hbar , and the proton (I_p), neutron (I_n) and total (I) aligned angular momenta are given in \hbar .

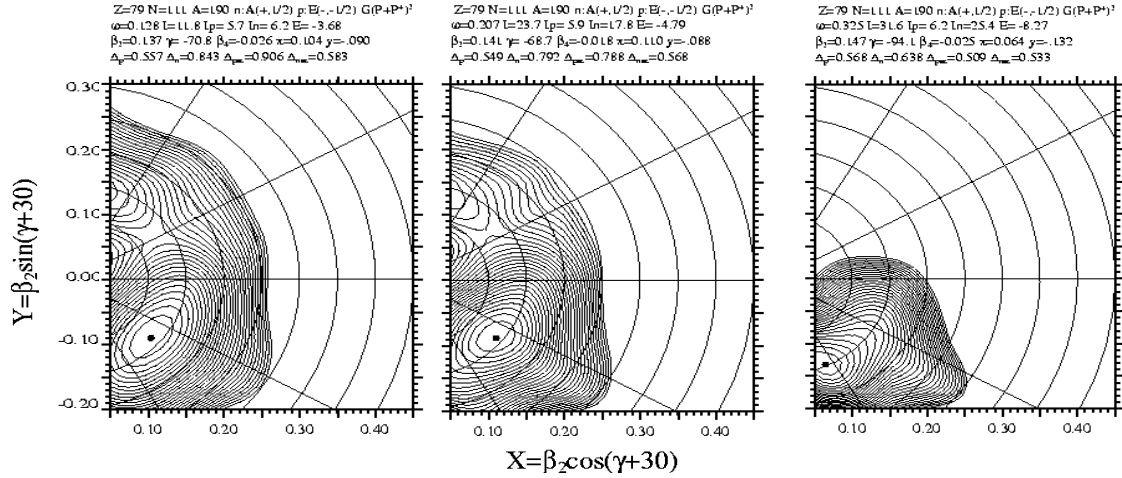


Figure 3.6: TRS plots showing the nuclear shapes for the eA configuration of ^{190}Au as the rotational frequency increases. The left plot corresponds to the 12^- band, the middle plot shows the potential energy surface above the first $\nu_{i_{13/2}}$ band crossing (22^- band) and the right plot is related to the nuclear shape above the second $\nu_{i_{13/2}}$ band crossing. The rotational frequency is measured in MeV/\hbar and the proton (I_p), neutron (I_n) and total (I) aligned angular momenta are given in \hbar .

UNIVERSITY of the
WESTERN CAPE

3.3.2.2 The 22^- band of the odd-odd $^{186-194}\text{Au}$ isotopes

The values of the nuclear deformation parameters for the 22^- band were extracted from the TRS minima for the e proton and A neutron configuration with $I_p \approx 5.5 \hbar$ and $I_n \approx 16.5 \hbar$ at rotational frequency between the first and second band crossings. In this case A is the lowest neutron configuration with $\pi = +$ and $\alpha = +1/2$. The values of β_2 , γ , β_4 for the 22^- band in the odd-odd $^{186-194}\text{Au}$ nuclei are shown in Table 3.5. In the lighter mass odd-odd Au nuclei, TRS model predicts a competition between prolate and oblate nuclear shapes (see Figure 3.4), whereas in heavier odd-odd Au nuclei no prolate shapes are predicted (see Figure 3.6). In the Figures 3.4 and 3.6, TRS shows that the shape of the nucleus becomes very triaxial ($\gamma \sim -90^\circ$) after the second band crossing. This second band crossing takes place in the rotational frequency region of $0.246 \text{ MeV}/\hbar < \omega < 0.328 \text{ MeV}/\hbar$ with a gain in the alignment of $\sim 8-10 \hbar$.

Table 3.5: The values of the nuclear deformation parameters β_2 , γ , β_4 corresponding to the 22^- bands of the odd-odd $^{186-194}\text{Au}$ nuclei.

Odd-odd Au nuclei	I^π	Band configuration		$\hbar\omega$ (MeV)	Nuclear deformation parameters		
		Assignment	TRS configuration		β_2	γ (degree)	β_4
^{186}Au	22^-	eABC	eA	0.248	0.151	-56.4	-0.008
^{188}Au	22^-	eABC	eA	0.247	0.158	-61.6	-0.011
^{190}Au	22^-	eABC	eA	0.207	0.141	-68.7	-0.018
^{192}Au	22^-	eABC	eA	0.206	0.136	-73.5	-0.022
^{194}Au	22^-	eABC	eA	0.206	0.134	-75.4	-0.027

3.3.2.3 The 20^+ , 21^+ and 22^+ bands of the odd-odd $^{186-194}\text{Au}$ isotopes

The TRS calculations for the 20^+ band were performed for the e proton and F neutron configurations, while for the 22^+ band the e proton and FAB neutron configurations were used. For the 21^+ band, the calculations were performed for the e proton and FAC neutron configuration. The calculations for the 20^+ and 22^+ bands were performed for F and FAB neutron configurations because these are the lowest and second lowest odd-quasiparticle neutron configuration with $\pi = -$ and $\alpha = +1/2$ respectively.

The nuclear deformation parameters were extracted from the TRS minima corresponding to eF configuration at rotational frequency just above the first band crossing with $I_p \approx 5.5 \hbar$ and $I_n \approx 14.5 \hbar$ for the 20^+ band.

In the case of the eFAC configuration, the nuclear deformation parameters were extracted from the TRS plots corresponding to $I_p \approx 5.5 \hbar$ and $I_n \approx 15.5 \hbar$ at rotational frequency below the first band crossing for the 21^+ band.

TRS plots for the eFAB configuration with minima corresponding to $I_p \approx 5.5 \hbar$ and $I_n \approx 16.5 \hbar$ and at rotational frequency below the first band crossing were selected for the 22^+ band.

The values of nuclear deformation parameters corresponding to the 20^+ , 21^+ and 22^+ bands of odd-odd $^{186-194}\text{Au}$ nuclei are shown in Table 3.6.

In the 20^+ band, a band crossing occurs in the rotational frequency region of $0.248 \text{ MeV}/\hbar < \omega < 0.328 \text{ MeV}/\hbar$ and corresponds to an alignment gain of about $5-7 \hbar$ (e.g. see Figure 3.7 and 3.10).

In the 21^+ band, the first band crossing occurs in the rotational frequency region of $0.248 \text{ MeV}/\hbar < \omega < 0.288 \text{ MeV}/\hbar$ and corresponds to an alignment gain of about 8-10 \hbar (e.g. see Figure 3.8 and 3.11).

In the 22^+ band, TRS predict a band crossing which takes place in the rotational frequency region of $0.208 \text{ MeV}/\hbar < \omega < 0.248 \text{ MeV}/\hbar$, and corresponds to an alignment gain of ~ 7.8 -9 \hbar (e.g. see Figure 3.9 and 3.12).

Generally, the TRS calculations predict triaxial shape of the nucleus for these three bands in each odd-odd $^{186-194}\text{Au}$ nuclei.

Table 3.6: The values of the nuclear deformation parameters β_2 , γ , β_4 corresponding to the 20^+ , 21^+ and 22^+ bands of the odd-odd $^{186-194}\text{Au}$ nuclei.

Odd-odd Au nuclei	I^π	Band configuration		$\hbar\omega$ (MeV)	Nuclear deformation parameters		
		Assignment	TRS configuration		β_2	γ (degree)	β_4
^{186}Au	22^+	eFAB	eFAB	0.169	0.141	-80.0	-0.021
	20^+	eFBC	eF	0.248	0.150	-70.7	-0.017
	21^+	eFAC	eFAC	0.169	0.140	-75.1	-0.015
^{188}Au	22^+	eFAB	eFAB	0.168	0.143	-84.7	-0.025
	20^+	eFBC	eF	0.208	0.144	-82.4	-0.023
	21^+	eFAC	eFAC	0.168	0.136	-77.4	-0.019
^{190}Au	22^+	eFAB	eFAB	0.128	0.146	-87.8	-0.030
	20^+	eFBC	eF	0.207	0.146	-88.4	-0.028
	21^+	eFAC	eFAC	0.168	0.135	-80.6	-0.024
^{192}Au	22^+	eFAB	eFAB	0.128	0.143	-85.3	-0.032
	20^+	eFBC	eF	0.206	0.138	-83.6	-0.029
	21^+	eFAC	eFAC	0.167	0.135	-79.9	-0.027
^{194}Au	22^+	eFAB	eFAB	0.206	0.143	-85.4	-0.033
	20^+	eFBC	eF	0.245	0.137	-83.3	-0.031
	21^+	eFAC	eFAC	0.206	0.134	-78.2	-0.030

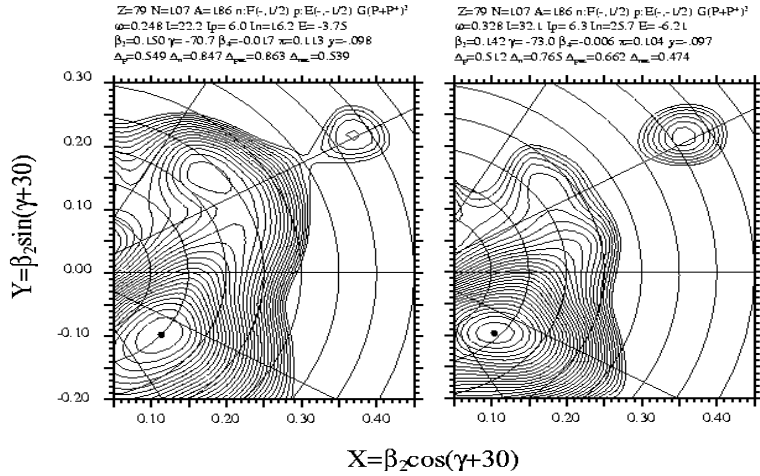


Figure 3.7: TRS plots showing the nuclear shapes for the eF configuration of ^{186}Au as the rotational frequency increases. The left plot corresponds to the 20^+ band, and the right plot corresponds to the same configuration but after the $\nu i_{13/2}$ band crossing. The rotational frequency is measured in MeV/\hbar and the proton (I_p), neutron (I_n) and total (I) aligned angular momenta are given in \hbar .

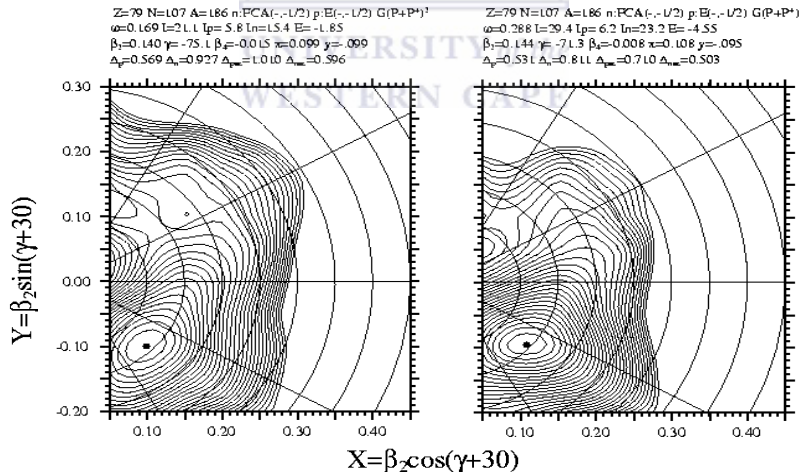


Figure 3.8: TRS plots showing the nuclear shapes for the $eFAC$ configuration of ^{186}Au as the rotational frequency increases. The left plot corresponds to the 21^+ band, and the right plot corresponds to the same configuration but after the $\nu i_{13/2}$ band crossing. The rotational frequency is measured in MeV/\hbar and the proton (I_p), neutron (I_n) and total (I) aligned angular momenta are given in \hbar .

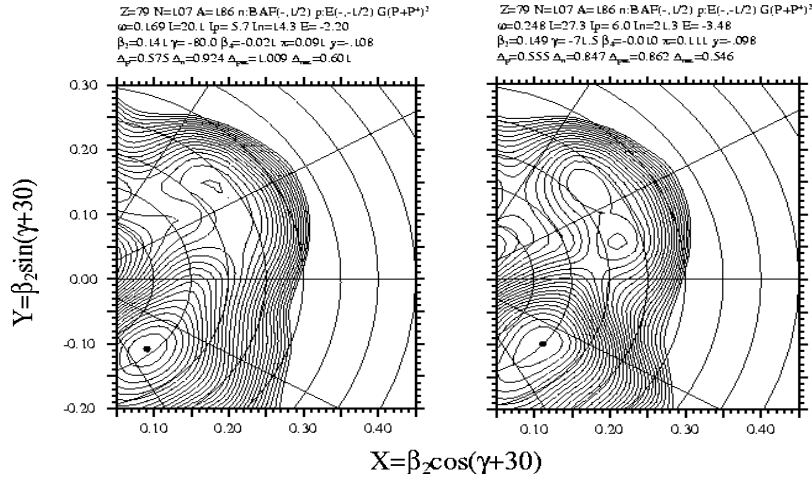


Figure 3.9: TRS plots showing the nuclear shapes for the eFAB configuration of ^{186}Au as the rotational frequency increases. The left plot corresponds to the 22^+ band, and the right plot corresponds to the same configuration but after the $\nu_{i_{13/2}}$ band crossing. The rotational frequency is measured in MeV/\hbar and the proton (I_p), neutron (I_n) and total (I) aligned angular momenta are given in \hbar .

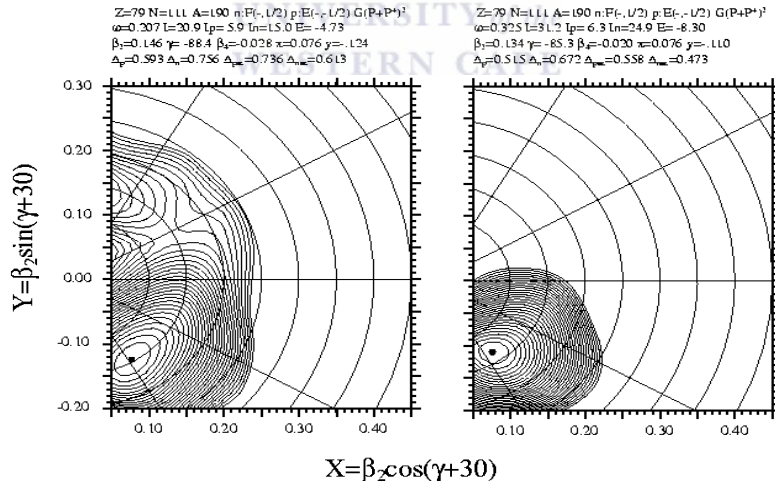


Figure 3.10: TRS plots showing the nuclear shapes for the eF configuration of ^{186}Au as the rotational frequency increases. The left plot corresponds to the 20^+ band, and the right plot corresponds to the same configuration but after the $\nu_{i_{13/2}}$ band crossing. The rotational frequency is measured in MeV/\hbar and the proton (I_p), neutron (I_n) and total (I) aligned angular momenta are given in \hbar .

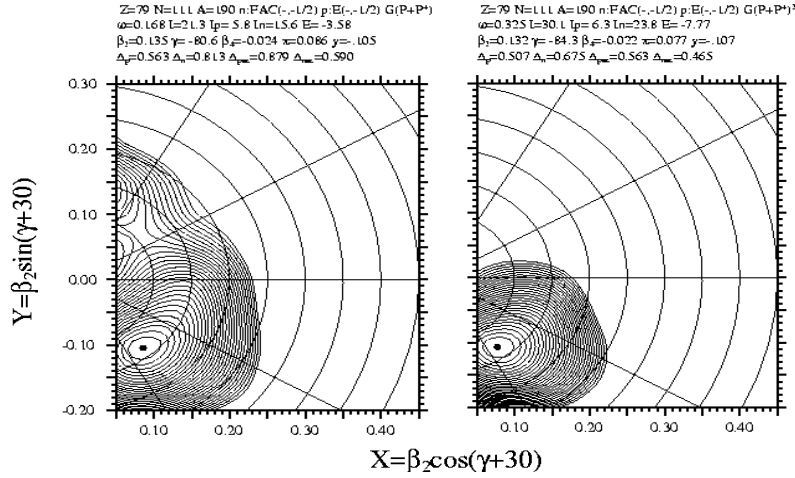


Figure 3.11: TRS plots showing the nuclear shapes for the eFAC configuration of ^{190}Au as the rotational frequency increases. The left plot corresponds to the 21^+ band, and the right plot corresponds to the same configuration but after the $\nu_{13/2}$ band crossing. The rotational frequency is measured in MeV/\hbar and the proton (I_p), neutron (I_n) and total (I) aligned angular momenta are given in \hbar .

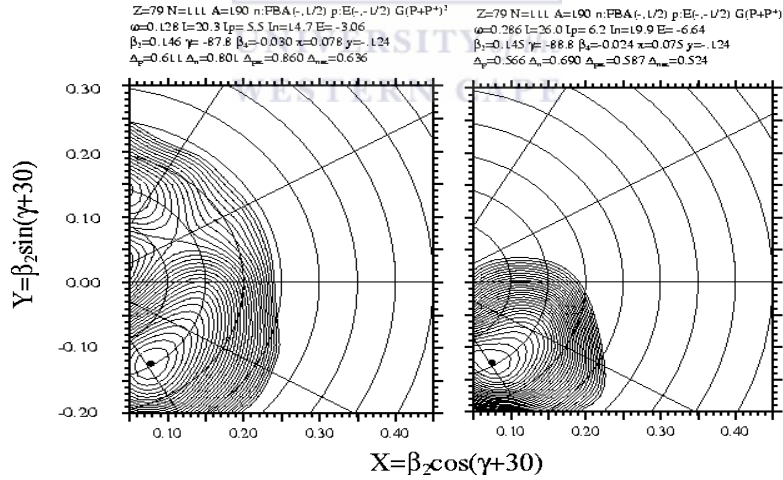


Figure 3.12: TRS plots showing the nuclear shapes for the eFAB configuration of ^{190}Au as the rotational frequency increases. The left plot corresponds to the 22^+ band, and the right plot corresponds to the same configuration but after the $\nu_{13/2}$ band crossing. The rotational frequency is measured in MeV/\hbar and the proton (I_p), neutron (I_n) and total (I) aligned angular momenta are given in \hbar .

3.3.3 TRS calculations for the odd-even ¹⁸⁷⁻¹⁹³Au nuclei

In the ^{187,189,191,193}Au nuclei we were interested in the $\pi h_{11/2}^{-1}$, $\pi h_{11/2}^{-1} \otimes \nu i_{13/2}^{-2}$ and $\pi h_{11/2}^{-1} \otimes \nu i_{13/2}^{-1} h_{9/2}^{-1}$ bands. The $\pi h_{11/2}^{-1} \otimes \nu i_{13/2}^{-2}$ configuration was assigned to a set of three rotation aligned bands (i.e. $31/2^-$, $33/2^-$ and $35/2^-$ bands), and the $\pi h_{11/2}^{-1} \otimes \nu i_{13/2}^{-1} h_{9/2}^{-1}$ configuration was associated with a set of two bands (i.e. $31/2^+$ and $33/2^+$ bands). In terms of the CSM model the $\pi h_{11/2}^{-1} (11/2^-)$ band is assigned to e configuration, the $31/2^-$, $33/2^-$ and $35/2^-$ bands are assigned to eAB, eAC and eBC configurations respectively, whereas the $31/2^+$ and $33/2^+$ bands are assigned to eBF and eAF configurations respectively.

3.3.3.1 The $11/2^-$ bands of the odd-even ¹⁸⁷⁻¹⁹³Au nuclei

To extract the values of the nuclear deformation parameters for the $11/2^-$ band in the odd-even ¹⁸⁷⁻¹⁹³Au nuclei, the TRS calculations were performed for the e proton and the vacuum neutron configuration, and TRS minima with $I_p \approx 5.5 \hbar$ and $I_n \approx 0 \hbar$ at a rotational frequency below the first band crossing frequency were selected. The TRS calculations predict triaxiality in the $11/2^-$ band of each odd-even ¹⁸⁷⁻¹⁹³Au nuclei. The values of the nuclear deformations are summarized in Table 3.7.

In ¹⁸⁷Au, TRS calculations predict a first band crossing which takes place at a rotational frequency of $0.167 \text{ MeV}/\hbar < \omega < 0.248 \text{ MeV}/\hbar$ with alignment gain of $13.1 \hbar$ (see Figure 3.13).

In ^{189,191}Au, TRS calculations predict a first band crossing which takes place at a rotational frequency of $0.167 \text{ MeV}/\hbar < \omega < 0.207 \text{ MeV}/\hbar$ with alignment gain of $12.2 \hbar$ and $12.4 \hbar$ respectively.

In ¹⁹³Au, TRS calculations predict a first band crossing which takes place at a rotational frequency of $0.127 \text{ MeV}/\hbar < \omega < 0.206 \text{ MeV}/\hbar$ with alignment gain of $12.2 \hbar$ (see Figure 3.16).

TRS calculations show that after the first band crossing, the gamma deformation of the odd-even ^{189,191}Au does not change, while that of ¹⁸⁷Au decreases and that of ¹⁹³Au increases.

Table 3.7: The values of the nuclear deformation parameters β_2 , γ , β_4 corresponding to the $11/2^-$ band of the odd-even $^{187-193}\text{Au}$ nuclei.

Odd-even Au nuclei	I^π	Band configuration		$\hbar\omega$ (MeV)	Nuclear deformation parameters		
		Assignment	TRS configuration		β_2	γ (degree)	β_4
^{187}Au	$11/2^-$	e	e	0.168	0.141	-77.1	-0.024
^{189}Au	$11/2^-$	e	e	0.168	0.139	-76.5	-0.026
^{191}Au	$11/2^-$	e	e	0.167	0.136	-75.7	-0.029
^{193}Au	$11/2^-$	e	e	0.127	0.131	-75.8	-0.031

3.3.3.2 The $31/2^-$, $33/2^-$ and $35/2^-$ bands of the odd-even $^{187-193}\text{Au}$ nuclei

To extract the values of the nuclear deformation parameters for the $31/2^-$ band in the odd-even $^{187-193}\text{Au}$ nuclei, the TRS calculations were performed for the e proton and a vacuum neutron configuration, and TRS minima at rotational frequency above the first band crossing with $I_p \approx 5.5 \hbar$ and $I_n \approx 12 \hbar$ were selected.

In the case of the $33/2^-$ band, the nuclear deformation parameters were extracted from the TRS plots performed for the e proton and AC neutron configurations. The TRS minima with $I_p \approx 5.5 \hbar$ and $I_n \approx 11 \hbar$ at the rotational frequency below the first band crossing were selected.

In the case of the $35/2^-$ band, the nuclear deformation parameters were extracted from the TRS plots performed for the e proton and AB neutron configurations. The TRS minima with $I_p \approx 5.5 \hbar$ and $I_n \approx 10 \hbar$ at the rotational frequency below the first band crossing were selected.

For these bands (i.e. $31/2^-$, $33/2^-$ and $35/2^-$), the TRS calculations predict triaxial shape of the nucleus with deformation parameters as shown in Table 3.8. For the $31/2^-$ and $35/2^-$ bands TRS model predicts no shape changes in each odd-even $^{187-193}\text{Au}$ nuclei after the band crossing (e.g. see Figure 3.13, 3.15, 3.16 and 3.18). For the $33/2^-$ band TRS calculations predict no shape changes in the $^{187,191,193}\text{Au}$ nuclei after the band crossing (e.g. see Figures 3.14 and 3.17), whereas the ^{189}Au nuclei become more triaxial after the band crossing.

Table 3.8: The values of the nuclear deformation parameters β_2 , γ , β_4 corresponding to the $31/2^-$, $33/2^-$ and $35/2^-$ bands of the odd-even $^{187-193}\text{Au}$ nuclei.

Odd-even Au nuclei	I^π	Band Configuration		$\hbar\omega(\text{MeV})$	Nuclear deformation parameters		
		Assignment	TRS configuration		β_2	γ (degree)	β_4
^{187}Au	$31/2^-$	eAB	e	0.248	0.152	-58.1	-0.014
	$35/2^-$	eBC	eAB	0.168	0.142	-68.9	-0.020
	$33/2^-$	eAC	eAC	0.168	0.141	-66.8	-0.015
^{189}Au	$31/2^-$	eAB	e	0.207	0.142	-64.7	-0.020
	$35/2^-$	eBC	eAB	0.168	0.140	-69.0	-0.022
	$33/2^-$	eAC	eAC	0.168	0.138	-69.2	-0.020
^{191}Au	$31/2^-$	eAB	e	0.207	0.139	-68.7	-0.025
	$35/2^-$	eBC	eAB	0.167	0.138	-71.6	-0.025
	$33/2^-$	eAC	eAC	0.167	0.136	-71.1	-0.024
^{193}Au	$31/2^-$	eAB	e	0.206	0.134	-72.6	-0.027
	$35/2^-$	eBC	eAB	0.127	0.133	-74.4	-0.028
	$33/2^-$	eAC	eAC	0.167	0.134	-72.3	-0.027

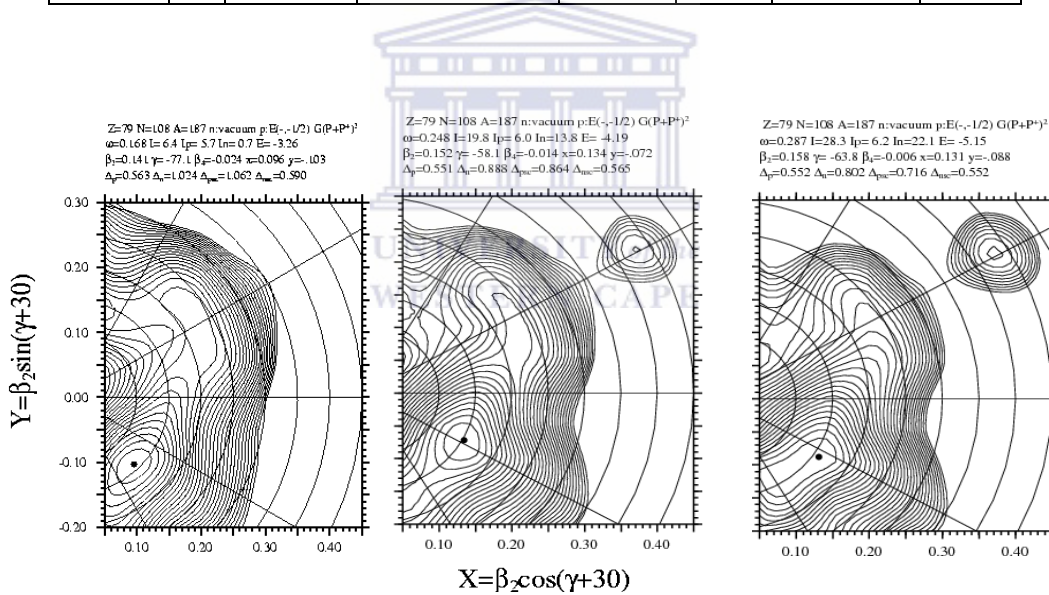


Figure 3.13: TRS plots showing the nuclear shapes for the e proton and vacuum neutron configuration of ^{187}Au as the rotational frequency increases. The left plot corresponds to the $11/2^-$ band, the middle plot correspond to the $31/2^-$ band, and the right plot corresponds to the same band, but above the $\nu_{i_{13/2}}$ band crossing. The rotational frequency is measured in MeV/\hbar and the proton (I_p), neutron (I_n) and total (I) aligned angular momenta are given in \hbar .

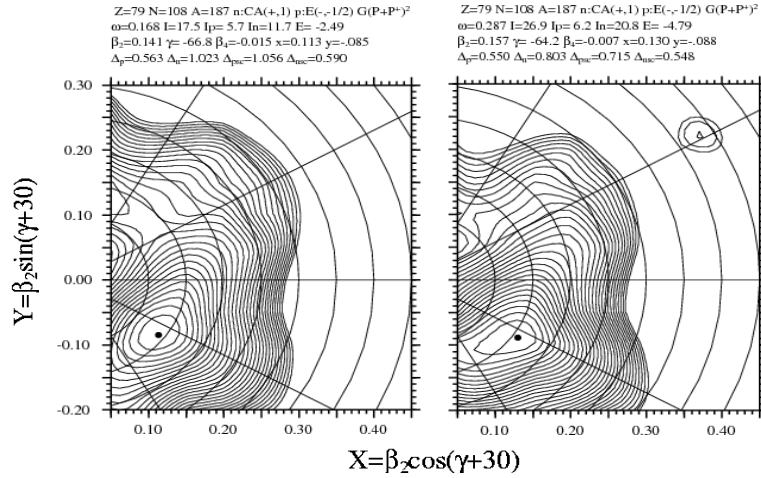


Figure 3.14: TRS plots showing the nuclear shapes for the eAC configuration of ^{187}Au as the rotational frequency increases. The left plot corresponds to the $33/2^-$ band, and the right plot corresponds to the same band above the $\nu_{i13/2}$ band crossing. The rotational frequency is measured in MeV/\hbar and the proton (I_p), neutron (I_n) and total (I) aligned angular momenta are given in \hbar .

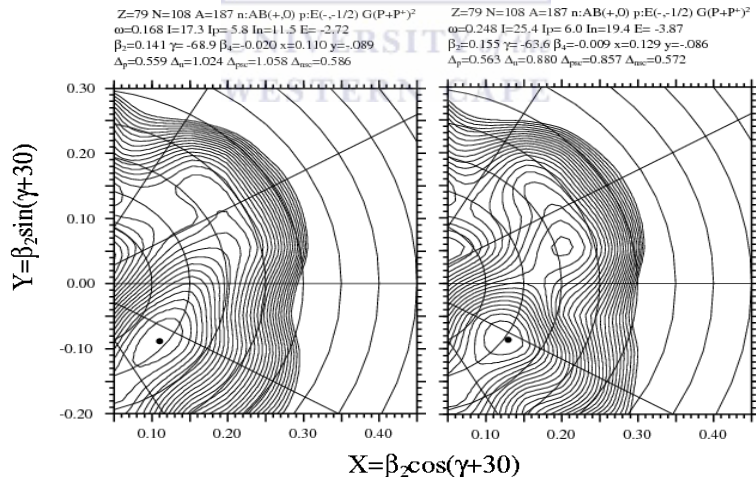


Figure 3.15: TRS plots showing the nuclear shapes for the eAB configuration of ^{187}Au as the rotational frequency increases. The left plot corresponds to the $35/2^-$ band, and the right plot corresponds to the same band above the $\nu_{i13/2}$ band crossing. The rotational frequency is measured in MeV/\hbar and the proton (I_p), neutron (I_n) and total (I) aligned angular momenta are given in \hbar .

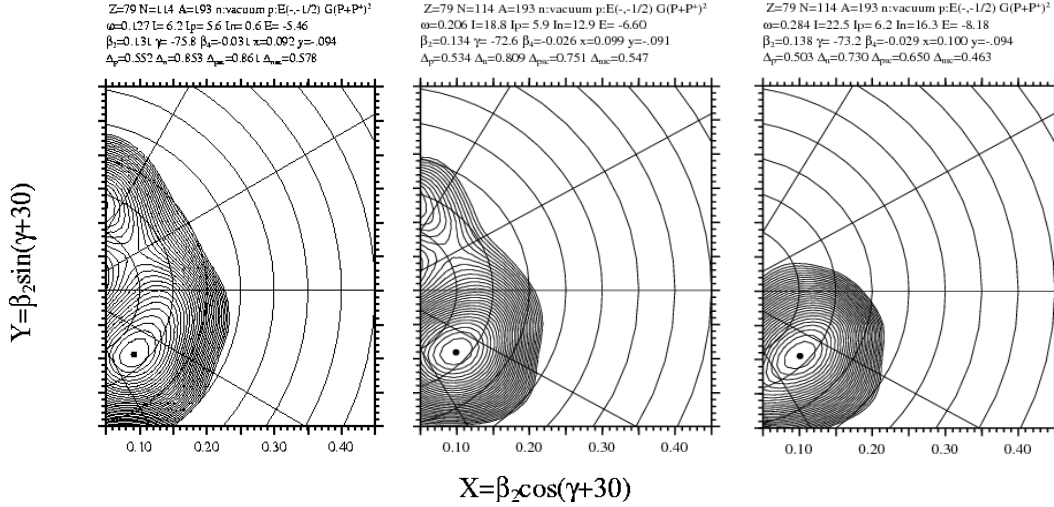


Figure 3.16: TRS plots showing the nuclear shapes for the *e* proton and vacuum neutron configuration of ^{193}Au as the rotational frequency increases. The left plot corresponds to the $11/2^-$ band, the middle plot correspond to the $31/2^-$ band, and the right plot corresponds to the same band, but above the $\nu_{i13/2}$ band crossing. The rotational frequency is measured in MeV/\hbar and the proton (I_p), neutron (I_n) and total (I) aligned angular momenta are given in \hbar .

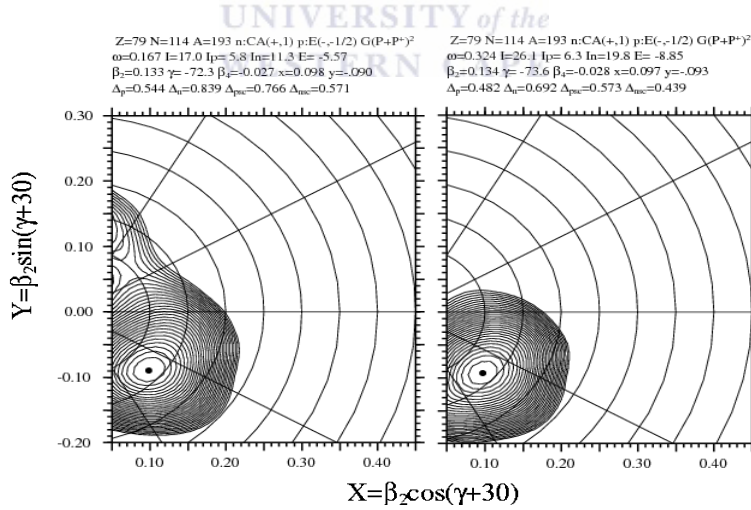


Figure 3.17: TRS plots showing the nuclear shapes for the *eAC* configuration of ^{193}Au as the rotational frequency increases. The left plot corresponds to the $33/2^-$ band, and the right plot corresponds to the same band above the $\nu_{i13/2}$ band crossing. The rotational frequency is measured in MeV/\hbar and the proton (I_p), neutron (I_n) and total (I) aligned angular momenta are given in \hbar .

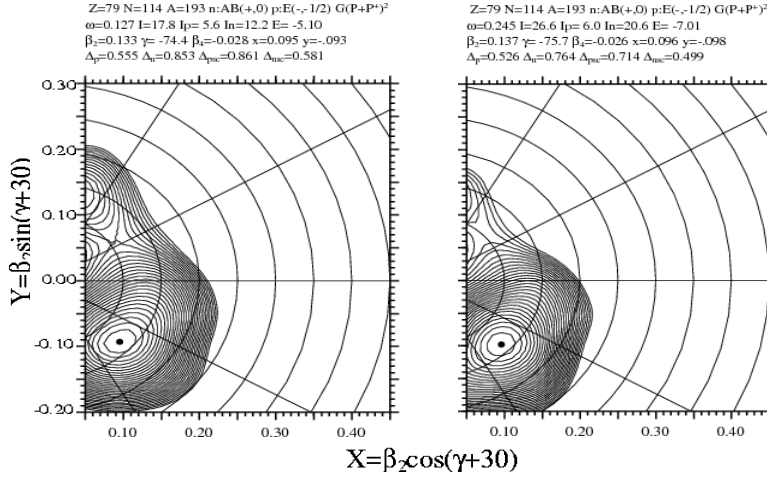


Figure 3.18: TRS plots showing the nuclear shapes for the eAB configuration of ^{193}Au as the rotational frequency increases. The left plot corresponds to the $35/2^-$ band, and the right plot corresponds to the same band above the $\nu_{i_{13/2}}$ band crossing. The rotational frequency is measured in MeV/\hbar and the proton (I_p), neutron (I_n) and total (I) aligned angular momenta are given in \hbar .

3.3.3.3 The $31/2^+$ and $33/2^+$ bands of the odd-even $^{187-193}\text{Au}$ nuclei

To extract the values of nuclear deformation parameters corresponding to the $33/2^+$ band, the TRS calculations for the e proton and AF neutron configurations were performed. The TRS minima with $I_p \approx 5.5 \hbar$ and $I_n \approx 11 \hbar$ at rotational frequency below the first band crossing were selected

Similarly, in the case of the $31/2^+$ band, the TRS calculations for the e proton and BF neutron configuration were performed. The TRS minima with $I_p \approx 5.5 \hbar$ and $I_n \approx 10 \hbar$ at the rotational frequency below the first band crossing were selected.

For these two bands, the TRS calculations predict triaxial shape of the nucleus for each odd-even $^{187-193}\text{Au}$ nucleus and the values of the nuclear deformation parameters are shown in Table 3.9.

For the $31/2^+$ and $33/2^+$ bands in $^{187-193}\text{Au}$, TRS calculations predict band crossings which take place in the rotational frequency region of $0.207 \text{ MeV}/\hbar < \omega < 0.286 \text{ MeV}/\hbar$ and $0.207 \text{ MeV}/\hbar < \omega < 0.248 \text{ MeV}/\hbar$ with the alignment gain of $\sim 10-12 \hbar$ and $\sim 9-11 \hbar$ respectively. For these bands no shape changes are predicted in any odd-even $^{187-193}\text{Au}$ nuclei after these band crossings (e.g. see Figures 3.19-3.22).

Table 3.9: The values of the nuclear deformation parameters β_2 , γ , β_4 corresponding to the $31/2^-$ and $33/2^-$ bands of the odd-even $^{187-193}\text{Au}$ nuclei.

Odd-even Au nuclei	I^π	Band Configuration		$\hbar\omega$ (MeV)	Nuclear deformation parameters		
		Assignment	TRS configuration		β_2	γ (degree)	β_4
^{187}Au	$33/2^+$	eAF	eAF	0.208	0.146	-84.1	-0.023
	$31/2^+$	eBF	eBF	0.208	0.142	-81.7	-0.024
^{189}Au	$33/2^+$	eAF	eAF	0.207	0.146	-84.9	-0.025
	$31/2^+$	eBF	eBF	0.207	0.142	-85.0	-0.027
^{191}Au	$33/2^+$	eAF	eAF	0.167	0.140	-82.7	-0.030
	$31/2^+$	eBF	eBF	0.207	0.141	-87.1	-0.031
^{193}Au	$33/2^+$	eAF	eAF	0.167	0.134	-77.1	-0.030
	$31/2^+$	eBF	eBF	0.127	0.141	-86.7	-0.035

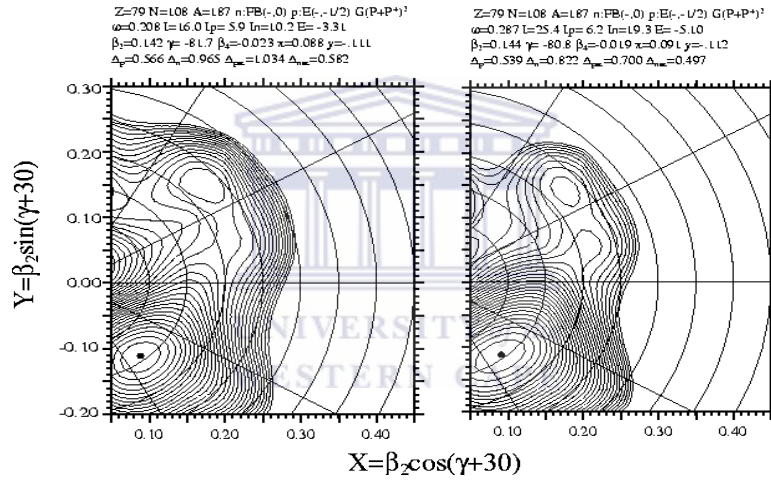


Figure 3.19: TRS plots showing the nuclear shapes for the eFB configuration of ^{187}Au as the rotational frequency increases. The left plot corresponds to the $31/2^+$ band, and the right plot corresponds to the same band above the band crossing. The rotational frequency is measured in MeV/\hbar and the proton (l_p), neutron (l_n) and total (l) aligned angular momenta are given in \hbar .

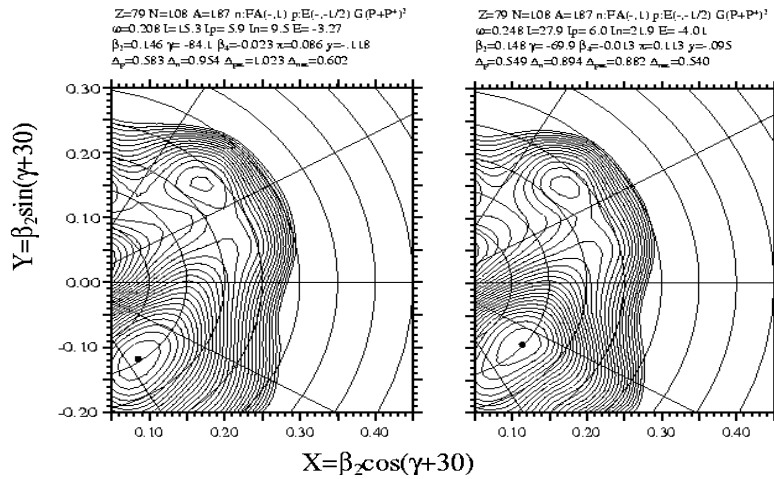


Figure 3.20: TRS plots showing the nuclear shapes for the eFA configuration of ^{187}Au as rotational frequency increases. The left plot corresponds to the $33/2^+$ band, and the right plot corresponds to the same band, but above the band crossing. The rotational frequency is measured in MeV/\hbar and the proton (I_p), neutron (I_n) and total (I) aligned angular momenta are given in \hbar .

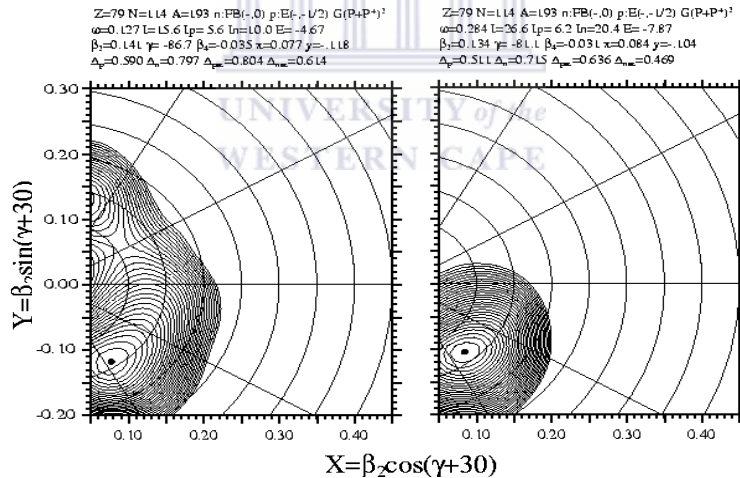


Figure 3.21: TRS plots showing the nuclear shapes for the eFB configuration of ^{193}Au as the rotational frequency increases. The left plot corresponds to the $31/2^+$ band, and the right plot corresponds to the same band above the band crossing. The rotational frequency is measured in MeV/\hbar and the proton (I_p), neutron (I_n) and total (I) aligned angular momenta are given in \hbar .

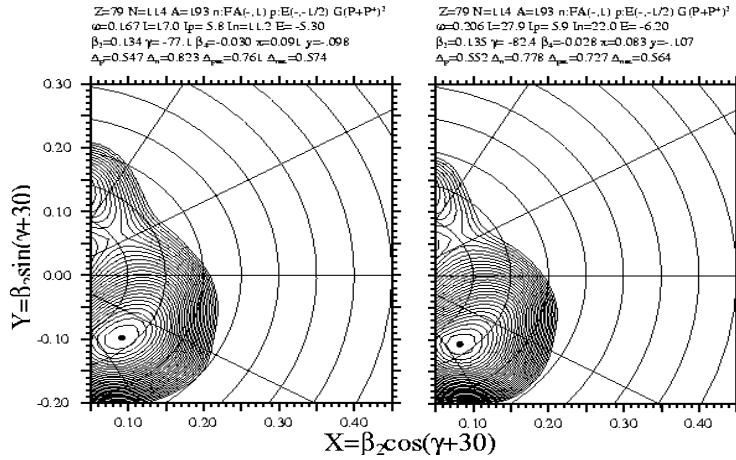


Figure 3.22: TRS plots showing the nuclear shapes for the eFA configuration of ^{193}Au as rotational frequency increases. The left plot corresponds to the $33/2^+$ band, and the right plot corresponds to the same band, but above the band crossing. The rotational frequency is measured in MeV/\hbar and the proton (l_p), neutron (l_n) and total (l) aligned angular momenta are given in \hbar .

3.3.4 CSM calculations

The programs SWGAMMA and SWBETA calculate the single particle energies of a nucleus in a deformed Woods-Saxon potential. These and other programs (i.e. JXGAMMA, WHFB, HFBC, SPAGAFI) are part of the uniform code system for nuclear structure, which has been developed by the Warsaw group, mainly by J. Dudek and W. Nazarewicz in collaboration with S. Ćwiok. There exists a very good and extensive description of SWBETA in [Ćwi87]. The present versions are written in standard FORTRAN and set up to run on VAX computers, but with small changes they can run on any computer. The easiest way of running the code is with the help of command files.

The codes SWGAMMA and SWBETA are used for triaxial and axially symmetric shapes respectively. The input parameters of SWGAMMA are Z , N and the values of the nuclear deformation parameters β_2 , γ , and β_4 predicted by the TRS model. In SWBETA, one needs to specify only β_2 , β_4 , and β_6 . However the code can also be used for odd multipoles such as β_3 and β_5 . The deformation values determine the shape of the potential and Z , N determines the depth of the potential. No other variables are necessary in order to calculate the single particle energies.

The Woods-Saxon potential has twelve parameters, which had been fitted in order to reproduce the experimental levels. The values as well as the shape parameterization can be found in [Naz85].

The programs SWGAMMA and SWBETA solve the Schrödinger equation for the potential described by the input and the eigenvalues (energies, parities, etc) are tabulated in the output. Each state is doubly degenerate due to the time reversal symmetry. In order to calculate the energies as a function of rotational frequency, a j_x matrix has to be constructed, which operates upon the single particles or quasiparticle wavefunctions. This matrix is set up in the program JXGAMMA or JXBETA where in addition the BCS equation is solved, and the pairing gap and Fermi surface are determined. In the next step, the single particle Routhians as a function of the rotational frequency (no pairing) are calculated using the code WHFB, whereas the quasiparticle Routhians (with pairing) with respect to the vacuum configuration are calculated using the code HFBC. The output can be used to plot the Routhians as a function of the rotational frequency. The code SPAGAFI is used to create such plots of single particle and quasiparticle Routhians. It can also be used to plot the single particle energies as a function of the nuclear deformation for axially symmetric nuclei. CSM calculations were performed for the $^{186-194}\text{Au}$ nuclei using the values of the nuclear deformation parameters predicted by the TRS calculations discussed in the previous section. They were carried out for fifteen different nuclear rotational frequencies starting from 0 MeV/ \hbar up to 0.7 MeV/ \hbar with an increasing step of 0.05 MeV/ \hbar . Some examples of the CSM plots obtained are shown in the following sections, while the values of the extracted Routhians are included in Appendix C.

3.3.5 CSM calculations for the odd-odd $^{186-194}\text{Au}$ nuclei

CSM calculations were performed for the 11^- , 12^- , 20^+ , 21^+ , 22^+ and 22^- bands of the odd-odd $^{186-194}\text{Au}$ nuclei, and the results obtained are described in the following sections.

3.3.5.1 The 11^- and 12^- bands of the odd-odd $^{186-194}\text{Au}$ nuclei

The CSM results for the quasiparticle protons and neutrons were used to calculate the quasiparticle Routhian of a band. For example, calculations for the Routhians of the 11^- and 12^- bands in ^{190}Au will be described.

All quasiparticle Routhians are calculated relative to the vacuum configuration defined as the lowest configuration for an even-even nucleus with positive parity $\pi = +1$ and a signature of $\alpha = 0$. For the vacuum configuration all the Routhians with $e'(\omega = 0) < 0$, remain occupied. At $\omega > 0$, the positive energy Routhians are labelled with latin letters A, B, C, etc according to the convention shown in Table 3.1 under section 3.3.1. It should be noted that for large non-axiality the lowest lying positive parity positive-signature Routhian has smaller alignment at low rotational frequency than the second lowest one which is opposite for axially symmetric nuclei. Thus in this study, the Routhian with larger alignment is labelled A for all γ deformations and frequencies, while the one with smaller alignment is labelled C.

In the CSM quasiparticle plots for protons the e and f^+ Routhians come close, interact and exchange their wave functions at a rotational frequency of $\hbar\omega \approx 0.21 \text{ MeV}$ (see Figure 3.23). This frequency is called band crossing frequency. At this frequency the ef two-quasiparticle configuration crosses the vacuum configuration and becomes lower in energy. Since for many Routhians strong interaction and mixing is observed, diabatic Routhians are constructed by linear extrapolation from the adiabatic Routhians as shown in the Figure 3.23-24 by the red straight line. The slope of each Routhian corresponds to the magnitude of the aligned angular momentum j of the particle at that frequency. Figure 3.24 shows an example of the quasineutron Routhian diagram performed for ^{190}Au using deformation parameters predicted by TRS calculations.

The 11^- and 12^- bands in the odd-odd $^{186-194}\text{Au}$ nuclei were assigned to eB and eA configurations [Nes82, Tok79]. Thus, the Routhian of the 11^- band is obtained as the sum of the proton Routhian e and the neutron Routhian B calculated using the deformation parameters of the 11^- band. The exact values of the e and B Routhians, and also their alignments are taken directly from the CSM output tables. Similarly, the Routhian of the 12^- band is calculated as the sum of the e proton and A neutron quasiparticle Routhians calculated using the deformation parameters for the 12^- band.

The values of band alignments, signature inversion frequencies, signature splitting, band crossing frequencies, and alignment gains are summarized in Table 4.1 and 4.9 in Chapter 4. The Routhians are plotted in Figures 4.5, 4.8, 4.11, 4.14, and 4.17 in Chapter 4.

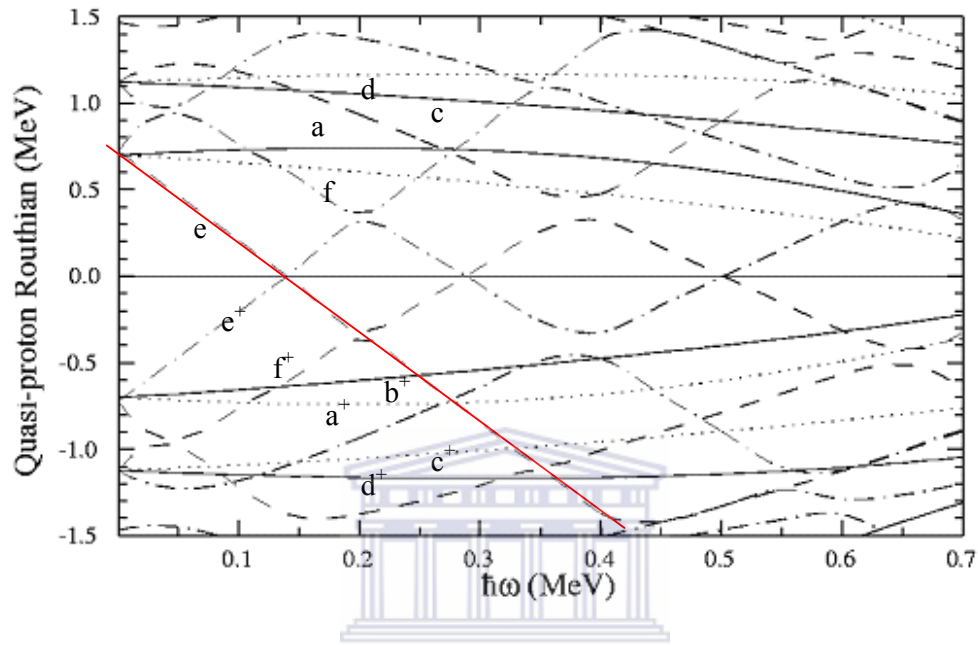


Figure 3.23: *Quasiproton Routhian diagram for ^{190}Au , performed using $\beta_2 = 0.137$, $\beta_4 = -0.026$ and $\gamma = -70.8^\circ$ predicted by the TRS for the eB configuration. Solid lines represent $(\pi, \alpha) = (+, +1/2)$, dotted $(+, -1/2)$, dash-dotted $(-, +1/2)$ and dashed $(-, -1/2)$.*

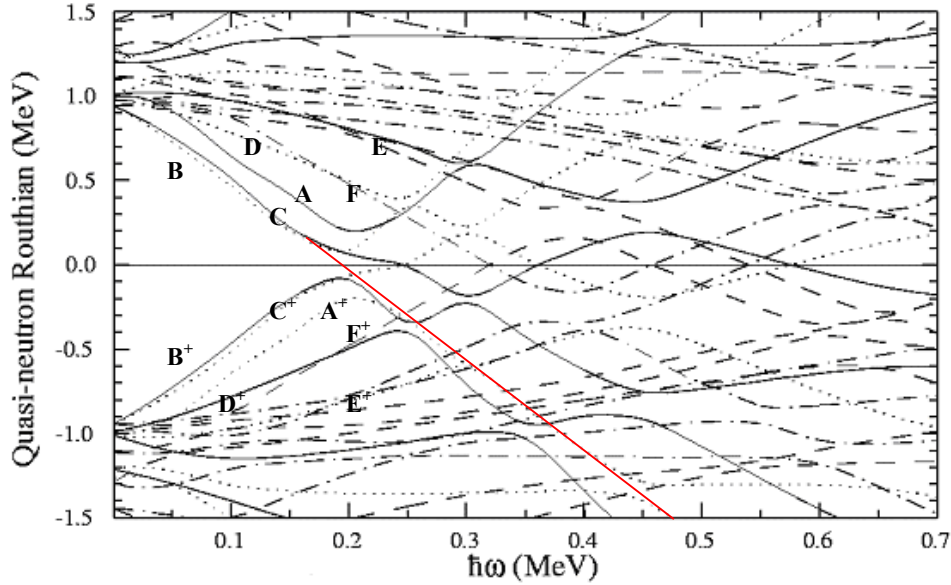


Figure 3.24: Quasineutron Routhian diagram for ^{190}Au , performed using $\beta_2 = 0.137$, $\beta_4 = -0.026$ and $\gamma = -70.8^\circ$ predicted by the TRS for the eB configuration. Solid lines represent $(\pi, \alpha) = (+, +1/2)$, dotted $(+, -1/2)$, dash-dotted $(-, +1/2)$ and dashed $(-, -1/2)$.

3.3.5.2 The 22^- band of the odd-odd $^{186-194}\text{Au}$ nuclei

The 22^- band was assigned to eABC configuration in ^{190}Au [Gue03]. The quasiparticle Routhians of the 22^- band were calculated as the sum of the e proton and the A, B, C neutron Routhians calculated for the deformation parameters of the 22^- band. CSM predicts EF band crossing in the 22^- band. Figure 3.25 shows an example of the quasineutron Routhian diagram for ^{190}Au performed using nuclear deformation parameters of the 22^- band. The theoretical quasiparticle Routhians for the 22^- band in each odd-odd $^{186-194}\text{Au}$ nucleus are shown in Figures 4.5, 4.8, 4.11, 4.14 and 4.17 in Chapter 4. The values of the band alignments, band crossing frequencies and alignment gains are summarized in Table 4.4 in Chapter 4.

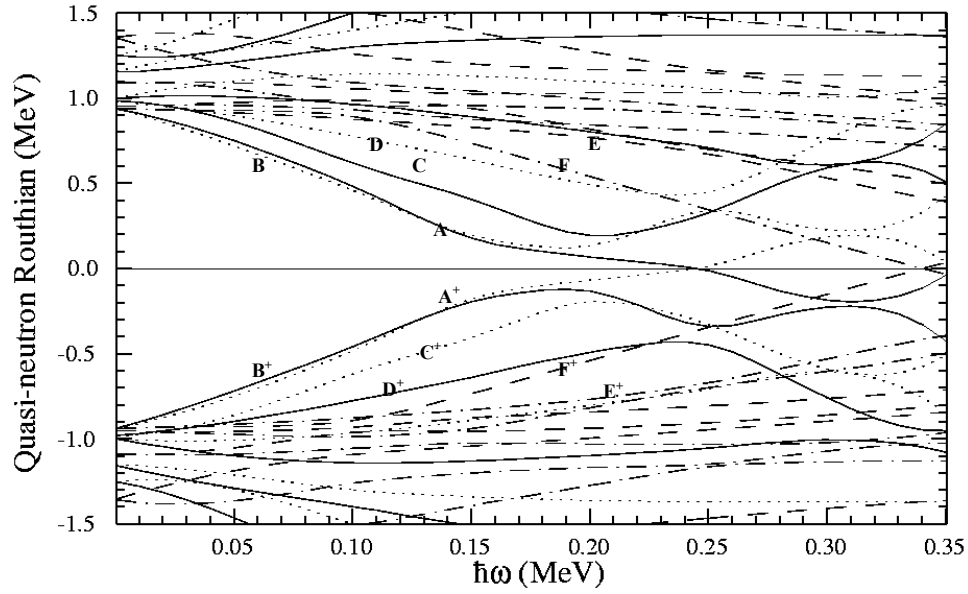


Figure 3.25: Quasineutron Routhian diagram for ^{190}Au , performed using $\beta_2 = 0.141$, $\beta_4 = -0.018$ and $\gamma = -68.7^\circ$ predicted by the TRS for the eA configuration after an alignment of a pair of $i_{13/2}$ neutron. Solid lines represent $(\pi, \alpha) = (+, +1/2)$, dotted $(+, -1/2)$, dash-dotted $(-, +1/2)$ and dashed $(-, -1/2)$.

UNIVERSITY of the
WESTERN CAPE

3.3.5.3 The 20^+ , 21^+ and 22^+ bands of the odd-odd $^{186-194}\text{Au}$ nuclei

The quasiparticle Routhians of these bands were calculated as the sum of the occupied Routhians for the 20^+ , 21^+ and 22^+ bands calculated for the corresponding nuclear deformations. Due to the large triaxiality associated with these bands, the negative parity F Routhian is pushed down in energy and starts to compete with the positive parity A, B and C Routhians (e.g. see Figure 3.25). In ^{190}Au , the 20^+ , 21^+ and 22^+ bands are assigned to eFBC, eFAC and eFAB configurations respectively [Gue03]. For axially symmetric shape one expects to see the Routhian of the 22^+ bands to have the lowest energy compared to that of the 20^+ and 21^+ bands, but in this case the three Routhians compete strongly. At a frequency of $0.18 \text{ MeV} \leq \hbar\omega \leq 0.23 \text{ MeV}$, one can see that the A and C Routhians interact with each other, and the A Routhian becomes lower in energy than the C Routhian (see Figure 3.26). This reflects a crossing of the eFAB and eFBC Routhians. Figure 3.26 shows an example of the quasineutron Routhian diagram for the ^{190}Au performed using nuclear deformation parameters of

the eFAC band. CSM calculations predict CD, BI and AD band crossings in the 22^+ , 21^+ and 20^+ bands of each odd-odd $^{186-194}\text{Au}$ nuclei respectively. The values of the band alignments, band crossing frequencies and alignment gains are summarized in Table 4.3 in Chapter 4. The Routhians of the 20^+ , 21^+ and 22^+ bands are plotted in Figure 4.5, 4.8, 4.11, 4.14 and 4.17 in Chapter 4.

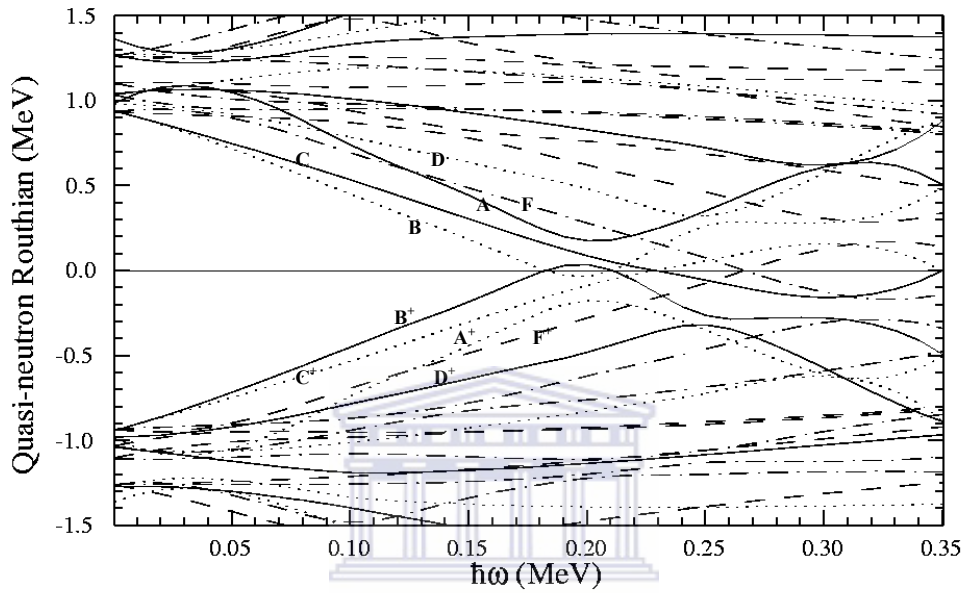


Figure 3.26: Quasineutron Routhian diagram for ^{190}Au , performed using $\beta_2 = 0.135$, $\beta_4 = -0.024$ and $\gamma = -80.6^\circ$ predicted by the TRS calculations for the eFAC configuration. Solid lines represent $(\pi, \alpha) = (+, +1/2)$, dotted $(+, -1/2)$, dash-dotted $(-, +1/2)$ and dashed $(-, -1/2)$.

3.3.6 CSM calculations for the odd-even $^{187-193}\text{Au}$ nuclei

The quasiparticle Routhians of the e $(11/2^-)$ eAB $(31/2^-)$, eAC $(33/2^-)$, eBC $(35/2^-)$, eBF $(31/2^+)$, and eAF $(33/2^+)$ bands in the odd-even $^{187-193}\text{Au}$ were calculated.

3.3.6.1 The $11/2^-$ band of the odd-even $^{187-193}\text{Au}$ nuclei

The Routhians of the $11/2^-$ band have been extracted as the e Routhians in the CSM calculations performed with the deformation parameters of the $11/2^-$ band and are shown in Figures 4.20, 4.23, 4.26 and 4.29 in Chapter 4. Band crossing frequencies,

alignments and alignment gains of the $11/2^-$ band predicted by the CSM calculations are shown in Table 4.5 and 4.6 in Chapter 4.

3.3.6.2 The $31/2^-$, $33/2^-$ and $35/2^-$ bands of the odd-even $^{187-193}\text{Au}$ nuclei

The quasiparticle Routhians of these bands were calculated as the sum of the occupied Routhians for the $31/2^-$, $33/2^-$ and $35/2^-$ bands (i.e. the sum of the e, A and B Routhians for the $31/2^-$ band, the sum of the e, A and C Routhians for the $33/2^-$ band and the sum of the e, B and C Routhians for the $35/2^-$ band) calculated for the corresponding nuclear deformations. The CSM predicts CD, BI, and AD band crossings in the $31/2^-$, $33/2^-$ and $35/2^-$ bands of the odd-even $^{187-193}\text{Au}$ nuclei respectively. Figure 3.27 shows an example of the quasineutron Routhian diagram for the ^{191}Au performed using nuclear deformation parameters of the eAC band. The quasiparticle Routhians for these bands are shown in Figures 4.20, 4.23, 4.26, and 4.29 in Chapter 4. The values of the band alignments, band crossing frequencies, alignment gains and signature splitting for these bands are summarized in Tables 4.7 and 4.11 in Chapter 4.

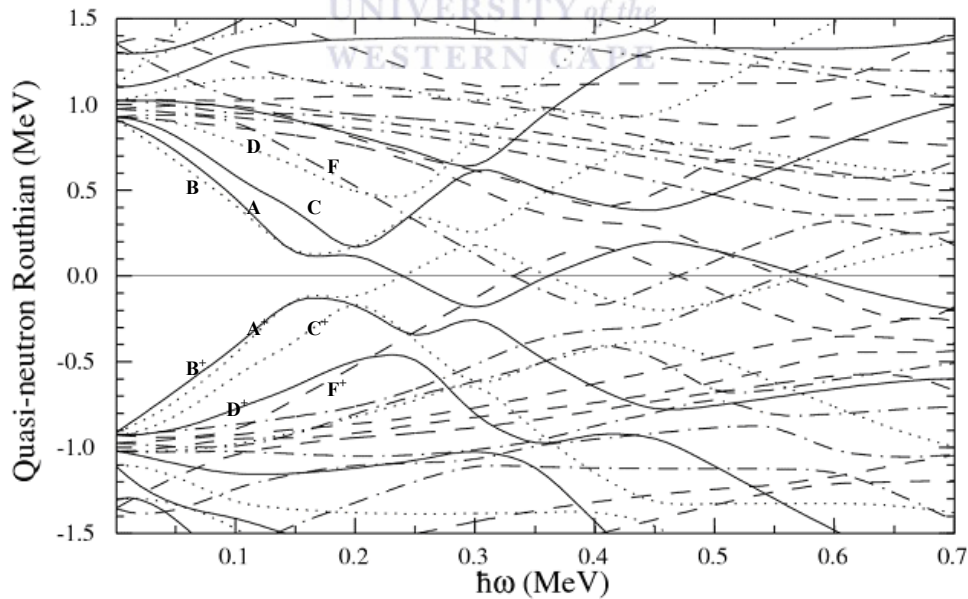


Figure 3.27: Quasineutron Routhian diagram for ^{191}Au performed using $\beta_2 = 0.136$, $\beta_4 = -0.024$ and $\gamma = -71.1^\circ$ predicted by the TRS for the eAC configuration. Solid lines represent $(\pi, \alpha) = (+, +1/2)$, dotted $(+, -1/2)$, dash-dotted $(-, +1/2)$ and dashed $(-, -1/2)$.

3.3.6.3 The $31/2^+$ and $33/2^+$ bands of the odd-even $^{187-193}\text{Au}$ nuclei

The $31/2^+$ and $33/2^+$ bands are assigned to eBF and eAF configurations. The quasiparticle Routhians of these bands were calculated as the sum of the occupied Routhians for the $31/2^+$ and $33/2^+$ bands (i.e. the sum of the e, B and F Routhians for the $31/2^+$ band and the sum of the e, A and F Routhians for the $33/2^+$ band) calculated for the corresponding nuclear deformations. Figure 3.28 shows an example of the quasineutron Routhian diagram for the ^{191}Au performed using nuclear deformation parameters of the eBF band. CSM also predicts signature inversion in these bands because the Routhian of the favored eAF band lies at higher energy than the unfavored eBF band. In the frequency region of $0.18 \text{ MeV} \leq \hbar\omega \leq 0.23 \text{ MeV}$, the A and C Routhians for the $^{187,189}\text{Au}$ nuclei interact strongly, such that in this region the eAF Routhian changes its slope and decreases rapidly (e.g. see Figure 3.28). The Routhians of the $31/2^+$ and $33/2^+$ band are shown in Figures 4.20, 4.23, 4.23 and 4.29 in Chapter 4. CSM predicts BC and AD band crossings in the eAF and eBF bands respectively. These band crossings are due to the excitation of a pair of $\nu i_{13/2}$ neutrons. The values of the band alignments, alignment gains, band crossing frequencies and signature splitting predicted by CSM are summarized in Table 4.8 in Chapter 4.

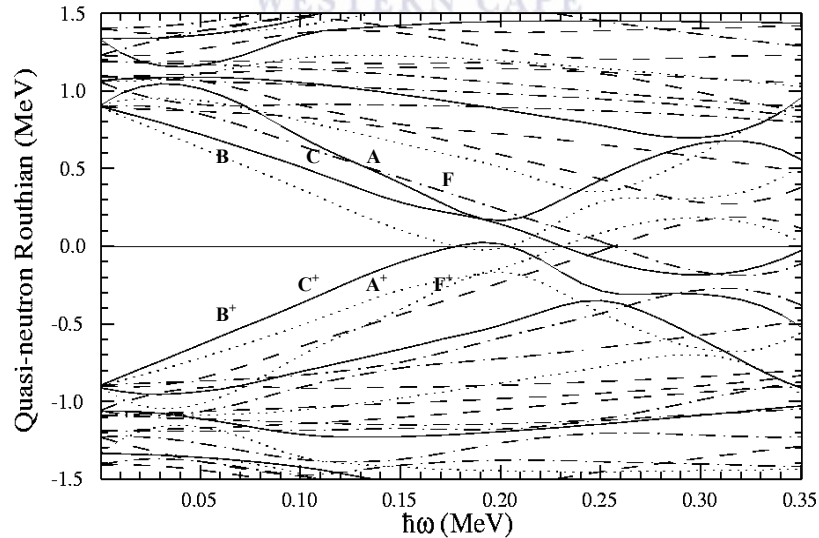


Figure 3.28: Quasineutron Routhian diagram for ^{191}Au performed using $\beta_2 = 0.140$, $\beta_4 = -0.030$ and $\gamma = -82.7^\circ$ predicted by the TRS for the eBF configuration. Solid lines represent $(\pi, \alpha) = (+, +1/2)$, dotted $(+, -1/2)$, dash-dotted $(-, +1/2)$ and dashed $(-, -1/2)$.

CHAPTER 4 Discussion

This chapter details the comparison of the experimental data in relation to the theoretical predictions of the total Routhian surface (TRS) and cranked shell model (CSM) calculations. Features of the bands that are compared are alignments, alignment gains, band crossing frequencies, signature inversion and splitting, and relative position of the quasiparticle Routhians of the bands.

4.1.1 Experimental and theoretical band crossing frequencies, alignments and alignment gains

4.1.1.1 The 11^- and 12^- bands of the odd-odd $^{186-194}\text{Au}$ nuclei

Triaxiality predicted by TRS in these bands, show that A, B and C Routhians lie close to each other, and thus three sets of rotation aligned bands are expected (i.e. eA, eB, eC bands), but experimentally two bands are observed (see level schemes of $^{186,188,190,192,194}\text{Au}$ in Appendix A.1-5). The theoretical alignments of the 11^- and 12^- bands are in good agreement with the experimentally measured ones (see Table 4.1). CSM predicts AD and BC band crossings in the 11^- and 12^- bands respectively of each odd-odd $^{186-194}\text{Au}$ nuclei. These band crossings are due to the excitation of a pair of $\nu i_{13/2}$ neutrons.

From the level scheme of ^{190}Au [Gue03], a band crossing occurs between the 17^- and 22^- levels as indicated by the irregularities of the gamma ray energies. This band crossing was associated with the alignment of a pair of particles in the neutron $\nu i_{13/2}$ orbital [Gue03], based on the consideration that among all orbitals close to the Fermi surface, only the addition of a $\nu i_{13/2}$ pair of particles can produce the large aligned angular momentum of about $21.5 \hbar$. Alignment of a $\nu i_{13/2}$ pair was also suggested for the first band crossing in the neighboring $^{191,193}\text{Hg}$ [Hüb86] isotopes and $^{187,189,191,193}\text{Au}$ [Bou89, Bou92, Gue02, Joh89, Köl85, Ven92] isotopes.

Table 4.1: The alignment, band crossing frequency and alignment gain for the 11^- and 12^- bands of the odd-odd $^{186-194}\text{Au}$ nuclei predicted by CSM calculations. The experimental results are calculated with Harris parameters of $J_0 = 6 \hbar^2 (\text{MeV})^{-1}$ and $J_1 = 30 \hbar^4 (\text{MeV})^{-3}$ and $K = 0$.

Odd-odd Au nuclei	Band alignment (\hbar)				Theoretical band crossing frequency (MeV)	Theoretical gain in alignment (\hbar)
	theoretical		experimental			
	$i_x(\text{eB})$	$i_x(\text{eA})$	$i_x(11^-)$	$i_x(12^-)$	$\hbar\omega_{BC}$ (eA)	i_{BC} (eA)
^{186}Au	10.6	11.4	10.9	11.8	0.252	8.8
^{188}Au	10.7	11.4	10.9	11.7	0.246	9.1
^{190}Au	10.6	11.5	10.9	11.8	0.215	9.4
^{192}Au	10.6	11.5	11.0	11.9	0.195	9.4
^{194}Au	10.5	11.5	11.2	12.0	0.187	9.4

The Routhian of 12^- band is crossed by that of the 22^- band at a band crossing frequency of ~ 0.274 MeV (see Figure 4.10). The band crossing frequency of 0.215 MeV predicted by CSM (see Figure 4.11) is rather smaller than the experimentally measured one of 0.274 MeV, but there is good agreement in the corresponding theoretical and experimental gain in alignment of 9.4 \hbar and 9.7 \hbar respectively. The experimental band crossing frequency and alignment gain are comparable with 0.266 MeV, 0.265 MeV and 9.3 \hbar , 9.2 \hbar obtained for $^{191,193}\text{Hg}$ isotopes respectively [Hüb86].

4.1.1.2 The 22^- bands of the odd-odd $^{186-194}\text{Au}$ nuclei

The positive parity Routhians A, B, and C that lie close to each other in energy are occupied, thus one rotation aligned band is expected (i.e. eABC), and this is in good agreement with the experimental observation (see level scheme of ^{190}Au in Appendix A.3). Table 4.2 shows the comparison between the theoretical and experimental alignments for the 22^- bands of the odd-odd $^{186-194}\text{Au}$ nuclei.

Table 4.2: Comparison between theoretical and experimental alignments for the 22^- bands of the odd-odd $^{186-194}\text{Au}$ nuclei predicted by CSM calculations. The experimental results are calculated with Harris parameters of $J_0 = 6 \hbar^2 (\text{MeV})^{-1}$ and $J_1 = 30 \hbar^4 (\text{MeV})^{-3}$ and $K = 0$.

Odd-odd Au nuclei	Theoretical band alignments (\hbar)	Experimental band alignments (\hbar)
	$i_x(\text{eABC})$	$i_x(22^-)$
^{186}Au	20.2	
^{188}Au	20.5	
^{190}Au	20.9	21.5
^{192}Au	20.9	
^{194}Au	20.9	

4.1.1.3 The 20^+ , 21^+ and 22^+ bands of the odd-odd $^{186-194}\text{Au}$ nuclei

TRS predicts triaxiality for the 20^+ , 21^+ and 22^+ bands of the $^{186-194}\text{Au}$ nuclei, such that the F Routhian is pushed down in energy and competes with the positive parity A, B and C Routhians, such that three sets of rotation aligned bands are expected (i.e. eFAB, eFAC, eFBC), and this is in good agreement with the experimental observation (see level scheme of ^{190}Au nuclei in Appendix A.3). There is a good agreement between the theoretical and experimental alignments of these bands in the odd-odd $^{186-194}\text{Au}$ nuclei (see Table 4.3).

Table 4.3: Comparison of the theoretical and experimental alignments for the 20^+ , 21^+ and 22^+ bands of the odd-odd $^{186-194}\text{Au}$ nuclei. The experimental results are calculated with Harris parameters of $J_0 = 6 \hbar^2 (\text{MeV})^{-1}$ and $J_1 = 30 \hbar^4 (\text{MeV})^{-3}$ and $K = 0$.

Odd-odd Au nuclei	Theoretical alignment (\hbar)			Experimental alignment (\hbar)		
	$i_x(\text{eFBC})$	$i_x(\text{eFAC})$	$i_x(\text{eFAB})$	$i_x(20^+)$	$i_x(21^+)$	$i_x(22^+)$
^{186}Au	19.3	19.9	20.8	19.6		
^{188}Au	19.7	20.0	21.0	19.4	20.2	
^{190}Au	19.7	20.0	20.8	19.4	19.8	20.6
^{192}Au	19.1	20.0	21.0	19.8		
^{194}Au	19.0	19.6	21.1			

4.1.1.4 The $11/2^-$ band of the odd-even $^{187-193}\text{Au}$ nuclei

The alignments of the $11/2^-$ band in each odd-even $^{187-193}\text{Au}$ are shown in Table 4.4. A band crossing takes place in each odd-even $^{187-193}\text{Au}$ nuclei around a spin of $27/2^-$ (see the level schemes in Appendix A). For the $31/2^-$ band, the band crossing in $^{187,189,191,193}\text{Au}$ occurs at a rotational frequency of about 0.245 MeV, 0.230 MeV, 0.220 MeV, 0.201 MeV (see Figures 4.19, 4.22, 4.25, 4.28) with alignment gain of about 10.5 \hbar , 10.6 \hbar , 11.3 \hbar , 11.4 \hbar respectively (see Figures 4.21, 4.24, 4.27, 4.30). For the $35/2^-$ band the band crossings in $^{187,189,191}\text{Au}$ occur around 0.278 MeV, 0.250 MeV, 0.225 MeV (see Figures 4.19, 4.22, 4.25) with alignment gain of 10.2 \hbar , 10.4 \hbar , 9.8 \hbar (see Figures 4.21, 4.24, 4.27) respectively. The crossing frequency between the $11/2^-$ and $31/2^-$ band predicted by CSM calculations is smaller than the experimentally measured ones (see Table 4.4), but a good agreement is obtained in the corresponding theoretical and experimental gain in alignments (see Tables 4.5). Both the theory and experiment show a decrease in the band crossing frequencies of the $11/2^-$ band with an increase in the nuclear mass in each odd-even $^{187-193}\text{Au}$ nuclei (see Figure 4.1). This is similar to the band crossing frequencies and alignments between $11/2^-$ and $35/2^-$ bands. Similar band crossing frequencies of 0.250 MeV, 0.217 MeV, 0.210 MeV and alignments of 11 \hbar , 11.9 \hbar , 11.9 \hbar have been found for the AB crossing in the neighboring $^{188,190,192}\text{Hg}$ isotopes respectively [Hüb86].

Table 4.4: Comparison between the theoretical and experimental alignment and band crossing frequency for the $11/2^-$ band of the odd-even $^{187-193}\text{Au}$ nuclei. The experimental results are calculated with Harris parameters of $J_0 = 6 \hbar^2 (\text{MeV})^{-1}$ and $J_1 = 30 \hbar^4 (\text{MeV})^{-3}$ and $K = 0$.

Odd-even Au nuclei	Band alignment (\hbar)		Band crossing frequency (MeV)			
	theoretical	experimental	theoretical		experimental	
	$i_x(e)$	$i_x(11/2^-)$	$\hbar\omega_{AB}(e)$	$\hbar\omega_{BC}(e)$	$11/2^-$ and $31/2^-$ band	$11/2^-$ and $35/2^-$ band
^{187}Au	5.3	5.7	0.236	0.255	0.245	0.278
^{189}Au	5.3	5.4	0.205	0.235	0.230	0.250
^{191}Au	5.3	5.4	0.182	0.213	0.220	0.225
^{193}Au	5.3	5.5	0.157	0.194	0.201	

Table 4.5: Comparison between the theoretical and experimental gains in alignment for the $11/2^-$ band of the odd-even $^{187-193}\text{Au}$ nuclei.

Odd-even Au nuclei	Theoretical alignment gain (\hbar)		Experimental alignment gain (\hbar)	
	i_{AB} (e)	i_{BC} (e)	$11/2^-$ and $31/2^-$ band	$11/2^-$ and $35/2^-$ band
^{187}Au	10.9	9.3	10.5	10.2
^{189}Au	11.1	9.3	10.6	10.4
^{191}Au	11.2	9.2	11.3	9.8
^{193}Au	11.2	9.2	11.4	

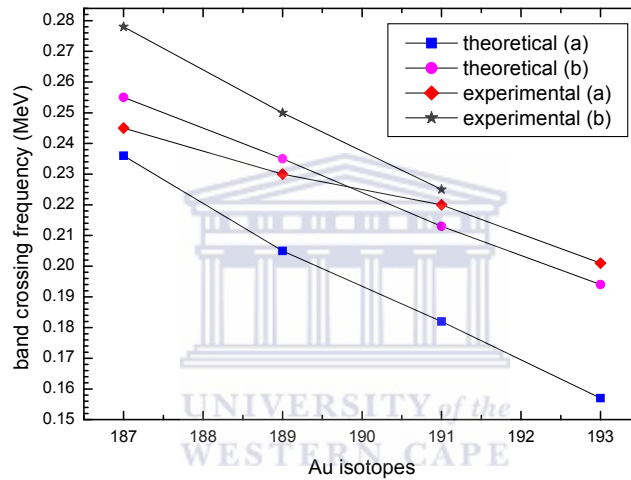


Figure 4.1: Comparison of the band crossing frequencies for the $11/2^-$ band with $31/2^-$ (a) and $35/2^-$ (b) bands of the odd-even $^{187-193}\text{Au}$ nuclei.

4.1.1.5 The $31/2^-$, $33/2^-$ and $35/2^-$ bands of the odd-even $^{187-193}\text{Au}$ nuclei

Large triaxiality predicted by TRS in these bands shows that the positive parity A, B and C Routhian lie close to each other in energy, thus three sets of rotation aligned bands are expected (i.e. eAB, eAC, eBC) and this is in good agreement with the experimental observation (see the level scheme of $^{187,189,191}\text{Au}$ in Appendix A.6-9).

An alignment of another pair of $\nu i_{13/2}$ particles takes place around the levels of $47/2^-$ in the $31/2^-$ band in ^{191}Au (see level scheme of ^{191}Au in Appendix A.9) at a band crossing frequency of 0.333 MeV (see Figure 4.25), while in the other Au isotopes no band crossing is observed, probably because the $31/2^-$ band is not yet extended to very high spins. In ^{191}Au this band crossing corresponds to a gain in the alignment of about

7.7 \hbar (see Figure 4.27). This band crossing frequency observed in the $31/2^-$ band is similar to the band crossing frequency of 0.352 MeV and 0.362 MeV observed for the $\nu i_{13/2}^2$ bands of $^{190,192}\text{Hg}$ [Hüb86]. Alignment gain of 7.7 \hbar for the $31/2^-$ band of ^{191}Au is also similar to the one of ~ 6.8 \hbar , 6.7 \hbar and 6.4 \hbar observed for the $\nu i_{13/2}^2$ bands of $^{190,192,194}\text{Hg}$ [Hüb86].

Good agreement was found between the theoretical and experimental alignments for these bands in $^{187,189,191,193}\text{Au}$ (see Table 4.6).

Table 4.6: Comparison between theoretical and experimental alignments for the $31/2^-$, $33/2^-$ and $35/2^-$ bands of the odd-even $^{187-193}\text{Au}$ nuclei. The experimental results are calculated with Harris parameters of $J_0 = 6 \hbar^2 (\text{MeV})^{-1}$ and $J_1 = 30 \hbar^4 (\text{MeV})^{-3}$ and $K = 0$.

Odd-even Au nuclei	Band alignment (\hbar)					
	theoretical			experimental		
	$i_x(\text{eAB})$	$i_x(\text{eAC})$	$i_x(\text{eBC})$	$i_x(31/2^-)$	$i_x(33/2^-)$	$i_x(35/2^-)$
^{187}Au	16.2	15.4	14.6	16.2	16.1	15.9
^{189}Au	16.4	15.7	14.6	16.0	16.2	15.8
^{191}Au	16.5	15.5	14.5	16.7	16.2	15.2
^{193}Au	16.5	15.4	14.5	16.9		

4.1.1.6 The $31/2^+$ and $33/2^+$ bands of the odd-even $^{187-193}\text{Au}$ nuclei

TRS predict large triaxiality in these bands and for this triaxiality CSM shows that the F Routhian is pushed down in energy and starts to compete with positive parity A, B and C Routhians, thus three sets of rotation aligned bands are expected (i.e. eAF, eBF, eCF), but experimentally two bands have been observed (see level scheme of $^{187,189,191,193}\text{Au}$ in Appendix A.6-10). Good agreement was obtained between the theoretical and experimental alignment in these bands of odd-even $^{187-193}\text{Au}$ nuclei (see Table 4.7).

Around spins of $39/2^+ - 43/2^+$ in the $31/2^+$ bands of $^{187,189,191}\text{Au}$ an alignment of a pair of $\nu i_{13/2}$ particles takes place (see level schemes of odd-even Au isotopes in Appendix A). These correspond to a gain in the alignment of 7.3 \hbar , 7.4 \hbar and 7.8 \hbar in the $31/2^+$ bands of $^{187,189,191}\text{Au}$ respectively (see Figures 4.21, 4.24, 4.27), and occur at band

crossing frequencies of 0.286 MeV, 0.275 MeV and 0.276 MeV (see Figures 4.19, 4.22, 4.25).

Table 4.7: *The alignment, band crossing frequency and alignment gain for the $31/2^+$ and $33/2^+$ bands of the odd-even $^{187-193}\text{Au}$ nuclei predicted by CSM calculations. The experimental results are calculated with Harris parameters of $J_0 = 6 \hbar^2 (\text{MeV})^{-1}$ and $J_1 = 30 \hbar^4 (\text{MeV})^{-3}$ and $K = 0$.*

Odd-even Au nuclei	Band alignment (\hbar)				Band crossing frequency (MeV)	Gain in alignment (\hbar)
	theoretical		experimental		experimental	experimental
	$i_x(\text{eBF})$	$i_x(\text{eAF})$	$i_x(31/2^+)$	$i_x(33/2^+)$	$\hbar\omega (31/2^+)$	$\Delta i (31/2^+)$
^{187}Au	14.8	15.8	15.1		0.286	7.3
^{189}Au	14.9	15.8	14.9	16.0	0.275	7.4
^{191}Au	14.9	15.7	14.8	15.7	0.275	7.8
^{193}Au	14.8	15.6	15.4			

4.2 Routhians and signature splitting

In the rotational frequencies region of $0.25 \text{ MeV} < \hbar\omega < 0.35 \text{ MeV}$, $0.30 \text{ MeV} < \hbar\omega < 0.42 \text{ MeV}$, $0.30 \text{ MeV} < \hbar\omega < 0.450 \text{ MeV}$, $0.23 \text{ MeV} < \hbar\omega < 0.40 \text{ MeV}$, $0.18 \text{ MeV} < \hbar\omega < 0.36 \text{ MeV}$ the theory predicts very well the relative position of the Routhians of the 11^- , 12^- and 20^+ bands in $^{186,188,190,192,194}\text{Au}$, but fails to predict that of the 22^+ band in ^{190}Au (see Figures 4.4 and 4.5, 4.7 and 4.8, 4.10 and 4.11, 4.13 and 4.14, 4.18 and 4.19), while at low rotational frequencies this Routhian is predicted to lie above the Routhians of the 20^+ band, at higher rotational frequencies the theory predicts that it becomes lower with respect to this Routhian which is not observed experimentally. The calculated signature splitting between the 20^+ , 21^+ , and 22^+ bands of ^{190}Au in Table 4.10 also confirms this situation. The magnitude of the experimental signature splitting between the Routhians of the 20^+ and 21^+ bands of ^{188}Au is also slightly different from the theoretical one (see Table 4.10).

Both the theory and experiment show signature inversion at low rotational frequency in the quasiparticle Routhians of the 11^- and 12^- bands of each odd-odd $^{186-194}\text{Au}$ nuclei (see Figures 4.4, 4.7, 4.10, 4.13, 4.18). At higher rotational frequency the

normal order of the Routhians is recovered. Signature inversion frequencies at which the two Routhians cross each other and restore their normal positions were determined and also listed in Table 4.8. The values of the theoretical signature inversion frequencies are generally in good agreement with the experimentally measured ones, except in ^{194}Au where a larger difference was found. Both theory and experiment show a decrease in signature inversion frequency with an increase in the nuclear mass (see Figure 4.2). In the 11^- and 12^- bands of the odd-odd $^{186-194}\text{Au}$ nuclei, both the theory and experiment show a small signature splitting between these bands. These values of signature splitting decrease with an increase in the nuclear mass (see Table 4.9)

Table 4.8: Comparison of the theoretical and experimental signature inversion frequency for the 11^- and 12^- of the odd-odd $^{186-194}\text{Au}$ nuclei. The experimental results are calculated with Harris parameters of $J_0 = 6 \hbar^2 (\text{MeV})^{-1}$ and $J_1 = 30 \hbar^4 (\text{MeV})^{-3}$ and $K = 0$.

Odd-odd Au nuclei	Signature inversion frequency (MeV)	
	theoretical	experimental
^{186}Au	0.367	0.360
^{188}Au	0.333	0.362
^{190}Au	0.276	0.313
^{192}Au	0.240	0.250
^{194}Au	0.097	0.180

Table 4.9: Comparison of the theoretical and experimental signature splitting for the 11^- and 12^- of the odd-odd $^{186-194}\text{Au}$ nuclei. The experimental results are calculated with Harris parameters of $J_0 = 6 \hbar^2 (\text{MeV})^{-1}$ and $J_1 = 30 \hbar^4 (\text{MeV})^{-3}$ and $K = 0$.

Odd-odd Au nuclei	Signature splitting at 0.3 MeV (MeV)	
	theoretical	experimental
	$e'(eA - eB)$	$e'(12^- - 11^-)$
^{186}Au	0.045	0.056
^{188}Au	0.022	0.049
^{190}Au	-0.032	0.012
^{192}Au	-0.049	-0.042
^{194}Au	-0.180	-0.140

Table 4.10: Comparison between theoretical and experimental signature splitting for the 20^+ , 21^+ and 22^+ bands of the odd-odd $^{188-190}\text{Au}$ nuclei. The experimental results are calculated with Harris parameters of $J_0 = 6 \hbar^2(\text{MeV})^{-1}$ and $J_1 = 30 \hbar^4(\text{MeV})^{-3}$ and $K = 0$.

		Signature splitting (MeV)					
Odd-odd Au nuclei	$\hbar\omega$ (MeV)	theoretical			experimental		
		$e'(e\text{FBC})-e'(e\text{FAC})$	$e'(e\text{FAB})-e'(e\text{FBC})$	$e'(e\text{FAB})-e'(e\text{FAC})$	$e'(20^+)-e'(21^+)$	$e'(22^+)-e'(20^+)$	$e'(22^+)-e'(21^+)$
^{188}Au	0.267	-0.3000			-0.1870		
^{190}Au	0.338	-0.2700	-0.1780	-0.4400	-0.2100	0.2511	0.0411

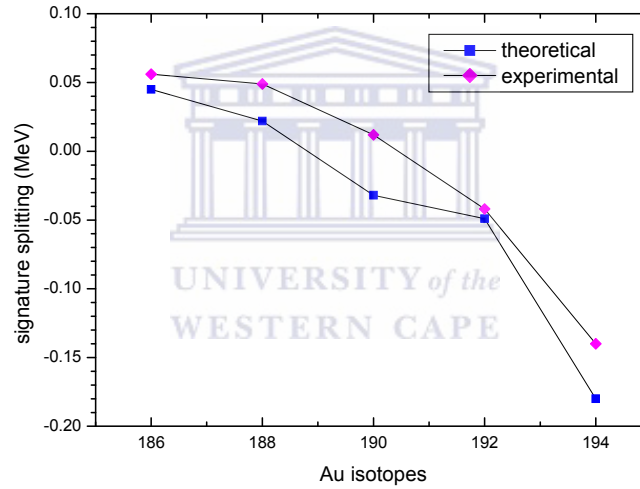


Figure 4.2: Comparison of theoretical and experimental signature splitting for the 11^- and 12^- bands of the odd-odd $^{186-194}\text{Au}$ nuclei.

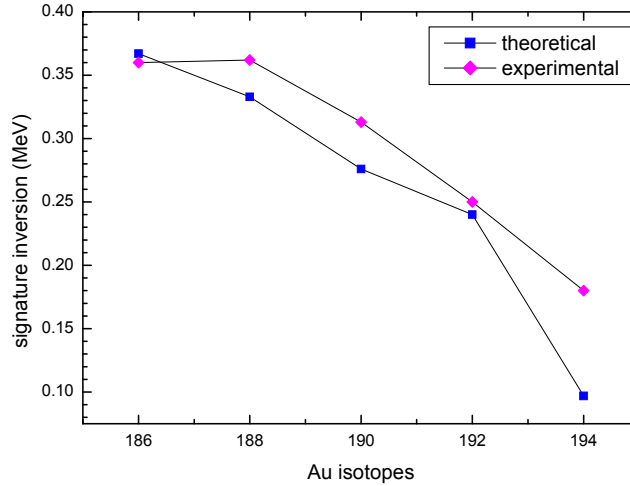


Figure 4.3: Comparison of theoretical and experimental signature inversion frequencies for the 11^- and 12^- bands of the odd-odd $^{186-194}\text{Au}$ nuclei.

In the rotational frequency region of $0.30 \text{ MeV} < \hbar\omega < 0.39 \text{ MeV}$, $0.25 \text{ MeV} < \hbar\omega < 0.40 \text{ MeV}$, $0.30 \text{ MeV} < \hbar\omega < 0.40 \text{ MeV}$, $0.20 \text{ MeV} < \hbar\omega < 0.37 \text{ MeV}$, the theory predicts very well the relative position of the Routhians of the $11/2^-$, $31/2^-$, $33/2^-$, $35/2^-$ and $31/2^+$ bands in $^{187,189,191,193}\text{Au}$, (see Figures 4.19 and 4.20, 4.22 and 4.23, 4.25 and 4.26, 4.28 and 4.29).

The experimental and theoretical signature splitting between the Routhians of the $31/2^-$ with $33/2^-$ and $31/2^-$ with $35/2^-$ bands in the $^{187,189,191}\text{Au}$ nuclei show large difference, whereas a good agreement was found between the Routhians of $33/2^-$ and $35/2^-$ bands of $^{187,189,191}\text{Au}$ (see Table 4.11). It should be noted that the Routhian of the $35/2^-$ band lies at higher energy in $^{187,189,191}\text{Au}$ (see Figures 4.19, 4.22, 4.25). This might be due to large interaction between the Routhians of $31/2^-$ and $35/2^-$ bands.

Signature inversion is observed for the $31/2^+$ and $33/2^+$ quasiparticle Routhians of $^{189,191}\text{Au}$ (see Figures 4.22, 4.25). These two bands do not restore their normal position before a band crossing. Generally, a good agreement is obtained for the theoretical and experimental signature splitting between the Routhians of the $31/2^+$ and $33/2^+$ bands in ^{189}Au , whereas a small difference is obtained in ^{191}Au (see Table 4.12).

The theory predicts well the order of the Routhians of the 11^- , 12^- , 20^+ , 21^+ , $11/2^-$, $31/2^-$, $33/2^-$, $35/2^-$ and $31/2^+$ bands in the $^{186-194}\text{Au}$ nuclei respectively, except that of the 20^+ and 21^+ bands in the rotational frequencies region of $0.185 \text{ MeV} < \hbar\omega < 0.300 \text{ MeV}$ and $0.350 \text{ MeV} < \hbar\omega < 0.430 \text{ MeV}$ respectively and the relative position

of the Routhians of the $11/2^-$ band in the ^{187}Au nucleus. Both the theory and experiment show a decrease in the Routhians of these bands when the mass of the $^{186-194}\text{Au}$ nuclei increases except in the experimental Routhians of the $11/2^-$ band of the ^{187}Au nucleus (see Figure 4.31-4.48).

Table 4.11: Comparison between the theoretical and experimental signature splitting for the $31/2^-$, $33/2^-$ and $35/2^-$ bands of the odd-even $^{187-191}\text{Au}$ nuclei. The experimental results are calculated with Harris parameters of $J_0 = 6 \hbar^2 (\text{MeV})^{-1}$ and $J_1 = 30 \hbar^4 (\text{MeV})^{-3}$ and $K = 0$.

Odd-even Au nuclei	Rotational frequency (MeV)	Signature splitting (MeV)					
		theoretical			experimental		
		$e'(eAB)-e'(eAC)$	$e'(eAB)-e'(eBC)$	$e'(eAC)-e'(eBC)$	$e'(31/2^-)-e'(33/2^-)$	$e'(31/2^-)-e'(35/2^-)$	$e'(33/2^-)-e'(35/2^-)$
^{187}Au	0.320	-0.1700	-0.3700	-0.1100	-0.0800	-0.1900	-0.1400
^{189}Au	0.340	-0.5000	-0.6000	-0.1000	-0.1800	-0.2600	-0.0800
^{191}Au	0.238	-0.3100	-0.4000	-0.0900			-0.1400
	0.300	-0.3703	-0.5114	-0.1411	-0.1100		

Table 4.12: Comparison between the theoretical and experimental signature splitting for the $31/2^+$ and $33/2^+$ bands of the odd-even $^{189-191}\text{Au}$ nuclei. The experimental results are calculated with Harris parameters of $J_0 = 6 \hbar^2 (\text{MeV})^{-1}$ and $J_1 = 30 \hbar^4 (\text{MeV})^{-3}$ and $K = 0$.

Odd-even Au nuclei	Signature splitting at 0.40 MeV (MeV)	
	theoretical	experimental
	$e'(eAF)-e'(eBF)$	$e'(33/2^+)-e'(31/2^+)$
^{187}Au	0.1250	
^{189}Au	0.1380	0.1200
^{191}Au	0.1380	0.0960
^{193}Au	0.2100	

Another method for calculating signature splitting is as follows. Signature splitting depends on the nuclear deformation, pairing gap and shell filling. This makes it difficult to calculate it with accuracy comparable to that determined experimentally. Mueller *et al.*, [Mue94] used another approach of calculating signature splitting of the

high-j $\nu j_{13/2}$ orbital at high spins in several nuclei with $A \sim 160$, using different deformation parameters and pairing gaps at high spins as suggested by [Ham83]. In their approach the total signature splitting $\Delta e'$ is decomposed into two components:

$$\Delta e' = \Delta E_{def} + \Delta E_{rot} \quad (4.1)$$

where ΔE_{def} is the difference in the vacuum (or bandhead) energy resulting from a difference in the nuclear deformation between the two signature partners taken from the TRS calculations, and ΔE_{rot} is the energy difference that results from the different dependence of the signature partners of a band as a function of the rotational frequency. In their treatment for ΔE_{rot} , deformation parameters are extracted from the TRS model at rotational frequency ω_0 (at which signature splitting is calculated) for the favored and unfavored signatures of high-j configuration and used in separate cranking calculations for the blocked configuration to extract the Routhians for each signature. The quantity $\Delta E_{rot}(\omega_0)$ then is the difference between the changes in energy due to rotation at frequency ω_0 for the unfavored signature and that for the favored signature.

To obtain the energy difference of the vacua of the two states ΔE_{def} , they used the Strutinsky renormalization procedure. The difference between the vacuum energies of the favored and unfavored signatures is the energy difference resulting from different nuclear deformations.

The improvement of this new technique over the previous methods for calculating signature splitting result from the fact that

- 1) a self-consistent pairing treatment can be used with the TRS calculated deformation parameters and
- 2) different deformations and pairing for the two signatures are included.

This method was applied to rotational bands built on one $\nu i_{13/2}$ configuration in the odd-N even-Z $^{155-161}\text{Dy}$, $^{157-165}\text{Er}$, $^{161-171}\text{Yb}$, $^{167-175}\text{Hf}$, $^{171-181}\text{W}$ and $^{173-183}\text{Os}$ isotopes. This approach was successful in predicting the signature splitting at $\hbar\omega = 0.2 \text{ MeV}$

for these $\nu i_{13/2}$ rotational bands compared to that determined experimentally, with the exceptions of ^{175}W , ^{175}Os and ^{177}Os due to a slightly improper $N = 102$ gap in the single particle level energies. They found that for these isotopes the difference in energy ΔE_{def} due to difference in the nuclear deformation between the two signatures was small compared to ΔE_{rot} , except for $^{173-183}\text{Os}$ isotopes. That was because the CSM calculations predict a band crossing near or before $\hbar\omega = 0.2 \text{ MeV}$. For these $\nu i_{13/2}$ rotational bands, TRS calculations predict small triaxiality of the nucleus with gamma values of $-6^\circ < \gamma < 2^\circ$, and for these gamma values no interaction between the Routhians of $\nu i_{13/2}$ is observed, hence it was easy to extract their energies (i.e. $E_{rot}(\omega = 0)$) at $\omega = 0$ from the CSM diagram.

Our study of the $^{186-194}\text{Au}$ nuclei concentrate on rotational bands built of one $h_{11/2}$ proton and one, two, three $i_{13/2}$ and/or one $h_{9/2}$ neutron. For these rotational bands, TRS calculations predict large triaxiality of the nucleus with gamma of $\gamma \leq -75^\circ$, and for these gamma values significant interaction between the Routhians of $\nu i_{13/2}$ orbitals is observed even at lower rotational frequency close to $\omega = 0$, hence it is not easy to extract their energies (i.e. $E_{rot}(\omega = 0)$) from the CSM diagram. It is easy to extract $\Delta E_{def}(\omega = 0)$ from the TRS calculations for the one-quasiparticle configuration, whereas for excited quasiparticle bands, the TRS model no longer calculates their energies at zero rotational frequencies because they are too high. Therefore it may not be possible to get the bandhead energy $\Delta E_{def}(\omega = 0)$ corresponding to the excited quasiparticle bands. As far as I know this approach has not been applied to more complicated cases where rotational bands built on more than one $\nu i_{13/2}$ neutron are observed.

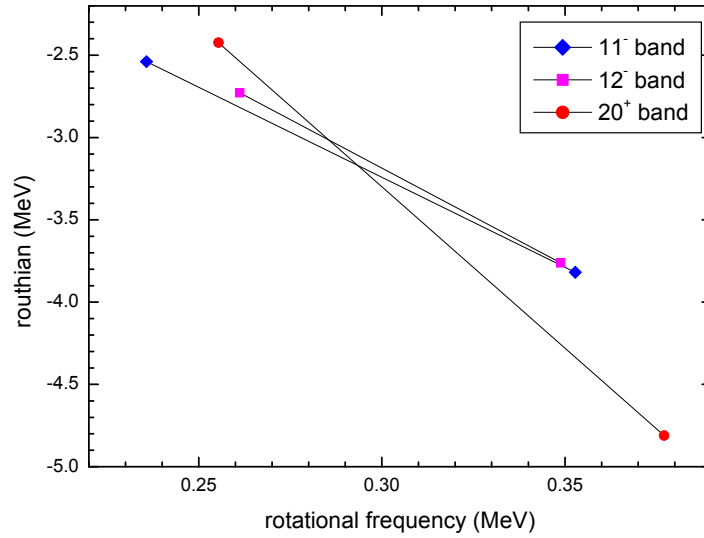


Figure 4.4: Experimental quasiparticle Routhians for the 11^- , 12^- and 20^+ bands of ^{186}Au calculated with Harris parameters of $J_0 = 6 \hbar^2 (\text{MeV})^{-1}$ and $J_1 = 30 \hbar^4 (\text{MeV})^{-3}$ and $K = 0$.

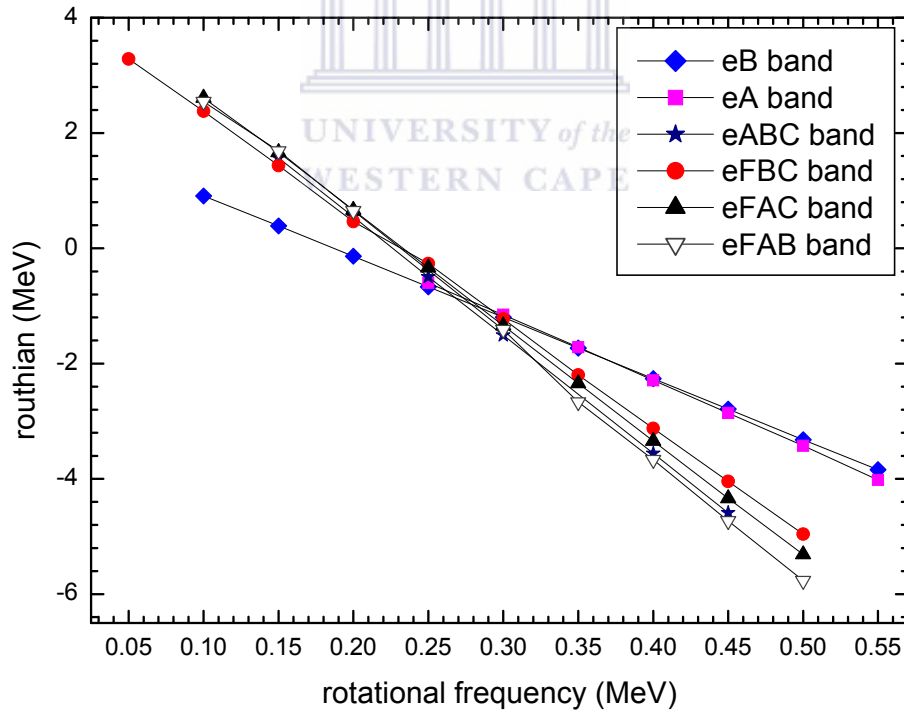


Figure 4.5: Theoretical quasiparticle Routhians for the 11^- , 12^- , 22^- , 20^+ , 21^+ , 22^+ bands of ^{186}Au .

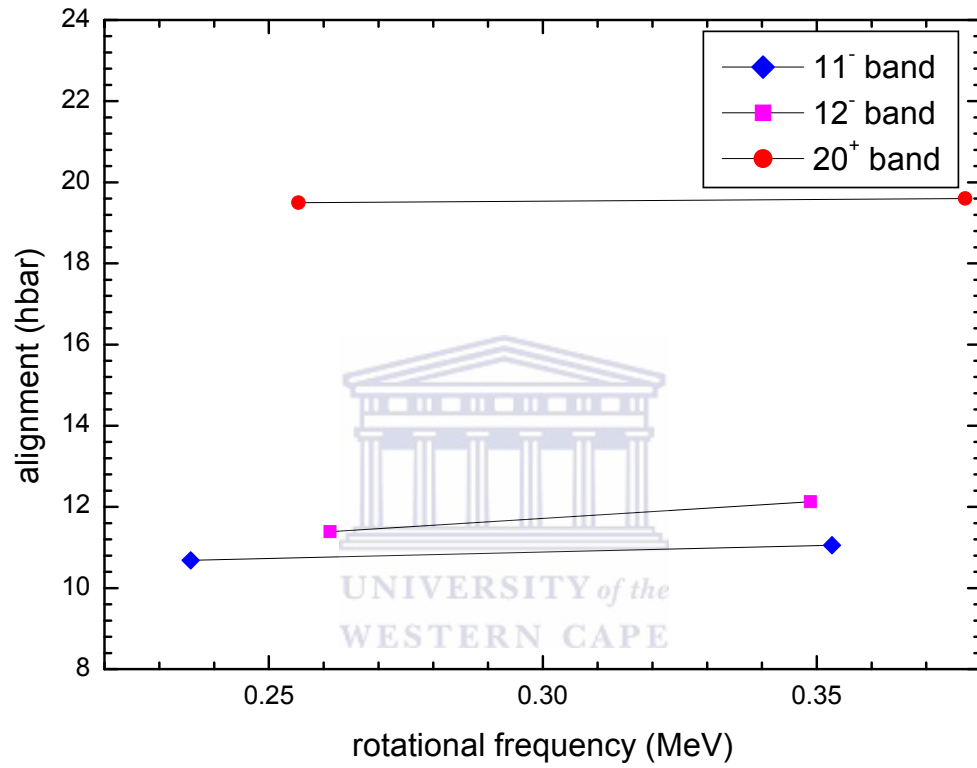


Figure 4.6: *Experimental quasiparticle alignments for the 11⁻, 12⁻ and 20⁺ bands of ¹⁸⁶Au calculated with Harris parameters of $J_0 = 6 \hbar^2 (\text{MeV})^{-1}$ and $J_1 = 30 \hbar^4 (\text{MeV})^{-3}$ and $K = 0$.*

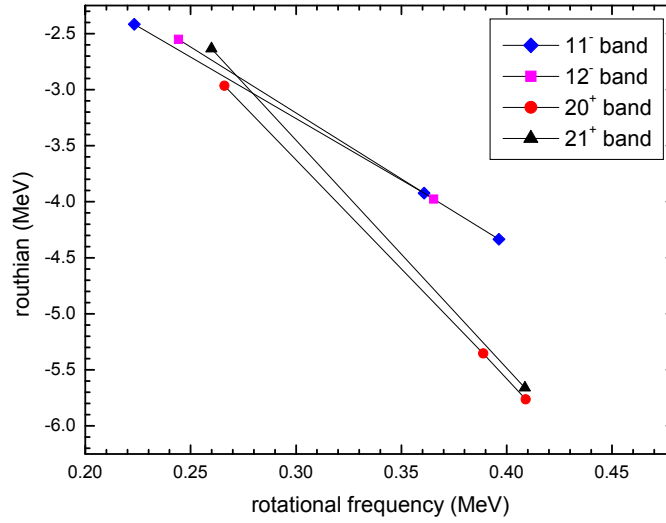


Figure 4.7: Experimental quasiparticle Routhians for the 11^- , 12^- , 20^+ and 21^+ bands of ^{188}Au calculated with Harris parameters of $J_0 = 6 \hbar^2 (\text{MeV})^{-1}$ and $J_1 = 30 \hbar^4 (\text{MeV})^{-3}$ and $K = 0$.

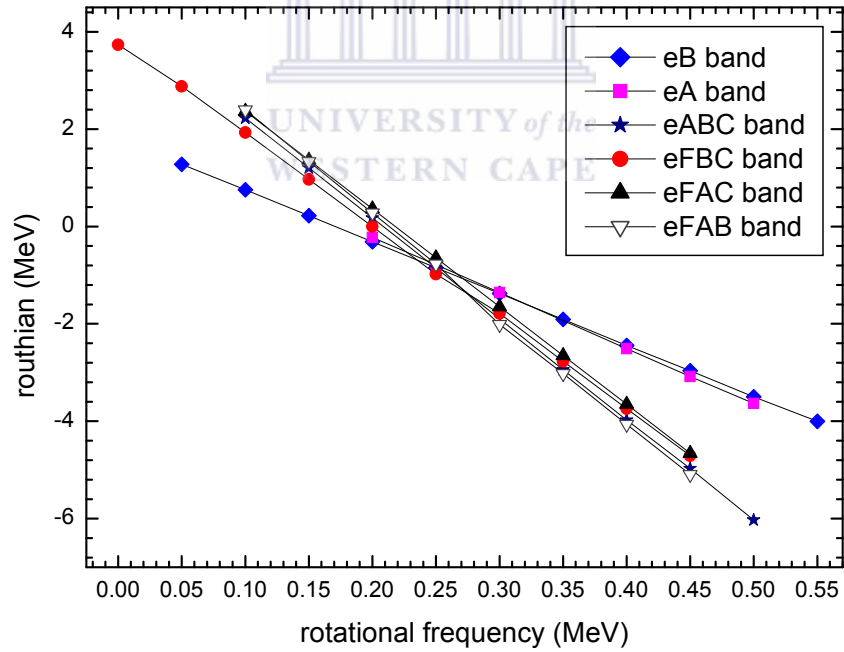


Figure 4.8: Theoretical quasiparticle Routhians for the 11^- , 12^- , 22^- , 20^+ , 21^+ , 22^+ bands of ^{188}Au .

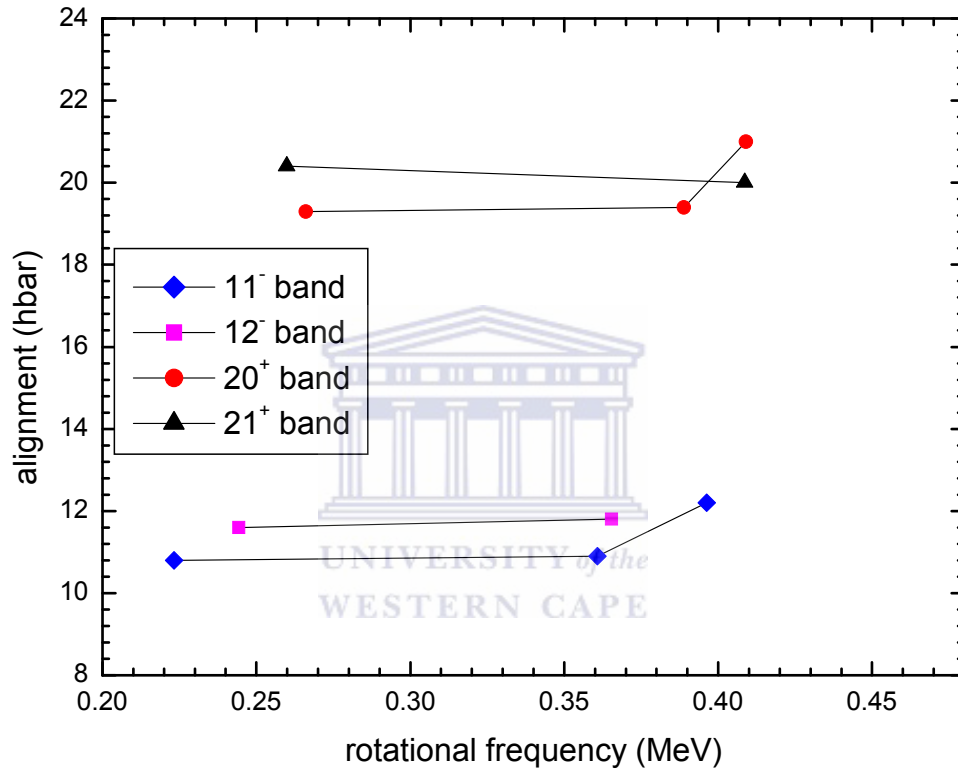


Figure 4.9: Experimental quasiparticle alignments for the 11^- , 12^- , 20^+ and 21^+ bands of ^{188}Au calculated with Harris parameters of $J_0 = 6 \hbar^2 (\text{MeV})^{-1}$ and $J_1 = 30 \hbar^4 (\text{MeV})^{-3}$ and $K = 0$.

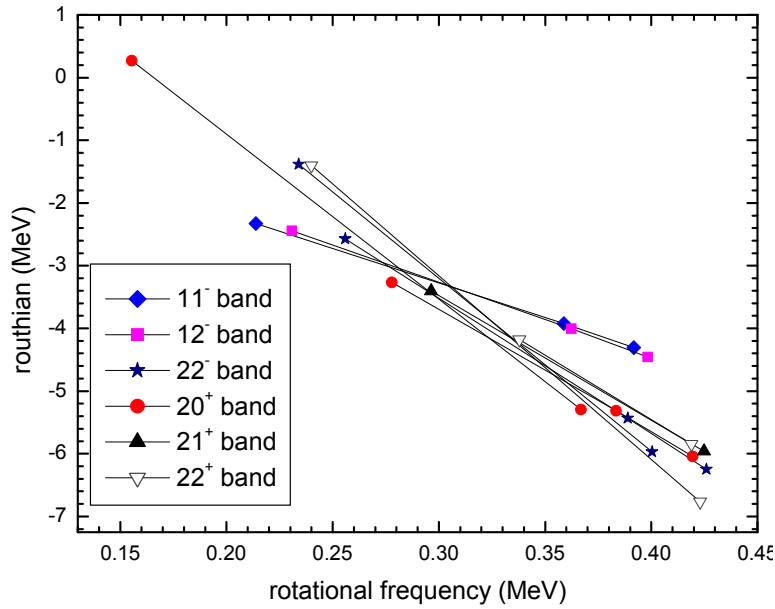


Figure 4.10: Experimental quasiparticle Routhians for the 11^- , 12^- , 22^- , 20^+ , 21^+ , 22^+ bands of ^{190}Au calculated with Harris parameters of $J_0 = 6 \hbar^2 (\text{MeV})^{-1}$ and $J_1 = 30 \hbar^4 (\text{MeV})^{-3}$ and $K = 0$.

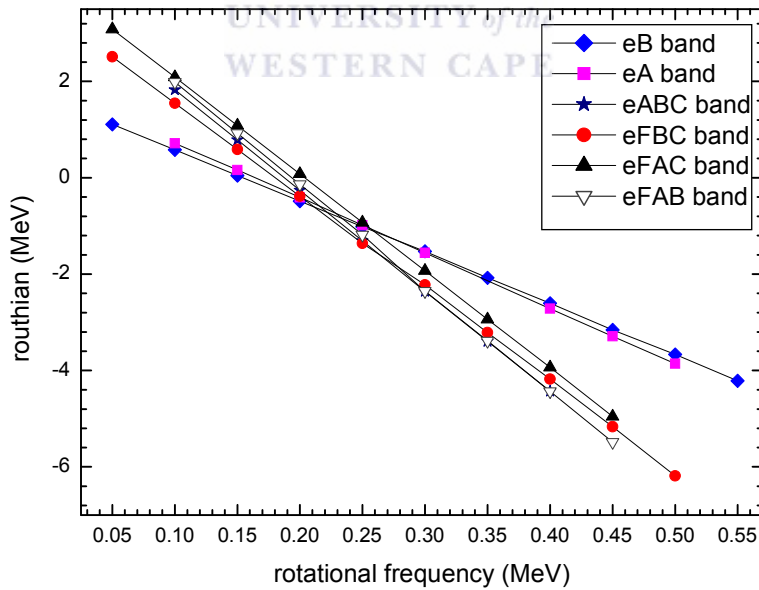


Figure 4.11: Theoretical quasiparticle Routhians for the 11^- , 12^- , 22^- , 20^+ , 21^+ , 22^+ bands of ^{190}Au .

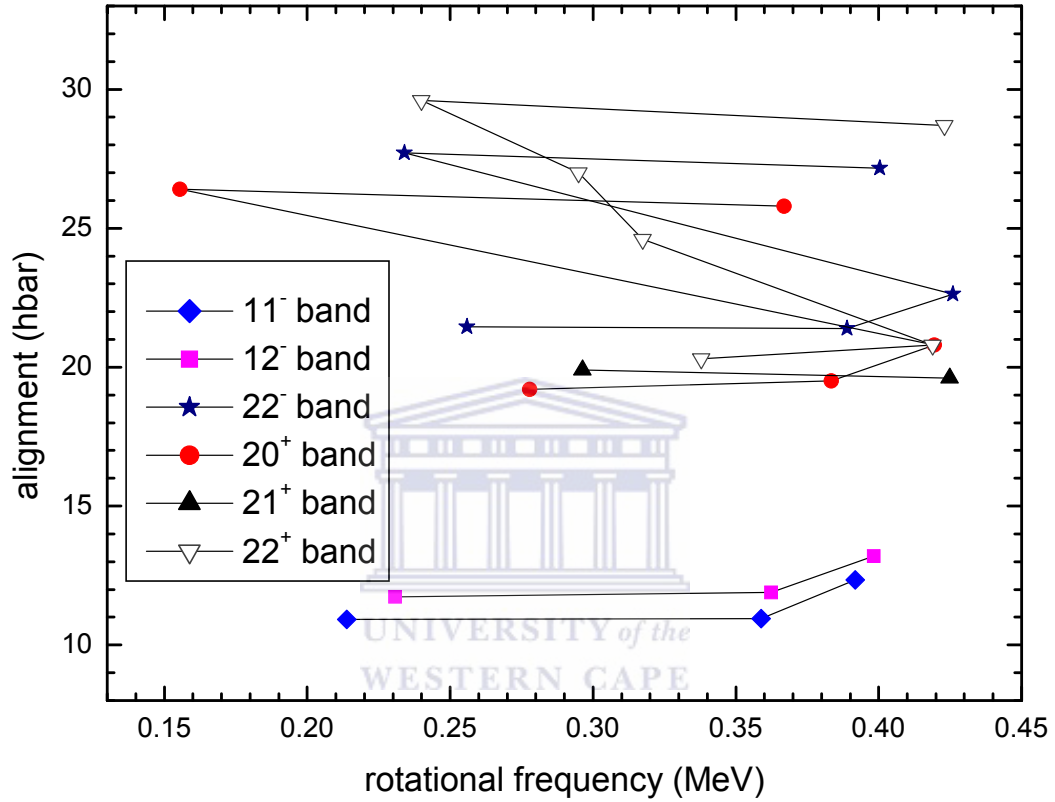


Figure 4.12: Experimental quasiparticle alignments for the 11^- , 12^- , 22^- , 20^+ , 21^+ , 22^+ bands of ^{190}Au calculated with Harris parameters of $J_0 = 6 \hbar^2 (\text{MeV})^{-1}$ and $J_1 = 30 \hbar^4 (\text{MeV})^{-3}$ and $K = 0$.

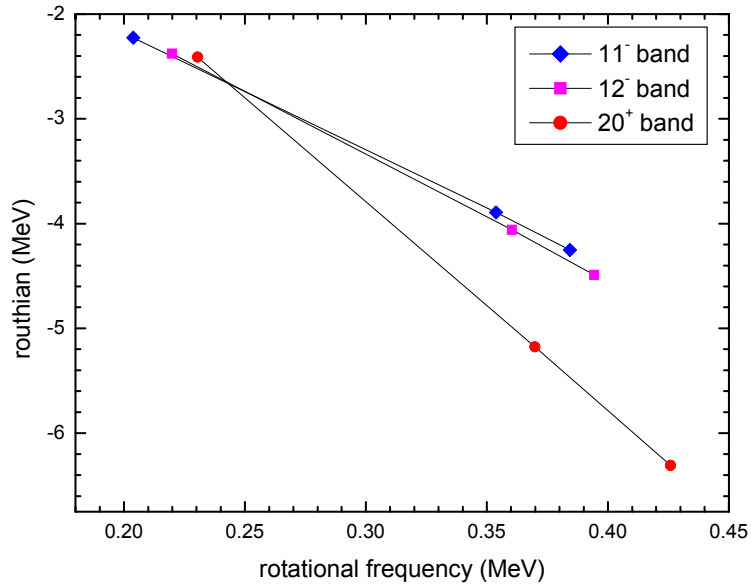


Figure 4.13: Experimental quasiparticle Routhians for the 11^- , 12^- , 20^+ bands of ^{192}Au calculated with Harris parameters of $J_0 = 6 \hbar^2 (\text{MeV})^{-1}$ and $J_1 = 30 \hbar^4 (\text{MeV})^{-3}$ and $K = 0$.

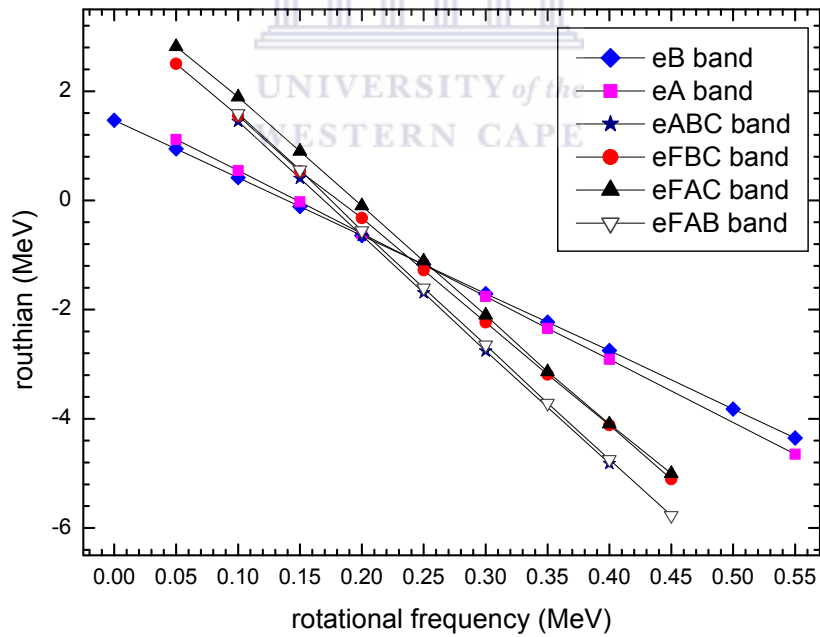


Figure 4.14: Theoretical quasiparticle Routhians for the 11^- , 12^- , 22^- , 20^+ , 21^+ , 22^+ bands of ^{192}Au .

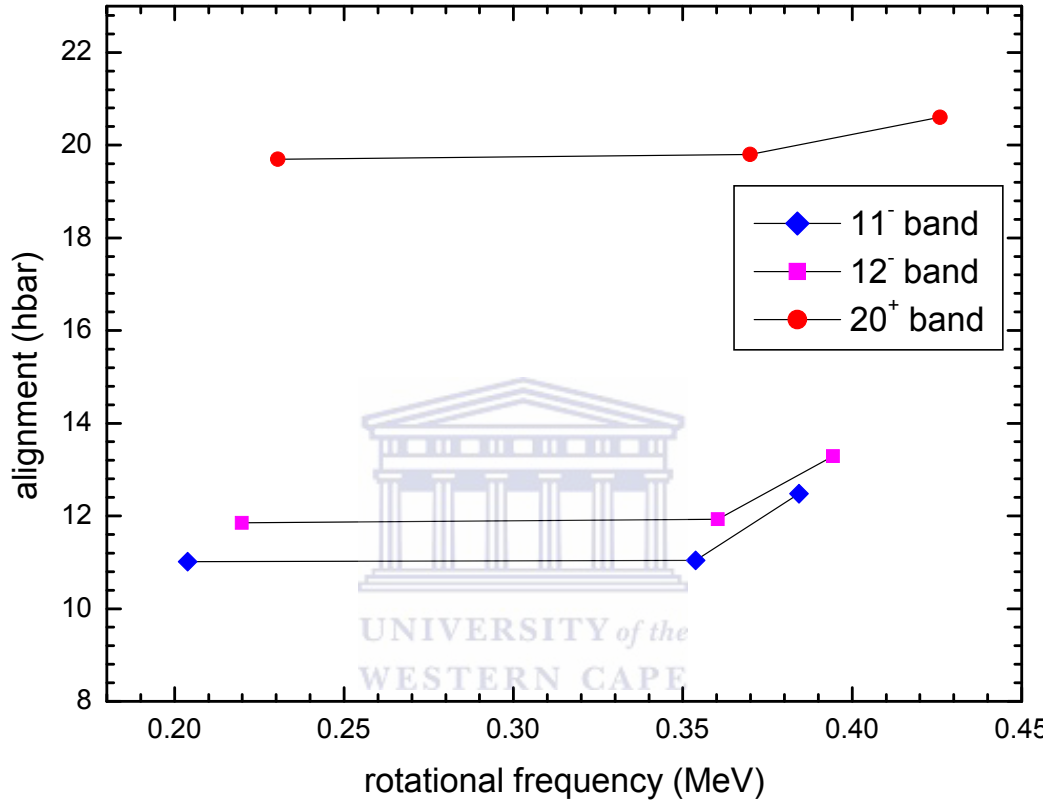


Figure 4.15: Experimental quasiparticle alignments for the 11^- , 12^- , 20^+ bands of ^{192}Au calculated with Harris parameters of $J_0 = 6 \hbar^2 (\text{MeV})^{-1}$ and $J_1 = 30 \hbar^4 (\text{MeV})^{-3}$ and $K = 0$.

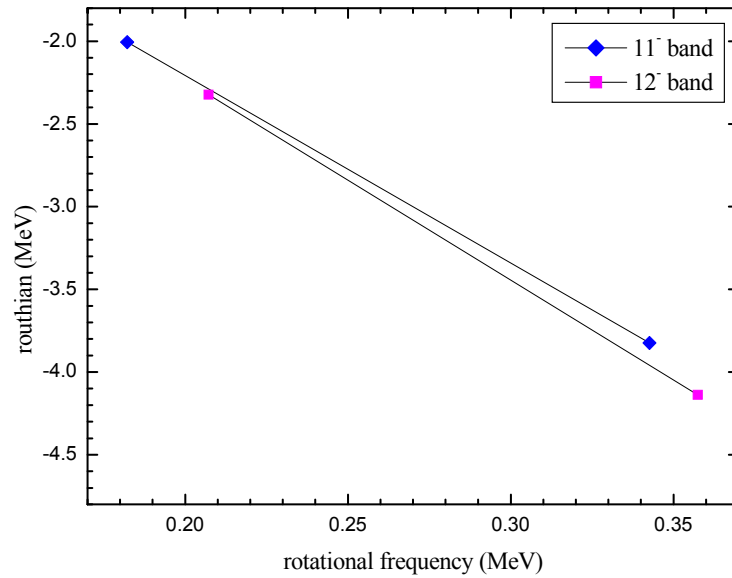


Figure 4.16: Experimental quasiparticle Routhians for the 11^- , 12^- bands of ^{194}Au calculated with Harris parameters of $J_0 = 6 \hbar^2 (\text{MeV})^{-1}$ and $J_1 = 30 \hbar^4 (\text{MeV})^{-3}$ and $K = 0$.

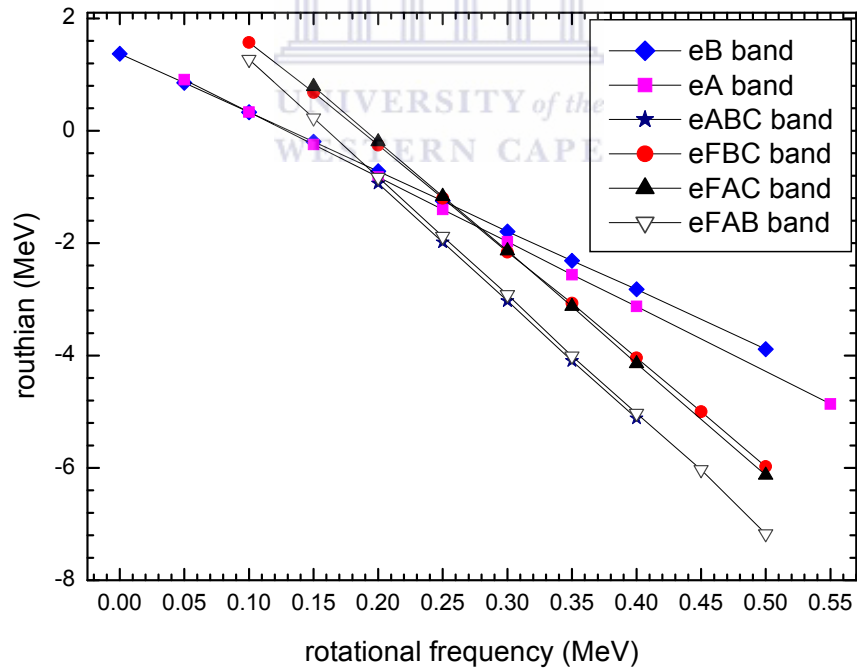


Figure 4.17: Theoretical quasiparticle Routhians for the 11^- , 12^- , 22^- , 20^+ , 21^+ , 22^+ bands of ^{194}Au .

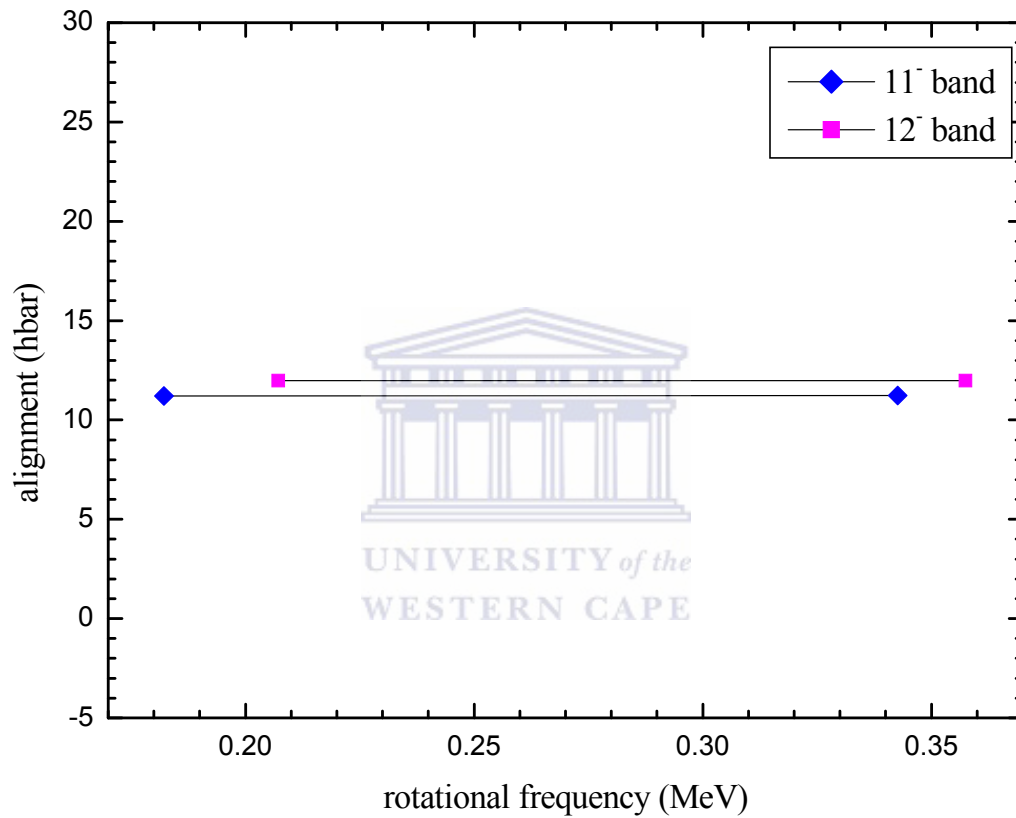


Figure 4.18: Experimental quasiparticle alignments for the 11^- , 12^- bands of ^{194}Au calculated with Harris parameters of $J_0 = 6 \hbar^2 (\text{MeV})^{-1}$ and $J_1 = 30 \hbar^4 (\text{MeV})^{-3}$ and $K = 0$.

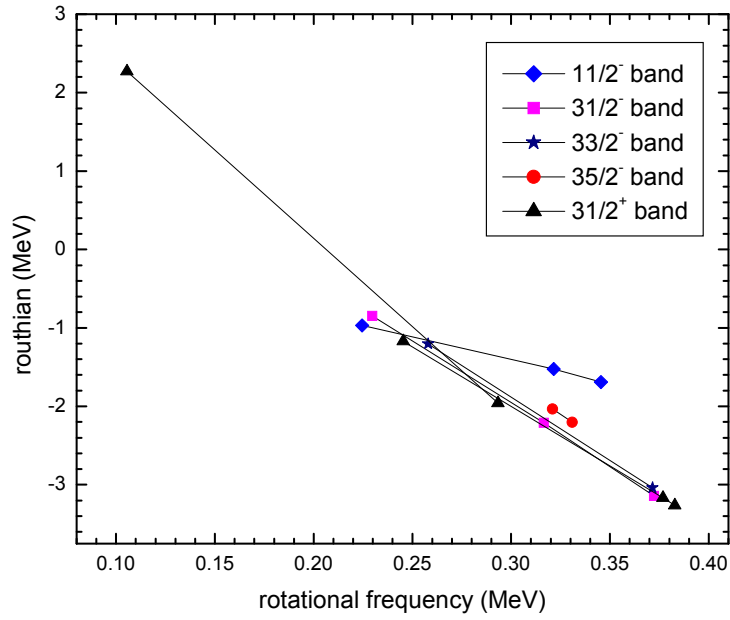


Figure 4.19: Experimental quasiparticle Routhians for the $11/2$, $31/2$, $33/2$, $35/2$, $31/2^+$ bands of ^{187}Au calculated with Harris parameters of $J_0 = 6 \hbar^2 (\text{MeV})^{-1}$ and $J_1 = 30 \hbar^4 (\text{MeV})^{-3}$ and $K = 0$.

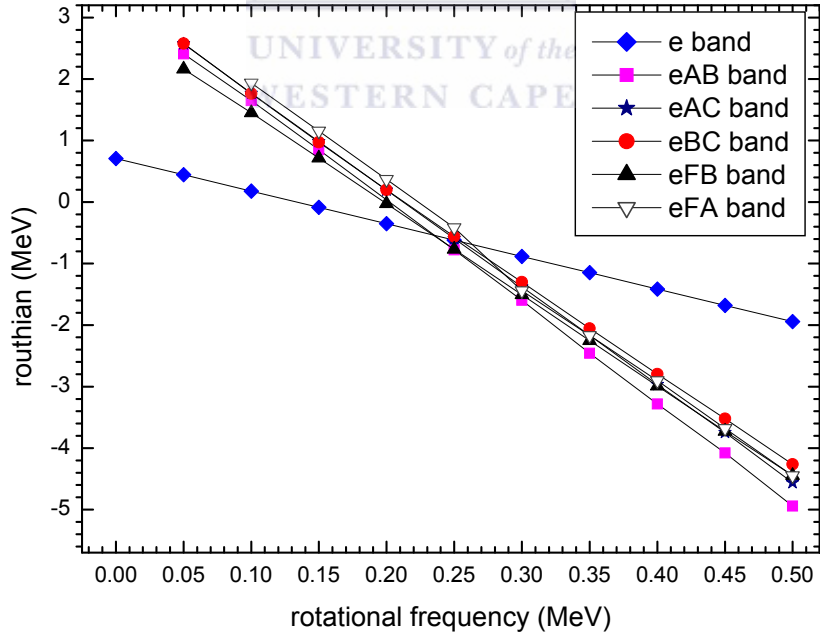


Figure 4.20: Theoretical quasiparticle Routhians for the $11/2$, $31/2$, $33/2^-$, $35/2$, $31/2^+$, $33/2^+$ bands of ^{187}Au .

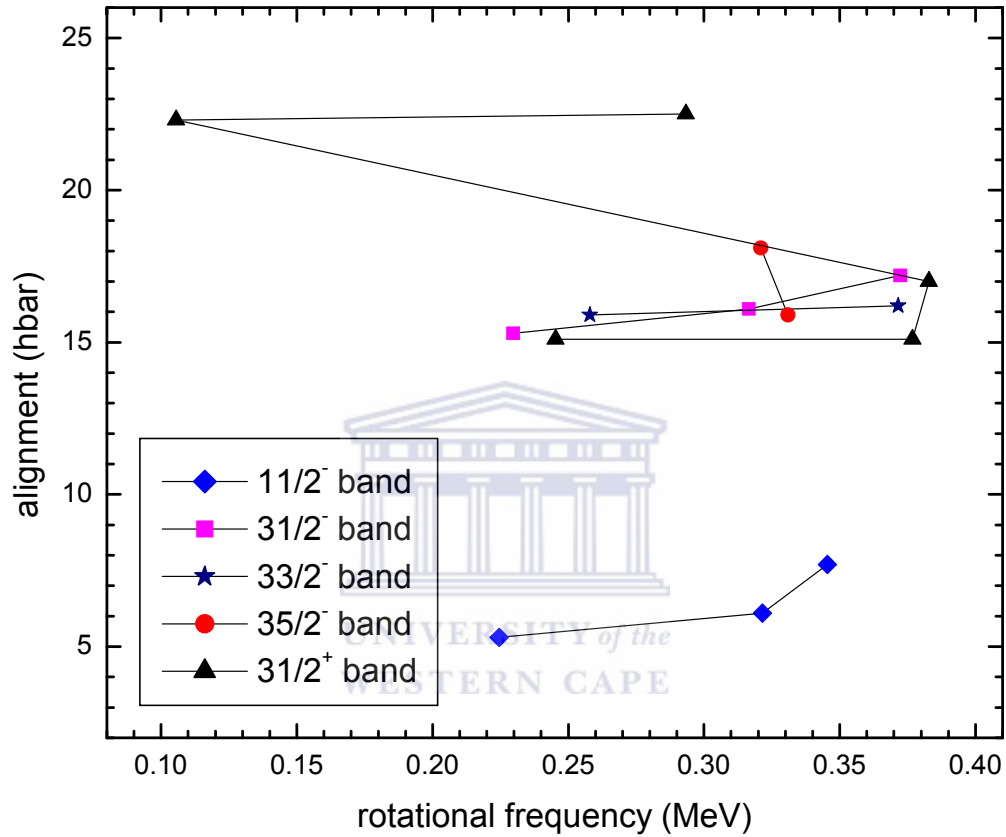


Figure 4.21: Experimental quasiparticle alignments for the $11/2^-$, $31/2^-$, $33/2^-$, $35/2^-$, $31/2^+$ bands of ^{187}Au calculated with Harris parameters of $J_0 = 6 \hbar^2 (\text{MeV})^{-1}$ and $J_1 = 30 \hbar^4 (\text{MeV})^{-3}$ and $K = 0$.

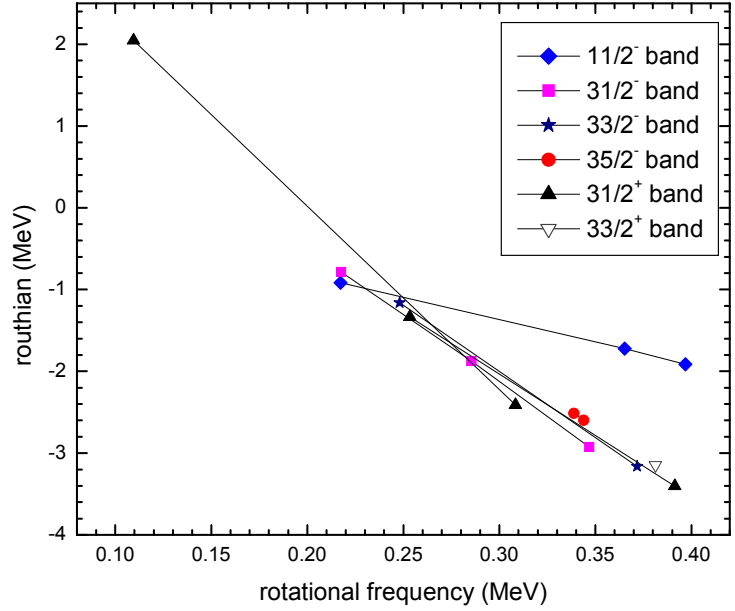


Figure 4.22: Experimental quasiparticle Routhians for the $11/2^-$, $31/2^-$, $33/2^-$, $35/2^-$, $31/2^+$, $33/2^+$ bands of ^{189}Au calculated with Harris parameters of $J_0 = 6 \hbar^2 (\text{MeV})^{-1}$ and $J_1 = 30 \hbar^4 (\text{MeV})^{-3}$ and $K = 0$.

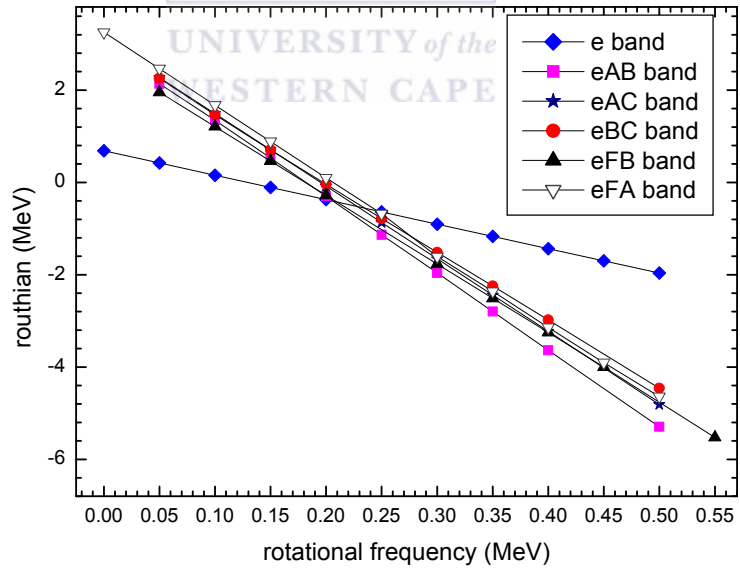


Figure 4.23: Theoretical quasiparticle Routhians for the $11/2^-$, $31/2^-$, $33/2^-$, $35/2^-$, $31/2^+$, $33/2^+$ bands of ^{189}Au .

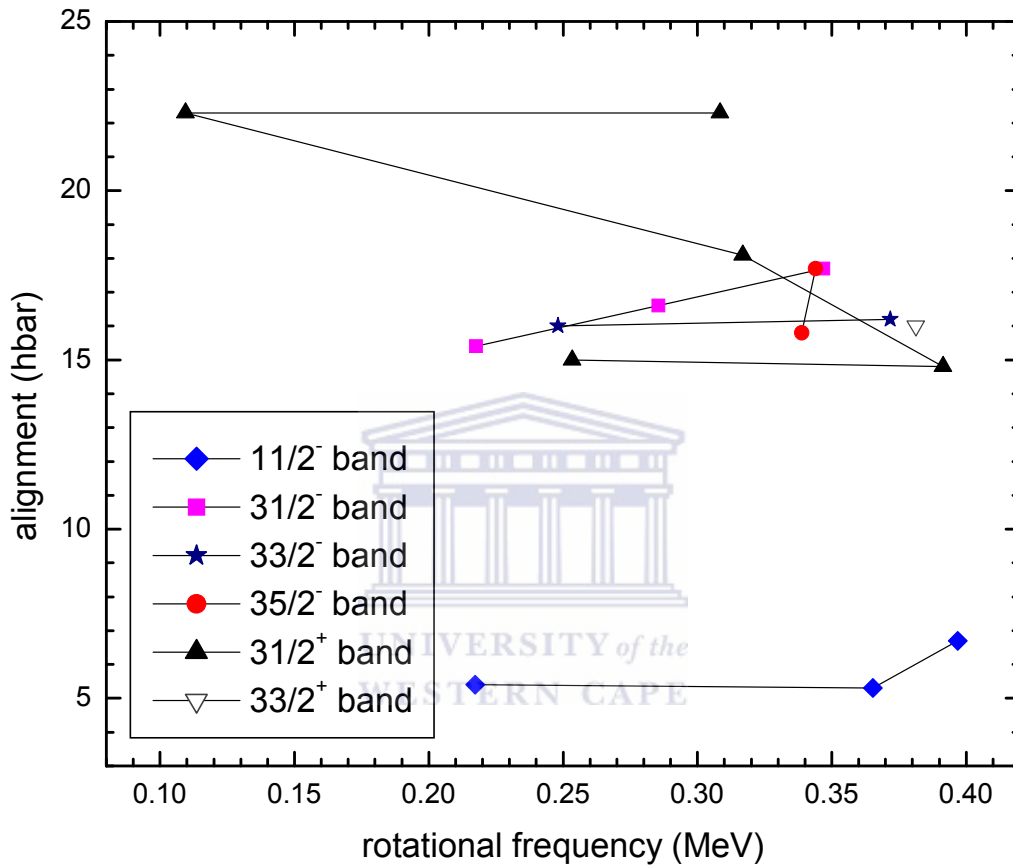


Figure 4.24: Experimental quasiparticle alignments for the $11/2^-$, $31/2^-$, $33/2^-$, $35/2^-$, $31/2^+$, $33/2^+$ bands of ^{189}Au calculated with Harris parameters of $J_0 = 6 \hbar^2 (\text{MeV})^{-1}$ and $J_1 = 30 \hbar^4 (\text{MeV})^{-3}$ and $K = 0$.

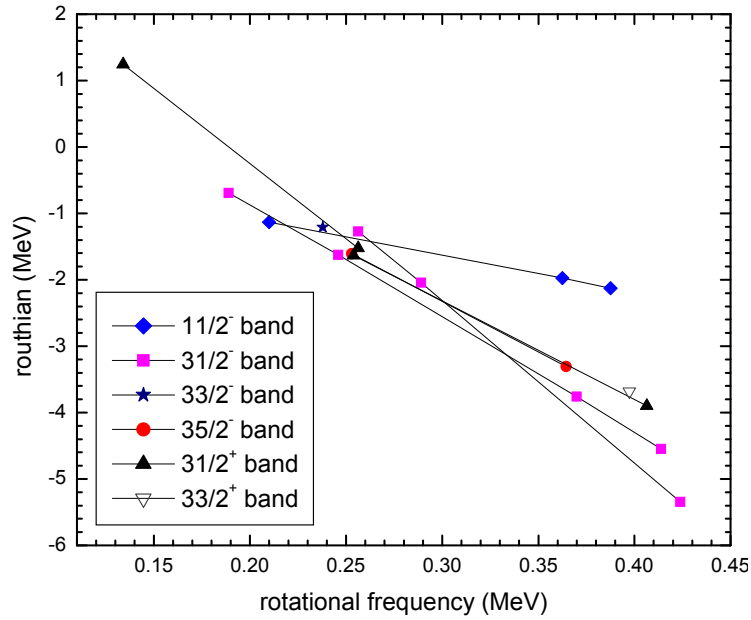


Figure 4.25: Experimental quasiparticle Routhians for the $11/2^-$, $31/2^-$, $33/2^-$, $35/2^-$, $31/2^+$, $33/2^+$ bands of ^{191}Au calculated with Harris parameters of $J_0 = 6 \hbar^2 (\text{MeV})^{-1}$ and $J_1 = 30 \hbar^4 (\text{MeV})^{-3}$ and $K = 0$.

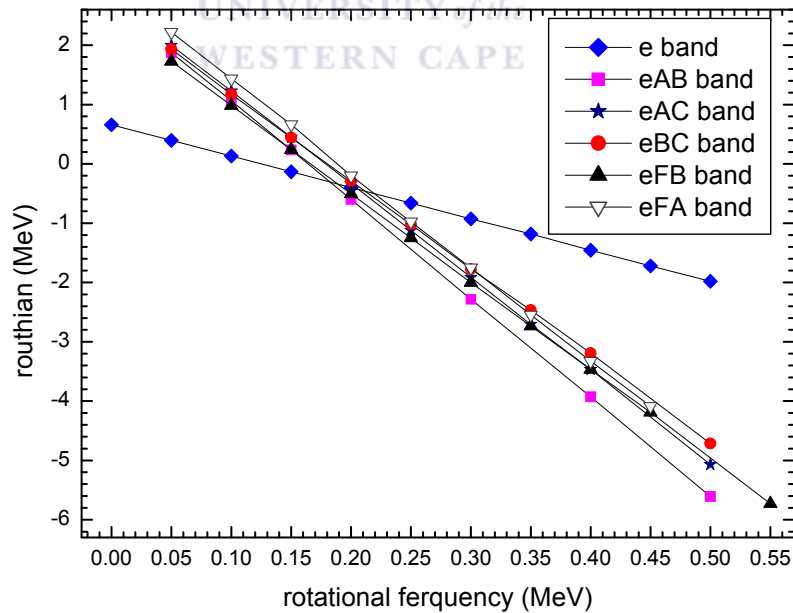


Figure 4.26: Theoretical quasiparticle Routhians for the $11/2^-$, $31/2^-$, $33/2^-$, $35/2^-$, $31/2^+$, $33/2^+$ bands of ^{191}Au .

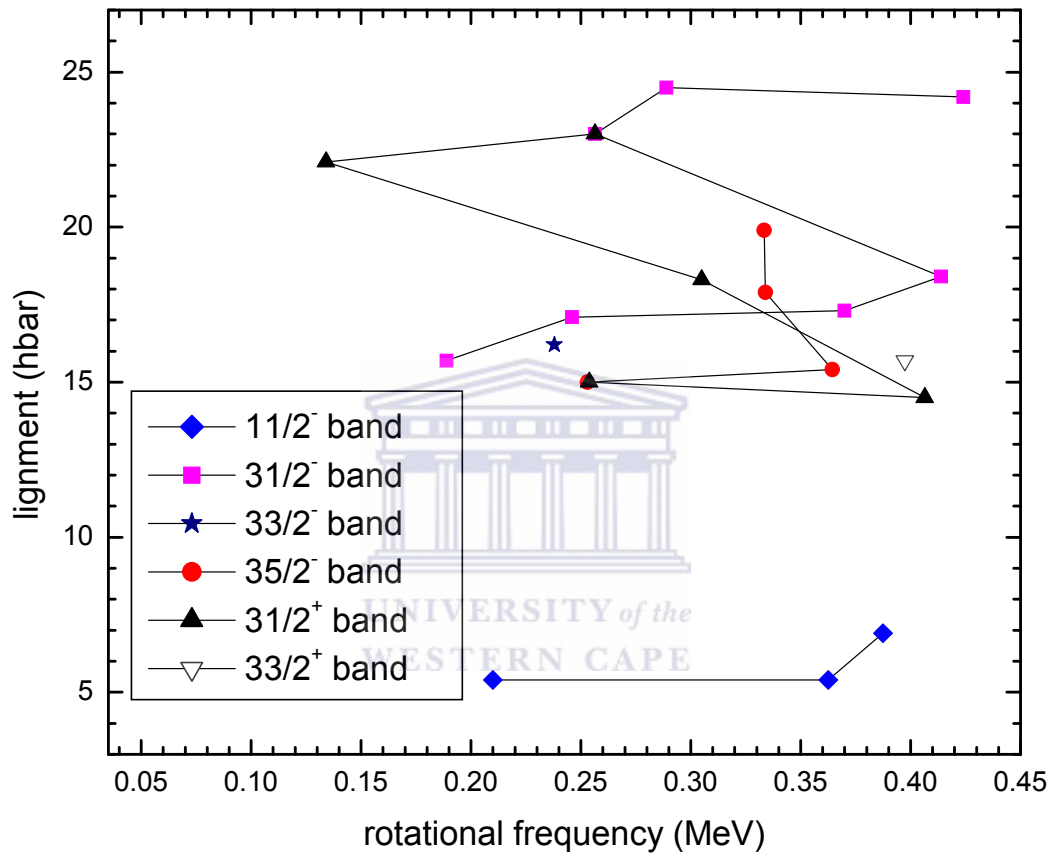


Figure 4.27: Experimental quasiparticle alignments for the $11/2^-$, $31/2^-$, $33/2^-$, $35/2^-$, $31/2^+$, $33/2^+$ bands of ^{189}Au calculated with Harris parameters of $J_0 = 6 \hbar^2 (\text{MeV})^{-1}$ and $J_1 = 30 \hbar^4 (\text{MeV})^{-3}$ and $K = 0$.

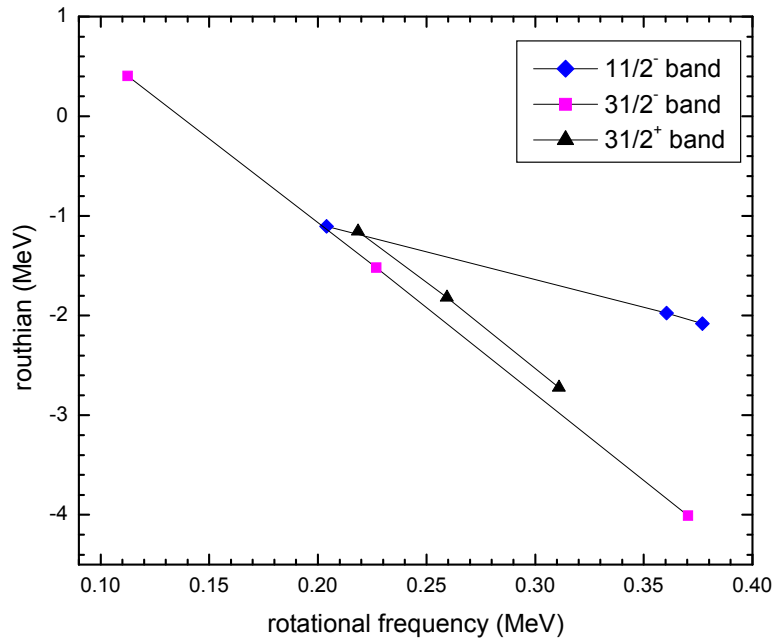


Figure 4.28: Experimental quasiparticle Routhians for the $11/2^-$, $31/2^-$, $31/2^+$ bands of ^{193}Au calculated with Harris parameters of $J_0 = 6 \hbar^2 (\text{MeV})^{-1}$ and $J_1 = 30 \hbar^4 (\text{MeV})^{-3}$ and $K = 0$.

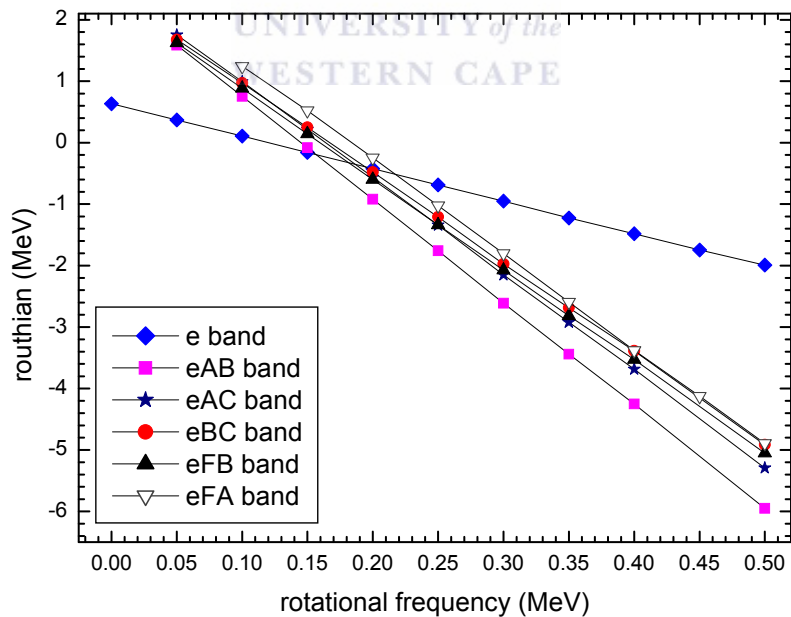


Figure 4.29: Theoretical quasiparticle Routhians for the $11/2^-$, $31/2^-$, $33/2^-$, $35/2^-$, $31/2^+$, $33/2^+$ bands of ^{193}Au .

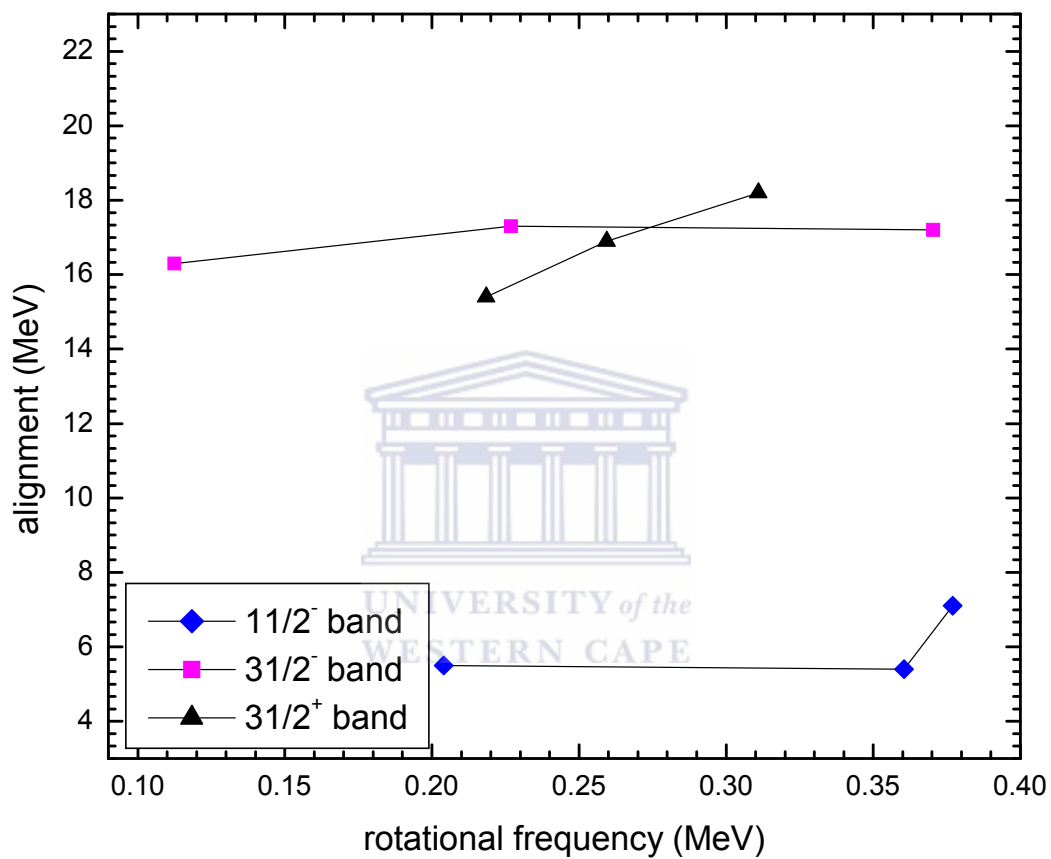


Figure 4.30: Experimental quasiparticle alignments for the $11/2^-$, $31/2^-$, $31/2^+$ bands of ^{193}Au calculated with Harris parameters of $J_0 = 6 \hbar^2 (\text{MeV})^{-1}$ and $J_1 = 30 \hbar^4 (\text{MeV})^{-3}$ and $K = 0$.

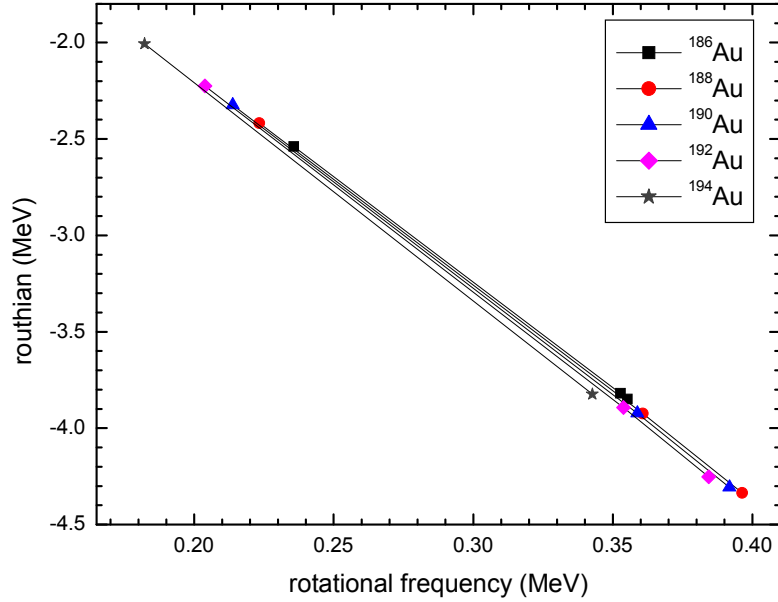


Figure 4.31: Experimental quasiparticle Routhians for the $1I^-$ bands of the odd-odd $^{186-194}\text{Au}$ nuclei calculated with Harris parameters of $J_0 = 6 \hbar^2 (\text{MeV})^{-1}$ and $J_1 = 30 \hbar^4 (\text{MeV})^{-3}$ and $K = 0$.

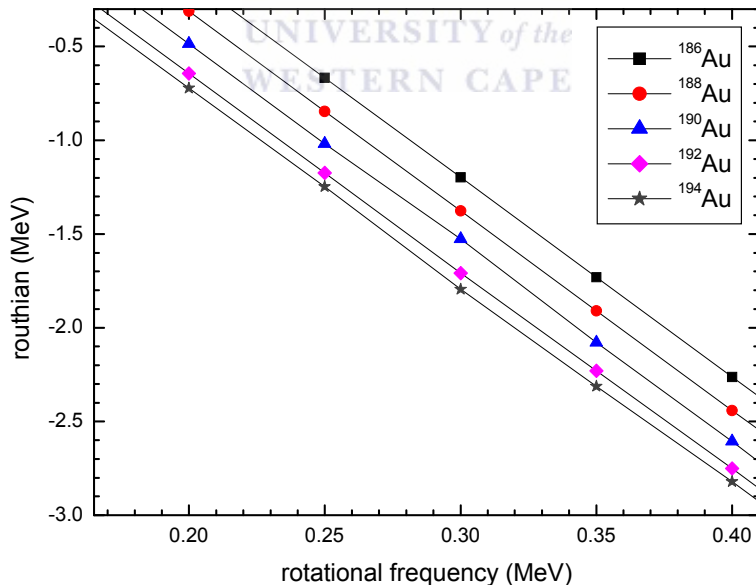


Figure 4.32: Theoretical quasiparticle Routhians for the $1I^-$ bands of the odd-odd $^{186-194}\text{Au}$ nuclei.

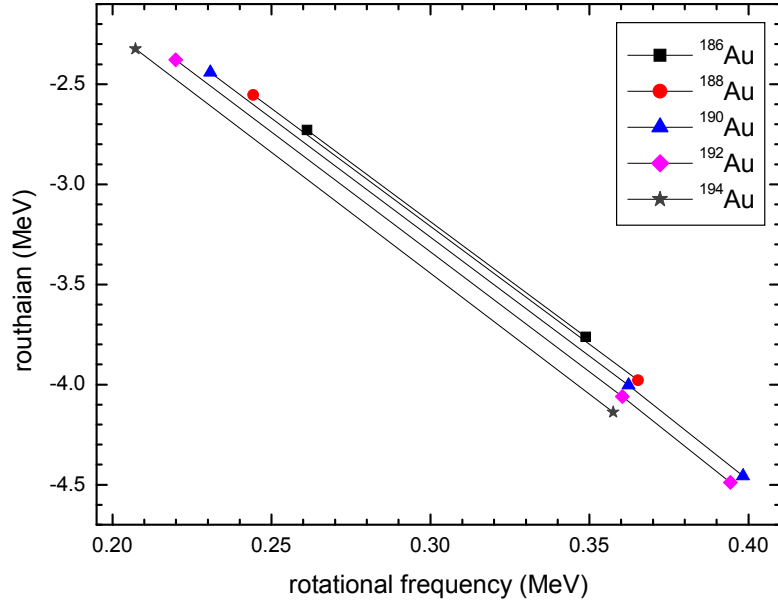


Figure 4.33: Experimental quasiparticle Routhians for the 12^- bands of the odd-odd $^{186-194}\text{Au}$ nuclei calculated with Harris parameters of $J_0 = 6 \hbar^2 (\text{MeV})^{-1}$ and $J_1 = 30 \hbar^4 (\text{MeV})^{-3}$ and $K = 0$.

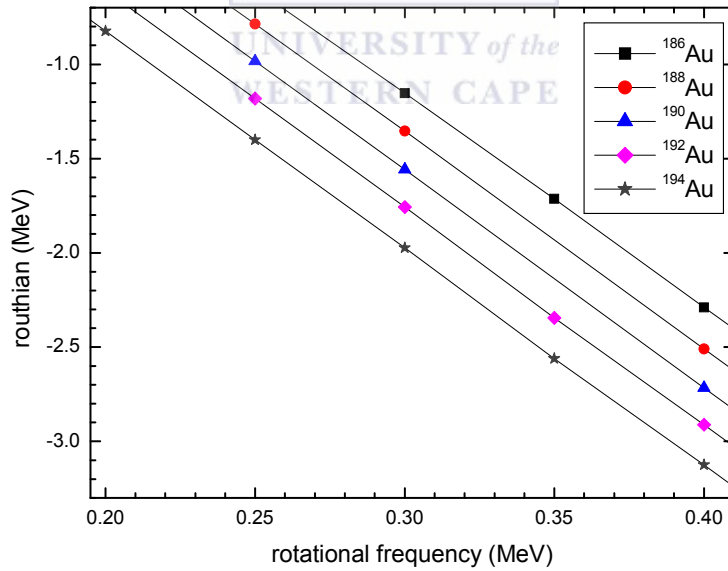


Figure 4.34: Theoretical quasiparticle Routhians for the 12^- bands of the odd-odd $^{186-194}\text{Au}$ nuclei.

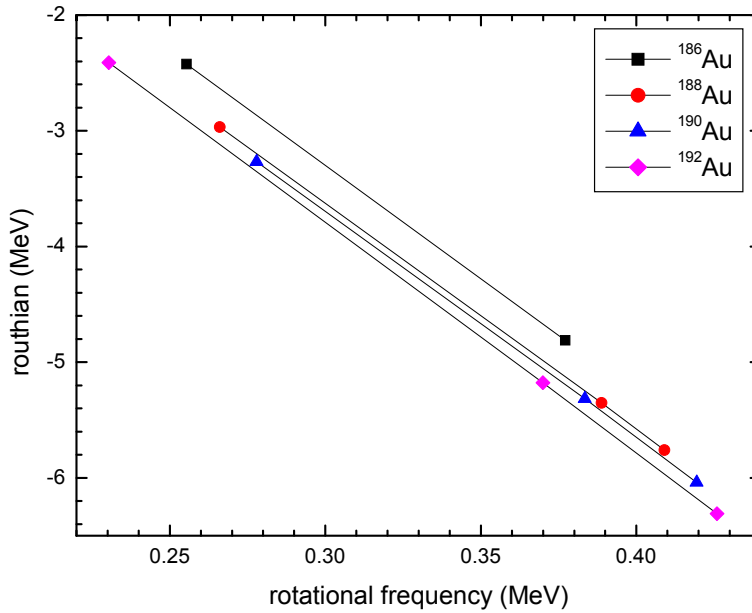


Figure 4.35: Experimental quasiparticle Routhians for the 20^+ bands of the odd-odd $^{186-192}\text{Au}$ nuclei calculated with Harris parameters of $J_0 = 6 \hbar^2 (\text{MeV})^{-1}$ and $J_1 = 30 \hbar^4 (\text{MeV})^{-3}$ and $K = 0$.

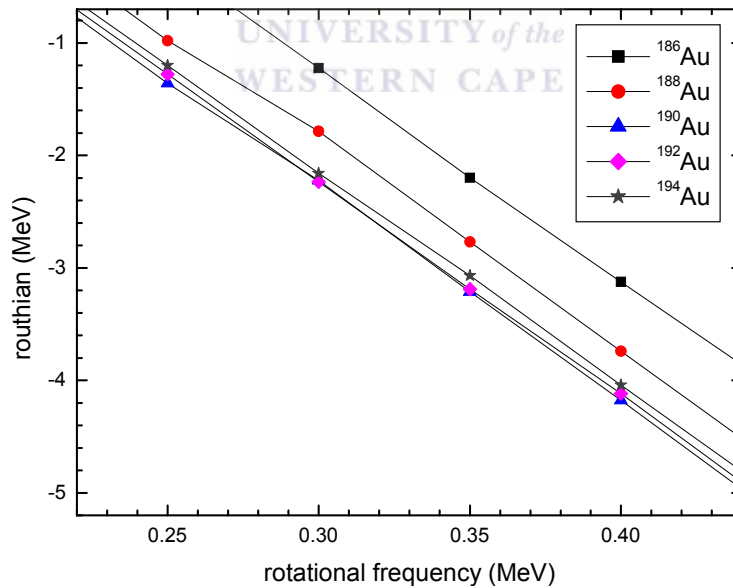


Figure 4.36: Theoretical quasiparticle Routhians for the 20^+ bands of the odd-odd $^{186-194}\text{Au}$ nuclei.

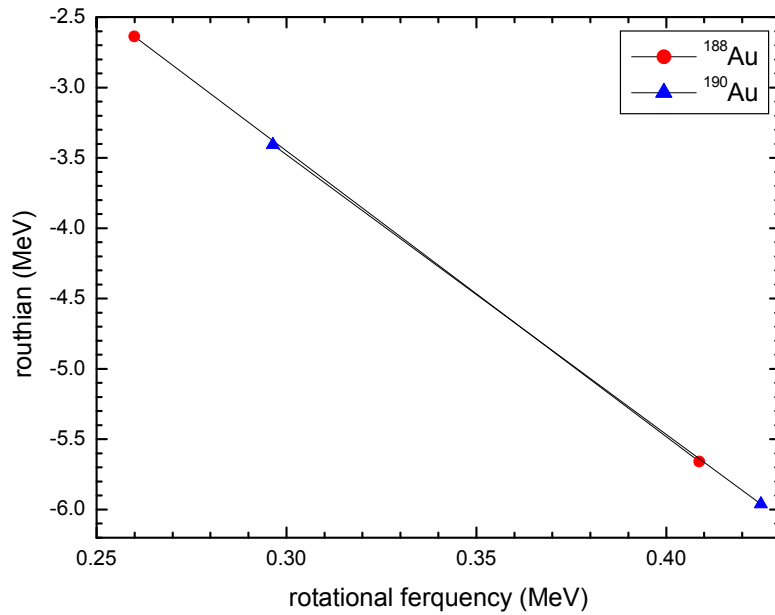


Figure 4.37: Experimental quasiparticle Routhians for the 21^+ bands of the odd-odd $^{188-190}\text{Au}$ nuclei calculated with Harris parameters of $J_0 = 6 \hbar^2 (\text{MeV})^{-1}$ and $J_1 = 30 \hbar^4 (\text{MeV})^{-3}$ and $K = 0$.

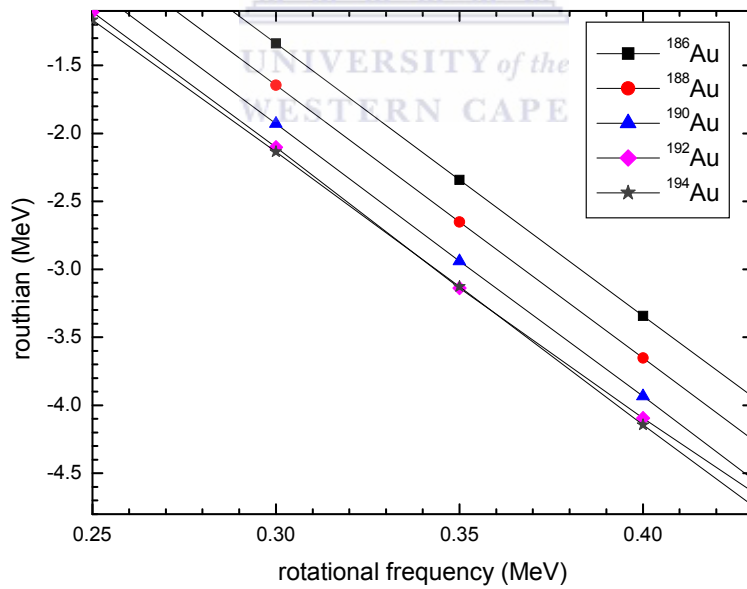


Figure 4.38: Theoretical quasiparticle Routhians for the 21^+ bands of the odd-odd $^{186-194}\text{Au}$ nuclei.

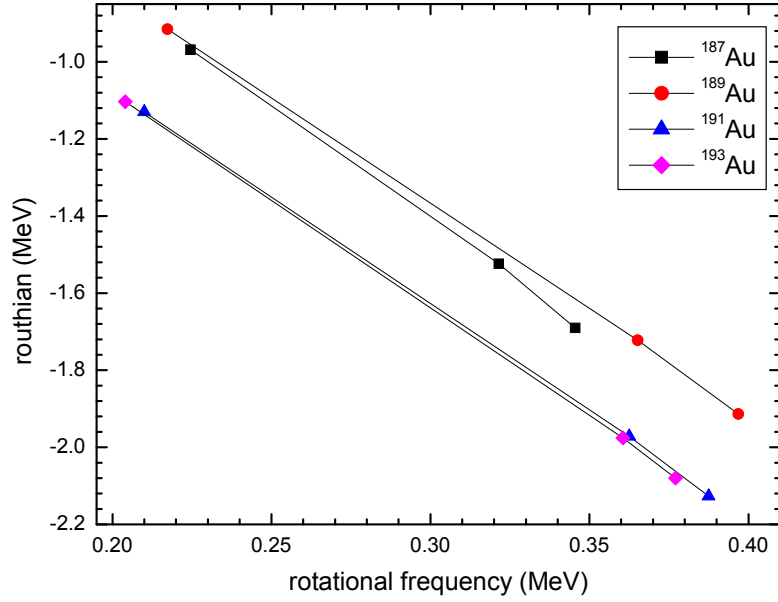


Figure 4.39: Experimental quasiparticle Routhians for the $11/2^-$ bands of the odd-even $^{187-193}\text{Au}$ nuclei calculated with Harris parameters of $J_0 = 6 \hbar^2 (\text{MeV})^{-1}$ and $J_1 = 30 \hbar^4 (\text{MeV})^{-3}$ and $K = 0$.

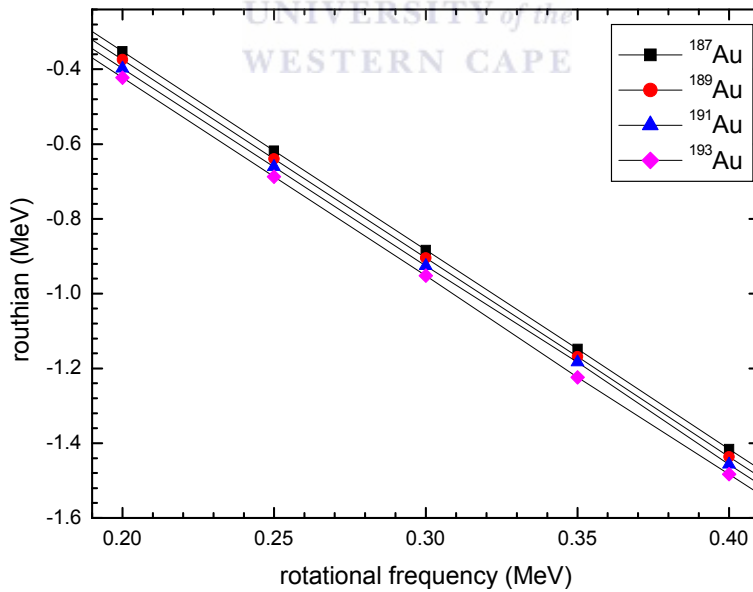


Figure 4.40: Theoretical quasiparticle Routhians for the $11/2^-$ bands of the odd-even $^{187-193}\text{Au}$ nuclei.

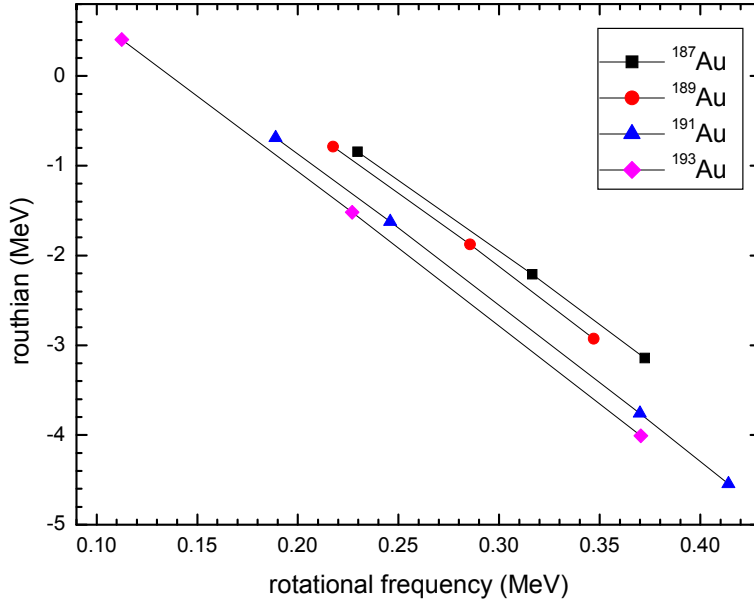


Figure 4.41: Experimental quasiparticle Routhians for the $31/2^-$ bands of the odd-even $^{187-193}\text{Au}$ nuclei calculated with Harris parameters of $J_0 = 6 \hbar^2 (\text{MeV})^{-1}$ and $J_1 = 30 \hbar^4 (\text{MeV})^{-3}$ and $K = 0$.

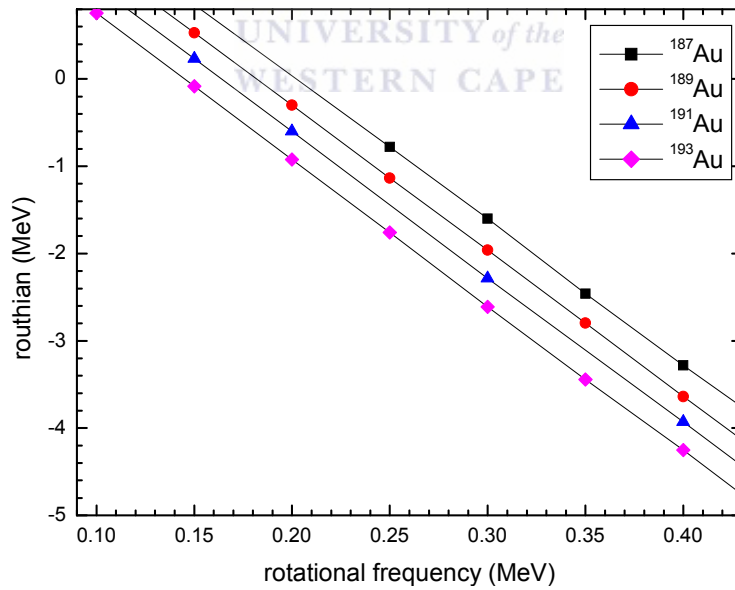


Figure 4.42: Theoretical quasiparticle Routhians for the $31/2^-$ bands of the odd-even $^{187-193}\text{Au}$ nuclei.

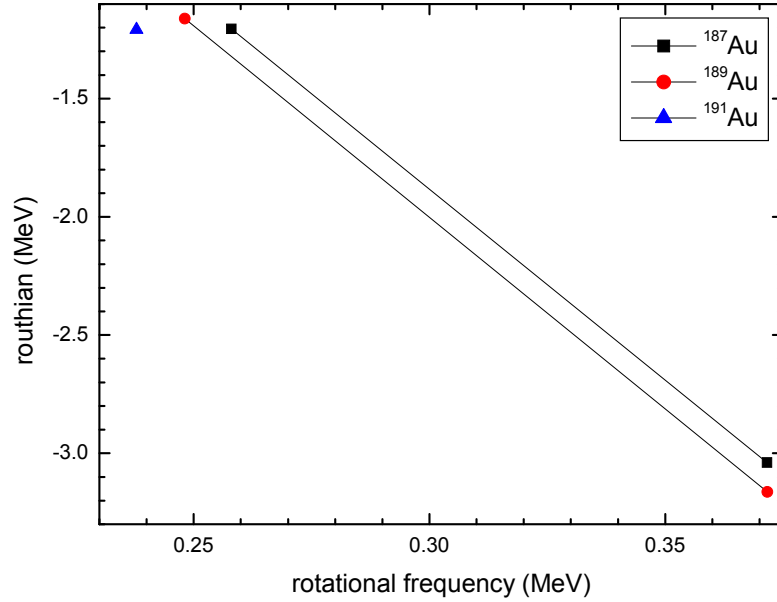


Figure 4.43: Experimental quasiparticle Routhians for the $33/2^-$ bands of the odd-even $^{187-191}\text{Au}$ nuclei calculated with Harris parameters of $J_0 = 6 \hbar^2 (\text{MeV})^{-1}$ and $J_1 = 30 \hbar^4 (\text{MeV})^{-3}$ and $K = 0$.

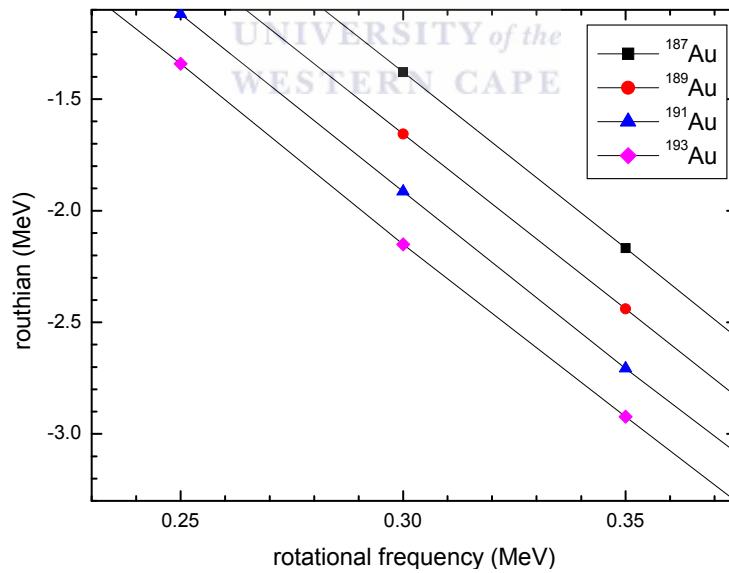


Figure 4.44: Theoretical quasiparticle Routhians for the $33/2^-$ bands of the odd-even $^{187-193}\text{Au}$ nuclei.

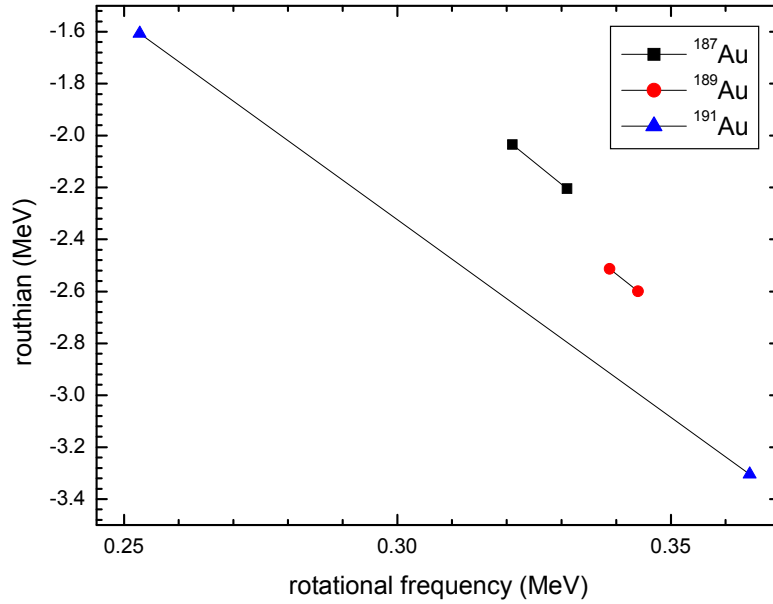


Figure 4.45: Experimental quasiparticle Routhians for the $35/2^-$ bands of the odd-even $^{187-191}\text{Au}$ nuclei calculated with Harris parameters of $J_0 = 6 \hbar^2 (\text{MeV})^{-1}$ and $J_1 = 30 \hbar^4 (\text{MeV})^{-3}$ and $K = 0$.

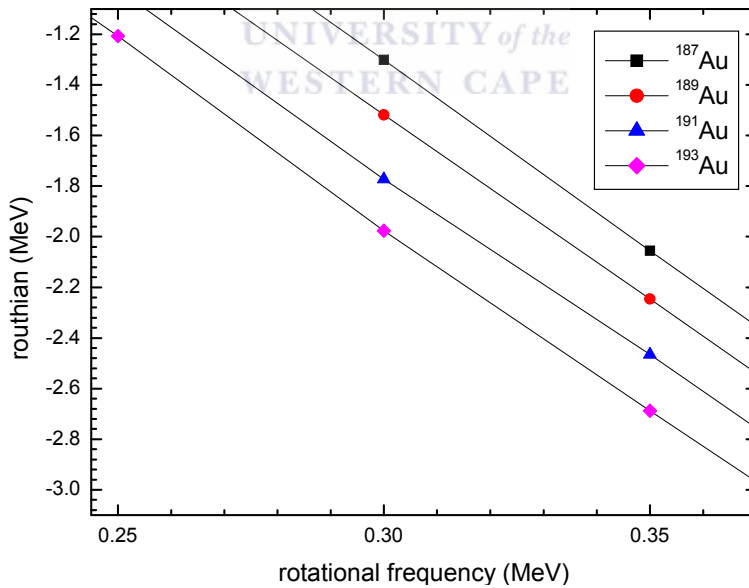


Figure 4.46: Theoretical quasiparticle Routhians for the $35/2^-$ bands of the odd-even $^{187-193}\text{Au}$ nuclei.

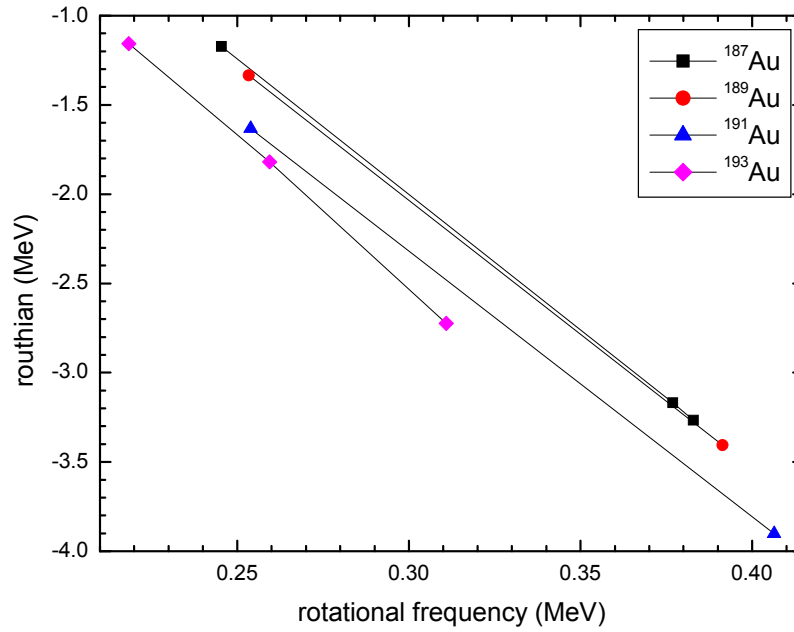


Figure 4.47: Experimental quasiparticle Routhians for the $31/2^+$ bands of the odd-even $^{187-193}\text{Au}$ nuclei calculated with Harris parameters of $J_0 = 6 \hbar^2 (\text{MeV})^{-1}$ and $J_1 = 30 \hbar^4 (\text{MeV})^{-3}$ and $K = 0$.

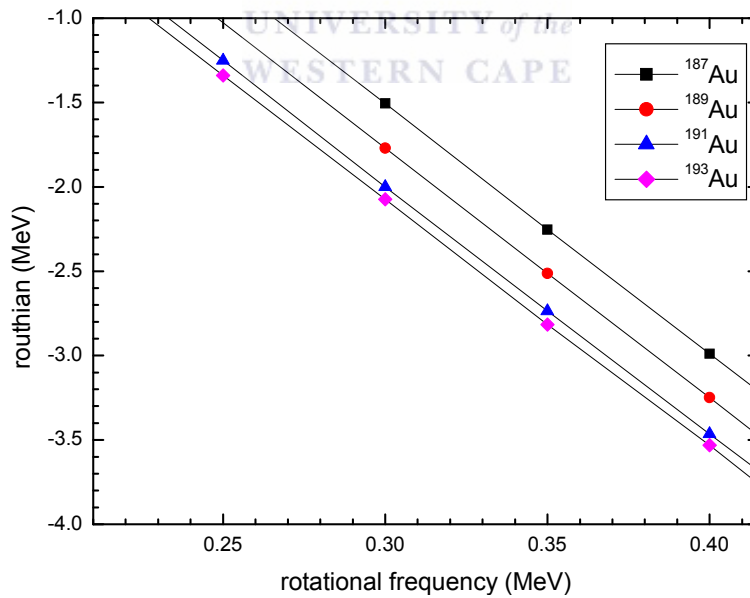


Figure 4.48: Theoretical quasiparticle Routhians for the $35/2^+$ bands of the odd-even $^{187-193}\text{Au}$ nuclei.

CHAPTER 5 SUMMARY

In this study, TRS and CSM calculations were performed for the $\pi h_{11/2}^{-1} \otimes \nu i_{13/2}^{-1}$, $\pi h_{11/2}^{-1} \otimes \nu i_{13/2}^{-3}$, $\pi h_{11/2}^{-1} \otimes \nu i_{13/2}^{-2} h_{9/2}^{-1}$ bands in the odd-odd $^{186-194}\text{Au}$ and $\pi h_{11/2}^{-1}$, $\pi h_{11/2}^{-1} \otimes \nu i_{13/2}^{-2}$, $\pi h_{11/2}^{-1} \otimes \nu i_{13/2}^{-1} h_{9/2}^{-1}$ bands in the odd-even $^{187-193}\text{Au}$ nuclei. In summary the TRS calculations predict triaxial shapes for all these bands in the $^{186-194}\text{Au}$ nuclei except for the $\pi h_{11/2}^{-1} \otimes \nu i_{13/2}^{-3}$ bands where a small triaxiality is predicted for the lighter odd-odd $^{186,188}\text{Au}$ nuclei. CSM calculations performed using these deformation parameters show that the positive parity A, B and C Routhians lie close to each other and for $\gamma \leq -75^\circ$ the negative parity F Routhian is pushed down in energy and compete with these positive parity Routhians. Thus the theory (TRS and CSM calculations) account very well for the observed sets of rotation aligned bands in the $^{186-194}\text{Au}$ nuclei. Good agreement between the theory and experiment was also obtained for the alignments in all these bands of $^{186-194}\text{Au}$. Alignment gains for the 12^- and $11/2^-$ bands predicted by CSM are in good agreement with the experimentally measured ones. Discrepancies has been found for the band crossing frequencies of the 12^- band in ^{190}Au , $11/2^-$ with $31/2^-$, and $11/2^-$ with $35/2^-$ bands in $^{187,189,191}\text{Au}$, because the predicted band crossing frequencies are smaller than the experimentally measured ones.

The theory predicts very well the relative position of the Routhians for all these bands in the $^{186-194}\text{Au}$ nuclei, except that for the 22^+ band of ^{190}Au . Signature inversion frequencies predicted by CSM in the Routhians of the 11^- and 12^- bands are generally in good agreement with the experimentally measured ones, except in ^{194}Au where a larger difference was found. Both the theory and experiment show small signature splitting for the Routhians of the 11^- and 12^- bands, but a large difference between the predicted and measured value was found in ^{188}Au . Both the theory and experiment show that the signature inversion frequencies and splitting for the 11^- and 12^- bands decrease with an increase in the nuclear mass of each odd-odd $^{186-194}\text{Au}$ nucleus. Discrepancies between predicted and measured values have been found for the signature splitting between the Routhians of the 20^+ , 21^+ and 22^+ bands in the $^{188,190}\text{Au}$ nuclei, and between the Routhians of the $31/2^-$ with $33/2^-$ and $31/2^-$ with $35/2^-$ bands in the $^{187,189,191}\text{Au}$ nuclei, whereas a good agreement was found between the

Routhians of $33/2^-$ and $35/2^-$ bands of $^{187,189,191}\text{Au}$ nuclei. A small difference between the theoretical and experimental signature splitting was found for the Routhians of $31/2^+$ and $33/2^+$ bands in the $^{189,191}\text{Au}$ nuclei.

These sets of rotation aligned bands are explained very well by the theory, although it fails to satisfactorily reproduce the magnitude of the band crossing frequencies and signature splitting. This is not a surprise because thus far no model can reproduce all features of these kind of bands with that high precision. It is possible that if some of the parameters were adjusted in the CSM model the experimental observations could be reproduced even better.



REFERENCES

- [And76] G. Andersson, S. E. Larsson, G. Leander, P. Möller, S. G. Nilsson, I. Ragnarsson, S. Åberg, R. Bengtsson, J. Dudek, B. Nerlo-Pomorska, K. Pomorski, Z. Szymański, Nucl. Phys. A **268**, 205 (1976)
- [Bar03] R. A. Bark, A. M. Baxter, A. P. Byrne, P. M. Davidson, G. D. Dracoulis, S. M. Mullis, T. R. McGoram, R. T. Newman, Phys. Rev. C **67**, 014320 (2003)
- [Bar57] J. Bardeen, L. N. Cooper, J. R. Schrieffer, Phys. Rev. **108**, 1175 (1957)
- [Ben79] R. Bengtsson and S. Frauendorf, Nucl. Phys. A **327**, 139 (1979)
- [Ben86] R. Bengtsson, S. Frauendorf and F. R. May, Atomic data and nuclear data tables. **35**, 15-122 (1986)
- [Bet36] H. A. Bethe and R. F. Bacher, Rev. Mod. Phys. **8**, 82 (1936)
- [Boh53] A. Bohr and B. R. Mottelson, Mat. Fys. Medd. Dan. Vid. Selsk. **27**, 16 (1953)
- [Boh75] A. Bohr and B. R. Mottelson, Nuclear Structure, Vol. **2**. Benjamin, New York, 1975
- [Boh76a] A. Bohr, Rev. Mod. Phys. **48**, 365 (1976)
- [Boh76b] A. Bohr, Varenna Lectures **69**, (1976)
- [Boh81] A. Bohr and B. R. Mottelson, Phys. Scr. **24**, 71 (1981)
- [Bou89] C. Bourgeois, M. G. Porquet, N. Perrin, H. Sergolle, F. Hannachi, G. Bastin, F. Beck, Z. Phys. A-Atomic Nuclei **333**, 5-14 (1989)
- [Bou92] C. Bourgeois, A. Korichi, N. Perrin, D. G. Popescu, F. Azaiez, D. Hojman, H. Sergolle, G. Bastun, Z. Phys. A-Hadrons and Nuclei **343**, 243-244 (1992)
- [Cha02] H. J. Chantler, E. S. Paul, A. J. Boston, M. P. Carpenter, R. Charity, C. J. Chiara, P. T. W. Choy, C. N. Davids, M. Devlin, A. M. Fletcher, D. B. Fossan, D. G. Jenkins, N. S. Kelsall, T. Koike, D. R. LaFosse, P. J. Nolan, D. G. Sarantites, D. Seweryniak, J. F. Smith, K. Starosta, R. Wadsworth, A. N. Wilson, Phys. Rev. C **66**, 014311 (2002)
- [Cun76] J. C. Cunnane, M. Piiparinen, P. J. Daly, C. L. Dors, T. L. Koo, F. M. Bernthal, Phys. Rev. C **13**, 2197 (1976)

- [Ćwi87] S. Cwiok, J. Dudek, W. Nazarewicz, J. Skalski and T. Werner, *Comput. Phys. Commun.* **46**, 379 (1987)
- [Dav58] A. S. Davydov and B. F. Filippov, *Nucl. Phys.* **8**, 237 (1958)
- [Dav59a] A. S. Davydov and V. S. Rostovsky, *Nucl. Phys.* **12**, 58 (1959)
- [Dav59b] A. S. Davydov, *Sov. Phys. JETP* **9**, 1103 (1959)
- [Dav65] J. P. Davidson, *Rev. Mod. Phys.* **37**, 105 (1965)
- [Dud81] J. Dudek, Z. Szymański, T. Werner, *Phys. Rev. C* **23**, 920 (1981)
- [Edm57] A. R. Edmonds, *Angular Momentum in Quantum Mechanics*. Princeton Univ. Press, Princeton, (1957)
- [Flü71] S. Flügge, *Practical Quantum Mechanics*, Springer-Verlag, Berlin, (1971)
- [Gre99] P. T. Greenlees, PhD thesis, University of Liverpool, (1999)
- [Gue01] E. Gueorguieva, Ch. Vieu, C. Schüch, A. Minkova, B. Kharraja, M. Kaci, F. Hannachi, J. S. Dionisio, A. Korichi, A. Lopez-Martens, Z. Meliani, Ts. Venkova, *Phys. Rev. C* **64**, 064304 (2001)
- [Gue02] E. Gueorguieva, C. Schüch, A. Minkova, Ch. Vieu, F. Hannachi, M. Kaci, M.-G. Porquet, R. Wyss, J. S. Dionisio, A. Korichi, A. Lopez-Martens, *Phys. Rev. C* **68**, 054308 (2003)
- [Gue03] E. Gueorguieva, C. Schüch, A. Minkova, Ch. Vieu, M. Kaci, F. Hannachi, R. Wyss, J. S. Dionisio, A. Korichi, A. Lopez-Martens, *Phys. Rev. C* **69**, 044320 (2004)
- [Gus67] C. Gustafson, I. L. Lamm, B. Nilsson, S. G. Nilsson, *Ark. Fys.* **36**, 613 (1967)
- [Ham83] I. Hamamoto and B. R. Mottelson, *Phys. Lett. B* **127**, 281 (1983)
- [Har65] S. M. Harris, *Phys. Rev. B* **138**, 509 (1965)
- [Hax49] O. Haxel, J. H. D. Jensen, H. E. Suess, *Phys. Rev.* **75**, 1766 (1949)
- [Hey83] K. Heyde, P. Van Isacker, M. Waroquier, J. L. Wood, R. A. Meyer, *Phys. Rep.* **102**, 291 (1983)
- [Hil53] D. L. Hill and J. A. Wheeler, *Phys. Rev.* **89**, 1102 (1953)
- [Hjo76] S. A. Hjorth, A. Johnson, Th. Lindblad, L. Funke, P. Kemnitz, G. Winter, *Nucl. Phys. A* **262**, 328 (1976)
- [Hüb86] H. Hübel, A. P. Bryne, S. Ogaza, A. E. Stuchbery, G. D. Dracoulis, M. Guttormsen, *Nucl. Phys. A* **453**, 316-348 (1986)
- [Ing54] D. R. Inglis, *Phys. Rev.* **96**, 1059 (1954)

- [Ing56] D. R. Inglis, Phys. Rev. **103**, 1786 (1956)
- [Jan92] V. P. Janzen, Z. -M. Liu, M. P. Carpenter, L. H. Courtney, H. -Q. Jin, A. J. Larabee, L. L. Riedinger, J. K. Johansson, D. G. Popescu, J. C. Waddington, S. Pilotte, F. Donau, Phys. Rev. C **45**, 613 (1992)
- [Joh89] J. K. Johansson, D. G. Popescu, D. D. Rajnauth, J. C. Waddington, M. D. Carpenter, L. H. Courtney, V. P. Janzen, A. J. Larabee, Z.M. Liu, L. L. Riedinger, Phys. Rev. C **40**, 132 (1989)
- [Kee99] A. Keenan, PhD thesis, University of Liverpool, (1999)
- [Köl85] V. Kölschbach, P. Schüler, K. Hardt, D. Rosendaal, C. Günther, K. Euler, T. Tölle, M. Marten-Tölle, P. Zeyen, Nucl. Phys. A **439**, 189 (1985)
- [Kra98a] K. S. Krane, Introductory Nuclear Physics, Copyright © 1998, by John Wiley and Sons, p. 125
- [Kra98b] K. S. Krane, Introductory Nuclear Physics, Copyright © 1998, by John Wiley and Sons, p. 152
- [Mab03] G. K. Mabala, PhD thesis, University of Cape Town, (2003)
- [May49] M. G. Mayer, Phys. Rev. **75**, 1969 (1949)
- [Mey74] J. Meyer-ter-Vehn, F. S. Stephens, R. M. Diamond, Phys. Rev. Lett. **32**, 1383 (1974)
- [Mey75] J. Meyer-ter-Vehn, Nucl. Phys. A **249**, 141 (1975)
- [Möl81] P. Möller and J. R. Nix, Nucl. Phys. A **361**, 117 (1981)
- [Mue94] W. F. Mueller, H. J. Jensen, W. Reviol, L. L. Riedinger, C. -H. Yu, J. -Y. Zhang, Phys. Rev. C **50**, 1901 (1994)
- [Mye67] W. D. Myers and W. Swiatecki, Ark. Fys. **36**, 343 (1967)
- [Naz65] W. Nazarewicz, P. Olander, I. Ragnarsson, J. Dudek, G. A. Leander, P. Möller and E. Ruchouske, Phys. Rev. B **138**, 509 (1965)
- [Naz85] W. Nazarewicz, J. Dudek, R. Bengtsson, T. Bengtsson and I. Ragnarsson, Nucl. Phys. A **435**, 397 (1985)
- [Nes82] A. Neskakis, R. M. Lieder, H. Beuscher, Y. Gono, D.R. Haenmi, M. Müller-Veggian, Nucl. Phys. A **390**, 53 (1982)
- [Nil55] S. G. Nilsson, Mat. Fys. Medd. Dan. Vid. Selsk, **29**, 16 (1955)
- [Per79] N. Perrin, C. Bourgeois, A. Korichi, M. Pautrat, H. Sergolle, N. Barré, Ch. Vieu, N. Benouaret, J. Vanhorenbeeck, Z. Phys. A **359**, 373 (1997)

- [Per93] N. Perrin, C. Bourgeois, F. Azaiez, J. Duprat, D. Hojman, F. Le Blanc, D. G. Popescu, H. Sergolle, *Z. Phys. A* **347**, 81-85 (1993)
- [Rin90] P. Ring and P. Schuck, *The Nuclear Many-Body Problem*, Copyright © 1980, by Springer-Verlag New York Inc, p. 111
- [Ste75] F. S. Stephens, *Rev. Mod. Phys.* **47**, 43 (1975)
- [Str67] V. M. Strutinsky, *Nucl. Phys. A* **95**, 420 (1967)
- [Str68] V. M. Strutinsky, *Nucl. Phys. A* **122**, 1 (1968)
- [Szy83] Z. Szymański, *Fast Nuclear Rotation*, Clarendon press, Oxford, (1983)
- [Tok77] H. Toki, H. L. Yadav, A. Faessler, *Phys. Lett. B* **66**, 310 (1977)
- [Tok79] H. Toki, H. L. Yadav, A. Faessler, *Z. Physik. A* **292**, 79-94 (1979)
- [Ven92] Ts. Venkova, G. V. Marti, R. M. Lieder, W. Gast, A. Georgiev, D. Kutchin, H. Schnare, K. Strähle, T. Rzaca-Urban, J. Heese, K. H. Maier, *Z. Phys. A-Hadrons and Nuclei* **344**, 231-232 (1992)
- [Wei35] C. F. von Weizsäcker, *Z. Phys.* **96**, 431 (1935)
- [Wys90] R. Wyss, W. Satula, W. Nazarewicz, A. Johnson *Nucl. Phys. A* **511**, 324 (1990)
- [Wys99] R. Wyss, private communication with iThemba LABS, (1999)
- [Xie05] C. Y. Xie, X. H. Zhou, Y. H. Zhang, Y. X. Guo, G. Lei, Y. Zheng, M. L. Liu, L. T. Song, H. L. Wang, W. T. Guo, H. P. Yu, L. H. Zhu, X. G. Wu and F. R. Xu, *Phys. Rev. C* **72**, 044302 (2005)
- [Ye92] D. Ye, K. B. Beard, U. Garg, R. V. Janssens, M. P. Carpenter, I. Ahmad, T. L. Khoo, E. F. Moore, F. L. H. Wolfs, Ph. Benet, Z. W. Grabowski, M.W. Drigert, *Nucl. Phys. A* **537**, 207 (1992)

Appendix A Level schemes of the $^{186-194}\text{Au}$ nuclei



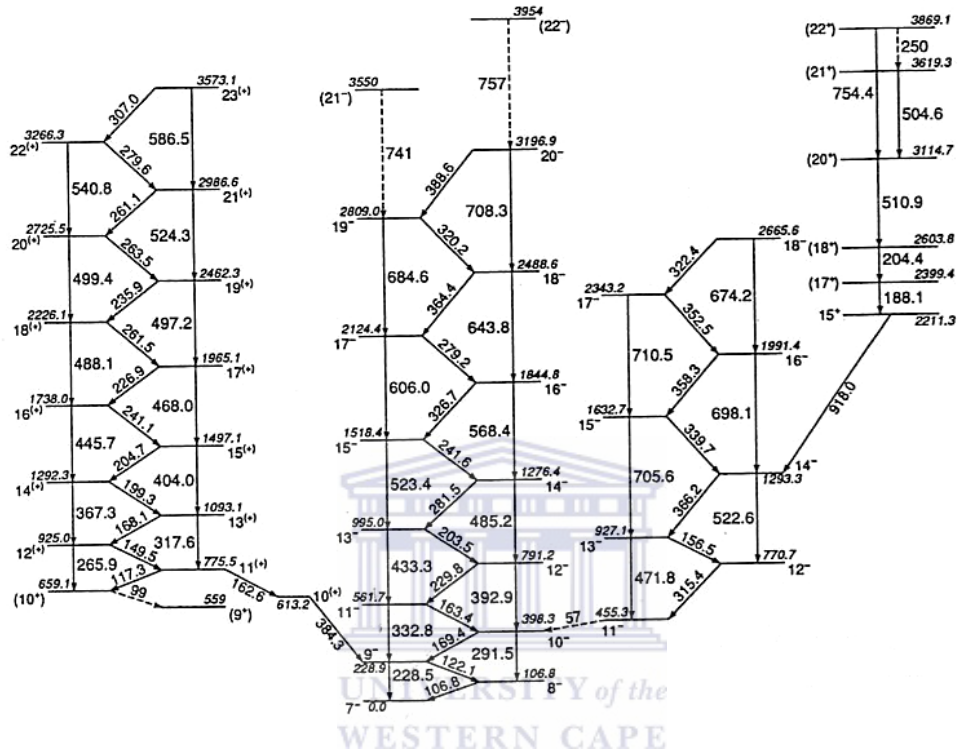


Figure A.1: Level scheme of ^{186}Au [Jan92].

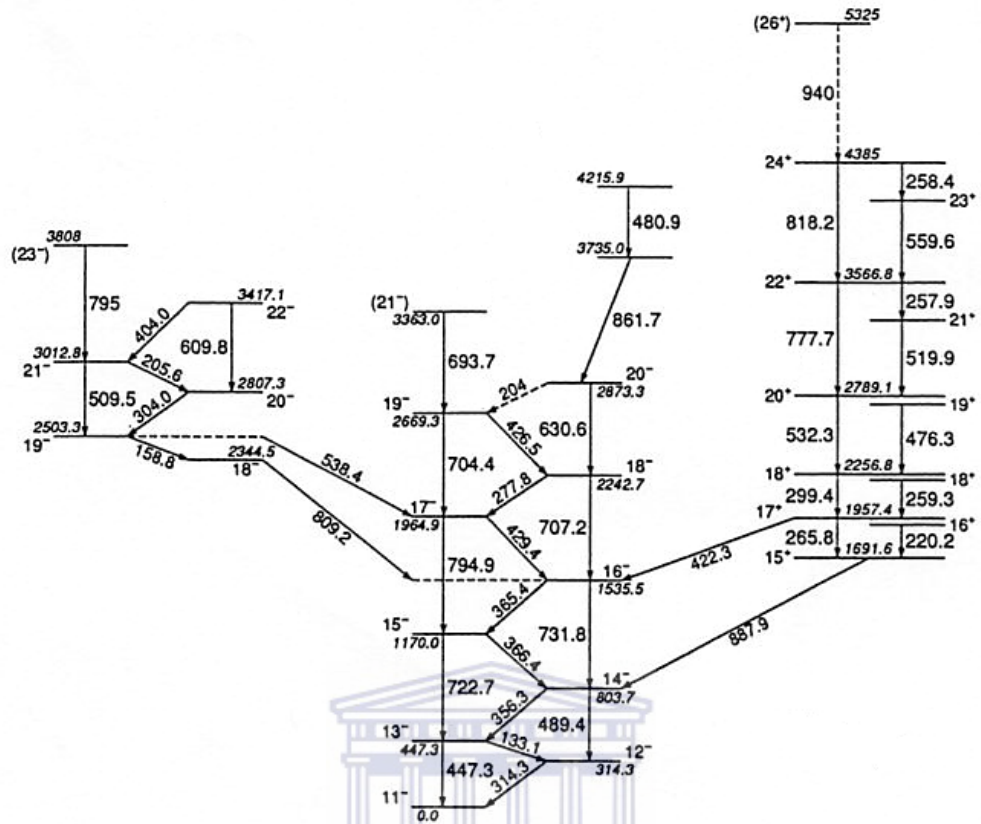


Figure A.2: Level scheme of ^{188}Au [Jan92].

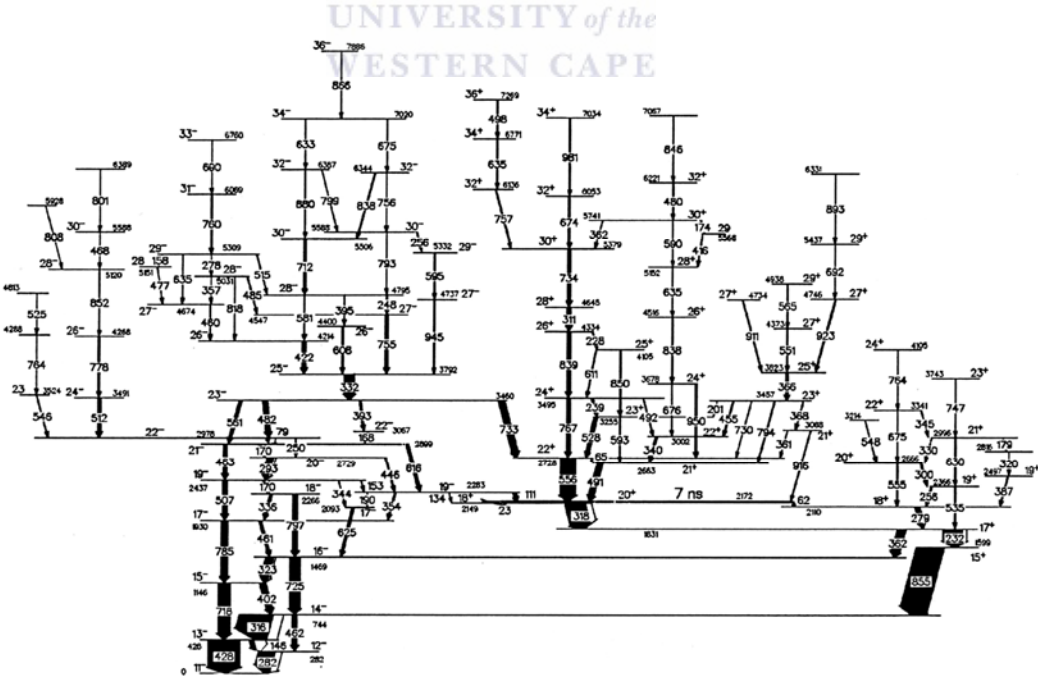


Figure A.3: Level scheme of ^{190}Au [Gue03].

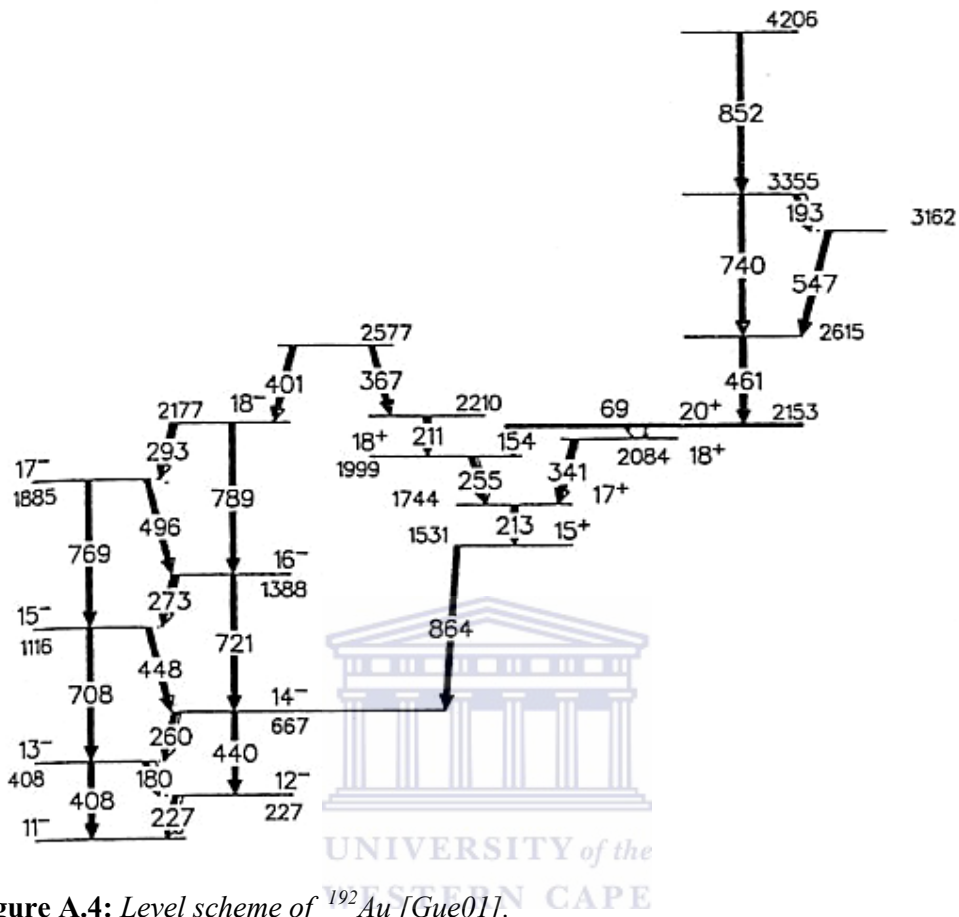


Figure A.4: Level scheme of ^{192}Au [Gue01].

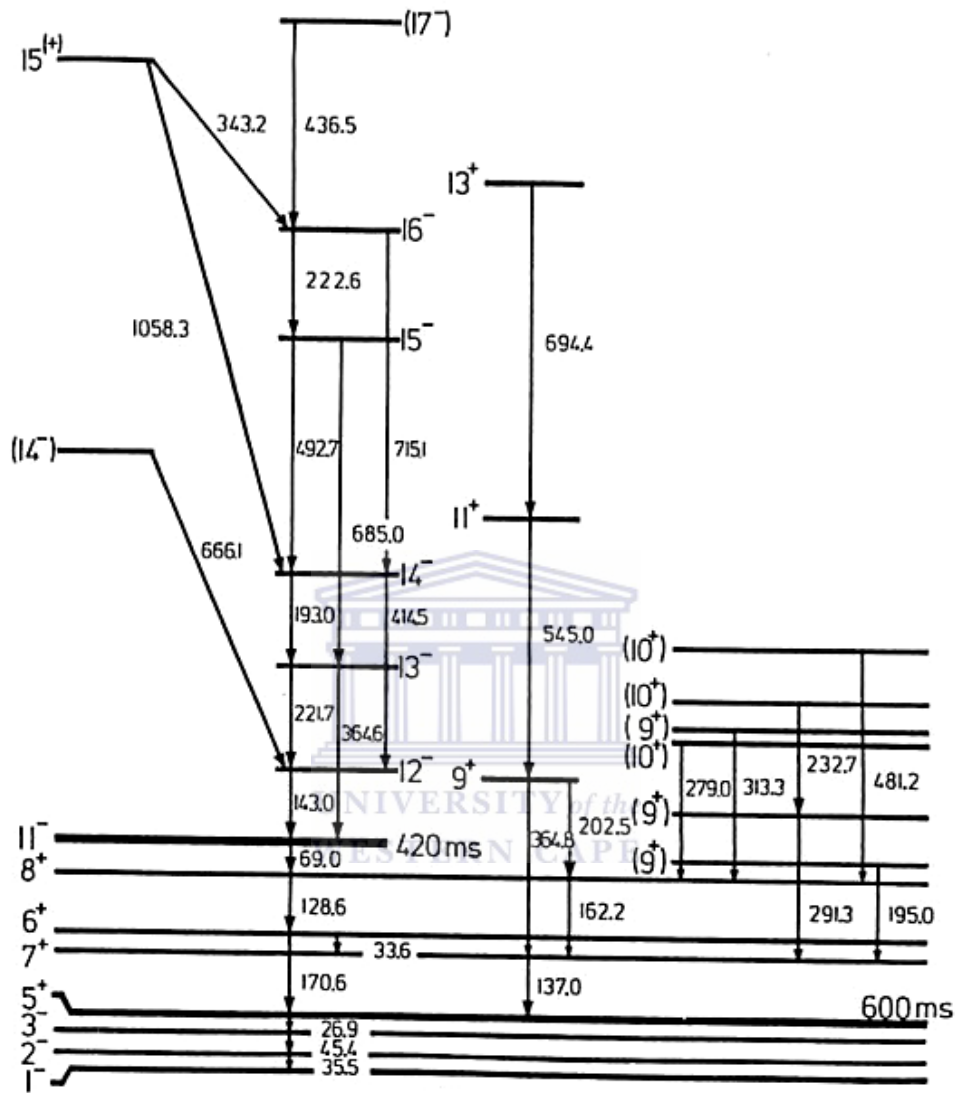


Figure A.5: Level scheme of ^{194}Au [Nes82].

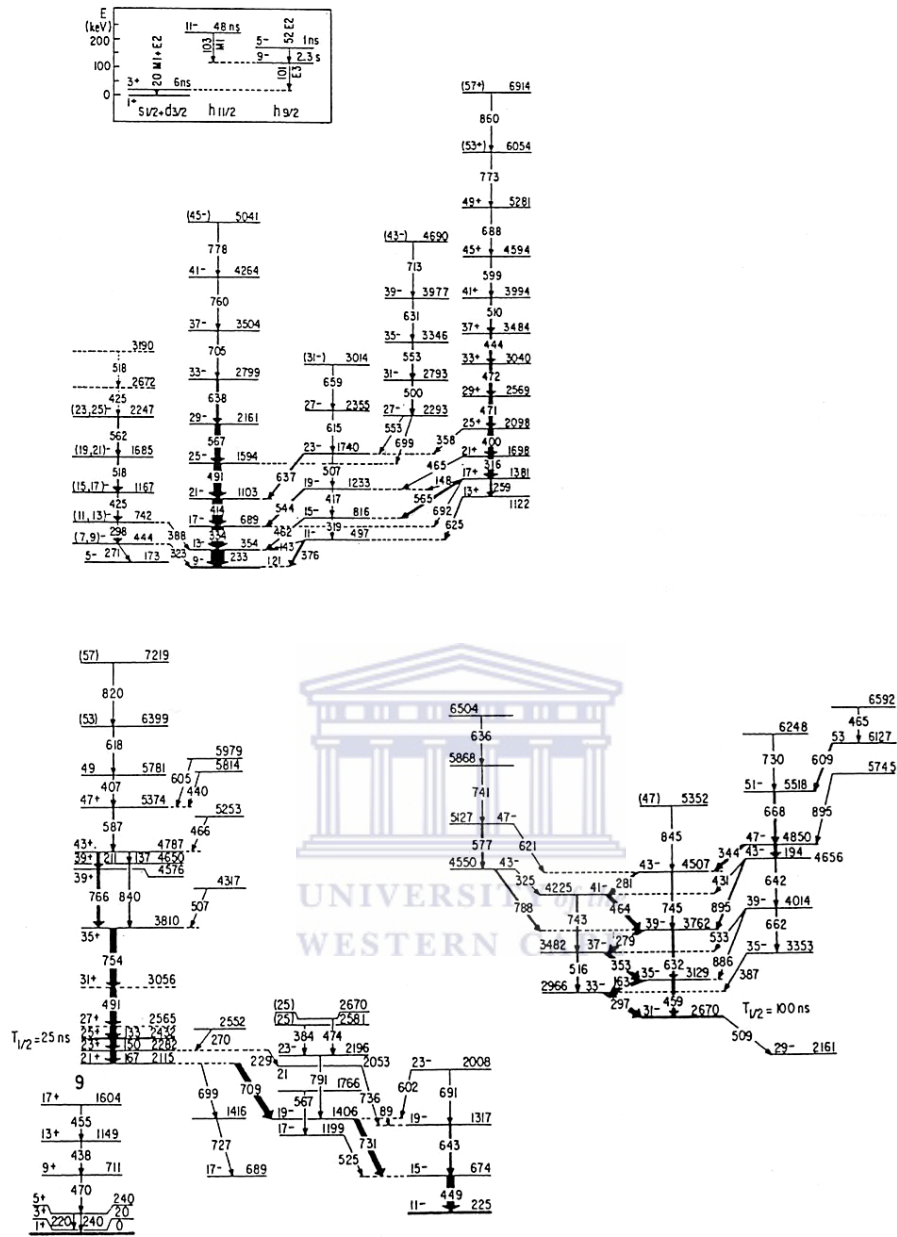


Figure A.7: Level scheme of ^{187}Au [Bou89].

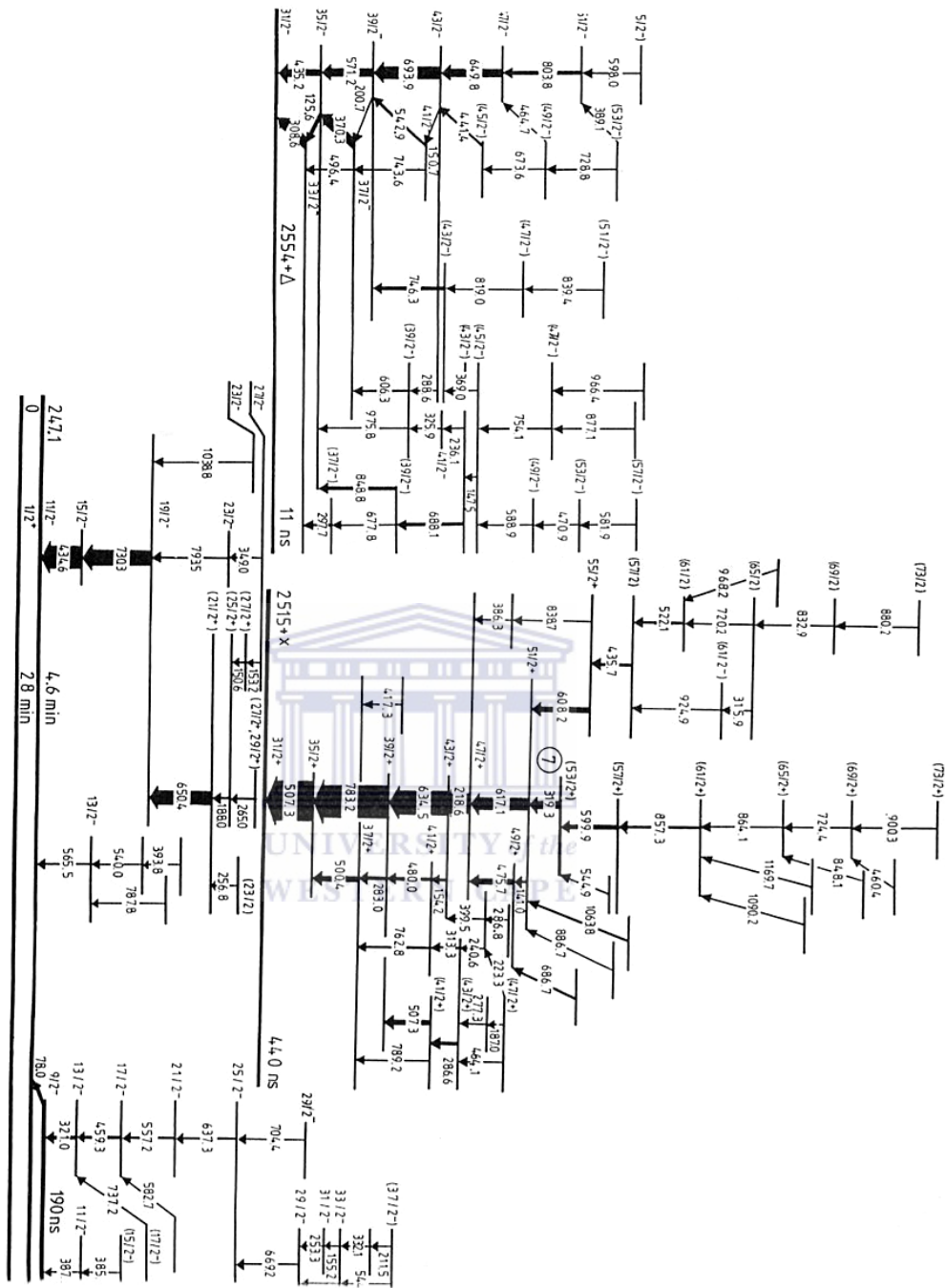


Figure A.8: Level scheme of ^{189}Au [Ven92].

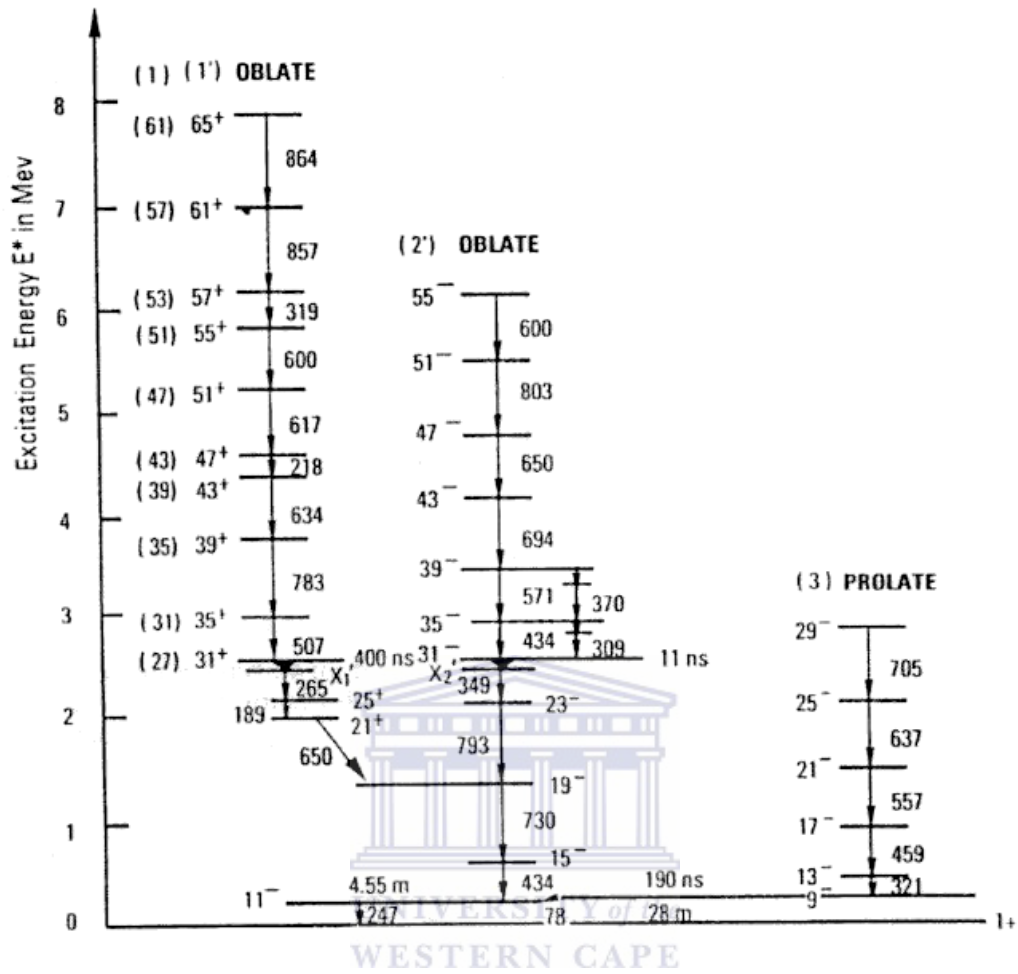


Figure A.9: Level scheme of ^{189}Au [Per93]. Spins are multiplied by two.

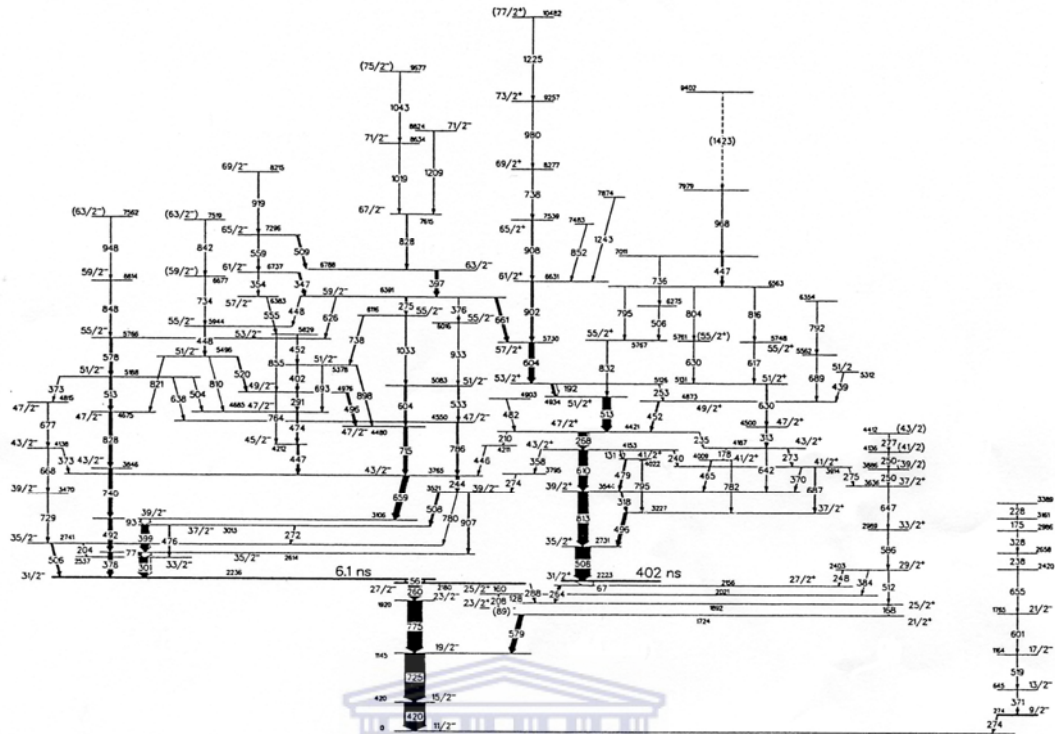


Figure A.10: Level scheme of ^{191}Au [Gue02].

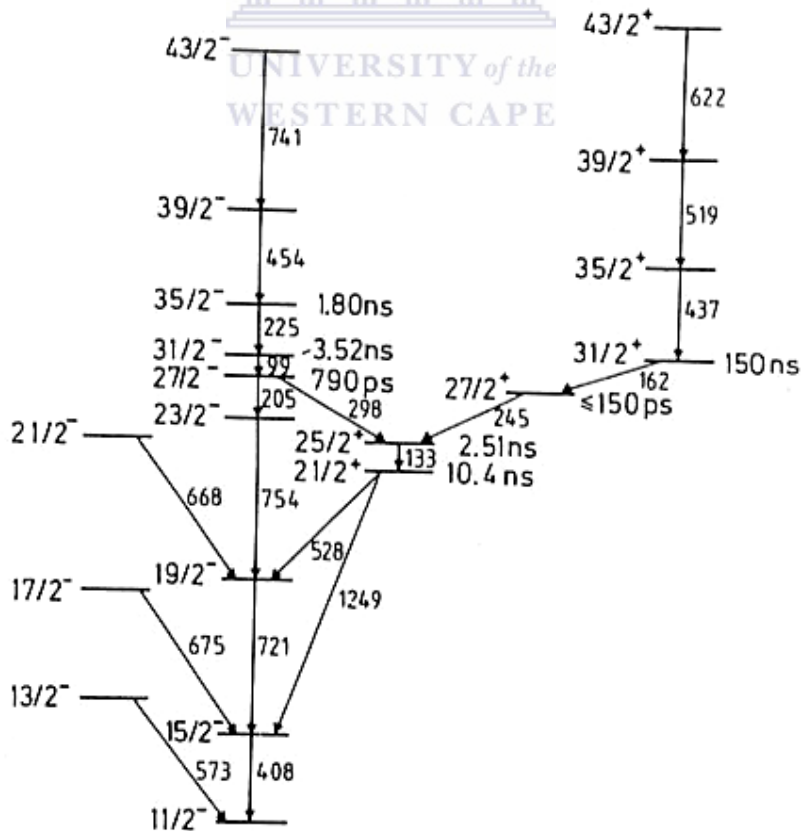


Figure A.11: Level scheme of ^{193}Au [Köl84].

Appendix B Tables of experimental quantities



Table B.1-5: Spins I (\hbar), aligned angular momentum I_x (\hbar), rotational frequency $\hbar\omega$ (MeV), Routhians E' (MeV) and e' (MeV), reference Routhians E'_{ref} (MeV) and reference aligned angular momentum I_{xref} (\hbar) and alignment i_x (\hbar) for the 11^- and 12^- band of the odd-odd $^{186-194}\text{Au}$ nuclei calculated with Harris parameters of $J_0 = 6\hbar^2(\text{MeV})^{-1}$ and $J_1 = 30\hbar^4(\text{MeV})^{-3}$ and $K = 0$.

Table B.1

^{186}Au								
I	$E_{exc}(I)$	$I_x(I)$	$\hbar\omega(I-1)$	$E'(I-1)$	$E'_{ref}(I-1)$	$I_{xref}(I-1)$	$e'(I-1)$	$i_x(I-1)$
11	0	11.5	0	0	0	0	0	0
13	0.4718	13.5	0.2357	-2.7081	-0.1690	1.8	-2.5391	10.7
15	1.1778	15.5	0.3528	-4.2876	-0.4687	3.4	-3.8189	11.1
17	1.8886	17.5	0.3552	-4.3255	-0.4772	3.5	-3.8483	13.0
12	0.3154	12.5	0	0	0	0	0	0
14	0.8381	14.5	0.2612	-2.9466	-0.2187	2.1	-2.7279	11.4
16	1.5361	16.5	0.3488	-4.2168	-0.4552	3.4	-3.7615	12.1
18	2.2110	18.5	0.3373	-4.0270	-0.4176	3.2	-3.6094	14.3

Table B.2

^{188}Au								
I	$E_{exc}(I)$	$I_x(I)$	$\hbar\omega(I-1)$	$E'(I-1)$	$E'_{ref}(I-1)$	$I_{xref}(I-1)$	$e'(I-1)$	$i_x(I-1)$
11	0	11.5	0	0	0	0	0	0
13	0.4470	13.5	0.2233	-2.5658	-0.1474	1.7	-2.4183	10.8
15	1.1690	15.5	0.3608	-4.4203	-0.4967	3.6	-3.9235	10.9
17	1.9620	17.5	0.3963	-4.9707	-0.6354	4.2	-4.3353	12.2
19	2.6680	19.5	0.3529	-4.2107	-0.4690	3.4	-3.7417	15.1
21	3.5660	21.5	0.4489	-6.0820	-0.8881	5.4	-5.1940	15.1
12	0.3140	12.5	0	0	0	0	0	0
14	0.8030	14.5	0.2443	-3.2267	-0.1850	1.9	-3.0417	11.6
16	1.5340	16.5	0.3653	-5.2218	-0.5131	3.7	-4.7087	11.8
18	2.2410	18.5	0.3534	-5.0007	-0.4707	3.4	-4.5300	14.0
20	2.8720	20.5	0.3154	-4.2227	-0.3518	2.8	-3.8709	16.7

Table B.3

^{190}Au								
I	$E_{exc}(I)$	$I_x(I)$	$\hbar\omega(I-1)$	$E'(I-1)$	$E'_{ref}(I-1)$	$I_{xref}(I-1)$	$e'(I-1)$	$i_x(I-1)$
11	0	11.5	0	0	0	0	0	0
13	0.4280	13.5	0.2138	-2.4567	-0.1320	1.6	-2.3247	10.9
15	1.1460	15.5	0.3588	-4.4123	-0.4896	3.5	-3.9227	11.0
17	1.9300	17.5	0.3918	-4.9240	-0.6165	4.2	-4.3075	12.3
19	2.4370	19.5	0.2534	-2.5028	-0.2027	2.0	-2.3001	16.5
21	2.8990	21.5	0.2309	-2.0647	-0.1605	1.8	-1.9042	18.7
12	0.2820	12.5	0	0	0	0	0	0
14	0.7440	14.5	0.2308	-2.6012	-0.1603	1.8	-2.4409	11.7

Table B.3 (Continued)

I	$E_{exc}(I)$	$I_x(I)$	$\hbar\omega(I-1)$	$E'(I-1)$	$E'_{ref}(I-1)$	$I_{xref}(I-1)$	$e'(I-1)$	$i_x(I-1)$
16	1.4690	16.5	0.3623	-4.5064	-0.5022	3.6	-4.0042	11.9
18	2.2660	18.5	0.3983	-5.1005	-0.6440	4.3	-4.4565	13.2
20	2.7290	20.5	0.2314	-2.0138	-0.1614	1.8	-1.8524	17.7

Table B.4

^{192}Au								
I	$E_{exc}(I)$	$I_x(I)$	$\hbar\omega(I-1)$	$E'(I-1)$	$E'_{ref}(I-1)$	$I_{xref}(I-1)$	$e'(I-1)$	$i_x(I-1)$
11	0	11.5	0	0	0	0	0	
13	0.4080	13.5	0.2038	-2.3419	-0.1168	1.5	-2.2251	11.0
15	1.1160	15.5	0.3538	-4.3649	-0.4722	3.5	-3.8927	11.0
17	1.8850	17.5	0.3843	-4.8379	-0.5859	4.0	-4.2520	12.5
12	0.2270	12.5	0	0	0	0	0	
14	0.6670	14.5	0.2198	-2.5189	-0.1417	1.6	-2.3772	11.9
16	1.3880	16.5	0.3603	-4.5544	-0.4950	3.6	-4.0594	11.9
18	2.1770	18.5	0.3943	-5.1156	-0.6270	4.2	-4.4886	13.3

Table B.5

^{194}Au								
I	$E_{exc}(I)$	$I_x(I)$	$\hbar\omega(I-1)$	$E'(I-1)$	$E'_{ref}(I-1)$	$I_{xref}(I-1)$	$e'(I-1)$	$i_x(I-1)$
11	0	11.5	0	0	0	0	0	
13	0.3647	13.5	0.1822	-2.0934	-0.0870	1.3	-2.0063	11.2
15	1.0504	15.5	0.3426	-4.2578	-0.4348	3.3	-3.8231	11.2
17	1.7095	17.5	0.3294	-4.0526	-0.3930	3.0	-3.6596	13.4
12	0.1430	12.5	0	0	0	0	0	
14	0.5577	14.5	0.2072	-2.4450	-0.1218	1.5	-2.3232	12.0
16	1.2730	16.5	0.3575	-4.6224	-0.4850	3.5	-4.1375	12.0

Table B.6-10: Rotational frequency $\hbar\omega$, Routhians e' (MeV), and signature splitting [$e'(12^-)-e'(11^-)$] (MeV) for the 11^- and 12^- bands of the odd-odd $^{186-192}\text{Au}$ nuclei.

Table B.6

^{186}Au			
$\hbar\omega$	$e'(11^-)$	$e'(12^-)$	$e'(12^-)-e'(11^-)$
0.261	-2.8180	-2.728	0.0901
0.349	-3.7755	-3.762	0.0140

Table B.7

^{188}Au			
$\hbar\omega$	$e'(11^-)$	$e'(12^-)$	$e'(12^-)-e'(11^-)$
0.244	-2.6490	-2.5527	0.0963
0.361	-3.9235	-3.9245	-0.0009
0.365	-3.9760	-3.9776	-0.0016

Table B.8

¹⁹⁰ Au			
$\hbar\omega$	$e'(11')$	$e'(12')$	$e'(12')-e'(11')$
0.231	-2.5125	-2.4409	0.0716
0.359	-3.9227	-3.9620	-0.0393
0.362	-3.9640	-4.0042	-0.0402
0.392	-4.3076	-4.3750	-0.0675

Table B.9

¹⁹² Au			
$\hbar\omega$	$e'(11')$	$e'(12')$	$e'(12')-e'(11')$
0.220	-2.4031	-2.3772	0.0259
0.354	-3.8927	-3.9800	-0.0873
0.360	-3.9700	-4.0594	-0.0894
0.384	-4.2520	-4.3620	-0.1100

Table B.10

¹⁹⁴ Au			
$\hbar\omega$	$e'(11')$	$e'(12')$	$e'(12')-e'(11')$
0.207	-2.2892	-2.3232	-0.0340
0.343	-3.8231	-3.9590	-0.1359

Table B.11: Spins I (\hbar), aligned angular momentum I_x (\hbar), rotational frequency $\hbar\omega$ (MeV), Routhians E' (MeV) and e' (MeV), reference Routhians E'_{ref} (MeV) and reference aligned angular momentum I_{xref} (\hbar) and alignment i_x (\hbar) for the 22^- band of the odd-odd ¹⁹⁰Au nuclei calculated with Harris parameters of $J_0 = 6\hbar^2(\text{MeV})^{-1}$ and $J_1 = 30\hbar^4(\text{MeV})^{-3}$ and $K = 0$.

¹⁹⁰ Au								
I	$E_{exc}(I)$	$I_x(I)$	$\hbar\omega(I-1)$	$E'(I-1)$	$E'_{ref}(I-1)$	$I_{xref}(I-1)$	$e'(I-1)$	$i_x(I-1)$
22	2.9780	22.5	0	0	0	0	0	
24	3.4900	24.5	0.2559	-2.7793	-0.2079	2.0	-2.5714	21.5
26	4.2680	26.5	0.3889	-6.0367	-0.6046	4.1	-5.4321	21.4
28	5.1200	28.5	0.4259	-7.0171	-0.7703	4.9	-6.2469	22.6
30	5.5880	30.5	0.2340	-1.5470	-0.1659	1.8	-1.3812	27.7
32	6.3890	32.5	0.4004	-6.6241	-0.6531	4.3	-5.9710	27.2

Table B.12-15: Spins I (\hbar), aligned angular momentum I_x (\hbar), rotational frequency $\hbar\omega$ (MeV), Routhians E' (MeV) and e' (MeV), reference Routhians E'_{ref} (MeV) and reference aligned angular momentum I_{xref} (\hbar) and alignment i_x (\hbar) for the 20^+ , 21^+ and 22^+ bands of the odd-odd ^{190}Au nuclei calculated with Harris parameters of $J_0 = 6\hbar^2(\text{MeV})^{-1}$ and $J_1 = 30\hbar^4(\text{MeV})^{-3}$ and $K = 0$.

Table B.12

^{186}Au								
I	E_{exc} (I)	I_x (I)	$\hbar\omega$ (I-1)	E' (I-1)	E'_{ref} (I-1)	I_{xref} (I-1)	e' (I-1)	i_x (I-1)
20	2.6038	20.5	0	0	0	0	0	0
22	3.1147	22.5	0.2554	-2.6300	-0.2067	2.0	-2.4232	19.5
24	3.8691	24.5	0.3771	-5.3683	-0.5575	3.9	-4.8108	19.6

Table B.13

^{188}Au								
I	E_{exc} (I)	I_x (I)	$\hbar\omega$ (I-1)	E' (I-1)	E'_{ref} (I-1)	I_{xref} (I-1)	e' (I-1)	i_x (I-1)
20	2.2568	20.5	0	0	0	0	0	0
22	2.7891	22.5	0.2661	-3.1962	-0.2292	2.2	-2.9670	19.3
24	3.5668	24.5	0.3888	-5.9559	-0.6039	4.1	-5.3520	19.4
26	4.3850	26.5	0.4090	-6.4521	-0.6910	4.5	-5.7612	21.0
21	2.7331	21.5	0	0	0	0	0	0
23	3.2530	23.5	0.2599	-2.8529	-0.2160	2.1	-2.6369	20.4
25	4.0705	25.5	0.4087	-6.3485	-0.6894	4.5	-5.6591	20.0

Table B.14

^{190}Au								
I	E_{exc} (I)	I_x (I)	$\hbar\omega$ (I-1)	E' (I-1)	E'_{ref} (I-1)	I_{xref} (I-1)	e' (I-1)	i_x (I-1)
20	2.1720	20.5	0	0	0	0	0	0
22	2.7280	22.5	0.2779	-3.5238	-0.2556	2.3	-3.2681	19.2
24	3.4950	24.5	0.3834	-5.8967	-0.5823	4.0	-5.3144	19.5
26	4.3340	26.5	0.4194	-6.7786	-0.7390	4.7	-6.0396	20.8
28	4.6450	28.5	0.1555	0.2147	-0.0561	1.0	0.2707	26.4
30	5.3790	30.5	0.3669	-5.8114	-0.5191	3.7	-5.2923	25.8
32	6.0530	32.5	0.3370	-4.8968	-0.4165	3.2	-4.4804	28.3
34	7.0340	34.5	0.4904	-9.8846	-1.1347	6.5	-8.7499	27.0
21	2.6630	21.5	0	0	0	0	0	0
23	3.2560	23.5	0.2964	-3.7085	-0.3007	2.6	-3.4078	19.9
25	4.1060	25.5	0.4249	-6.7272	-0.7653	4.9	-5.9619	19.6
22	3.0030	22.5	0	0	0	0	0	0
24	3.6790	24.5	0.3379	-4.5984	-0.4195	3.2	-4.1789	20.3
26	4.5170	26.5	0.4189	-6.5824	-0.7366	4.7	-5.8458	20.8
28	5.1520	28.5	0.3174	-3.8939	-0.3576	2.9	-3.5362	24.6
30	5.7420	30.5	0.2950	-3.2530	-0.2969	2.5	-2.9561	27.0
32	6.2220	32.5	0.2400	-1.5761	-0.1768	1.9	-1.3993	29.6

Table B.14 (Continued)

I	E _{exc} (I)	I _x (I)	$\hbar\omega$ (I-1)	E' (I-1)	E' _{ref} (I-1)	I _{xref} (I-1)	e' (I-1)	i _x (I-1)
34	7.0680	34.5	0.4230	-7.5223	-0.7558	4.8	-6.7665	28.7

Table B.15

¹⁹² Au								
I	E _{exc} (I)	I _x (I)	$\hbar\omega$ (I-1)	E' (I-1)	E' _{ref} (I-1)	I _{xref} (I-1)	e' (I-1)	i _x (I-1)
20	2.1530	20.5	0	0	0	0	0	
22	2.6140	22.5	0.2304	-2.5696	-0.1596	1.7	-2.4099	19.7
24	3.3540	24.5	0.3699	-5.7071	-0.5301	3.7	-5.1769	19.8
26	4.2060	26.5	0.4259	-7.0788	-0.7702	4.9	-6.3086	20.6

Table B.16-17: Rotational frequency $\hbar\omega$ (MeV), Routhians e' (MeV), and signature splitting $[e'(20^+)-e'(21^+)]$ (MeV), $[e'(22^+)-e'(20^+)]$ (MeV) and $[e'(22^+)-e'(21^+)]$ (MeV) for the 20^+ , 21^+ and 22^+ bands of the odd-odd ^{188,190}Au nuclei calculated with Harris parameters of $J_0 = 6\hbar^2(\text{MeV})^{-1}$ and $J_1 = 30\hbar^4(\text{MeV})^{-3}$ and $K = 0$.

Table B.16

¹⁸⁸ Au			
$\hbar\omega$ (MeV)	Quasiparticle Routhians (MeV)		Signature splitting (MeV)
	e'(20 ⁺)	e'(21 ⁺)	e'(20 ⁺)-e'(21 ⁺)
0.267	-2.9670	-2.7800	-0.1870
0.389	-5.3520	-5.2500	-0.1020
0.409	-5.7500	-5.6591	-0.0909

Table B.17

¹⁹⁰ Au						
$\hbar\omega$ (MeV)	Quasiparticle Routhians (MeV)			Signature splitting (MeV)		
	e'(20 ⁺)	e'(21 ⁺)	e'(22 ⁺)	e'(20 ⁺)-e'(21 ⁺)	e'(22 ⁺)-e'(20 ⁺)	e'(22 ⁺)-e'(21 ⁺)
0.296	-3.6200	-3.4078		-0.2122		
0.338	-4.4300	-4.2200	-4.1789	-0.2100	0.2511	0.0411
0.383	-5.3144	-5.1400	-5.1500	-0.1744	0.1644	-0.0100
0.419	-6.0000	-5.8800	-5.8458	-0.1200	0.1542	0.0342

Table B.18-21: Spins I (\hbar), aligned angular momentum I_x (\hbar), rotational frequency $\hbar\omega$ (MeV), Routhians E' (MeV) and e' (MeV), reference Routhians E'_{ref} (MeV) and reference aligned angular momentum I_{xref} (\hbar) and alignment i_x (\hbar) for the $11/2^-$ band of the odd-even $^{187-193}\text{Au}$ nuclei calculated with Harris parameters of $J_0 = 6\hbar^2(\text{MeV})^{-1}$ and $J_1 = 30\hbar^4(\text{MeV})^{-3}$ and $K = 0$.

Table B.18

^{187}Au								
I	$E_{exc}(\text{I})$	$I_x(\text{I})$	$\hbar\omega(\text{I-1})$	$E'(\text{I-1})$	$E'_{ref}(\text{I-1})$	$I_{xref}(\text{I-1})$	$e'(\text{I-1})$	$i_x(\text{I-1})$
5.5	0.225	6.0	0	0	0	0	0	
7.5	0.674	8.0	0.2245	-1.1180	-0.1494	1.7	-0.9686	5.3
9.5	1.317	10.0	0.3215	-1.8935	-0.3694	2.9	-1.5241	6.1
11.5	2.008	12.0	0.3455	-2.1341	-0.4441	3.3	-1.6899	7.7

Table B.19

^{189}Au								
I	$E_{exc}(\text{I})$	$I_x(\text{I})$	$\hbar\omega(\text{I-1})$	$E'(\text{I-1})$	$E'_{ref}(\text{I-1})$	$I_{xref}(\text{I-1})$	$e'(\text{I-1})$	$i_x(\text{I-1})$
5.5	0.2471	6.0	0	0	0	0	0	
7.5	0.6817	8.0	0.2173	-1.0528	-0.1375	1.6	-0.9153	5.4
9.5	1.412	10.0	0.3652	-2.2344	-0.5125	3.7	-1.7219	5.3
11.5	2.2055	12.0	0.3968	-2.5510	-0.6372	4.3	-1.9138	6.7

Table B.20

^{191}Au								
I	$E_{exc}(\text{I})$	$I_x(\text{I})$	$\hbar\omega(\text{I-1})$	$E'(\text{I-1})$	$E'_{ref}(\text{I-1})$	$I_{xref}(\text{I-1})$	$e'(\text{I-1})$	$i_x(\text{I-1})$
5.5	0	6.0	0	0	0	0	0	
7.5	0.42	8.0	0.2100	-1.2562	-0.1261	1.5	-1.1302	5.4
9.5	1.145	10.0	0.3625	-2.4750	-0.5029	3.6	-1.9721	5.4
11.5	1.92	12.0	0.3875	-2.7256	-0.5987	4.1	-2.1269	6.9
13.5	2.18	14.0	0.1300	0.3613	-0.0320	0.8	0.3933	12.1

Table B.21

^{193}Au								
I	$E_{exc}(\text{I})$	$I_x(\text{I})$	$\hbar\omega(\text{I-1})$	$E'(\text{I-1})$	$E'_{ref}(\text{I-1})$	$I_{xref}(\text{I-1})$	$e'(\text{I-1})$	$i_x(\text{I-1})$
5.5	0	6.0	0	0	0	0	0	
7.5	0.408	8.0	0.2040	-1.2204	-0.1170	1.5	-1.1033	5.5
9.5	1.129	10.0	0.3605	-2.4710	-0.4957	3.6	-1.9753	5.4
11.5	1.883	12.0	0.3770	-2.6367	-0.5571	3.9	-2.0797	7.1
13.5	2.088	14.0	0.1025	0.6540	-0.0115	0.6	0.6655	12.3

Table B.22-25: Spins I (\hbar), aligned angular momentum I_x (\hbar), rotational frequency $\hbar\omega$ (MeV), Routhians E' (MeV) and e' (MeV), reference Routhians E'_{ref} (MeV) and reference aligned angular momentum I_{xref} (\hbar) and alignment i_x (\hbar) for the $31/2^-$, $33/2^-$ and $35/2^-$ bands of the odd-even $^{187-191}\text{Au}$ nuclei calculated with Harris parameters of $J_0 = 6\hbar^2(\text{MeV})^{-1}$ and $J_1 = 30\hbar^4(\text{MeV})^{-3}$ and $K = 0$.

Table B.22

^{187}Au									
I	$E_{exc}(I)$	$I_x(I)$	$\hbar\omega(I-1)$	$E'(I-1)$	$E'_{ref}(I-1)$	$I_{xref}(I-1)$	$e'(I-1)$	$i_x(I-1)$	
15.5	2.6698	16.0	0	0	0	0	0	0	
17.5	3.1292	18.0	0.2297	-1.0037	-0.1583	1.7	-0.8454	15.3	
19.5	3.7621	20.0	0.3165	-2.5648	-0.3548	2.8	-2.2100	16.1	
21.5	4.5067	22.0	0.3723	-3.6817	-0.5391	3.8	-3.1426	17.2	
16.5	2.9669	17.0	0.2580	-1.4173	-0.2121	2.1	-1.2052	15.9	
18.5	3.4829	19.0	0.3716	-3.5752	-0.5364	3.8	-3.0387	16.2	
20.5	4.2261	21.0							
17.5	3.3540	18.0	0.3309	-2.5996	-0.3975	3.1	-2.2021	15.9	
19.5	4.0160	20.0	0.3209	-2.4002	-0.3677	2.9	-2.0325	18.1	
21.5	4.6580	22.0							

Table B.23

^{189}Au									
I	$E_{exc}(I)$	$I_x(I)$	$\hbar\omega(I-1)$	$E'(I-1)$	$E'_{ref}(I-1)$	$I_{xref}(I-1)$	$e'(I-1)$	$i_x(I-1)$	
15.5	2.5540	16.0	0	0	0	0	0	0	
17.5	2.9892	18.0	0.2175	-0.9244	-0.1379	1.6	-0.7865	15.4	
19.5	3.5604	20.0	0.2855	-2.1478	-0.2735	2.4	-1.8743	16.6	
21.5	4.2543	22.0	0.3469	-3.3745	-0.4486	3.3	-2.9258	17.7	
23.5	4.9041	24.0	0.3248	-2.8900	-0.3792	3.0	-2.5108	20.0	
25.5	5.7079	26.0	0.4018	-4.7375	-0.6591	4.4	-4.0784	20.6	
27.5	6.3059	28.0	0.2989	-2.0633	-0.3072	2.6	-1.7562	24.4	
16.5	2.8626	17.0	0	0	0	0	0	0	
18.5	3.3590	19.0	0.2481	-1.3533	-0.1923	1.9	-1.1611	16.0	
20.5	4.1026	21.0	0.3717	-3.7005	-0.5368	3.8	-3.1638	16.2	
17.5	3.1603	18.0	0	0	0	0	0	0	
19.5	3.8381	20.0	0.3388	-2.9354	-0.4223	3.2	-2.5132	15.8	
21.5	4.5262	22.0	0.3440	-3.0388	-0.4390	3.3	-2.5998	17.7	

Table B.24

^{191}Au									
I	$E_{exc}(I)$	$I_x(I)$	$\hbar\omega(I-1)$	$E'(I-1)$	$E'_{ref}(I-1)$	$I_{xref}(I-1)$	$e'(I-1)$	$i_x(I-1)$	
15.5	2.2360	16.0	0	0	0	0	0	0	
17.5	2.6140	18.0	0.1889	-0.7852	-0.0958	1.3	-0.6894	15.7	
19.5	3.1060	20.0	0.2459	-1.8108	-0.1880	1.9	-1.6227	17.1	

Table B.24 (Continued)

I	E _{exc} (I)	I _x (I)	$\hbar\omega$ (I-1)	E' (I-1)	E' _{ref} (I-1)	I _{xref} (I-1)	e' (I-1)	i _x (I-1)
21.5	3.8460	22.0	0.3699	-4.2896	-0.5300	3.7	-3.7596	17.3
23.5	4.6740	24.0	0.4139	-5.2575	-0.7132	4.6	-4.5442	18.4
25.5	5.1870	26.0	0.2564	-1.4794	-0.2089	2.0	-1.2705	23.0
27.5	5.7650	28.0	0.2890	-2.3243	-0.2819	2.5	-2.0424	24.5
29.5	6.6130	30.0	0.4239	-6.1033	-0.7606	4.8	-5.3428	24.2
31.5	7.5610	32.0	0.4739	-7.6032	-1.0314	6.0	-6.5718	25.0
16.5	2.6610	17.0	0	0	0	0	0	
18.5	3.1370	19.0	0.2379	-1.3817	-0.1730	1.8	-1.2087	16.2
15.5	2.2360	16.0	0	0	0	0	0	
17.5	2.7420	18.0	0.2529	-1.8083	-0.2017	2.0	-1.6066	15.0
19.5	3.4710	20.0	0.3644	-3.8142	-0.5097	3.6	-3.3045	15.4
21.5	4.1390	22.0	0.3339	-3.2050	-0.4069	3.1	-2.7981	17.9
23.5	4.8060	24.0	0.3334	-3.1944	-0.4054	3.1	-2.7890	19.9

Table B.25

¹⁹³ Au								
I	E _{exc} (I)	I _x (I)	$\hbar\omega$ (I-1)	E' (I-1)	E' _{ref} (I-1)	I _{xref} (I-1)	e' (I-1)	i _x (I-1)
15.5	2.1870	16.0	0	0	0	0	0	
17.5	2.4120	18.0	0.1125	0.3887	-0.0183	0.7	0.4070	16.3
19.5	2.8660	20.0	0.2269	-1.6710	-0.1535	1.7	-1.5175	17.3
21.5	3.6070	22.0	0.3704	-4.5396	-0.5319	3.7	-4.0077	17.2

Table B.26-28: Rotational frequency $\hbar\omega$ (MeV), Routhians e' (MeV), and signature splitting $[e'(31/2)-e'(35/2)]$ (MeV), $[e'(31/2)-e'(33/2)]$ (MeV) and $[e'(33/2)-e'(35/2)]$ (MeV) for the $31/2^-$, $33/2^-$ and $35/2^-$ bands of the odd-even ¹⁸⁷⁻¹⁹¹Au nuclei calculated with Harris parameters of $J_0 = 6\hbar^2(\text{MeV})^{-1}$ and $J_1 = 30\hbar^4(\text{MeV})^{-3}$ and $K = 0$.

Table B.26

¹⁸⁷ Au						
$\hbar\omega$ (MeV)	Quasiparticle Routhians (MeV)			Signature splitting (MeV)		
	e'(31/2)	e'(33/2)	e'(35/2)	e'(31/2)- e'(35/2)	e'(31/2)- e'(33/2)	e'(33/2)- e'(35/2)
0.258	-1.2800	-1.2052			-0.0748	
0.317	-2.2100	-2.1800			-0.0300	
0.321	-2.2800	-2.2000	-2.0325	-0.2475	-0.0800	-0.1675
0.331	-2.4400	-2.4000	-2.2021	-0.2379	-0.0400	-0.1979
0.372	-3.1000	-3.0387			-0.0613	

Table B.27

¹⁸⁹ Au						
$\hbar\omega$ (MeV)	Quasiparticle Routhians (MeV)			Signature splitting (MeV)		
	e'(31/2)	e'(33/2)	e'(35/2)	e'(31/2)- e'(35/2)	e'(31/2)- e'(33/2)	e'(33/2)- e'(35/2)
0.248	-1.2300	-1.1611			-0.0689	
0.286	-1.8743	-1.7800			-0.0943	
0.339	-2.8000	-2.6100	-2.5132	-0.2868	-0.1900	-0.0968
0.344	-2.8800	-2.7000	-2.5998	-0.2802	-0.1800	-0.1002

Table B.28

¹⁹¹ Au					
$\hbar\omega$ (MeV)	Quasiparticle Routhians (MeV)			Signature splitting (MeV)	
	e'(31/2)	e'(33/2)	e'(35/2)	e'(31/2)- e'(35/2)	e'(31/2)- e'(33/2)
0.238	-1.4500	-1.2087			-0.2413
0.253	-1.7300		-1.6066	-0.1234	
0.364	-3.6300		-3.3045	-0.3255	

Table B.29-32: Spins I (\hbar), aligned angular momentum I_x (\hbar), rotational frequency $\hbar\omega$ (MeV), Routhians E' (MeV) and e' (MeV), reference Routhians E'_{ref} (MeV) and reference aligned angular momentum I_{xref} (\hbar) and alignment i_x (\hbar) for the $31/2^+$ and $33/2^+$ bands of the odd-even ¹⁸⁷⁻¹⁹¹Au nuclei calculated with Harris parameters of $J_0 = 6\hbar^2(\text{MeV})^{-1}$ and $J_1 = 30\hbar^4(\text{MeV})^{-3}$ and $K = 0$.

Table B.29

¹⁸⁷ Au								
I	E_{exc} (I)	I_x (I)	$\hbar\omega$ (I-1)	E' (I-1)	E'_{ref} (I-1)	I_{xref} (I-1)	e' (I-1)	i_x (I-1)
15.5	2.5650	16.0	0	0	0	0	0	0
17.5	3.0560	18.0	0.2454	-1.3594	-0.1870	1.9	-1.1724	15.1
19.5	3.8100	20.0	0.3769	-3.7250	-0.5566	3.9	-3.1685	15.1
21.5	4.5760	22.0	0.3829	-3.8454	-0.5802	4.0	-3.2653	17.0
23.5	4.7870	24.0	0.1055	2.2561	-0.0135	0.7	2.2696	22.3
25.5	5.3740	26.0	0.2934	-2.2541	-0.2931	2.5	-1.9610	22.5

Table B.30

¹⁸⁹ Au								
I	E_{exc} (I)	I_x (I)	$\hbar\omega$ (I-1)	E' (I-1)	E'_{ref} (I-1)	I_{xref} (I-1)	e' (I-1)	i_x (I-1)
15.5	2.5150	16.0	0	0	0	0	0	0
17.5	3.0220	18.0	0.2534	-1.5373	-0.2027	2.0	-1.3346	15.0
19.5	3.8050	20.0	0.3914	-4.0198	-0.6146	4.1	-3.4052	14.8
21.5	4.4390	22.0	0.3169	-2.5312	-0.3561	2.9	-2.1751	18.1
23.5	4.6580	24.0	0.1095	2.0312	-0.0162	0.7	2.0474	22.3
25.5	5.2750	26.0	0.3084	-2.7429	-0.3324	2.7	-2.4105	22.3
18.5	3.5227	19.0	0.3813	-3.7191	-0.5738	4.0	-3.1453	16.0

Table B.30 (Continued)

I	E_{exc} (I)	I_x (I)	$\hbar\omega$ (I-1)	E' (I-1)	E'_{ref} (I-1)	I_{xref} (I-1)	e' (I-1)	i_x (I-1)
20.5	4.2855	21.0						

Table B.31

¹⁹¹ Au								
I	E_{exc} (I)	I_x (I)	$\hbar\omega$ (I-1)	E' (I-1)	E'_{ref} (I-1)	I_{xref} (I-1)	e' (I-1)	i_x (I-1)
15.5	2.2230	16.0	0	0	0	0	0	0
17.5	2.7310	18.0	0.2539	-1.8373	-0.2037	2.0	-1.6335	15.0
19.5	3.5440	20.0	0.4064	-4.5806	-0.6791	4.5	-3.9016	14.5
21.5	4.1540	22.0	0.3049	-2.5524	-0.3229	2.7	-2.2295	18.3
23.5	4.4220	24.0	0.1340	1.2075	-0.0354	0.9	1.2429	22.1
25.5	4.9350	26.0	0.2564	-1.7314	-0.2089	2.0	-1.5225	23.0
18.5	3.2270	19.0	0	0	0	0	0	
20.5	4.0220	21.0	0.3974	-4.3205	-0.6399	4.3	-3.6806	15.7

Table B.32

¹⁹³ Au								
I	E_{exc} (I)	I_x (I)	$\hbar\omega$ (I-1)	E' (I-1)	E'_{ref} (I-1)	I_{xref} (I-1)	e' (I-1)	i_x (I-1)
15.5	2.1970	16.0	0	0	0	0	0	
17.5	2.6340	18.0	0.2184	-1.2958	-0.1393	1.6	-1.1564	15.4
19.5	3.1530	20.0	0.2594	-2.0336	-0.2150	2.1	-1.8186	16.9
21.5	3.7750	22.0	0.3109	-3.0633	-0.3392	2.8	-2.7240	18.2



Appendix C Tables of results from CSM calculations



Table C.1-5: Rotational frequency $\hbar\omega$ (MeV), quasiproton Routhian $e'(e)$ (MeV), quasineutron Routhians $e'(B)$ (MeV) and $e'(A)$ (MeV), and the total quasiparticle Routhians $e'(eA)$ (MeV) and $e'(eA)$ (MeV) for the 11^- and 12^- bands of the odd-odd $^{186-194}\text{Au}$ nuclei.

Table C.1

^{186}Au							
$\hbar\omega$	$e'(e)$	$e'(B)$	$e'(eB)$		$e'(e)$	$e'(A)$	$e'(eA)$
0	0.7394	1.0725	1.8119		0.7939	1.1426	1.9365
0.05	0.4760	0.9202	1.3962		0.5347	0.8942	1.4289
0.10	0.2118	0.6955	0.9073		0.2736	0.6710	0.9446
0.15	-0.0531	0.4424	0.3893		0.0116	0.4362	0.4478
0.20	-0.3182	0.1809	-0.1373		-0.2510	0.1628	-0.0882
0.25	-0.5837	-0.0834	-0.6671		-0.5142	-0.0854	-0.5996
0.30	-0.8490	-0.3481	-1.1971		-0.7773	-0.3752	-1.1525
0.35	-1.1139	-0.6168	-1.7307		-1.0396	-0.6744	-1.7140
0.40	-1.3810	-0.8811	-2.2621		-1.3061	-0.9834	-2.2895
0.45	-1.6453	-1.1447	-2.7900		-1.5676	-1.2909	-2.8585
0.50	-1.9089	-1.4133	-3.3222		-1.8287	-1.5969	-3.4256
0.55	-2.1639	-1.6760	-3.8399		-2.0813	-1.9365	-4.0178

Table C.2

^{188}Au							
$\hbar\omega$	$e'(e)$	$e'(B)$	$e'(eB)$		$e'(e)$	$e'(A)$	$e'(eA)$
0	0.6940	1.0170	1.7110		0.7525	1.0201	1.7726
0.05	0.4298	0.8491	1.2789		0.4938	0.8314	1.3252
0.10	0.1648	0.5880	0.7528		0.2332	0.5957	0.8289
0.15	-0.1007	0.3217	0.2210		-0.0286	0.3451	0.3165
0.20	-0.3664	0.0548	-0.3116		-0.2909	0.0663	-0.2246
0.25	-0.6342	-0.2123	-0.8465		-0.5541	-0.2317	-0.7858
0.30	-0.8983	-0.4784	-1.3767		-0.8169	-0.5380	-1.3549
0.35	-1.1635	-0.7454	-1.9089		-1.0765	-0.8426	-1.9191
0.40	-1.4310	-1.0104	-2.4414		-1.3455	-1.1638	-2.5093
0.45	-1.6958	-1.2670	-2.9628		-1.6068	-1.4754	-3.0822
0.50	-1.9595	-1.5388	-3.4983		-1.8656	-1.7678	-3.6334
0.55	-2.2051	-1.7983	-4.0034		-2.1726	-2.1092	-4.2818

Table C.3

^{190}Au							
$\hbar\omega$	$e'(e)$	$e'(B)$	$e'(eB)$		$e'(e)$	$e'(A)$	$e'(eA)$
0	0.6566	0.9376	1.5942		0.7213	0.9406	1.6619
0.05	0.3919	0.7172	1.1091		0.4636	0.7573	1.2209
0.10	0.1265	0.4518	0.5783		0.2035	0.5118	0.7153
0.15	-0.1393	0.1857	0.0464		-0.0579	0.2198	0.1619
0.20	-0.4050	-0.0805	-0.4855		-0.3190	-0.0880	-0.4070
0.25	-0.6715	-0.3464	-1.0179		-0.5828	-0.4017	-0.9845
0.30	-0.9376	-0.5892	-1.5268		-0.8450	-0.7138	-1.5588
0.35	-1.2027	-0.8756	-2.0783		-1.0871	-1.0318	-2.1189
0.40	-1.4707	-1.1353	-2.6060		-1.3735	-1.3437	-2.7172

Table C.3 (Continued)

$\hbar\omega$	$e'(e)$	$e'(B)$	$e'(eB)$		$e'(e)$	$e'(A)$	$e'(eA)$
0.45	-1.7357	-1.4229	-3.1586		-1.6339	-1.6574	-3.2913
0.50	-1.9989	-1.6686	-3.6675		-1.8873	-1.9707	-3.8580
0.55	-2.2940	-1.9203	-4.2143		-2.1818	-2.2827	-4.4645

Table C.4

¹⁹² Au							
$\hbar\omega$	$e'(e)$	$e'(B)$	$e'(eB)$		$e'(e)$	$e'(A)$	$e'(eA)$
0	0.6278	0.8381	1.4659		0.6940	0.8689	1.5629
0.05	0.3629	0.5809	0.9438		0.4376	0.6793	1.1169
0.10	0.0973	0.3190	0.4163		0.1768	0.3709	0.5477
0.15	-0.1687	0.0556	-0.1131		-0.0843	0.0567	-0.0276
0.20	-0.4354	-0.2085	-0.6439		-0.3497	-0.2580	-0.6077
0.25	-0.7014	-0.4720	-1.1734		-0.6090	-0.5730	-1.1820
0.30	-0.9676	-0.7418	-1.7094		-0.8707	-0.8872	-1.7579
0.35	-1.2319	-0.9983	-2.2302		-1.1441	-1.2008	-2.3449
0.40	-1.5009	-1.2494	-2.7503		-1.3992	-1.5123	-2.9115
0.45	-1.7659	-1.5509	-3.3168		-1.6586	-1.7996	-3.4582
0.50	-2.0281	-1.7934	-3.8215		-1.9010	-2.1411	-4.0421
0.55	-2.3125	-2.0394	-4.3519		-2.2031	-2.4451	-4.6482

Table C.5

¹⁹⁴ Au							
$\hbar\omega$	$e'(e)$	$e'(B)$	$e'(eB)$		$e'(e)$	$e'(A)$	$e'(eA)$
0	0.6127	0.7568	1.3695		0.6505	0.7835	1.4340
0.05	0.3489	0.5050	0.8539		0.3900	0.5191	0.9091
0.10	0.0842	0.2472	0.3314		0.1297	0.2046	0.3343
0.15	-0.1810	-0.0131	-0.1941		-0.1352	-0.1102	-0.2454
0.20	-0.4467	-0.2751	-0.7218		-0.3994	-0.4247	-0.8241
0.25	-0.7121	-0.5359	-1.2480		-0.6628	-0.7387	-1.4015
0.30	-0.9775	-0.8171	-1.7946		-0.9261	-1.0482	-1.9743
0.35	-1.2518	-1.0618	-2.3136		-1.1960	-1.3655	-2.5615
0.40	-1.5096	-1.3115	-2.8211		-1.4562	-1.6692	-3.1254
0.45	-1.7731	-1.6262	-3.3993		-1.7166	-1.8812	-3.5978
0.50	-2.0268	-1.8618	-3.8886		-1.9281	-2.3077	-4.2358
0.55	-2.3151	-2.1125	-4.4276		-2.2590	-2.6030	-4.8620

Table C.6-8: Rotational frequency $\hbar\omega$ (MeV), the total quasiparticles Routhians $e'(eA)$ (MeV) and $e'(eB)$ (MeV), and quasiparticle signature splitting [$e'(eA) - e'(eB)$] (MeV) for the 11^- and 12^- bands of the odd-odd ¹⁸⁶⁻¹⁹⁴Au nuclei.

Table C.6

¹⁸⁶ Au				¹⁸⁸ Au			
$\hbar\omega$	$e'(eA)$	$e'(eB)$	$e'(eA) - e'(eB)$	$e'(eA)$	$e'(eB)$	$e'(eA) - e'(eB)$	
0	1.9365	1.8119	0.1246	1.7726	1.7110	0.0616	
0.05	1.4289	1.3962	0.0327	1.3252	1.2789	0.0463	
0.10	0.9446	0.9073	0.0373	0.8289	0.7528	0.0761	

Table C.6 (Continued)

$\hbar\omega$	$e'(eA)$	$e'(eB)$	$e'(eA) - e'(eB)$		$e'(eA)$	$e'(eB)$	$e'(eA) - e'(eB)$
0.15	0.4478	0.3893	0.0585		0.3165	0.2210	0.0955
0.20	-0.0882	-0.1373	0.0491		-0.2246	-0.3116	0.0870
0.25	-0.5996	-0.6671	0.0675		-0.7858	-0.8465	0.0607
0.30	-1.1525	-1.1971	0.0446		-1.3549	-1.3767	0.0218
0.35	-1.7140	-1.7307	0.0167		-1.9191	-1.9089	-0.0102
0.40	-2.2895	-2.2621	-0.0274		-2.5093	-2.4414	-0.0679
0.45	-2.8585	-2.7900	-0.0685		-3.0822	-2.9628	-0.1194
0.50	-3.4256	-3.3222	-0.1034		-3.6334	-3.4983	-0.1351
0.55	-4.0178	-3.8399	-0.1779		-4.2818	-4.0034	-0.2784

Table C.7

^{190}Au				^{192}Au			
$\hbar\omega$	$e'(eA)$	$e'(eB)$	$e'(eA) - e'(eB)$		$e'(eA)$	$e'(eB)$	$e'(eA) - e'(eB)$
0	1.6619	1.5942	0.0677		1.5629	1.4659	0.0970
0.05	1.2209	1.1091	0.1118		1.1169	0.9438	0.1731
0.10	0.7153	0.5783	0.1370		0.5477	0.4163	0.1314
0.15	0.1619	0.0464	0.1155		-0.0276	-0.1131	0.0855
0.20	-0.4070	-0.4855	0.0785		-0.6077	-0.6439	0.0362
0.25	-0.9845	-1.0179	0.0334		-1.1820	-1.1734	-0.0086
0.30	-1.5588	-1.5268	-0.0320		-1.7579	-1.7094	-0.0485
0.35	-2.1189	-2.0783	-0.0406		-2.3449	-2.2302	-0.1147
0.40	-2.7172	-2.6060	-0.1112		-2.9115	-2.7503	-0.1612
0.45	-3.2913	-3.1586	-0.1327		-3.4582	-3.3168	-0.1414
0.50	-3.8580	-3.6675	-0.1905		-4.0421	-3.8215	-0.2206
0.55	-4.4645	-4.2143	-0.2502		-4.6482	-4.3519	-0.2963

Table C.8

^{194}Au			
$\hbar\omega$	$e'(eA)$	$e'(eB)$	$e'(eA) - e'(eB)$
0	1.4340	1.3695	0.0645
0.05	0.9091	0.8539	0.0552
0.10	0.3343	0.3314	0.0029
0.15	-0.2454	-0.1941	-0.0513
0.20	-0.8241	-0.7218	-0.1023
0.25	-1.4015	-1.2480	-0.1535
0.30	-1.9743	-1.7946	-0.1797
0.35	-2.5615	-2.3136	-0.2479
0.40	-3.1254	-2.8211	-0.3043
0.45	-3.5978	-3.3993	-0.1985
0.50	-4.2358	-3.8886	-0.3472
0.55	-4.8620	-4.4276	-0.4344

Table C.9-11: Rotational frequency $\hbar\omega$ (MeV), quasiproton Routhians $e'(e)$ (MeV), quasineutron Routhians $e'(A)$ (MeV), $e'(B)$ (MeV), $e'(C)$ (MeV), and the total quasiparticle Routhians $e'(eABC)$ (MeV) for the 22^- bands of the odd-odd $^{186-194}\text{Au}$ nuclei.

Table C.9

^{186}Au						^{188}Au				
$\hbar\omega$	$e'(e)$	$e'(A)$	$e'(B)$	$e'(C)$	$e'(eABC)$	$e'(e)$	$e'(A)$	$e'(B)$	$e'(C)$	$e'(eABC)$
0	0.9646	1.0488	1.0488	1.1593	4.2215	0.9686	0.9808	0.9808	1.0156	3.9458
0.05	0.8318	0.8445	0.8579	0.9982	3.5324	0.7436	0.7799	0.7803	0.9213	3.2251
0.10	0.6163	0.5626	0.6109	0.7841	2.5739	0.4988	0.5027	0.5280	0.6962	2.2257
0.15	0.3787	0.2631	0.3559	0.5708	1.5685	0.2479	0.2033	0.2707	0.4826	1.2045
0.20	0.1325	-0.0427	0.0986	0.3594	0.5478	-0.0058	-0.1036	0.0118	0.2734	0.1758
0.25	-0.1172	-0.3501	-0.1689	0.1403	-0.4959	-0.2585	-0.4123	-0.2467	0.0656	-0.8519
0.30	-0.3724	-0.6618	-0.4164	-0.0560	-1.5066	-0.5183	-0.7207	-0.4985	-0.1328	-1.8703
0.35	-0.6252	-0.9631	-0.6903	-0.2866	-2.5652	-0.7743	-1.0464	-0.7714	-0.3529	-2.9450
0.40	-0.8581	-1.2827	-0.9375	-0.4810	-3.5593	-1.0517	-1.3472	-1.0249	-0.5523	-3.9761
0.45	-1.1430	-1.5877	-1.1819	-0.6757	-4.5883	-1.2936	-1.6549	-1.2786	-0.7435	-4.9706
0.50	-1.3968	-1.9425	-1.4903	-0.9310	-5.7606	-1.5492	-1.9775	-1.5320	-0.9681	-6.0268

Table C.10

^{190}Au						^{192}Au				
$\hbar\omega$	$e'(e)$	$e'(A)$	$e'(B)$	$e'(C)$	$e'(eABC)$	$e'(e)$	$e'(A)$	$e'(B)$	$e'(C)$	$e'(eABC)$
0	0.7846	0.9380	0.9396	0.9857	3.6479	0.6920	0.8587	0.8540	0.8909	3.2956
0.05	0.5287	0.7491	0.7179	0.8602	2.8559	0.4305	0.6944	0.6026	0.7480	2.4755
0.10	0.2697	0.4807	0.4568	0.6178	1.8250	0.1676	0.3893	0.3437	0.5456	1.4462
0.15	0.0090	0.1766	0.1945	0.4039	0.7840	-0.0961	0.0743	0.0826	0.3439	0.4047
0.20	-0.2523	-0.1349	-0.0678	0.1946	-0.2604	-0.3561	-0.2415	-0.1794	0.1389	-0.6381
0.25	-0.5148	-0.4492	-0.3309	-0.0149	-1.3098	-0.6248	-0.5576	-0.4407	-0.0671	-1.6902
0.30	-0.7769	-0.7625	-0.5925	-0.2261	-2.3580	-0.8891	-0.8733	-0.7110	-0.2866	-2.7600
0.35	-1.0334	-1.0796	-0.8524	-0.4289	-3.3943	-1.1703	-1.1884	-0.9631	-0.4864	-3.8082
0.40	-1.3043	-1.3925	-1.1076	-0.6255	-4.4299	-1.4196	-1.5024	-1.2112	-0.6842	-4.8174
0.45	-1.5652	-1.7062	-1.4124	-0.9223	-5.6061	-1.6825	-1.8078	-1.5265	-0.9809	-5.9977
0.50	-1.8232	-2.0191	-1.6384	-1.0785	-6.5592	-1.9402	-2.1337	-1.7587	-1.1447	-6.9773

Table C.11

^{194}Au					
$\hbar\omega$	$e'(e)$	$e'(A)$	$e'(B)$	$e'(C)$	$e'(eABC)$
0	0.6411	0.8469	0.7619	0.9086	3.1585
0.05	0.3785	0.5323	0.5128	0.7451	2.1687
0.10	0.1149	0.2167	0.2565	0.5583	1.1464
0.15	-0.1495	-0.0991	-0.0026	0.3606	0.1094
0.20	-0.4146	-0.4147	-0.2637	0.1566	-0.9364
0.25	-0.6793	-0.7298	-0.5234	-0.0488	-1.9813
0.30	-0.9439	-1.0428	-0.8051	-0.2359	-3.0277
0.35	-1.2164	-1.3591	-1.0479	-0.4719	-4.0953
0.40	-1.4750	-1.6673	-1.2963	-0.6776	-5.1162

Table C.11 (Continued)

$\hbar\omega$	$e'(e)$	$e'(A)$	$e'(B)$	$e'(C)$	$e'(eABC)$
0.45	-1.7379	-2.0243	-1.6197	-0.8643	-6.2462
0.50	-1.9915	-2.3048	-1.8491	-1.1358	-7.2812

Table C.12-16: Rotational frequency $\hbar\omega$ (MeV), quasiproton Routhians $e'(e)$, quasineutron Routhians $e'(A)$ (MeV), $e'(B)$ (MeV), $e'(C)$ (MeV), $e'(F)$ (MeV) and the total quasiparticle Routhians $e'(eFBC)$ (MeV) and $e'(eFAB)$ (MeV) for the 20^+ and 22^+ bands of the odd-odd $^{186-194}\text{Au}$ nuclei.

Table C.12

^{186}Au											
$\hbar\omega$	$e'(e)$	$e'(A)$	$e'(B)$	$e'(F)$	$e'(eFAB)$		$e'(e)$	$e'(B)$	$e'(C)$	$e'(F)$	$e'(eFBC)$
0	0.7112	1.1070	1.0716	1.0743	3.9641		0.8170	1.0553	1.0556	1.1260	4.0539
0.05	0.4452	1.0684	0.9245	0.8742	3.3123		0.5585	0.8989	0.8876	0.9406	3.2856
0.10	0.1787	0.9848	0.7093	0.6709	2.5437		0.2982	0.6690	0.6649	0.7470	2.3791
0.15	-0.0881	0.8516	0.4577	0.4659	1.6871		0.0367	0.4169	0.4298	0.5509	1.4343
0.20	-0.3551	0.5518	0.1954	0.2601	0.6522		-0.2253	0.1577	0.1782	0.3540	0.4646
0.25	-0.6222	0.2530	-0.7020	0.0539	-1.0170		-0.4880	-0.1038	0.1685	0.1573	-0.2660
0.30	-0.8893	-0.0318	-0.3365	-0.1522	-1.4100		-0.7505	-0.3654	-0.0688	-0.0379	-1.2226
0.35	-1.1562	-0.5448	-0.6051	-0.3600	-2.6660		-1.0125	-0.6352	-0.3018	-0.2487	-2.1982
0.40	-1.4240	-0.8100	-0.8715	-0.5623	-3.6680		-1.2788	-0.8950	-0.5216	-0.4287	-3.1241
0.45	-1.6902	-1.1382	-1.1377	-0.7623	-4.7280		-1.5394	-1.1544	-0.7375	-0.6130	-4.0443
0.50	-1.9562	-1.4454	-1.4055	-0.9590	-5.7660		-1.8003	-1.4255	-0.9498	-0.7818	-4.9574

Table C.13

^{188}Au											
$\hbar\omega$	$e'(e)$	$e'(A)$	$e'(B)$	$e'(F)$	$e'(eFAB)$		$e'(e)$	$e'(B)$	$e'(C)$	$e'(F)$	$e'(eFBC)$
0	0.6608	1.5575	1.0524	1.0055	4.2762		0.6743	1.0404	0.9940	1.0232	3.7319
0.05	0.3929	1.3929	0.8642	0.8018	3.4518		0.4074	0.8596	0.7904	0.8218	2.8792
0.10	0.1248	1.0770	0.5980	0.5956	2.3954		0.1401	0.5956	0.5755	0.6175	1.9287
0.15	-0.1435	0.7617	0.3291	0.3883	1.3356		-0.1273	0.3277	0.3551	0.4119	0.9674
0.20	-0.4119	0.4501	0.0601	0.1805	0.2788		-0.3949	0.0594	0.1287	0.2059	-0.0009
0.25	-0.6803	0.1448	-0.2090	-0.0274	-0.7720		-0.6626	-0.2090	-0.1082	-0.0001	-0.9799
0.30	-0.9487	-0.3485	-0.4777	-0.2354	-2.0100		-0.9302	-0.4769	-0.1680	-0.2098	-1.7849
0.35	-1.2169	-0.6163	-0.7460	-0.4426	-3.0220		-1.1977	-0.7446	-0.4198	-0.4052	-2.7673
0.40	-1.4866	-0.9185	-1.0135	-0.6462	-4.0650		-1.4661	-1.0113	-0.6508	-0.6116	-3.7398
0.45	-1.7534	-1.2156	-1.2767	-0.8470	-5.0930		-1.7327	-1.2739	-0.8947	-0.8085	-4.7098
0.50	-2.0210	-1.5260	-1.5476	-1.0284	-6.1230		-1.9993	-1.5437	-1.1021	-0.9829	-5.6280

Table C.14

¹⁹⁰ Au											
$\hbar\omega$	e'(e)	e'(A)	e'(B)	e'(F)	e'(eFAB)		e'(e)	e'(B)	e'(C)	e'(F)	e'(eFBC)
0	0.6276	1.5765	0.9653	0.9370	4.1064		0.6333	0.9649	0.9288	0.9335	3.4605
0.05	0.3589	1.2584	0.6988	0.7312	3.0473		0.3642	0.6979	0.7228	0.7270	2.5119
0.10	0.0900	0.9411	0.4306	0.5237	1.9854		0.0950	0.4249	0.5094	0.5190	1.5483
0.15	-0.1789	0.6253	0.1619	0.3156	0.9239		-0.1743	0.1604	0.2916	0.3102	0.5879
0.20	-0.4480	0.3128	-0.1068	0.1073	-0.1350		-0.4437	-0.1087	0.0690	0.1013	-0.3821
0.25	-0.7170	0.0093	-0.3753	-0.1004	-1.1830		-0.7130	-0.3776	-0.1624	-0.1070	-1.3600
0.30	-0.9860	-0.4174	-0.6425	-0.3082	-2.3540		-0.9824	-0.6455	-0.2776	-0.3152	-2.2207
0.35	-1.2546	-0.7058	-0.9109	-0.5138	-3.3850		-1.2509	-0.9141	-0.5258	-0.5213	-3.2121
0.40	-1.5234	-1.0174	-1.1763	-0.7160	-4.4330		-1.5206	-1.1803	-0.7531	-0.7233	-4.1773
0.45	-1.7927	-1.3271	-1.4656	-0.9007	-5.4860		-1.7900	-1.4714	-0.9964	-0.9093	-5.1671
0.50	-2.0610	-1.6429	-1.7126	-1.2024	-6.6190		-2.0587	-1.7170	-1.2034	-1.2085	-6.1876

Table C.15

¹⁹² Au											
$\hbar\omega$	e'(e)	e'(A)	e'(B)	e'(F)	e'(eFAB)		e'(e)	e'(B)	e'(C)	e'(F)	e'(eFBC)
0	0.6018	1.2682	0.8066	0.8762	3.5528		0.6108	0.8208	0.8260	0.8849	3.1425
0.05	0.3342	0.9517	0.5438	0.8134	2.6431		0.3436	0.5590	0.7199	0.8812	2.5037
0.10	0.0664	0.6392	0.2787	0.6069	1.5912		0.0760	0.2944	0.5032	0.6760	1.5496
0.15	-0.2017	0.3489	0.0128	0.4001	0.5601		-0.1918	0.0288	0.2299	0.4686	0.5355
0.20	-0.4697	-0.0251	-0.2534	0.1942	-0.5540		-0.4596	-0.2373	0.1111	0.2619	-0.3239
0.25	-0.7379	-0.3379	-0.5193	-0.0099	-1.6050		-0.7277	-0.5030	-0.1041	0.0568	-1.2780
0.30	-1.0060	-0.6545	-0.7903	-0.1982	-2.6490		-0.9956	-0.7726	-0.3231	-0.1427	-2.2340
0.35	-1.2738	-0.9717	-1.0502	-0.4171	-3.7130		-1.2632	-1.0335	-0.5357	-0.3564	-3.1888
0.40	-1.5428	-1.2891	-1.3085	-0.6061	-4.7470		-1.5317	-1.2909	-0.7471	-0.5480	-4.1177
0.45	-1.8097	-1.6061	-1.6012	-0.7549	-5.7720		-1.7988	-1.5825	-1.0080	-0.7145	-5.1038
0.50	-2.0767	-1.9195	-1.8483	-1.0672	-6.9120		-2.0652	-1.8312	-1.1931	-0.9986	-6.0881

Table C.16

¹⁹⁴ Au											
$\hbar\omega$	e'(e)	e'(A)	e'(B)	e'(F)	e'(eFAB)		e'(e)	e'(B)	e'(C)	e'(F)	e'(eFBC)
0	0.5822	0.7013	0.6961	0.8308	2.8104		0.5884	0.7276	0.9348	0.9439	3.1947
0.05	0.3146	0.6632	0.4341	0.8090	2.2209		0.3215	0.4624	0.7833	0.7947	2.3619
0.10	0.0468	0.3448	0.1700	0.7084	1.2700		0.0541	0.1995	0.5832	0.7347	1.5715
0.15	-0.2211	0.0266	-0.0950	0.5169	0.2274		-0.2134	-0.0646	0.3767	0.5838	0.6825
0.20	-0.4892	-0.2916	-0.3607	0.3151	-0.8260		-0.4813	-0.3297	0.1665	0.3895	-0.2550
0.25	-0.7573	-0.6096	-0.6263	0.1137	-1.8800		-0.7488	-0.5944	-0.0457	0.1889	-1.2000
0.30	-1.0253	-0.9271	-0.8824	-0.0822	-2.9170		-1.0165	-0.8756	-0.2570	-0.0103	-2.1594
0.35	-1.2933	-1.2420	-1.1582	-0.3159	-4.0090		-1.2837	-1.1252	-0.4759	-0.1842	-3.0690
0.40	-1.5619	-1.5608	-1.4191	-0.4855	-5.0270		-1.5521	-1.3841	-0.6901	-0.4154	-4.0417
0.45	-1.8289	-1.8739	-1.7236	-0.6073	-6.0340		-1.8188	-1.6848	-0.9010	-0.5955	-5.0001
0.50	-2.0956	-2.2091	-1.9611	-0.9072	-7.1730		-2.0844	-1.9271	-1.1404	-0.8240	-5.9759

Table C.17-19: Rotational frequency $\hbar\omega$ (MeV), quasiproton Routhians $e'(e)$ (MeV), quasineutron Routhians $e'(A)$ (MeV), $e'(C)$ (MeV), $e'(F)$ (MeV) and the total quasiparticle Routhians $e'(eFAC)$ (MeV) for the 21^+ band of the odd-odd $^{186-194}\text{Au}$ nuclei.

Table C.17

^{186}Au						^{188}Au				
$\hbar\omega$	$e'(e)$	$e'(A)$	$e'(C)$	$e'(F)$	$e'(eFAC)$	$e'(e)$	$e'(A)$	$e'(C)$	$e'(F)$	$e'(eFAC)$
0	0.7700	1.1275	1.0732	1.1106	4.0813	0.7133	1.0361	1.0180	1.0216	3.7890
0.05	0.5063	1.0687	0.8967	0.9149	3.3866	0.4483	1.0458	0.8150	0.9140	3.2231
0.10	0.2418	0.9786	0.6744	0.7143	2.6091	0.1827	0.8796	0.5965	0.7101	2.3689
0.15	-0.0234	0.7343	0.4445	0.5119	1.6673	-0.0835	0.5785	0.3663	0.5051	1.3664
0.20	-0.2888	0.4429	0.2032	0.3087	0.6660	-0.3498	0.2954	0.1163	0.2997	0.3616
0.25	-0.5546	0.1689	-0.0568	0.1053	-0.3372	-0.6165	-0.1621	0.0400	0.0948	-0.6438
0.30	-0.8203	-0.3392	-0.0825	-0.0973	-1.3393	-0.8831	-0.4613	-0.1944	-0.1082	-1.6470
0.35	-1.0857	-0.6365	-0.3202	-0.3001	-2.3425	-1.1491	-0.7689	-0.4181	-0.3161	-2.6522
0.40	-1.3527	-0.9446	-0.5463	-0.4997	-3.3433	-1.4168	-1.0847	-0.6345	-0.5150	-3.6510
0.45	-1.6176	-1.2542	-0.7711	-0.6943	-4.3372	-1.6826	-1.3987	-0.8698	-0.7076	-4.6587
0.50	-1.8820	-1.5645	-0.9837	-0.8816	-5.3118	-1.9474	-1.7101	-1.0728	-0.8854	-5.6157

Table C.18

^{190}Au					^{192}Au					
$\hbar\omega$	$e'(e)$	$e'(A)$	$e'(C)$	$e'(F)$	$e'(eFAC)$	$e'(e)$	$e'(A)$	$e'(C)$	$e'(F)$	$e'(eFAC)$
0	0.6562	0.9848	0.9406	0.9345	3.5161	0.6308	0.9054	0.8416	0.8987	3.2765
0.05	0.3899	1.0485	0.7464	0.8987	3.0835	0.3651	0.8194	0.7183	0.9124	2.8152
0.10	0.1231	0.7380	0.5328	0.6926	2.0865	0.0990	0.5480	0.4726	0.7755	1.8951
0.15	-0.1440	0.4404	0.3013	0.4856	1.0833	-0.1676	0.1654	0.3313	0.5708	0.8999
0.20	-0.4113	0.0341	0.1761	0.2788	0.0777	-0.4347	-0.1502	0.1196	0.3656	-0.0997
0.25	-0.6788	-0.2647	-0.0569	0.0729	-0.9275	-0.7012	-0.4777	-0.0918	0.1614	-1.1093
0.30	-0.9462	-0.5764	-0.2801	-0.1279	-1.9306	-0.9680	-0.7842	-0.3101	-0.0395	-2.1018
0.35	-1.2131	-0.8902	-0.4961	-0.3406	-2.9400	-1.2336	-1.1012	-0.5189	-0.2852	-3.1389
0.4	-1.4814	-1.2084	-0.7053	-0.5385	-3.9336	-1.5021	-1.4177	-0.7255	-0.4501	-4.0954
0.5	-1.7479	-1.5252	-0.9525	-0.7288	-4.9544	-1.7679	-1.7323	-0.8676	-0.6337	-5.0015
0.5	-2.0135	-1.8381	-1.1513	-0.8696	-5.8725	-2.0316	-2.0525	-1.1752	-0.7415	-6.0008

Table C.19

^{194}Au					
$\hbar\omega$	$e'(e)$	$e'(A)$	$e'(C)$	$e'(F)$	$e'(eFAC)$
0	0.6123	0.8762	0.9272	0.7844	3.2001
0.05	0.3480	0.5604	0.7569	0.7623	2.4276
0.10	0.0830	0.2439	0.5659	0.7159	1.6087
0.15	-0.1825	-0.0228	0.3655	0.6286	0.7888
0.20	-0.4485	-0.3889	0.1595	0.4826	-0.1953
0.25	-0.7142	-0.7048	-0.0482	0.3013	-1.1659
0.30	-0.9798	-1.0194	-0.2464	0.1091	-2.1365

Table C.19 (Continued)

$\hbar\omega$	$e'(e)$	$e'(A)$	$e'(C)$	$e'(F)$	$e'(eFAC)$
0.35	-1.2342	-1.3360	-0.4737	-0.0831	-3.1270
0.40	-1.5123	-1.6463	-0.6826	-0.3032	-4.1444
0.45	-1.7764	-1.9249	-0.8788	-0.4865	-5.0666
0.50	-2.0346	-2.2835	-1.1367	-0.6760	-6.1308

Table C.20-24: Rotational frequency $\hbar\omega$ (MeV), total quasiparticle Routhians $e'(eFAB)$ (MeV), $e'(eFBC)$ (MeV), $e'(eFAC)$ (MeV) and signature splitting $[e'(eFAB) - e'(eFBC)]$ (MeV), $[e'(eFAB) - e'(eFAC)]$ (MeV), $[e'(eFBC) - e'(eFAC)]$ (MeV) for the 20^+ , 21^+ and 22^+ bands of the odd-odd $^{186-194}\text{Au}$ nuclei.

Table C.20

^{186}Au						
$\hbar\omega$	$e'(eFAB)$	$e'(eFBC)$	$e'(eFAC)$	$e'(eFAB) - e'(eFBC)$	$e'(eFAB) - e'(eFAC)$	$e'(eFBC) - e'(eFAC)$
0	3.9641	4.0539	4.0813	-0.0898	-0.1172	-0.0274
0.05	3.3123	3.2856	3.3866	0.0267	-0.0743	-0.1010
0.10	2.5437	2.3791	2.6091	0.1646	-0.0654	-0.2300
0.15	1.6871	1.4343	1.6673	0.2528	0.0198	-0.2330
0.20	0.6522	0.4646	0.6660	0.1876	-0.0138	-0.2014
0.25	-1.0173	-0.2660	-0.3372	-0.7513	-0.6801	0.0712
0.30	-1.4098	-1.2226	-1.3393	-0.1872	-0.0705	0.1167
0.35	-2.6661	-2.1982	-2.3425	-0.4679	-0.3236	0.1443
0.40	-3.6678	-3.1241	-3.3433	-0.5437	-0.3245	0.2192
0.45	-4.7284	-4.0443	-4.3372	-0.6841	-0.3912	0.2929
0.50	-5.7661	-4.9574	-5.3118	-0.8087	-0.4543	0.3544

Table C.21

^{188}Au						
$\hbar\omega$	$e'(eFAB)$	$e'(eFBC)$	$e'(eFAC)$	$e'(eFAB) - e'(eFBC)$	$e'(eFAB) - e'(eFAC)$	$e'(eFBC) - e'(eFAC)$
0	4.2762	3.7319	3.7890	0.5443	0.4872	-0.0571
0.05	3.4518	2.8792	3.2231	0.5726	0.2287	-0.3439
0.10	2.3954	1.9287	2.3689	0.4667	0.0265	-0.4402
0.15	1.3356	0.9674	1.3664	0.3682	-0.0308	-0.3990
0.20	0.2788	-0.0009	0.3616	0.2797	-0.0828	-0.3625
0.25	-0.7720	-0.9799	-0.6438	0.2080	-0.1281	-0.3361
0.30	-2.0100	-1.7849	-1.6470	-0.2254	-0.3633	-0.1379
0.35	-3.0220	-2.7673	-2.6522	-0.2545	-0.3696	-0.1151
0.40	-4.0650	-3.7398	-3.6510	-0.3250	-0.4138	-0.0888
0.45	-5.0930	-4.7098	-4.6587	-0.3829	-0.4340	-0.0511
0.50	-6.1230	-5.6280	-5.6157	-0.4950	-0.5073	-0.0123

Table C.22

¹⁹⁰ Au						
$\hbar\omega$	e'(eFAB)	e'(eFBC)	e'(eFAC)	e'(eFAB)- e'(eFBC)	e'(eFAB)- e'(eFAC)	e'(eFBC)- e'(eFAC)
0	4.1064	3.4605	3.5161	0.6459	0.5903	-0.0556
0.05	3.0473	2.5119	3.0835	0.5354	-0.0362	-0.5716
0.10	1.9854	1.5483	2.0865	0.4371	-0.1011	-0.5382
0.15	0.9239	0.5879	1.0833	0.3360	-0.1594	-0.4954
0.20	-0.1347	-0.3821	0.0777	0.2474	-0.2124	-0.4598
0.25	-1.1834	-1.3600	-0.9275	0.1766	-0.2559	-0.4325
0.30	-2.3541	-2.2207	-1.9306	-0.1334	-0.4235	-0.2901
0.35	-3.3851	-3.2121	-2.9400	-0.1730	-0.4451	-0.2721
0.40	-4.4331	-4.1773	-3.9336	-0.2558	-0.4995	-0.2437
0.45	-5.4861	-5.1671	-4.9544	-0.3190	-0.5317	-0.2127
0.50	-6.6189	-6.1876	-5.8725	-0.4313	-0.7464	-0.3151

Table C.23

¹⁹² Au						
$\hbar\omega$	e'(eFAB)	e'(eFBC)	e'(eFAC)	e'(eFAB)- e'(eFBC)	e'(eFAB)- e'(eFAC)	e'(eFBC)- e'(eFAC)
0	3.5528	3.1425	3.2765	0.4103	0.2763	-0.1340
0.05	2.6431	2.5037	2.8152	0.1394	-0.1721	-0.3115
0.10	1.5912	1.5496	1.8951	0.0416	-0.3039	-0.3455
0.15	0.5601	0.5355	0.8999	0.0246	-0.3398	-0.3644
0.20	-0.5540	-0.3239	-0.0997	-0.2301	-0.4543	-0.2242
0.25	-1.6050	-1.2780	-1.1093	-0.3270	-0.4957	-0.1687
0.30	-2.6490	-2.2340	-2.1018	-0.4150	-0.5472	-0.1322
0.35	-3.7130	-3.1888	-3.1389	-0.5240	-0.5739	-0.0499
0.40	-4.7470	-4.1177	-4.0954	-0.6288	-0.6511	-0.0223
0.45	-5.7720	-5.1038	-5.0015	-0.6681	-0.7704	-0.1023
0.50	-6.9120	-6.0881	-6.0008	-0.8236	-0.9109	-0.0873

Table C.24

¹⁹⁴ Au						
$\hbar\omega$	e'(eFAB)	e'(eFBC)	e'(eFAC)	e'(eFAB)- e'(eFBC)	e'(eFAB)- e'(eFAC)	e'(eFBC)- e'(eFAC)
0	2.8104	3.1947	3.2001	-0.3843	-0.3897	-0.0054
0.05	2.2209	2.3619	2.4276	-0.1410	-0.2067	-0.0657
0.10	1.2700	1.5715	1.6087	-0.3015	-0.3387	-0.0372
0.15	0.2274	0.6825	0.7888	-0.4551	-0.5614	-0.1063
0.20	-0.8264	-0.2550	-0.1953	-0.5714	-0.6311	-0.0597
0.25	-1.8795	-1.2000	-1.1659	-0.6795	-0.7136	-0.0341
0.30	-2.9170	-2.1594	-2.1365	-0.7576	-0.7805	-0.0229
0.35	-4.0094	-3.0690	-3.1270	-0.9404	-0.8824	0.0580
0.40	-5.0273	-4.0417	-4.1444	-0.9856	-0.8829	0.1027
0.45	-6.0337	-5.0001	-5.0666	-1.0336	-0.9671	0.0665
0.50	-7.1730	-5.9759	-6.1308	-1.1971	-1.0422	0.1549

Table C.25-30: Rotational frequency $\hbar\omega$ (MeV), quasiproton Routhians $e'(e)$ (MeV), quasineutron Routhians $e'(A)$ (MeV), $e'(B)$ (MeV), $e'(C)$ (MeV) and the total quasiparticle Routhians $e'(eAB)$ (MeV), $e'(eBC)$ (MeV) and $e'(eAC)$ (MeV) for the $31/2^-$, $33/2^-$ and $35/2^-$ bands of the odd-even $^{187-193}\text{Au}$ nuclei.

Table C.25

^{187}Au									
$\hbar\omega$	$e'(e)$	$e'(A)$	$e'(B)$	$e'(eAB)$		$e'(e)$	$e'(C)$	$e'(B)$	$e'(eBC)$
0.05	0.7678	0.8151	0.8259	2.4088		0.5490	1.1627	0.8667	2.5784
0.10	0.5399	0.5324	0.5769	1.6492		0.2901	0.8545	0.6185	1.7631
0.15	0.2974	0.2322	0.3209	0.8505		0.0297	0.5844	0.3585	0.9726
0.20	0.0489	-0.0760	-0.0610	-0.0881		-0.2316	0.3356	0.0957	0.1997
0.25	-0.1997	-0.3820	-0.1950	-0.7767		-0.4939	0.1037	-0.1678	-0.5580
0.30	-0.4582	-0.6918	-0.4481	-1.5981		-0.7559	-0.1161	-0.4293	-1.3013
0.35	-0.7108	-1.0203	-0.7280	-2.4591		-1.0154	-0.3403	-0.6992	-2.0549
0.40	-0.9885	-1.3157	-0.9769	-3.2811		-1.2835	-0.5538	-0.9605	-2.7978
0.45	-1.2305	-1.6203	-1.2266	-4.0774		-1.5441	-0.7562	-1.2210	-3.5213
0.50	-1.4840	-1.9599	-1.4974	-4.9413		-1.8029	-0.9763	-1.4837	-4.2629

Table C.26

^{189}Au									
$\hbar\omega$	$e'(e)$	$e'(A)$	$e'(B)$	$e'(eAB)$		$e'(e)$	$e'(C)$	$e'(B)$	$e'(eBC)$
0.05	0.5860	0.7791	0.7694	2.1345		0.5138	0.9660	0.7760	2.2558
0.10	0.3332	0.5039	0.5111	1.3482		0.2551	0.6952	0.5148	1.4651
0.15	0.0771	0.2021	0.2500	0.5292		-0.0053	0.4571	0.2515	0.7033
0.20	-0.1806	-0.1072	-0.0116	-0.2994		-0.2662	0.2365	-0.0122	-0.0419
0.25	-0.4406	-0.4198	-0.2741	-1.1345		-0.5286	0.0208	-0.2760	-0.7838
0.30	-0.6995	-0.7304	-0.5319	-1.9618		-0.7903	-0.1906	-0.5372	-1.5181
0.35	-0.9504	-1.0505	-0.7965	-2.7974		-1.0443	-0.4002	-0.8010	-2.2455
0.40	-1.2247	-1.3596	-1.0535	-3.6378		-1.3178	-0.6024	-1.0600	-2.9802
0.45	-1.4824	-1.6710	-1.2887	-4.4421		-1.5780	-0.8801	-1.3495	-3.8076
0.50	-1.7368	-1.9853	-1.5715	-5.2936		-1.8343	-1.0425	-1.5826	-4.4594

Table C.27

^{191}Au									
$\hbar\omega$	$e'(e)$	$e'(A)$	$e'(B)$	$e'(eAB)$		$e'(e)$	$e'(C)$	$e'(B)$	$e'(eBC)$
0.05	0.4844	0.7154	0.6705	1.8703		0.4502	0.8212	0.6631	1.9345
0.10	0.2265	0.4252	0.4126	1.0643		0.1892	0.5817	0.4033	1.1742
0.15	-0.0332	0.1149	0.1526	0.2343		-0.0728	0.3724	0.1418	0.4414
0.20	-0.2927	-0.1981	-0.1075	-0.5983		-0.3342	0.1655	-0.1199	-0.2886
0.25	-0.5554	-0.5128	-0.3681	-1.4363		-0.5986	-0.0416	-0.3819	-1.0221
0.30	-0.8162	-0.8260	-0.6419	-2.2841		-0.8614	-0.2598	-0.6515	-1.7727
0.35	-1.0110	-1.1403	-0.8850	-3.0363		-1.1064	-0.4573	-0.9022	-2.4659
0.40	-1.3433	-1.4527	-1.1318	-3.9278		-1.3902	-0.6509	-1.1515	-3.1926
0.45	-1.6023	-1.7609	-1.4566	-4.8198		-1.6512	-0.9548	-1.4654	-4.0714
0.50	-1.8533	-2.0779	-1.6755	-5.6067		-1.9062	-1.1147	-1.6932	-4.7141

Table C.28

¹⁹³ Au									
$\hbar\omega$	e'(e)	e'(A)	e'(B)	e'(eAB)		e'(e)	e'(C)	e'(B)	e'(eBC)
0.05	0.4139	0.6106	0.5627	1.5872		0.3918	0.7311	0.5550	1.6779
0.10	0.1522	0.2953	0.3075	0.7550		0.1288	0.5438	0.2982	0.9708
0.15	-0.1105	-0.0202	0.0491	-0.0816		-0.1349	0.3460	0.0388	0.2499
0.20	-0.3749	-0.3356	-0.2110	-0.9215		-0.3997	0.1426	-0.2222	-0.4793
0.25	-0.6376	-0.6505	-0.4692	-1.7573		-0.6636	-0.0617	-0.4817	-1.2070
0.30	-0.9008	-0.9643	-0.7468	-2.6119		-0.9277	-0.2908	-0.7574	-1.9759
0.35	-1.1728	-1.2788	-0.9901	-3.4417		-1.2001	-0.4828	-1.0040	-2.6869
0.40	-1.4304	-1.5884	-1.2323	-4.2511		-1.4582	-0.6828	-1.2477	-3.3887
0.45	-1.6915	-1.9398	-1.5618	-5.1931		-1.7202	-0.9923	-1.5699	-4.2824
0.50	-1.9393	-2.2218	-1.7888	-5.9499		-1.9702	-1.1441	-1.8017	-4.9160

Table C.29

¹⁸⁷ Au					¹⁸⁹ Au				
$\hbar\omega$	e'(e)	e'(A)	e'(C)	e'(eAC)		e'(e)	e'(A)	e'(C)	e'(eAC)
0.05	0.5998	0.8574	1.1164	2.5736		0.5192	0.7892	0.9586	2.2670
0.10	0.3426	0.6177	0.8068	1.7671		0.2598	0.5441	0.6878	1.4917
0.15	0.0832	0.3482	0.5519	0.9833		-0.0012	0.2578	0.4516	0.7082
0.20	-0.1774	0.0556	0.3172	0.1954		-0.2629	-0.0473	0.2316	-0.0786
0.25	-0.4392	-0.2484	0.0937	-0.5939		-0.5257	-0.3604	0.0161	-0.8700
0.30	-0.7007	-0.5576	-0.1205	-1.3788		-0.7881	-0.6706	-0.1968	-1.6555
0.35	-0.9602	-0.8627	-0.3439	-2.1668		-1.0428	-0.9916	-0.4059	-2.4403
0.40	-1.2276	-1.1838	-0.5557	-2.9671		-1.3162	-1.3013	-0.6091	-3.2266
0.45	-1.4881	-1.4949	-0.7621	-3.7451		-1.5773	-1.6147	-0.8780	-4.0700
0.50	-1.7472	-1.8411	-0.9743	-4.5626		-1.8346	-1.9317	-1.0474	-4.8137

Table C.30

¹⁹¹ Au					¹⁹³ Au				
$\hbar\omega$	e'(e)	e'(A)	e'(C)	e'(eAC)		e'(e)	e'(A)	e'(C)	e'(eAC)
0.05	0.4586	0.7259	0.8120	1.9965		0.4150	0.6091	0.7283	1.7524
0.10	0.1979	0.4480	0.5822	1.2281		0.1535	0.2939	0.5447	0.9921
0.15	-0.0641	0.1386	0.3750	0.4495		-0.1089	-0.0214	0.3494	0.2191
0.20	-0.3255	-0.1750	0.1685	-0.3320		-0.3731	-0.3366	0.1479	-0.5618
0.25	-0.5900	-0.4904	-0.0386	-1.1190		-0.6356	-0.6514	-0.0541	-1.3411
0.30	-0.8528	-0.8049	-0.2561	-1.9138		-0.8985	-0.9649	-0.2871	-2.1505
0.35	-1.1324	-1.1203	-0.4541	-2.7068		-1.1704	-1.2793	-0.4730	-2.9227
0.40	-1.3817	-1.4342	-0.6481	-3.4640		-1.4278	-1.5885	-0.6693	-3.6856
0.45	-1.6428	-1.7458	-0.9487	-4.3373		-1.6885	-1.9395	-0.9915	-4.6195
0.50	-1.8965	-2.0619	-1.1104	-5.0688		-1.9345	-2.2218	-1.1369	-5.2932

Table C.31-34: Rotational frequency $\hbar\omega$ (MeV), total quasiparticle Routhians $e'(eAB)$ (MeV), $e'(eAC)$ (MeV), $e'(eBC)$ (MeV) and signature splitting [$e'(eAB) - e'(eAC)$] (MeV), [$e'(eAB) - e'(eBC)$] (MeV), [$e'(eAC) - e'(eBC)$] (MeV) for the $31/2^-$, $33/2^-$ and $35/2^-$ bands of the odd-even $^{187-193}\text{Au}$ nuclei.

Table C.31

^{187}Au						
$\hbar\omega$	$e'(eAB)$	$e'(eAC)$	$e'(eBC)$	$e'(eAB) - e'(eAC)$	$e'(eAB) - e'(eBC)$	$e'(eAC) - e'(eBC)$
0.05	2.4088	2.5736	2.5784	-0.1648	-0.1696	-0.0048
0.10	1.6492	1.7671	1.7631	-0.1179	-0.1139	0.0040
0.15	0.8505	0.9833	0.9726	-0.1328	-0.1221	0.0107
0.20	-0.0881	0.1954	0.1997	-0.2835	-0.2878	-0.0043
0.25	-0.7767	-0.5939	-0.5580	-0.1828	-0.2187	-0.0359
0.30	-1.5981	-1.3788	-1.3013	-0.2193	-0.2968	-0.0775
0.35	-2.4591	-2.1668	-2.0549	-0.2923	-0.4042	-0.1119
0.40	-3.2811	-2.9671	-2.7978	-0.3140	-0.4833	-0.1693
0.45	-4.0774	-3.7451	-3.5213	-0.3323	-0.5561	-0.2238
0.50	-4.9413	-4.5626	-4.2629	-0.3787	-0.6784	-0.2997

Table C.32

^{189}Au						
$\hbar\omega$	$e'(eAB)$	$e'(eAC)$	$e'(eBC)$	$e'(eAB) - e'(eAC)$	$e'(eAB) - e'(eBC)$	$e'(eAC) - e'(eBC)$
0.05	2.1345	2.2670	2.2558	-0.1325	-0.1213	0.0112
0.10	1.3482	1.4917	1.4651	-0.1435	-0.1169	0.0266
0.15	0.5292	0.7082	0.7033	-0.1790	-0.1741	0.0049
0.20	-0.2994	-0.0786	-0.0419	-0.2208	-0.2575	-0.0367
0.25	-1.1345	-0.8700	-0.7838	-0.2645	-0.3507	-0.0862
0.30	-1.9618	-1.6555	-1.5181	-0.3063	-0.4437	-0.1374
0.35	-2.7974	-2.4403	-2.2455	-0.3571	-0.5519	-0.1948
0.40	-3.6378	-3.2266	-2.9802	-0.4112	-0.6576	-0.2464
0.45	-4.4421	-4.0700	-3.8076	-0.3721	-0.6345	-0.2624
0.50	-5.2936	-4.8137	-4.4594	-0.4799	-0.8342	-0.3543

Table C.33

^{191}Au						
$\hbar\omega$	$e'(eAB)$	$e'(eAC)$	$e'(eBC)$	$e'(eAB) - e'(eAC)$	$e'(eAB) - e'(eBC)$	$e'(eAC) - e'(eBC)$
0.05	1.8703	1.9965	1.9345	-0.1262	-0.0642	0.0620
0.10	1.0643	1.2281	1.1742	-0.1638	-0.1099	0.0539
0.15	0.2343	0.4495	0.4414	-0.2152	-0.2071	0.0081
0.20	-0.5983	-0.3320	-0.2886	-0.2663	-0.3097	-0.0434
0.25	-1.7063	-1.1190	-1.0221	-0.5873	-0.6842	-0.0969
0.30	-2.2841	-1.9138	-1.7727	-0.3703	-0.5114	-0.1411
0.35	-3.0363	-2.7068	-2.4659	-0.3295	-0.5704	-0.2409
0.40	-3.9278	-3.4640	-3.1926	-0.4638	-0.7352	-0.2714
0.45	-4.8198	-4.3373	-4.0714	-0.4825	-0.7484	-0.2659
0.50	-5.6067	-5.0688	-4.7141	-0.5379	-0.8926	-0.3547

Table C.34

¹⁹³ Au							
$\hbar\omega$	e'(eAB)	e'(eAC)	e'(eBC)	e'(eAB)- e'(eAC)	e'(eAB)- e'(eBC)	e'(eAC)- e'(eBC)	
0.05	1.5872	1.7524	1.6779	-0.1652	-0.0907	0.0745	
0.10	0.7550	0.9921	0.9708	-0.2371	-0.2158	0.0213	
0.15	-0.0816	0.2191	0.2499	-0.3007	-0.3315	-0.0308	
0.20	-0.9215	-0.5618	-0.4793	-0.3597	-0.4422	-0.0825	
0.25	-1.7573	-1.3411	-1.2070	-0.4162	-0.5503	-0.1341	
0.30	-2.6119	-2.1505	-1.9759	-0.4614	-0.6360	-0.1746	
0.35	-3.4417	-2.9227	-2.6869	-0.5190	-0.7548	-0.2358	
0.40	-4.2511	-3.6856	-3.3887	-0.5655	-0.8624	-0.2969	
0.45	-5.1931	-4.6195	-4.2824	-0.5736	-0.9107	-0.3371	
0.50	-5.9499	-5.2932	-4.9160	-0.6567	-1.0339	-0.3772	

Table C.35-38: Rotational frequency $\hbar\omega$ (MeV), quasiproton Routhians $e'(e)$ (MeV), quasineutron Routhians $e'(A)$ (MeV), $e'(B)$ (MeV), $e'(F)$ (MeV) and the total quasiparticle Routhians $e'(eAF)$ (MeV), and $e'(eBF)$ (MeV) for the $31/2^+$ and $33/2^+$ bands of the odd-even ¹⁸⁷⁻¹⁹³Au nuclei.

Table C.35

¹⁸⁷ Au									
$\hbar\omega$	e'(e)	e'(A)	e'(F)	e'(eAF)		e'(e)	e'(B)	e'(F)	e'(eBF)
0	0.6814	1.8168	1.0240	3.5222		0.6826	1.0492	1.0450	2.7768
0.05	0.4138	1.5368	0.8219	2.7725		0.4160	0.9015	0.8437	2.1612
0.10	0.1459	1.1840	0.6048	1.9347		0.1490	0.6620	0.6396	1.4506
0.15	-0.1221	0.8664	0.4107	1.1550		-0.1182	0.3987	0.4340	0.7145
0.20	-0.3902	0.5557	0.2035	0.3690		-0.3855	0.1319	0.2276	-0.0260
0.25	-0.6584	0.2474	-0.0039	-0.4149		-0.6530	-0.1358	0.0211	-0.7677
0.30	-0.9265	-0.3044	-0.2113	-1.4422		-0.9204	-0.4034	-0.1815	-1.5053
0.35	-1.1946	-0.5566	-0.4184	-2.1696		-1.1877	-0.6718	-0.3937	-2.2532
0.40	-1.4600	-0.8215	-0.6231	-2.9046		-1.4559	-0.9389	-0.5949	-2.9897
0.45	-1.7306	-1.1285	-0.8217	-3.6808		-1.7223	-1.2055	-0.7982	-3.7260
0.50	-1.9980	-1.4326	-1.0179	-4.4485		-1.9886	-1.4713	-0.9856	-4.4455
0.55	-2.2646	-1.7367	-1.1829	-5.1842		-2.2527	-1.7789	-1.1582	-5.1898

Table C.36

¹⁸⁹ Au									
$\hbar\omega$	e'(e)	e'(A)	e'(F)	e'(eAF)		e'(e)	e'(B)	e'(F)	e'(eBF)
0	0.6533	1.6162	0.9825	3.2520		0.6435	0.9614	0.9929	2.5978
0.05	0.3855	1.2992	0.7793	2.4640		0.3756	0.7884	0.7884	1.9524
0.10	0.1174	0.9830	0.5737	1.6741		0.1075	0.5196	0.5818	1.2089
0.15	-0.1508	0.6687	0.3671	0.8850		-0.1608	0.2506	0.3743	0.4641
0.20	-0.4191	0.3583	0.1603	0.0995		-0.4292	-0.0183	0.1665	-0.2810
0.25	-0.6874	0.0569	-0.0462	-0.6767		-0.6976	-0.2870	0.0410	-0.9436
0.30	-0.9557	-0.3967	-0.2531	-1.6055		-0.9660	-0.5552	-0.2495	-1.7707
0.35	-1.2238	-0.6792	-0.4581	-2.3611		-1.2343	-0.8228	-0.4562	-2.5133

Table C.36 (Continued)

$\hbar\omega$	e'(e)	e'(A)	e'(F)	e'(eAF)		e'(e)	e'(B)	e'(F)	e'(eBF)
0.40	-1.4974	-0.9878	-0.6573	-3.1425		-1.5035	-1.0890	-0.6566	-3.2491
0.45	-1.7601	-1.2941	-0.8497	-3.9039		-1.7708	-1.3762	-0.8523	-3.9993
0.50	-2.0276	-1.6077	-1.0031	-4.6384		-2.0384	-1.6233	-1.0101	-4.6718
0.55	-2.2943	-1.9363	-1.3499	-5.5805		-2.3045	-1.8839	-1.3378	-5.5262

Table C.37

¹⁹¹ Au									
$\hbar\omega$	e'(e)	e'(A)	e'(F)	e'(eAF)		e'(e)	e'(B)	e'(F)	e'(eBF)
0	0.6200	1.3302	0.8959	2.8461		0.6106	0.8866	0.8852	2.3824
0.05	0.3533	1.0149	0.8509	2.2191		0.3421	0.6216	0.7642	1.7279
0.10	0.0863	0.7031	0.6453	1.4347		0.0733	0.3545	0.5560	0.9838
0.15	-0.1809	0.4039	0.4390	0.6620		-0.1955	0.0867	0.3474	0.2386
0.20	-0.4482	0.0132	0.2332	-0.2018		-0.4645	-0.1812	0.1391	-0.5066
0.25	-0.7158	-0.2883	0.0287	-0.9754		-0.7334	-0.4489	-0.0682	-1.2505
0.30	-0.9832	-0.6014	-0.1688	-1.7534		-1.0024	-0.7209	-0.2781	-2.0014
0.35	-1.2502	-0.9164	-0.381	-2.5476		-1.2712	-0.9831	-0.4812	-2.7355
0.40	-1.5184	-1.2334	-0.5753	-3.3271		-1.5409	-1.2461	-0.6781	-3.4651
0.45	-1.7848	-1.5499	-0.7525	-4.0872		-1.8087	-1.5299	-0.8501	-4.1887
0.50	-2.0506	-1.8656	-1.0491	-4.9653		-2.0768	-1.7832	-1.1406	-5.0006
0.55	-2.308	-2.1826	-1.1945	-5.6851		-2.3436	-2.0398	-1.3458	-5.7292

Table C.38

¹⁹³ Au									
$\hbar\omega$	e'(e)	e'(A)	e'(F)	e'(eAF)		e'(e)	e'(B)	e'(F)	e'(eBF)
0	0.6272	0.7998	0.8801	2.3071		0.5828	0.7402	0.8966	2.2196
0.05	0.3637	0.6625	0.8564	1.8826		0.3147	0.4771	0.8333	1.6251
0.10	0.0993	0.3470	0.7962	1.2425		0.0464	0.2120	0.6256	0.8840
0.15	-0.1656	0.0305	0.6581	0.5230		-0.2220	-0.0539	0.4179	0.1420
0.20	-0.4312	-0.2859	0.4713	-0.2458		-0.4905	-0.3203	0.2111	-0.5997
0.25	-0.6963	-0.6021	0.2743	-1.0241		-0.7591	-0.5864	0.0064	-1.3391
0.30	-0.9614	-0.9176	0.0762	-1.8028		-1.0276	-0.8589	-0.1877	-2.0742
0.35	-1.2446	-1.2333	-0.1157	-2.5936		-1.2954	-1.1184	-0.4028	-2.8166
0.40	-1.4932	-1.5459	-0.3414	-3.3805		-1.5651	-1.3775	-0.5880	-3.5306
0.45	-1.7567	-1.8414	-0.5264	-4.1245		-1.8326	-1.6682	-0.8713	-4.3721
0.50	-2.0135	-2.1801	-0.6984	-4.8920		-2.1000	-1.9183	-1.0321	-5.0504
0.55	-2.3001	-2.4850	-0.9111	-5.6962		-2.3646	-2.1715	-1.2092	-5.7453

Table C.39-40: Rotational frequency $\hbar\omega$ (MeV), total quasiparticle Routhians $e'(eAF)$ (MeV), $e'(eBF)$ (MeV) and signature splitting $e'(eAF) - e'(eBF)$ (MeV) for the $31/2^+$ and $33/2^+$ bands of the odd-even $^{187-193}\text{Au}$ nuclei.

Table C.39

^{187}Au				^{189}Au		
$\hbar\omega$	$e'(eAF)$	$e'(eBF)$	$e'(eAF) - e'(eBF)$	$e'(eAF)$	$e'(eBF)$	$e'(eAF) - e'(eBF)$
0	3.5222	2.7768	0.7454	3.2520	2.5978	0.6542
0.05	2.7725	2.1612	0.6113	2.4640	1.9524	0.5116
0.10	1.9347	1.4506	0.4841	1.6741	1.2089	0.4652
0.15	1.1550	0.7145	0.4405	0.8850	0.4641	0.4209
0.20	0.3690	-0.0260	0.3950	0.0995	-0.2810	0.3805
0.25	-0.4149	-0.7677	0.3528	-0.6767	-0.9436	0.2669
0.30	-1.4422	-1.5053	0.0631	-1.6055	-1.7707	0.1652
0.35	-2.1696	-2.2532	0.0836	-2.3611	-2.5133	0.1522
0.40	-2.9046	-2.9897	0.0851	-3.1425	-3.2491	0.1066
0.45	-3.6808	-3.7260	0.0452	-3.9039	-3.9993	0.0954
0.50	-4.4485	-4.4455	-0.0030	-4.6384	-4.6718	0.0334
0.55	-5.1842	-5.1898	0.0056	-5.5805	-5.5262	-0.0543

Table C.40

^{191}Au				^{193}Au		
$\hbar\omega$	$e'(eAF)$	$e'(eBF)$	$e'(eAF) - e'(eBF)$	$e'(eAF)$	$e'(eBF)$	$e'(eAF) - e'(eBF)$
0	2.8461	2.3824	0.4637	2.3071	2.2196	0.0875
0.05	2.2191	1.7279	0.4912	1.8826	1.6251	0.2575
0.10	1.4347	0.9838	0.4509	1.2425	0.8840	0.3585
0.15	0.6620	0.2386	0.4234	0.5230	0.1420	0.3810
0.20	-0.2018	-0.5066	0.3048	-0.2458	-0.5997	0.3539
0.25	-0.9754	-1.2505	0.2751	-1.0241	-1.3391	0.3150
0.30	-1.7534	-2.0014	0.2480	-1.8028	-2.0742	0.2714
0.35	-2.5476	-2.7355	0.1879	-2.5936	-2.8166	0.2230
0.40	-3.3271	-3.4651	0.1380	-3.3805	-3.5306	0.1501
0.45	-4.0872	-4.1887	0.1015	-4.1245	-4.3721	0.2476
0.50	-4.9653	-5.0006	0.0353	-4.8920	-5.0504	0.1584
0.55	-5.6851	-5.7292	0.0441	-5.6962	-5.7453	0.0491